FIBER REINFORCED CONCRETE: CHARACTERIZATION OF FLEXURAL TOUGHNESS & SOME STUDIES ON FIBER-MATRIX BOND-SLIP INTERACTION

by

Ashish Dubey

B.Eng., Devi Ahilya University, 1988
M.Eng., Rani Durgavati University, 1991
M.A.Sc., The University of British Columbia, 1993

A THESIS SUBMITTED IN PARTIAL FULFILLMENT OF
THE REQUIREMENTS FOR THE DEGREE OF
DOCTOR OF PHILOSOPHY

in

THE FACULTY OF GRADUATE STUDIES
(The Department of Civil Engineering)

We accept this thesis as conforming
to the required standard

THE UNIVERSITY OF BRITISH COLUMBIA
April, 1999

In presenting this thesis in partial fulfilment of the requirements for an advanced degree at the University of British Columbia, I agree that the Library shall make it freely available for reference and study. I further agree that permission for extensive copying of this thesis for scholarly purposes may be granted by the head of my department or by his or her representatives. It is understood that copying or publication of this thesis for financial gain shall not be allowed without my written permission.

Department of Civil Engineering

The University of British Columbia
Vancouver, Canada

Date April 30, 1999

Abstract

One major problem associated with the testing of fiber reinforced concrete specimens under flexural loading is that the measured post-cracking response is severely affected by the stiffness of the testing machine. As a consequence, misleading results are obtained when such a flexural response is used for the characterization of composite toughness. Unfortunately, many existing standards allow the use of such a flexural response for toughness characterization. As a part of this research program, assessment of a new toughness characterization technique termed the Residual Strength Test Method (RSTM) has been made. In this technique, a stable narrow crack is first created in the specimen by applying a flexural load in parallel with a steel plate under controlled conditions. The plate is then removed, and the specimen is tested in a routine manner in flexure to obtain the post-crack load versus displacement response. Flexural response for a variety of fiber reinforced cementitious composites obtained using the Residual Strength Test Method has been found to correlate very well with those obtained with relatively stiffer test configurations such as closed-loop test machines. A good agreement between the flexural response obtained from the aforementioned methods seems to validate the Residual Strength Test Method. This method is simple, and can be carried out easily in any commercial laboratory equipped with a test machine with low stiffness. The Residual Strength Test Method is found to be effective in differentiating between different fiber types, fiber lengths, fiber configurations, fiber volume fractions, fiber geometries and fiber moduli. In particular, the technique has been found to be extremely useful for testing cement-based composites containing fibers at very low dosages (< 0.5% by volume).

As another major objective of this research program, an analytical model based on shear lag theory is introduced to study the problem of fiber pullout in fiber reinforced composites. The proposed model eliminates limitations of many earlier models and captures essential features of pullout process, including progressive interfacial debonding, Poisson's effect, and variation in interfacial properties during the fiber pullout process. Interfacial debonding is modeled using an interfacial shear strength criterion. Influence of normal contact stress at the fiber-matrix interface is considered using shrink-fit theory, and the interfacial frictional shear stress over the

debonded interface is modeled using Coulomb's Law. Stresses required to cause initial, partial and complete debonding of the fiber-matrix interface are analyzed, and closed form solutions are derived to predict the complete fiber pullout response. Analysis shows that the initial debonding stress strongly depends upon fiber length and fiber elastic modulus. The process of interfacial debonding turns catastrophic at the instant the fiber pullout stress begins to drop with an increase in debond length. This condition is satisfied when the difference between the change in the frictional component and the adhesional component of pullout stress occurring due to increase in debond length equals to zero. The magnitude of interfacial frictional shear stress along the embedded fiber length is found to vary as a result of the Poisson's contraction of the fiber. Moreover, Poisson's effect manifests itself in the form of a non-linear relationship between the peak pullout stress versus embedded fiber length plot. Based on energy considerations, an analytical solution is derived to compute the interfacial coefficient of friction. This solution depicts the dependence of the interfacial coefficient of friction on fiber pullout distance. For both steel and polypropylene fibers, interfacial coefficient of friction is found to decrease exponentially with increase in pullout distance. Matrix wear resulting from fiber pullout appears to be responsible for the aforementioned physical phenomena. Parametric studies are carried out to investigate the influence of fiber-matrix interfacial properties (adhesional bond shear strength, normal contact stress and coefficient of friction) and elastic modulus of the fiber. Results suggest that for a given set of interfacial properties, initial debonding stress, maximum pullout stress, stability of debonding process, catastrophic debond length, interfacial shear stress distribution, and overall pullout response significantly depend upon the elastic modulus of the fiber. Given the fiber elastic modulus, recommendations are made as to how efficiency of fiber in pullout may be improved by modifying different interfacial properties..

Table of Contents

Abstract		ii
Table of Contents		iv
List of Tables		ix
List of Figures		xi
Notations		xx
Acknowledgement		xxiii
1	Introduction	1
	1.0 Objectives and Scope	2
	1.1 Thesis Organization	3
2	Literature Review	5
	2.0 Introduction	5
	2.1 Issues of Significance Concerning Characterization of Toughness of Fiber Reinforced Concretes	6
	2.2 Micromechanical Models for Investigating the Fiber-Matrix Interfacial Behavior	10
	2.3 Experimental Studies on the Fiber Pullout Behavior	26
	2.4 Mechanical Behavior of Fiber Reinforced Cementitious Composites	30
3	Macromechanical Behavior of Fiber Reinforced Concrete (FRC) & Measurement of Flexural Response of Low Toughness FRC	37
	3.0 Introduction	37

3.1 Material Variables Influencing Macromechanical Behavior and Toughness of FRC 38
3.1.1 Mineral Admixtures 40
3.1.2 Fiber Volume Content 44
3.1.3 Fiber Aspect Ratio 46
3.1.4 Surface Characteristics of Fiber 47
3.1.5 Fiber Geometry 50
3.1.6 Shrinkage Properties of Matrix 51
3.2 Characterization of Flexural Toughness of Fiber Reinforced Concretes 53
3.2.1 Residual Strength Test Method (RSTM) – Assessment and Calibration 55
3.2.1.1 Experimental Procedure 57
3.2.1.2 Results 60
3.2.1.3 A Round-Robin Test Program to Validate RSTM 65
3.2.1.4 Discussion 67
3.2.2 Residual Strength Test Method (RSTM) – Performance of Various Composites 69
3.2.2.1 Materials, Mixes and Testing 69
3.2.2.2 Results 71
3.2.2.3 Discussion 79
3.3 Conclusions 80

4 Bond-Slip Performance of Fibers Embedded in Cementitious Matrices 82
4.0 Introduction 82
4.1 Bond-Slip Performance of Fibers – Influence of Pullout Parameters 82
4.1.1 Straight-smooth, Stainless Steel Fibers Embedded in Normal Strength Matrix 84
4.1.1.1 Influence of Fiber Length 85
4.1.2 Straight, Stainless Steel Fibers with Rough Surface

Embedded in Normal Strength Matrix 86
4.1.2.1 Influence of Surface Roughness 87
4.1.2.2 Influence of Fiber Length 88
4.1.3 Straight-smooth, Stainless Steel Fibers Embedded in Non-Shrink Grout Matrix 88
4.1.3.1 Influence of Matrix Shrinkage Behavior 90
4.1.3.2 Influence of Fiber Length 90
4.1.4 Straight-smooth, Stainless Steel Fibers Embedded in High-Strength Matrix 91
4.1.4.1 Influence of Water/Cement Ratio 92
4.1.5 Straight-smooth, Stainless Steel Fibers Embedded in Silica-fume Modified High-Strength Matrix 93
4.1.5.1 Influence of Silica-fume Modification 94
4.1.6 Straight, Smooth Polypropylene Fibers Embedded in Normal Strength Matrix 95
4.1.6.1 Influence of Fiber Length 96
4.2 Conclusions 97

5 Progressive Debonding Model for Fiber Pullout 99
5.0 Introduction 99
5.1 The Proposed Progressive Debonding Model 103
5.1.1 Stage 1: Fiber Completely Bonded Along Its Entire Embedded Length 104
5.1.1.1 Fiber Axial Stress Distribution, σ_f 109
5.1.1.2 Interfacial Shear Stress Distribution, τ_a 109
5.1.1.3 Fiber Displacement, U_b 110
5.1.1.4 Debonding Criterion and Initial Debonding Stress, σ_d 111

5.1.2 Stage 2: Fiber Partially Debonded Along Its Embedded Length 112
5.1.2.1 Fiber Axial Stress Distribution, σ_f 115
5.1.2.2 Interfacial Frictional Shear Stress Distribution, τ_f 115
5.1.2.3 Pullout Stress versus Debond Length Relationship, σ_o *vs.* l_d 116
5.1.2.4 Fiber Displacement versus Debond Length Relationship, U_{pd} *vs.* l_d 116
5.1.2.5 Bond and Frictional Components of Pullout Stress, $\sigma_{o,bond}$ and $\sigma_{o,fric}$ 117
5.1.2.6 Catastrophic Debonding 118
5.1.3 Stage 3: Fiber Completely Debonded and Pulling Out 119
5.1.3.1 Fiber Axial Stress Distribution, σ_f 120
5.1.3.2 Interfacial Frictional Shear Stress Distribution, τ_f 121
5.1.3.3 Fiber Pullout Stress, σ_o 121
5.1.3.4 Pullout Displacement, U_{p_d} 122
5.1.4 Calibration of Interfacial Parameters - σ_c, μ and τ_s 122
5.2 Conclusions 125

6 Progressive Debonding Model for Fiber Pullout : Validation 127
6.0 Introduction 127
6.1 Calibration of Interfacial Properties and Validation of Model 127
6.1.1 Source Code for Progressive Debonding Model 127
6.1.2 Straight-smooth, Stainless Steel Fiber Embedded in Normal Strength Matrix 128
6.1.3 Straight, Stainless Steel Fibers with Rough Surface Embedded in Normal Strength Matrix 130
6.1.4 Straight-smooth, Stainless Steel Fibers Embedded in Non-Shrink Grout Matrix 132

6.1.5 Straight, Smooth Polypropylene Fibers Embedded in Normal Strength Matrix 135
6.1.6 Pullout Data Found in the Literature 136
6.2 Conclusions 139

7 Progressive Debonding Model For Fiber Pullout: Parametric Studies 141
7.0 Introduction 141
7.1 Parametric Studies 141
7.1.1 Influence of Adhesional Bond Strength, τ_s 141
7.1.1.1 Fiber Elastic Modulus, $E_f = 210$ GPa 141
7.1.1.2 Fiber Elastic Modulus, $E_f = 3.5$ GPa 146
7.1.2 Influence of Interfacial Contact Stress, σ_c 151
7.1.2.1 Fiber Elastic Modulus, $E_f = 210$ GPa 151
7.1.2.2 Elastic Modulus, $E_f = 3.5$ GPa 154
7.1.3 Influence of Interfacial Coefficient of Friction, μ 157
7.1.3.1 Fiber Elastic Modulus, $E_f = 210$ GPa 157
7.1.3.2 Elastic Modulus, $E_f = 3.5$ GPa 160
7.2 Conclusions 163

8 Conclusions 166

Bibliography 173

Appendix A 188

Appendix B 193

Appendix C 209

List of Tables

Table 3.1.1	Mix Proportions	38
Table 3.1.2	Description of fibers investigated	38
Table 3.1.3	Properties of silica fume and high-reactivity metakaoline investigated	41
Table 3.1.4	JSCE Absolute Toughness and Flexural Toughness Factor – Influence of Pozzolan	42
Table 3.1.5	JSCE Absolute Toughness and Flexural Toughness Factor – Influence of Pozzolan Type	44
Table 3.1.6	JSCE Absolute Toughness and Flexural Toughness Factor – Influence of fiber volume	46
Table 3.1.7	JSCE Absolute Toughness and Flexural Toughness Factor – Influence of fiber aspect ratio	47
Table 3.1.8	JSCE Absolute Toughness and Flexural Toughness Factor – Influence of fiber surface characteristics	49
Table 3.1.9	JSCE Absolute Toughness and Flexural Toughness Factor – Influence of fiber geometry	51
Table 3.1.10	JSCE Absolute Toughness and Flexural Toughness Factor – Influence of matrix shrinkage	52
Table 3.2.1	Mix Proportions	57
Table 3.2.2	Fresh Properties of Concrete Mixes	58
Table 3.2.3	Residual Strengths, *RS* for various mixes	63
Table 3.2.4	Test planning	65
Table 3.2.5	Residual Strengths, RS - Canadian Round-Robin Test Program [221]	66
Table 3.2.6	Maximum concrete stress at peak load with and without steel plate [219]	68
Table 3.2.7	Mix Proportions	69
Table 3.2.8	Fibers Investigated in Set 1 and Details of Test Program [220]	70
Table 3.2.9	Fibers investigated in Set 2 [220]	70
Table 3.2.10	Various Mixes Investigated in Set 2 and Details of Test Program [220]	71
Table 3.2.11	Fresh properties of Mixes in Set 2 [220]	76
Table 3.2.12	Compressive strengths (28-Day) for Mixes in Set 1 [220]	76
Table 3.2.13	Compressive strengths (28-Day) for Mixes in Set 2 [220]	76

Table 3.2.14	Detailed results for fibers in Set 1	77
Table 3.2.15	Detailed results for fibers in Set 2	78
Table 4.1.1	Experimental pullout test results for straight-smooth, stainless steel fibers embedded in normal strength matrix	85
Table 4.1.2	Experimental pullout test results for straight, stainless steel fibers with rough surface embedded in normal strength matrix	86
Table 4.1.3	Experimental pullout test results for straight-smooth, stainless steel fibers embedded in non-shrink grout matrix	89
Table 4.1.4	Experimental pullout test results for straight-smooth, stainless steel fibers embedded in high strength matrix	91
Table 4.1.5	Experimental pullout test results for straight-smooth, stainless steel fibers embedded in silica-fume modified normal strength matrix	93
Table 4.1.6	Experimental pullout test results for straight, smooth polypropylene fibers embedded in normal strength matrix	95
Table 5.0.1	Various parameters taken into consideration in the theoretical models of fiber pullout	100
Table 6.1.1	Theoretical and experimental peak pullout load and displacement corresponding to peak pullout load for a straight-smooth, stainless steel fiber embedded in normal strength matrix	130
Table 6.1.2	Theoretical and experimental peak pullout load and the displacement corresponding to peak pullout load for a steel fiber with rough surface embedded in normal strength matrix	132
Table 6.1.3	Theoretical and experimental peak pullout load and the displacement corresponding to peak pullout load for a straight-smooth, stainless steel fiber embedded in non-shrink grout matrix	134
Table 6.1.4	Theoretical and experimental peak pullout load and the displacement corresponding to peak pullout load for a straight, smooth polypropylene fiber embedded in normal strength matrix	136
Table 6.1.5	Comparison of peak pullout loads as predicted by (i) the proposed progressive debonding model, and (ii) finite element analysis, Mallikarjuna, et al. [225]	138

List of Figures

Figure 2.2.1	Variation of maximum fiber pullout load with embedded fiber length factor for various friction conditions [55]	17
Figure 2.2.2	Variation of pullout load with fiber displacement for various interfacial frictions conditions [109]	17
Figure 2.2.4	Interfacial bond stress vs. slip relationship [61]	24
Figure 2.4.1	Stress-strain response for a fiber reinforced cementitious composite showing strain hardening response	31
Figure 3.1.1	Test setup for flexural toughness test according to ASTM C 1018 [4]	39
Figure 3.1.2	Comparison of flexural load versus deflection response for fiber reinforced concrete mixes with and without silica fume and containing straight-smooth, stainless steel fiber at a dosage of 0.76%	42
Figure 3.1.3	Comparison of flexural load versus deflection response for fiber reinforced concrete mixes different types of pozzolans	43
Figure 3.1.4a	Comparison of flexural load versus deflection response for fiber reinforced concrete mixes – Influence of fiber volume, $V_f = 0.76\%$ and 5.0% of straight-smooth, stainless steel fiber (STL-STR1)	45
Figure 3.1.4b	Comparison of flexural load versus deflection response for fiber reinforced concrete mixes – Influence of fiber volume, $V_f = 1.0\%$ and 5.0% of straight, smooth polypropylene fibers (PP-STR1)	45
Figure 3.1.4c	Comparison of flexural load versus deflection response for fiber reinforced concrete mixes – Influence of fiber volume, $V_f = 1.0\%$ and 5.0% of straight polyvinyl alcohol fibers (PVA-1)	46
Figure 3.1.5	Comparison of flexural load versus deflection response for fiber reinforced concrete mixes – Influence of fiber aspect ratio, $V_f = 0.50\%$ of straight, smooth polypropylene fibers (PP-STR1 and PP-STR2)	47
Figure 3.1.6a	Comparison of flexural load versus deflection response for fiber reinforced concrete mixes – Influence of fiber surface characteristics, Steel fiber – STL-STR @ $V_f = 0.76\%$	48
Figure 3.1.6b	Comparison of flexural load versus deflection response for fiber	

reinforced concrete mixes – Influence of fiber surface characteristics, Polyvinyl alcohol fiber – PVA-1 @ V_f = 1.00% 49
Figure 3.1.7 Comparison of flexural load versus deflection response for fiber reinforced concrete mixes – Influence of fiber geometry 50
Figure 3.1.8 Comparison of flexural load versus deflection response for fiber reinforced concrete mixes – Influence of shrinkage properties of matrix 52
Figure 3.2.1 Comparison of Closed-loop Test Method with Open-Loop Test Method for Flexural Tests on Fiber Reinforced Concrete. Notice the large load instability that occurs during at the peak load during an open-loop test, and the related damage [6] 54
Figure 3.2.2a Schematic of Residual Strength Test Method experimental setup 56
Figure 3.2.2b Test on a Fiber Reinforced Concrete Beam using the Residual Strength Test Method. Note the steel plate under the beam 58
Figure 3.2.3a Test on a Fiber Reinforced Concrete Beam using the Closed-Loop Test Method 59
Figure 3.2.3b Schematic of controls in a flexural Closed-loop Test Method 60
Figure 3.2.4 Comparison of Closed-loop and Open-loop curves for concrete with 0.1% of Fibrillated Polypropylene Fiber (PP1) 60
Figure 3.2.5 Comparison of Closed-Loop and Open-loop curves for concrete with 0.3% of Fibrillated Polypropylene Fiber (PP1) 60
Figure 3.2.6 Comparison of Closed-loop and Open-loop curves for concrete with 0.1% of Monofilament Polypropylene Fiber (PP2) 60
Figure 3.2.7 Comparison of Closed-Loop and Open-loop curves for concrete with 0.3% of Monofilament Polypropylene Fiber (PP2) 60
Figure 3.2.8 Comparison of Closed-Loop and Residual Strength Test Method Curves for Concrete with 0.1% of Fibrillated Polypropylene Fiber (PP1) 61
Figure 3.2.9 Comparison of Closed-Loop and Residual Strength Test Method Curves for Concrete with 0.3% of Fibrillated Polypropylene Fiber (PP1) 61
Figure 3.2.10 Comparison of Closed-Loop and Residual Strength Test Method Curves for Concrete with 0.5% of Fibrillated Polypropylene

Fiber (PP1) 62
Figure 3.2.11 Comparison of Closed-Loop and Residual Strength Test Method Curves for Concrete with 0.1% of Monofilament Polypropylene Fiber (PP2) 62
Figure 3.2.12 Comparison of Closed-Loop and Residual Strength Test Method Curves for Concrete with 0.3% of Monofilament Polypropylene Fiber (PP2) 62
Figure 3.2.13 Comparison of Closed-Loop and Residual Strength Test Method Curves for Concrete with 0.5% of Monofilament Polypropylene Fiber (PP2) 62
Figure 3.2.14 Comparison of Closed-Loop and Residual Strength Test Method Curves for Concrete with 0.5% of Monofilament Nylon Fiber (NL1) 62
Figure 3.2.15a Residual Strength for Various Mixes using the Closed-Loop Test Method 64
Figure 3.2.15b Residual Strength for Various Mixes using the Residual Strength Test Method 64
Figure 3.2.16 Percentage Difference (δ) in RS Values between the Closed-Loop Test Method and the Residual Strength Test Method 64
Figure 3.2.17 Comparison of Closed-Loop and Open-Loop Curves for Concrete with 0.3% of Fibrillated Polypropylene Fiber (PP1) 66
Figure 3.2.18 Comparison of Closed-Loop and Residual Strength Test Method Curves for Concrete with 0.3% of Fibrillated Polypropylene Fiber (PP1) 66
Figure 3.2.19a Load-Deflection Curves for FRC with PPF-1 Fiber at Dosage Rate of 0.2% 72
Figure 3.2.19b Load-Deflection Curves for FRC with PPF-1 Fiber at Dosage Rate of 0.4% 72
Figure 3.2.19c Load-Deflection Curves for FRC with PPF-1 Fiber at Dosage Rate of 0.5% 72
Figure 3.2.19d Load-Deflection Curves for FRC with PPF-1 Fiber at Dosage Rate of 0.6% 72
Figure 3.2.19e Load-Deflection Curves for FRC with PPF-1 Fiber at Dosage Rate of 0.8% 73

Figure 3.2.20 Load-Deflection Curves for FRC with NLM-1 Fiber at Dosage Rate of 0.4% 73
Figure 3.2.21 Residual Strength Values Plotted as a Function of Fiber Volume for Fibers in Set 1 74
Figure 3.2.22 Load-Deflection Curves for FRC with PP-STR Fiber at a Dosage Rate of 1.6% 75
Figure 3.2.23 Load-Deflection Curves for FRC with a Hybrid Combination of PP-STR Fiber @ 1.6% and Steel Fiber (ST-HKD) @ 0.25% 75
Figure 3.2.24 Load-Deflection Curves for FRC with PVA-1 Fiber at a Dosage Rate of 1.6% 75
Figure 3.2.25 Load-Deflection Curves for FRC with Steel Fiber ST-HKD at a Dosage Rate of 0.76% 79
Figure 3.2.26 Load-Deflection Curves for FRC with Steel Fiber ST-CR1 at a Dosage Rate of 0.76% 79
Figure 4.1.1a Schematic of a standard pullout test specimen 83
Figure 4.1.2 Pullout response of straight-smooth, stainless steel fibers embedded in normal strength matrix 85
Figure 4.1.3 Embedded fiber length vs. maximum pullout load curve for straight-smooth, stainless steel fibers 86
Figure 4.1.4 Pullout response of straight , stainless steel fibers with rough surface embedded in normal strength matrix 87
Figure 4.1.5 Comparison of the pullout response of 30 mm long straight-smooth, stainless steel fibers and 30 mm long straight, stainless fibers with rough surface (normal strength matrix) 87
Figure 4.1.6 Embedded fiber length vs. maximum pullout load curve for straight, stainless steel fibers with rough surface 88
Figure 4.1.7 Pullout response of straight-smooth, stainless steel fibers embedded in non-shrink grout matrix 89
Figure 4.1.8 Pullout response of 30 mm long fibers embedded in normal strength matrix (CSA Type 10 cement) and in non-shrink grout matrix 90
Figure 4.1.9 Embedded fiber length vs. maximum pullout load curve for straight-smooth, stainless steel fibers embedded in non-shrink grout matrix 91

Figure 4.1.10 Pullout response of straight-smooth, stainless steel fibers embedded in high strength matrix 92
Figure 4.1.11 Pullout response of straight-smooth, stainless steel fibers embedded in normal strength matrix and high strength matrix 93
Figure 4.1.12 Pullout response of straight-smooth, stainless steel fibers embedded in silica fume modified high strength matrix 94
Figure 4.1.13 Pullout response of straight-smooth, stainless steel fibers embedded in high strength matrix and silica fume modified high strength matrix 94
Figure 4.1.14 Pullout response of straight, smooth polypropylene fibers embedded in normal strength matrix 96
Figure 4.1.15 Embedded fiber length vs. maximum pullout load curve for straight, smooth polypropylene fibers 97
Figure 5.0.1 Single fiber embedded in concrete matrix. Figure depicts one side of a two-sided pullout test specimen 99
Figure 5.0.2 A comparison between the experimental pullout response for a steel fiber with the predicted responses using the existing pullout models. The experimental pullout response is by Naaman and Shah [142] 102
Figure 5.1.1 The principle of a single fiber pullout test – The three stages of pullout process (Stang and Shah [106]) 104
Figure 5.1.2 Fiber completely bonded over its embedded length 105
Figure 5.1.3 Fiber partially debonded along its embedded length 112
Figure 5.1.4 Free body diagram for a fiber element of length *dz* 112
Figure 5.1.5 Fiber completely debonded over its length and pulling out 120
Figure 6.1.1 Coefficient of friction versus pullout displacement curves for straight-smooth, stainless steel fibers embedded in normal strength matrix 129
Figure 6.1.2 Comparison of experimental and theoretical pullout response – straight-smooth, stainless steel fiber fiber (embedded length – 30 mm) embedded in normal strength matrix 130
Figure 6.1.3 Coefficient of friction versus pullout displacement curves for straight, stainless steel fibers with rough surface embedded in

normal strength matrix 131
Figure 6.1.4 Comparison of experimental and theoretical pullout response - straight, stainless steel fiber with rough surface (embedded length – 30 mm) embedded in normal strength matrix 132
Figure 6.1.5 Coefficient of friction versus pullout displacement curves for straight-smooth, stainless steel fibers embedded in non-shrink grout matrix 133
Figure 6.1.6 Comparison of experimental and theoretical pullout response – straight-smooth, stainless steel fiber (embedded length – 30 mm) embedded in non-shrink grout matrix 134
Figure 6.1.7 Coefficient of friction versus pullout displacement curves for straight, smooth polypropylene fibers embedded in normal strength matrix 135
Figure 6.1.8 Comparison of experimental and theoretical pullout response - straight, smooth polypropylene fiber (embedded length – 30 mm) embedded in normal strength matrix 136
Figure 6.1.9 Comparison of experimental and theoretical pullout response for a straight, smooth steel fiber. Experimental curve is by Naaman and Shah [142] 137
Figure 6.1.10 Comparison of experimental and theoretical pullout response for a straight, smooth polypropylene fiber. Experimental curve is by Wang, Li and Backer [69] 139
Figure 7.1.1a Influence of adhesional bond strength on pullout response (E_f=210 GPa) 142
Figure 7.1.1b Influence of adhesional bond strength on the pullout load at initial debonding and the peak pullout load (E_f=210 GPa) 144
Figure 7.1.1c Influence of adhesional bond strength on displacement at the peak pullout load (E_f=210 GPa) 144
Figure 7.1.1d Variation in pullout load and pullout load components as a function of debond length (E_f=210 GPa) 144
Figure 7.1.1e Variation in pullout load and its components as a function of debond length at different values of adhesional bond strength, τ_s (E_f=210 GPa) 145

Figure 7.1.1f Axial load distribution in fiber at initial debonding (E_f=210 GPa) 145
Figure 7.1.1g Interfacial shear stress distribution at initial debonding (E_f=210 GPa) 145
Figure 7.1.1h Axial load distribution at completion of debonding (E_f=210 GPa) 146
Figure 7.1.1i Interfacial shear stress distribution at completion of debonding (E_f=210 GPa) 146
Figure 7.1.2a Influence of adhesional bond strength on pullout response (E_f=3.5 GPa) 147
Figure 7.1.2b Influence of adhesional bond strength on pullout load at initial debonding and maximum pullout load (E_f=3.5 GPa) 147
Figure 7.1.2c Influence of adhesional bond strength on pullout displacement corresponding to peak pullout load (E_f=3.5 GPa) 147
Figure 7.1.2d Variation in pullout load and pullout load components as a function of debond length (E_f=3.5 GPa) 149
Figure 7.1.2e Variation in pullout load and its components as a function of debond length at different values of adhesional bond strength, τ_s (E_f=3.5 GPa) 149
Figure 7.1.2f Fiber Axial load distribution in fiber at initial debonding (E_f=3.5 GPa) 150
Figure 7.1.2g Interfacial shear stress distribution at initial debonding (E_f=3.5 GPa) 150
Figure 7.1.2h Fiber axial load distribution at completion of debonding, (E_f=3.5 GPa) 150
Figure 7.1.2i Interfacial shear stress distribution at completion of debonding, (E_f=3.5 GPa) 150
Figure 7.1.3a Influence of interfacial contact stress on pullout response (E_f=210 GPa) 151
Figure 7.1.3b Influence of interfacial contact stress on pullout response (E_f=210 GPa) 151
Figure 7.1.3c Influence of interfacial contact stress on pullout load at initial debonding and peak pullout load (E_f=210 GPa) 152
Figure 7.1.3d Influence of interfacial contact stress on pullout displacement at the peak pullout load (E_f=210 GPa) 152
Figure 7.1.3e Variation in pullout load and its components as a function of

debond length (E_f=210 GPa) 153
Figure 7.1.3f Fiber axial load distribution at completion of debonding (E_f=210 GPa) 153
Figure 7.1.3g Interfacial shear stress distribution at completion of debonding (E_f=210 GPa) 153
Figure 7.1.4a Influence of interfacial contact stress on prepeak pullout response (E_f=3.5 GPa) 154
Figure 7.1.4b Influence of interfacial contact stress on pullout response (E_f=3.5 GPa) 154
Figure 7.1.4c Influence of interfacial contact stress on pullout load at initial debonding and peak pullout load (E_f=3.5 GPa) 155
Figure 7.1.4d Influence of interfacial contact stress on pullout displacement at the peak pullout load (E_f=3.5 GPa) 155
Figure 7.1.4e Variation in pullout load and its components as a function of debond length (E_f=3.5 GPa) 156
Figure 7.1.4f Fiber axial load distribution at completion of debonding (E_f=3.5 GPa) 156
Figure 7.1.4g Interfacial shear stress distribution at completion of debonding (E_f=3.5 GPa) 156
Figure 7.1.5a Influence of interfacial coefficient of friction on pullout response (E_f=210 GPa) 158
Figure 7.1.5b Influence of interfacial coefficient of friction on pullout response (E_f=210 GPa) 158
Figure 7.1.5c Influence of interfacial coefficient of friction on pullout load at initial debonding and peak pullout load (E_f=210 GPa) 158
Figure 7.1.5d Influence of interfacial coefficient of friction on pullout displacement at the peak pullout load (E_f=210 GPa) 158
Figure 7.1.5e Variation in pullout load and its components as a function of debond length (E_f=210 GPa) 159
Figure 7.1.5f Fiber axial load distribution at completion of debonding (E_f=210 GPa) 160
Figure 7.1.5g Interfacial shear stress distribution at completion of debonding (E_f=210 GPa) 160

Figure 7.1.6a Influence of interfacial coefficient of friction on prepeak pullout response (E_f=3.5 GPa) 161
Figure 7.1.6b Influence of interfacial coefficient of friction on pullout response (E_f=3.5 GPa) 161
Figure 7.1.6c Influence of interfacial coefficient of friction on pullout load at initial debonding and peak pullout load (E_f=3.5 GPa) 161
Figure 7.1.6d Influence of interfacial coefficient of friction on pullout displacement at the peak pullout load (E_f=3.5 GPa) 161
Figure 7.1.6e Variation in pullout load and its components as a function of debond length (E_f=210 GPa) 162
Figure 7.1.6f Fiber axial load distribution at completion of debonding (E_f=3.5 GPa) 162
Figure 7.1.6g Interfacial shear stress distribution at completion of debonding (E_f=3.5 GPa) 162

Notations

n	-	modulus ratio between concrete and steel
b	-	width of concrete beam
d	-	depth of concrete beam
L	-	length of concrete beam
S	-	span of concrete beam
δ_{150}	-	beam deflection of magnitude *S/150*
T_{JCI}	-	JSCE Absolute Toughness
σ_b	-	JSCE Flexural Toughness Factor
d_p	-	depth of the steel plate
$\bar{y}$	-	depth of neutral axis
M_c	-	bending moment at cracking
σ_c	-	stress carried by the beam at cracking
σ_s	-	stress carried by steel plate at the instant beam cracks
P_{cr}	-	cracking load of beam
δ_{cr}	-	deflection at cracking load of beam
a	-	fiber radius
b	-	outer radius of the matrix coaxial cylinder in a pullout test geometry
r	-	radial direction in a pullout specimen
z	-	axial fiber direction in a pullout specimen
L	-	embedded fiber length in a pullout specimen
τ_m	-	matrix shear stress
τ_a	-	interfacial shear stress
τ_s	-	fiber-matrix interfacial shear strength
τ_f	-	interfacial shear stress over the debonded interface
w_m	-	matrix axial displacement
w_a	-	matrix displacement at the interface (i.e., $r=a$)
w_b	-	matrix displacement at the surface of coaxial cylinder (i.e., at $r=b$)
σ_o	-	fiber pullout stress
σ_f	-	fiber axial stress

σ_m - matrix axial stress

σ_a - matrix axial stress at the interface (i.e., $r=a$)

$\sigma_{o,bond}$ - bond component of pullout stress

$\sigma_{o,fric}$ - frictional component of pullout stress

$\sigma_{o,peak}$ - fiber peak pullout stress

σ_b - matrix axial stress at the surface of coaxial cylinder (i.e., at $r=b$)

σ_c - contact stress at the fiber-matrix interface

σ_{cp} - contact stress at fiber-matrix interface after Poisson's contraction of fiber

σ_d - fiber debonding stress

δ_r - fiber-matrix misfit

μ - interfacial coefficient of friction

μ_i - initial value of the interfacial coefficient of friction

μ_{ss} - steady-state value of the interfacial coefficient of friction

c - rate at which the interfacial coefficient of friction decays with increase in p_d

Δ - pullout displacement

Δ_{peak} - pullout displacement corresponding to peak pullout load

Δa - decrease in fiber radius due to Poisson's contraction of fiber

l_d - interfacial debond length

$l_{d,cat}$ - catastrophic debond length of interface

p_d - rigid body displacement of fiber in a pullout test

p_{d1} - rigid body displacement of the fiber in a pullout test

p_{d2} - rigid body displacement of the fiber in a pullout test

P_{pd1} - pullout load corresponding to the pullout distance, p_{d1}

P_{pd2} - pullout load corresponding to the pullout distance, p_{d2}

U_b - fiber displacement when fiber is completely bonded

U_{pd} - fiber displacement during partial interfacial debonding

$U_{pd,peak}$ - fiber displacement corresponding to peak pullout load

- fiber displacement beyond completion of interfacial debonding

W_p - Work of fiber pullout when the rigid body displacement of the fiber increases from p_{d1} to p_{d2}

ν_m - Poisson ratio of matrix material

ν_f	-	Poisson's ratio of fiber material
E_m	-	matrix elastic modulus
E_f	-	fiber elastic modulus
MOR	-	Modulus of Rupture
RS	-	Residual Strength
RSI	-	Residual Strength Index

Acknowledgement

I extend my deepest gratitude to my research supervisor, Dr. N. Banthia for providing the opportunity to work toward this research program, and for his continued advice, support and encouragement throughout the program. In particular, the freedom he allowed me during the course of this research greatly helped me to nurture research and independent thinking skills. I remain indebted for his direction, pragmatism and trust.

I am also profoundly grateful to Mr. Rick Hingson of Synthetic Industries, Chatanooga, USA, for his personal initiative and invaluable guidance. His involvement undoubtedly enabled blossoming of this research. Especial thanks are also due to Mr. Cheng Yan for his dynamism and help during my research. Thanks are also extended to Dr. Sydney Mindess, Dr. Reza Vaziri, and Dr. Tom Troczynski for the guidance they provided from time to time. I am also grateful to Mr. Dennis Teo for performing a part of the experimental work, and to all personnel of the Department of Civil Engineering, including, Mr. Doug Smith, Mr. John Wong, Mr. Max Nazar and Mr. Dick Postgate, who in one way or another contributed to the success of this study. Furthermore, I am grateful to all my colleagues at UBC who made the atmosphere quite enriching. Thanks are also due to researchers around the globe from whom I have benefited immeasurably either through their writings or through personal contacts.

I extend my deepest appreciation to Anima and Nandu for being there during the toughest moments and for sharing with me the joyous moments. Without them, my work would not have been as encouraging and fulfilling as it has been. Last but not least, I remain obligated to every being on this planet and to the mother-nature.

Chapter 1

Introduction

Plain concrete is a brittle material characterized by its low tensile strength, low tensile strain capacity and low fracture toughness. To render concrete a usable structural material, it has to be reinforced. Historically, concrete reinforcements have been in the form of continuous steel reinforcing bars and stirrups, which are placed strategically in the structure to withstand the imposed tensile and shear stresses. In the last couple of decades, another type of concrete reinforcement that has gained immense popularity is discontinuous short fibers [1-3]. Continuous bars and discontinuous short fibers perform different roles in concrete. While conventional reinforcing bars are used to increase the tensile and shear capacities of concrete, the primary reason for inclusion of discontinuous short fibers in the concrete matrix is to improve its post-cracking response (i.e., to augment apparent ductility, energy absorption capacity, impact resistance and cracking resistance of concrete). Because of its superior energy absorption capability, fiber reinforced concrete has been widely used in a variety of civil engineering applications including thin sheet products, large precast products, shotcrete, offshore structures, seismic structures, pavements, overlays, crash barriers, machine foundations, hydraulic structures and thin and thick repairs.

While the influence of fibers on the pre-cracking behavior is only marginal, the potency of fiber addition becomes apparent after the brittle concrete matrix has cracked. In the post-cracking stage, fibers that bridge a crack apply closing pressure at the crack front. Closing pressure suppresses the tendency of crack growth by reducing the stress intensity at the crack tip. In this context, efficiency of fibers in suppressing crack growth is directly dependent upon the magnitude and the nature of the closing pressure field generated due to the interaction between fiber and matrix in the wake region of the crack tip. With the opening of the crack, fibers pull out of the matrix and absorb energy in the process. This energy that is absorbed at the micromechanical level in the fiber pullout process appears at the macromechanical level as toughness of the fiber reinforced composite. In this context, the significance of interfacial

micromechanics becomes apparent, given the dependence of both the the fiber-matrix interaction and macromechanical composite properties on the micromechanical properties of the fiber-matrix interface. Despite numerous theoretical and experimental studies on the micromechanics of interfaces that have been carried out, it is not clear as to how micromechanical properties of an interface must be tailored to improve fiber pullout efficiency. It is also of utmost importance to understand the combined influence of fiber elastic modulus and interfacial properties on fiber pullout response, since fibers with a wide variety of elastic moduli are commonly employed to produce fiber reinforced cementitious composites. The aforementioned aspects are explored as part of this research program.

Ductility or the energy absorption capability of fiber reinforced concrete is commonly measured by loading a specimen in flexure and measuring the corresponding load versus displacement response. The area under the load versus displacement response represents the flexural toughness of the composite. Some testing standards for characterizing flexural toughness that fall under this category include ASTM C1018 [4] and JSCE-SF4 [5]. Although not widely recognized, one major problem that is associated with the testing of a specimen under flexural loading (for instance, as per ASTM C1018 or JSCE SF-4) is that the measured post-cracking response is severely affected by the stiffness of the testing machine [6]. For a given testing system, the severity of this effect is more pronounced at low fiber dosage rates and when fibers with a low modulus are used. To accurately characterize the flexural behavior of fiber reinforced cementitious composites, a new test method called the Residual Strength Test Method (RSTM) has recently been adopted as a testing standard by the American Society of Testing and Materials [7]. Another major objective this research program is to investigate the validity of the Residual Strength Test Method.

1.1 Objectives and Scope

The present work on fiber reinforced concrete is categorized under the following two categories:

- macromechanical studies, and
- micromechanical studies

The objectives that fall under the category of macromechanical studies are:

- to examine the influence of machine stiffness on the measured flexural load versus deflection response of fiber reinforced concretes (in particular, fiber reinforced concretes with low toughness);
- to assess the validity of the newly developed *Residual Strength Test Method* (RSTM)[1] for the measurement of the post cracking response of fiber reinforced concrete;
- to investigate the influence of various material variables on the flexural toughness of fiber reinforced concrete.

The objectives that fall under the category of micromechanical studies are:

- to examine the influence of various pullout parameters on the fiber pullout responsei;
- to develop a fiber pullout model in order to understand the mechanics of interaction between the fiber and the cement based matrices, and to understand the progressive debonding behavior of the fiber-matrix interfaces;
- to conduct parametric studies using the developed fiber pullout model from the viewpoint of understanding the influence of the fiber-matrix interfacial properties and the mechanical properties of the constituents on the fiber pullout response.

1.2 Thesis Organization

The pertinent literature is reviewed in Chapter 2. The influence of various material variables on the flexural toughness of FRC is described in Chapter 3. In addition, this chapter explores the influence of machine stiffness on the flexural load versus deflection response of FRC. Two testing schemes are used for this purpose - an open-loop test scheme and a closed-loop test scheme. The stiffness of the former testing machine is lower than that of the latter. Also, in the latter test scheme, a feedback signal from the beam deflection or the crack opening displacement is utilized in order to crack the beam at a controlled rate. Furthermore, in Chapter 3, an assessment of the Residual Strength Test Method is made. Apart from the intensive investigations carried out in this context at the University of British Columbia, a Round Robin Test Program was accomplished between the Ministry of Transportation of Ontario, the Technical University of Nova Scotia and the University of British Columbia. Results from this test program are also reported in this chapter.

[1] Residual Strength Test Method (RSTM) is now an American Society of Testing & Materials (ASTM) test standard – ASTM 1399-98 [7].

The influence of various pullout parameters on the fiber pullout response is described in Chapter 4. Pullout parameters investigated include water/binder ratio, matrix shrinkage properties, matrix modification by pozzolans, fiber length and fiber surface roughness. Pullout tests were carried out on fibers with different elastic moduli.

To understand the mechanics of interaction between the fiber and the matrix, an analytical model for the problem of fiber pullout is developed and presented in Chapter 5. Validation of the proposed model is carried out in Chapter 6. Further, parametric studies are carried out using the proposed pullout model to study the influence of the fiber-matrix interfacial properties and the mechanical properties of the constituents on the fiber pullout response. Results form the aforementioned parametric studies are presented in Chapter 7.

Finally, Chapter 8 summarizes the important conclusion drawn from this work.

Chapter 2

Literature Review

2.0 Introduction

The fundamental reason behind the addition of discontinuous fibers to cementitious materials is to suppress the inherent tendency of the brittle matrix to crack at low strains. While conventional reinforcing bars increase the tensile and shear capacities of concrete, discontinuous fibers, when added to a concrete matrix, enhance the material's ability to deform and absorb energy. Thus, toughness of fiber reinforced concrete is a measure of the energy absorption capability (i.e., deformability) of the composite and its ability to resist fracture when subjected to applied loads. There are several approaches that may be adopted to evaluate the toughness of fiber reinforced concrete. The primary difference between these approaches stems from the characteristics of the applied load on the structure. These characteristics include:

i. mode of loading: tension, compression, or flexure

ii. rate of loading: static, dynamic, or impact

Flexural toughness under static loading is most commonly used to characterize the toughness of fiber reinforced cementitious composites. Some flexural toughness testing standards that fall under this category include ASTM C1018 [4] and JSCE SF-4 [5]. A brief literature review on the characterization of flexural toughness of fiber reinforced concretes is presented in this chapter.

While the influence of fibers on the pre-cracking behavior is only marginal, the potency of fiber addition becomes apparent only after concrete has cracked. In the post-cracking stage, fibers that bridge a crack apply a closing pressure at the crack front. This tends to close the crack and suppresses the tendency of crack growth by reducing the stress intensity at the crack tip. In this context, efficiency of fibers in suppressing crack growth is directly dependent upon the magnitude and the nature of the closing pressure field resulting from the interaction between fiber and matrix. Given the dependence of composite response on interfacial micromechanical properties, it becomes critical to tailor the interfacial micromechanical properties for achieving

the desired composite properties. For this reason, experimental and theoretical investigations on the micromechanics of interfaces actively continue. Several experimental test methods have been developed for the characterization of the fiber-matrix interfacial properties, such as the single fiber pullout test, microdebond test, single fiber fragment test, and fiber pushout test (also known as indentation test) [8]. Among these, the single fiber pullout test is most commonly employed in the field of fiber reinforced concrete. Yet another objective of this chapter is to present a literature review on the topics of micromechanical and macromechanical properties of fiber reinforced cementitious composites. First, the relevant micromechanical models for the problem of fiber pullout are reviewed. This is followed by a review of important experimental fiber pullout studies carried out to this date. Finally, a brief review of important micromechanical models describing the tensile behavior of fiber reinforced cementitious composites is presented.

2.1 Issues Of Significance Concerning Characterization of Toughness of Fiber Reinforced Concretes

Several definitions of toughness, all in the form of energy absorption, have been developed to quantify the toughness of fiber reinforced cementitious composites under static loading. For instance, flexural toughness, compressive toughness and tensile toughness are some definitions, which correspond to toughness obtained through flexural, compressive and tensile tests, respectively. In the following, flexural toughness is discussed in detail, as it is one of the most common loading states for fiber reinforced concrete applications.

Extensive work [4,5,9-51] has been done towards the characterization of flexural toughness of fiber reinforced concretes, and many different test methods have been developed for this purpose. Most of these test methods use a static third-point bending configuration, and the energy absorbed by the specimen is computed from the area under the load-deflection curve. In addition, several different toughness definitions and descriptions exist in various test standards and in the literature. Kasperkiewicz and Skarendahl [9] have classified the various toughness characterization methods into two categories:

i. Absolute value descriptions

ii. Relative value descriptions

Methods based on an 'absolute value description' measure the total energy required either to fracture a specimen of arbitrary size, or to load the specimen to a particular end-point deflection. Thus, an absolute description of toughness does not use any ideal material as a reference. Methods that fall under this category include: Japanese Society of Civil Engineers, JSCE – SF4 [5], Dutch CUR-Recommendation N^{o} 10 [10], Belgian Standard NBN B15-238 [11], Spanish AENOR UNE 83-510-89 [12], German DBV Recommendations [13-15], RILEM Energy Absorption [16]. As an example of the absolute approach, the Japanese Society of Civil Engineers in its standard "Method of Test for Flexural Strength and Flexural Toughness of Fiber Reinforced Concrete - JSCE-SF4 [5]" defines a toughness parameter called the Absolute Toughness, T_{JCI} as the area under the load-deflection curve to a deflection of *loading span/150.*

Methods based on a 'relative value description' normalize the energy absorbed up to a specified deflection by the energy absorbed up to approximately the elastic limit of the material, or by the energy absorbed in fracturing the unreinforced matrix. Methods falling under this category include: ASTM C1018 [4], ACI Committee 544 Recommendations [17], Barr Indices [18-22], French Standard P18-409 [23], Wang and Backer Index [24], Ward and Li Indices [25], and Shah et al. [26]. An example of the relative approach is ASTM C1018 standard titled "Standard test method for flexural toughness and first-crack strength of fiber reinforced concrete (using beam with third-point loading)." Toughness parameters of the ASTM C1018 [4] technique are based on determining the amount of energy required first to deflect and crack a fiber reinforced concrete beam loaded at its third-points and then to selected multiples of the first crack deflection. Toughness Indices, I_5, I_{10}, I_{20}, I_{30} and I_{60} are then calculated by taking the ratios of the energy absorbed to a certain multiple of first crack deflection and the energy consumed up to the occurrence of the first crack itself.

In addition to the above definitions there exist several other toughness characterization schemes that do not fall in the aforementioned categories. For example, Mobasher and Shah [27] define the fracture toughness, G_f as the area under the load-deflection response (extrapolated to the value of zero load), divided by the net cross-sectional area of the specimen. A few other proposed methods describe the toughness in the form of equivalent flexural strength, for instance, Banthia and Trottier [28] quantify toughness by a parameter called 'post crack strength', which is evaluated at various deflections. Similarly, Norwegian Concrete Association's guidelines for shotcrete, NBP No 7 [29], describe the toughness parameters in the

form of residual flexural strength at specified deflections. According to the Norwegian NBP No 7 guidelines, toughness properties of shotcrete are determined according to four different classes - the two highest classes (Class 2 and Class 3) involve determination of:

- residual flexural strength from the load-deflection curve (residual flexural stress at fixed deflections of 1 and 3 mm, respectively)
- flexural strength
- minimum fiber content as a function of fiber length and material.

The EFNARC [30] recommendation also uses a toughness classification similar to that of the Norwegian NBP No 7.

As can be noted, there are several definitions of flexural toughness and several test standards to characterize the flexural toughness of fiber reinforced concretes. As a result of the multitude of definitions and standards, there is considerable controversy amongst the users of FRC about the best way to characterize flexural toughness. Both approaches (absolute and relative) provide important information about the mechanical properties of fiber reinforced concretes, but neither approach is sufficient. For instance, it is possible for two materials to have different mechanical performances but still have the same value of absolute toughness. Similarly, in context of the relative approaches, it is possible for two materials that are mechanically different to have the same ASTM C1018 toughness indices.

Several investigators [24,41,42,44,45,47,49,51] have expressed their doubts about the definition and determinations of first crack according to ASTM C1018. Doubts have also been cast about the measurement of net beam deflection and instability after the peak load for materials with low toughness, which could lead to substantial errors in the evaluation of toughness parameters. Gopalaratnam et al. [42] and Trottier and Banthia [45] pointed out that the toughness indices were not very sensitive in distinguishing amongst different fiber contents. Johnston [32-34] on the contrary, found the reverse to be true. Balaguru et al. [49] reported that ASTM indices I_5 and I_{10} were not good indicators of the variation present in the load-deflection response, and recommended that indices such as I_{100} occurring at much higher deflections, rather than I_5 and I_{10}, should be used for the toughness evaluation of FRC.

Some issues of significance pertinent to toughness testing and toughness characterization are summarized below:

i. Deflection measuring procedure

Large inaccuracies in toughness computation may result if beam deflections are not measured accurately. Large extraneous deformations result due to local crushing of the test beam at the supports, the elastic and inelastic deformations of the loading fixtures, and deformations in the support system. Note that, up to first crack, extraneous deformations contribute most of the measured deflections, and after the first crack, extraneous deformation constitute only a small fraction of the total beam deflection. For characterizing toughness accurately, these extraneous deflections should be excluded from the deflection measurements. Further details on this issue can be found in Reference 42.

ii. Specimen Geometry and Size Effect

It is well established that the strength of concrete structures is dependent on the size of the structure. Both strength (also, first-crack strength) and post-peak ductility decrease with an increase in structural size. Consequently, toughness parameters are also affected by the size of the specimen and hence are size dependent.

The extremely small ratio of shear-span to beam depth ratio as specified by most Standards causes high shear stresses similar to those in deep beams and walls. This could lead to a pronounced influence of shear on the test results. Furthermore, this state of stress is unrepresentative of the most common applications of fiber reinforced concrete, for example, tunnel linings and slabs-on-grade [41].

iii. Stiffness of testing machine

During testing, the loading system deforms and stores energy. At first crack or at the peak load, part of this energy is suddenly released and absorbed by the specimen. For concretes with low fiber content, this normally causes a sudden instability in the load-deformation response, which consequently affects the toughness evaluation. The degree of this instability depends on the relative stiffness of the loading system, with softer loading systems releasing larger amounts of energy. Banthia and Trottier [44] have pointed out the effects of instability on the measurement of ASTM Toughness Indices.

iv. Identification of first crack

In the ASTM C1018 method, the indices depend upon the energy absorbed by the specimen up to the occurrence of the first crack; therefore, it is very important to locate the first crack exactly. ASTM C1018 identifies the first crack on the load-deflection curve as "the point of the load-deflection curve at which the form of the curve first becomes nonlinear". Note that, according to this definition, objectively locating the point of first crack in the ascending part of the load-deflection response is not possible and is always subject to human-judgement error. This becomes an even bigger problem for beams that exhibit post-cracking strengthening. Thus the need is to establish an objective definition of first crack for fiber reinforced concretes with different volume fractions of fibers.

The following recommendations were made by Gopalaratnam and Gettu [41] with regard to the characterization of flexural toughness of FRC using the four-point bending test:

- Avoid the use of first-crack deflection to define toughness. If first crack is needed it should be objectively defined.
- Use shallow beams (l/d ratios > 5) to minimize structural effects and large shear spans to minimize the effect of shear stresses.
- Ensure stability of the test at all times through the use of a stiff machine and/or a servo-controlled machine.
- Use absolute energy and associated equivalent flexural strength at prescribed deflection limits for a standard beam as sensitive measures of toughness.
- Use deflection limits that are related to specimen size.

In addition, Gopalaratnam and Gettu [41] recommended the use of the equivalent post-cracking approach for incorporating energy absorption of FRC in structural design. Further, they suggest that this approach should be coupled with serviceability-related and application specific limits on deflection or crack width.

2.2 Micromechanical Models for Investigating the Fiber-Matrix Interfacial Behavior

Depending on the choice of criterion that is used for fiber-matrix interfacial debonding, the theoretical analysis of the problem of fiber pullout can be classified into two distinct approaches: strength based approach [52-78] and fracture mechanics based approach [78-99]. Theoretical

models based on the former approach use maximum interfacial shear stress as the interfacial debonding criterion such that when the interfacial shear stress exceeds the interfacial bond strength, debonding is supposed to occur. On the other hand, if theoretical models based on the concepts of fracture mechanics, the debonded zone is considered as an interfacial crack, and the extension of the crack is dependent on the energy criterion being satisfied.

Cox [52] developed the first strength-based analytical model to describe the transfer of stress between fiber and matrix. This model assumes that the tensile stresses in the matrix are negligible relative to those in the fiber and the shear stresses in the fiber are small compared to those in the matrix.[1] Assuming compatibility of fiber and matrix displacements at the interface, i.e., no slip, Cox [52] derived analytical expressions for the axial stress distribution in the fiber and the shear stress distribution at the interface. The analytical model by Greszczuk [53] was also based on similar assumptions. Greszczuk [53] further postulated that at the instant when the shear strength of the interface was attained, catastrophic debonding would occur over the entire embedded length of fiber. However, in reality, debonding may be limited to the zone in which the elastic shear stress exceeds the adhesional shear bond strength, and in that scenario, the process of load transfer will be comprised of frictional shear transfer at the debonded zone and elastic shear transfer over the remaining length of fiber. Greszczuk's model [53] did not include the possibility of the existence of frictional bond, which constituted a major limitation of the model. The combined stress transfer mechanism was first treated analytically by Lawrence [55]. In this model, interfacial frictional shear stresses over the entire debonded zone were assumed to remain constant. Models developed by Gopalratnam and Shah [55], Nammur et al. [61], Gopalaratnam and Cheng [65], Stang et al. [78] also took into account the combined stress transfer mechanisms. It is apparent that the shear stresses (both elastic and frictional) that develop parallel to the fiber-matrix interface are of utmost importance in controlling the fiber-matrix stress transfer mechanism. However, stresses and strains may also develop normal to the fiber-matrix interface as a result of the Poisson effect, volume changes, and multiaxial loading. They may induce considerable variations in the resistance to frictional slip, which is sensitive to normal stress. A comprehensive approach to the stress-transfer problem therefore requires simultaneous treatment of all the above-mentioned effects, namely, elastic shear transfer, frictional slip, debonding and normal stresses and strains. Analytical models developed by Takaku and Arridge [54] and Hsueh [66-68] are more comprehensive than the previously cited

[1] Models based on this assumption are now known as Shear-lag Models.

since these models take into consideration influence of Poisson's contraction of the fiber on the pullout response.

The fracture mechanics approach is characterized by the assumption that the propagation of the debonding zone requires a certain amount of energy, and that this energy is characteristic of the bond between the fiber and the matrix [106]. Thus, the debonding energy is proportional to the magnitude of the increase of the debonded zone. Based on the concepts of fracture mechanics, the total energy release rate, G, can be written as [106]:

$$G = \frac{\partial W_{ex}}{\partial a} - \frac{\partial W_e}{\partial a} - \frac{\partial W_f}{\partial a} \qquad 2.1$$

where, a is the increase in debonded area due to extension of the crack, W_{ex} is the work done by external load, W_e is the elastic strain energy stored in the system, and W_f is the energy dissipated in inelastic parts of the structure, e.g., work done by friction on the debonded interface. In fiber pullout problems it is often assumed that the critical energy release rate corresponds to the mode II toughness of the interface, G_{iII}^{crit}, i.e., the contribution of mode I to the energy release rate is insignificant. Thus, with this assumption, the criterion for interfacial debonding is given by equating the energy release rate with the critical energy release rate G_{iII}^{crit} of the interface:

$$G_{iII}^{crit} = G \qquad 2.2$$

Bowling and Groves [87], Stang and Shah [64, 78], Gao et al. [92], Morrison et al. [85], Zhou et al. [89], and Kim et al. [88] have proposed fiber pullout models based on the concepts of fracture mechanics.

A review of some important fiber pullout models follows.

Greszczuk [53]

Greszczuk [53] assumed that the fiber load was transferred to the matrix through the elastic shear stresses only. Further, it was assumed that, when the magnitude of this elastic shear stress exceeded the matrix shear strength at the location where fibers entered the matrix, catastrophic debonding took place along the fiber length. He proposed a method to determine the shear strength and shear modulus of the fiber. This method is based on the pullout test on fibers that

are embedded in the matrix to various lengths. Based on the shear lag theory, the final solution for the interfacial shear stress at a point located at a distance x from where the fiber enters the matrix in terms of the average shear stress $\tau_{av} = P/2\pi rl$ was derived as:

$$\frac{\tau(x)}{\tau_{av}} = \alpha l\{\sinh(\alpha x) - \coth(\alpha l)\cosh(\alpha x)\} \qquad 2.3$$

where,
$$\alpha = \left[\frac{2G_i}{b_i r E_f}\right]^{1/2} \qquad 2.4$$

and,

G_i = shear modulus of the matrix

b_i = effective thickness of the interface

r = fiber radius

E_f = fiber modulus

From the above equation, the maximum shear stress would occur at $x = 0$, hence:

$$\frac{\tau_{max}}{\tau_{av}} = \alpha l\{\coth(\alpha l)\} \qquad 2.5$$

According to the above equation, as $\alpha l \to 0$, the limit $\tau_{max}/\tau_{av} \to 1$, i.e., $\tau_{max} \to \tau_{av}$. Greszczuk proposed that this condition can be used to determine the shear strength of the interface. Since, in the above equation, α is a constant, therefore, τ_{max}/τ_{av} would be a function of embedded fiber length only. Thus, by conducting pullout tests on fibers that are embedded in the matrix to various lengths, the shear strength, τ_{max}, of the interface can be estimated by plotting a curve of τ_{av} versus l, and extrapolating τ_{av} at $l = 0$.

As mentioned above, for a given fiber and matrix type, the value of interfacial shear strength τ_{max} is established. Now, for a fiber with a given embedded length, the average shear stress τ_{av} can be obtained from the experimental pullout test result, and thereafter the ratio τ_{av}/τ_{max} be evaluated. Using Equation 2.5, a value of αl that corresponds to the calculated ratio τ_{av}/τ_{max} can be computed. With length of the fiber l and αl known, the value of α can be computed. Finally, using Equation 2.4, the shear modulus G_i of the interface can be calculated. Here, Equation 2.4 assumes that the thickness of the interface b_i is known.

Lawrence [55]

The model developed by Lawrence [55] includes the effects of both the interfacial elastic shear stresses and the frictional shear stresses, and it recognizes the conditions for either a gradual, or an instantaneous debonding of the interface. He has shown that the form of the distribution of the shear stress and the load along the fiber length depends upon the elastic properties of constituents and the fiber embedded length. Lawrence [55] extended the theory developed by Greszczuk [53] by taking into account the process of progressive debonding of the fiber-matrix interface. He suggested that the maximum fiber pullout load would occur at the instant when debonding of that part of fiber length where the elastic bond is still intact takes place in a catastrophic manner.

Lawrence [55] derived the following equation for the distribution of load $P(x)$ along the fiber length:

$$P(x) = P_f \frac{\sinh\sqrt{\alpha}\, x}{\sinh\sqrt{\alpha}\, l_e} \qquad 2.6$$

where, P_f is the fiber pullout load, x is the distance of the point under consideration measured from the embedded fiber end, l_e is the embedded fiber length, and α is an elastic constant given by:

$$\alpha = CK\left[\frac{1}{A_f E_f} - \frac{1}{A_m E_m}\right] \qquad 2.7$$

where, C is the fiber perimeter, A_f and A_m are the areas of the fiber and the matrix, respectively, E_f and E_m are the elastic modulus of the fiber and the matrix, respectively. K is a constant that relates the interfacial elastic shear stress τ with the virtual displacement $(u\text{-}v)$ of the interface by the equation $\tau=K\,(u\text{-}v)$, where u is the virtual displacement in the direction of the fiber at a point on the fiber located at a distance x from the embedded fiber end, and v is the virtual displacement of the matrix at the same point, if the fiber was replaced by the matrix.

Based on the Equation 2.6, Lawrence pointed out that the hyperbolic sine function is approximately linear for small values and exponential at large values. As a result, the distribution of the relative load $P(x)/P_f$ is affected by the embedded fiber length l_e. Accordingly,

for fibers with small lengths, the buildup of load along the fiber length is approximately linear, however, this is not the case for the fibers with longer lengths.

Further, Lawrence derived the following equation for the distribution of shear stress $\tau(x)$ along the embedded fiber length:

$$\tau(\mathrm{x}) = \frac{KP_f}{\sqrt{\alpha}} \frac{\cosh\sqrt{\alpha}\, x}{\sinh\sqrt{\alpha}\, l_e} \left[\frac{1}{A_f E_f} - \frac{1}{A_m E_m} \right] \qquad 2.8$$

Following Equation 2.8, the maximum shear stress occurs at the point where the fiber enters the matrix, and is given by:

$$\tau_{\max} = \frac{KP_f}{\sqrt{\alpha}} \coth\sqrt{\alpha}\, l_e \left[\frac{1}{A_f E_f} - \frac{1}{A_m E_m} \right] \qquad 2.9$$

The above equation also depicts that for a given value of α, the distribution of the relative shear stress along the embedded fiber length is influenced by the fiber length.

Lawrence assumed that it was possible for the fiber-matrix interface to partially debond, rather than the catastrophic debonding assumed by Greszczuk [53]. Further, in his analysis he took into consideration the existence of frictional shear stresses τ_i over the debonded fiber length. According to Equation 2.9, when the fiber load P_f is such that the interfacial shear stress τ_{max} equals τ_s (the interfacial elastic shear strength), the fiber would debond from the matrix at the point where it enters the matrix. Whether the fiber would continue to debond at a constant load P_f or whether an increase in pullout load would be necessary would depend on the embedded length of the fiber l_e, and the ratio of the elastic shear strength τ_s and the frictional shear strength τ_i of the fiber-matrix interface. The maximum value of fiber pullout load $P_f^{\max}$ would occur when the distance, x, of the debonded point from the embedded fiber end equals:

$$x = x_{\max} = \frac{1}{\sqrt{\alpha}} \cosh^{-1} \sqrt{\frac{\tau_s}{\tau_i}} \qquad 2.10$$

From the above equation, it is clear that the stage at which the debonding becomes catastrophic is dependent upon the ratio τ_s/τ_i. When $\tau_s / \tau_i \geq \cosh^2 \sqrt{\alpha}\, l_e$ (i.e., when $x = x_{max} = l_e$), the debonding process becomes catastrophic as soon as it commences. On the contrary, if

$\tau_s / \tau_i \leq \cosh^2 \sqrt{\alpha}\, l_e$, a further increase in fiber pullout load, P_f, is necessary for debonding to continue. Accordingly, the maximum value of the fiber pullout load P_f^{max} required to achieve complete debonding and initiate the fiber pullout is given by the following equations,

$$P_f^{max} = \frac{\tau_s \sqrt{\alpha}}{K}\left(\frac{A_m E_m - A_f E_f}{A_m E_m A_f E_f}\right)\tanh \sqrt{\alpha}\, l_e \qquad l_e \leq x_{max} \qquad 2.11$$

$$P_f^{max} = \frac{\tau_s \sqrt{\alpha}}{K}\left(\frac{A_m E_m - A_f E_f}{A_m E_m A_f E_f}\right)\tanh \sqrt{\alpha}\, x_{max} + \tau_i C(l_e - x_{max}) \qquad l_e \geq x_{max} \qquad 2.12$$

From the above equations it is clear that the maximum fiber pullout load that a fiber can achieve is not only a function of the ratio τ_s/τ_i *(i.e. x_{max})* but it is also a function of the embedded fiber length l_e. In addition, Equation 2.10 implies that, for any fiber length that is less than or equal to x_{max}, the process of debonding would be catastrophic.

At the instant when the entire fiber length is debonded, the resistance to fiber pullout would drop to a value of $\tau_i\, C\, l_e$, and subsequently it would decrease as the fiber pulls out from the matrix. When the interfacial frictional shear strength τ_i is equal to zero, then according to Equations 2.10 and 2.11 catastrophic debonding of the interface would take place; i.e., the fiber pullout load would drop from maximum to zero as soon as elastic shear stress at the location where the fiber enters the matrix equals the interfacial shear strength τ_s.

For the determination of the shear strength τ_s of the interface experimentally, the maximum pullout load P_f^{max} for fibers with different embedded length l_e is plotted against the function $\sqrt{\alpha}\, l_e$. The shape of the curve so obtained is a function of the ratio τ_s/τ_i as shown in Figure 2.2.1. The shape of the experimental fiber pullout load versus displacement curve obtained is also dependent on this ratio. Figure 2.2.2 depicts the schematic fiber pullout load versus displacement curves for the various ratios of τ_s/τ_i.

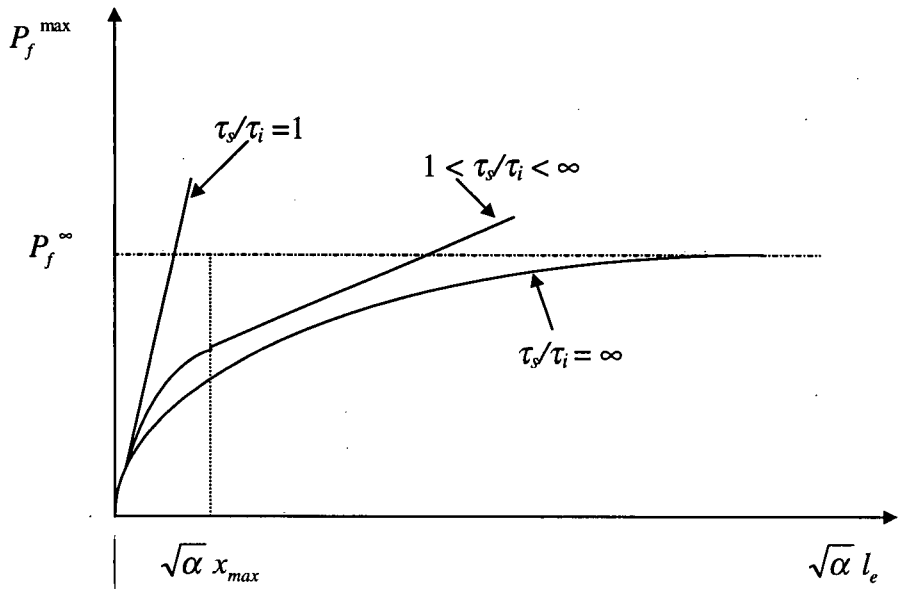

Figure 2.2.1: Variation of maximum fiber pullout load with embedded fiber length factor for various friction conditions [55]

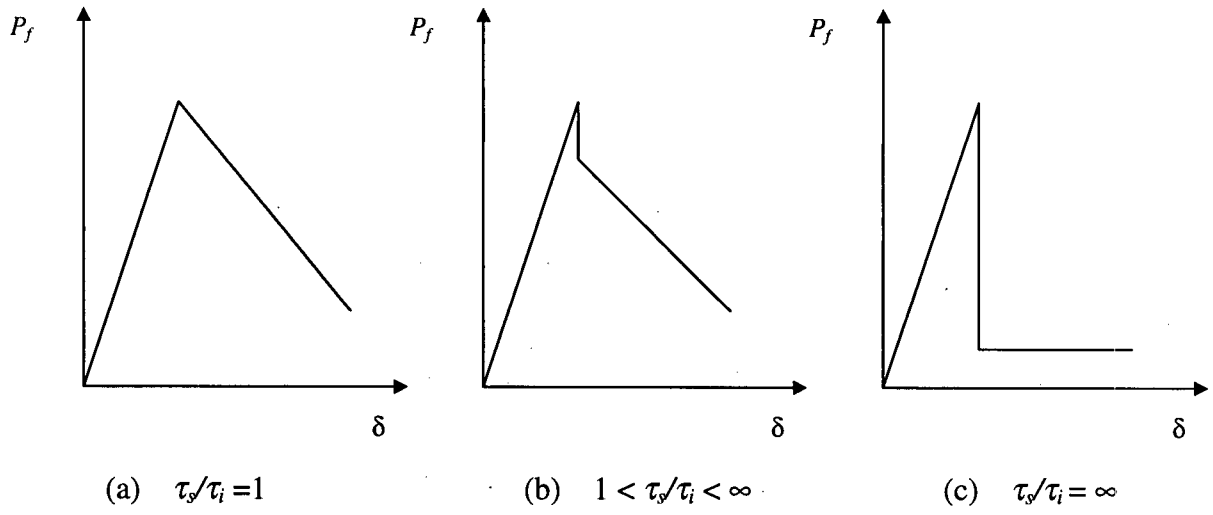

Figure 2.2.2: Variation of pullout load with fiber displacement for various interfacial frictions conditions [109]

When τ_s/τ_i =1, the fiber pullout load versus slip response is as shown in Figure 2.2.2a, and the P_f^{max} versus $\sqrt{\alpha}\, l_e$ curve is a straight line as shown in Figure 2.2.1. The shear strength of the interface can be computed from the equation,

$$\tau_s = \frac{P_f^{max}}{C\, l_e} \qquad 2.13$$

In this situation, debonding is not catastrophic, and the fiber pullout load decreases linearly from maximum to zero as shown in the Figure 2.2.2a.

When $1 < \tau_s/\tau_i < \infty$, the fiber pullout load versus displacement curve is as shown in Figure 2.2.2b, and the P_f^{max} versus $\sqrt{\alpha}\, l_e$ curve is as shown in Figure 2.2.1. In the P_f^{max} versus $\sqrt{\alpha}\, l_e$ curve a point of discontinuity occurs and the slope of the curve, Δ, becomes constant. The point of discontinuity corresponds to the fiber length l_e that equals x_{max} as given by Equation 2.10. Lawrence points out that the slope of the curve Δ is related to the frictional resistance to fiber pullout after the fiber-matrix interface has completely debonded, and it can be set equal to $\tau_i C/\alpha$. Thus,

$$\tau_i = \frac{\alpha\Delta}{C} \qquad 2.14$$

Also, from the definition of x_{max} (Equation 2.10), the magnitude of the interfacial shear strength can be determined as,

$$\tau_s = \frac{\sqrt{\alpha}\Delta}{C}\cosh^2\sqrt{\alpha}\, x_{max} \qquad 2.15$$

When the P_f^{max} versus $\sqrt{\alpha}\, l_e$ curve has no obvious discontinuity and becomes linear at long embedment lengths, this implies that the frictional shear resistance is very small, and for this case the fiber pullout load versus slip curve is as shown in the Figure 2.2.2c. Accordingly, the ratio $\tau_s/\tau_i = \infty$, and all embedded fiber lengths are less than x_{max} as given by the Equation 2.10. The interfacial shear strength τ_s can be determined from the asymptotic value of P_f^{max} (i.e., $P_f^{max} = P_f^{\infty}$) from the P_f^{max} versus $\sqrt{\alpha}\, l_e$ curve. Rearranging Equation 2.10, one can obtain,

$$\tau_s = \frac{P_f^{\infty}\alpha}{C} \qquad 2.16$$

Gopalaratnam and Shah [56]

With regard to interfacial shear stresses, Gopalaratnam and Shah [56] made similar assumptions to those made by Lawrence [55] to obtain the solution to the fiber pullout problem. Thus, this model takes into consideration the following: the existence of interfacial elastic shear stresses prior to the inception of fiber-matrix interfacial debonding, the existence of both the interfacial elastic shear stresses and the interfacial frictional shear stresses when the fiber-matrix interface is partially debonded, and the existence of interfacial frictional shear stresses after the fiber-matrix interface has completely debonded and is pulling out.

In the model developed by Lawrence [55], the parameter K that relates the interfacial elastic shear stresses, τ, with the virtual displacement of the interface, u-v, was inadequately defined. Gopalaratnam and Shah [56] assumed a square packing geometry of the fibers and related the interfacial elastic shear stress, τ, with the shear displacement of the matrix at the interface u-v in the following way,

$$\tau = \frac{G_m}{r\,\ln\left(\sqrt{\pi / V_f}\,/2\right)}(u-v) \qquad 2.17$$

where r is the fiber radius, G_m is the shear modulus of the matrix, V_f is the volume fraction of the fibers, v is the fiber displacement in the axial direction at the interface and u is the matrix displacement at the surface of the coaxial cylinder.

When the fiber is partially debonded, the axial stress distribution in the fiber, $F(x)$ and the interfacial shear stress distribution, $\tau_e(x)$, over the bonded length of fiber were derived as follows:

$$F(x) = C_1 \cosh \beta x + C_2 \sinh \beta x + C_3$$

$$\tau_e(x) = -\frac{\beta}{2\pi r}(C_1 \sinh \beta x + C_2 \cosh \beta x) \qquad 2.18$$

and, the axial stress distribution in the fiber, $F(x)$, and the interfacial shear stress distribution, $\tau_e(x)$ over the debonded length of fiber were derived as follows:

$$F(x) = P - 2\pi r\tau_i\left(\frac{l}{2} - x\right)$$

$$\tau_e(x) = -\tau_i \qquad 2.19$$

where P is the pullout load, τ_I is the interfacial frictional shear stress at the interface, and constants β, C_1, C_2 and C_3 are described in reference [56].

Takaku and Arridge [54]

Takaku and Arridge [54] developed Greszczuk [53] model by taking into consideration the existence of frictional shear stresses at the debonded interface when the fiber was completely debonded. However, the possibility of progressive interfacial debonding was not considered. Thus, according to this model, catastrophic debonding of the interface takes place at the instant when the interfacial elastic shear stress at the location where the fiber enters the matrix exceeds the elastic bond strength of the interface. The relationship between the embedded fiber length, l, and the shear strength, τ_{max}, was assumed to be the same as that derived by Greszczuk, i.e.,

$$\frac{\tau_{\max}}{\tau_{av}} = \alpha l\{\coth(\alpha l)\} \qquad 2.20$$

However, they defined the elastic parameter α in a different manner, as given by the following equation,

$$\alpha = \left[\frac{4\pi G_m}{r_f E_f \ln(r_m / r_f)}\right]^{1/2} \qquad 2.21$$

where G_m is the shear modulus of the matrix, r_f is the fiber radius, r_m is the radius of matrix surrounding the fiber, and E_f is the fiber modulus. To evaluate the values of shear strength of the interface, τ_{max}, and the elastic parameter α, they proposed a graphical method based on the results obtained from the experimental pullout tests.

Unlike Greszczuk [53], however Takaku and Arridge [54], considered the frictional resistance to fiber pullout after complete debonding had occurred, and derived the following relationship for the tensile stress $\sigma(x)$ in the fiber at any distance x from the embedded fiber end,

$$\sigma_f(x) = A\left[1-\exp(-Bx)\right] \qquad 2.22$$

Putting $x=x_e$ (embedded fiber length), the relationship between the initial fiber pullout stress σ_i and the embedded fiber length x_e was written as:

$$\sigma_i = A\left[1-\exp(-Bx_e)\right] \qquad 2.23$$

where A is a function of the normal compressive stress, σ_o, exerted by the matrix on the fiber across the interface, and the elastic properties of the fiber and the matrix. Its value can be obtained from the following equation:

$$A = \frac{\sigma_o E_f (1+\nu_m)}{E_m \nu_f} \qquad 2.24$$

where ν_m and ν_f are the Poisson's ratio for the matrix and the fiber, respectively; B is a function of the coefficient of friction between the fiber and matrix at the interface, μ, and the elastic properties of the fiber and the matrix; Its value can be obtained from the following equation:

$$B = \frac{2 E_m \nu_f \mu}{E_f r_f (1+\nu_m)} \qquad 2.25$$

σ_o and μ can be determined using Equation 2.23 and the experimental relationship between σ_i and x_e.

Pinchin and Tabor [57]

Pinchin and Tabor [57] hypothesized that a 'misfit' occurs between the fiber and the matrix since the matrix shrinks during the process of setting, hardening, and curing. Defining the fiber-matrix misfit, δ, as the difference between the radius of the fiber and the radius of the hole in the matrix in the absence of the fiber, they provided a theoretical elastic analysis of fiber pullout stress, $\sigma(x)$, in terms of the fiber-matrix misfit, δ, the coefficient of friction μ at the fiber-matrix interface, and the elastic constants of the materials. Their analysis demonstrated that the

frictional resistance to pullout, and hence the fiber pullout force, was very sensitive to the fiber-matrix misfit.

Due to fiber-matrix misfit, strain, ε_o ($=\delta/r_f$, where, r_f is fiber radius) between the fiber and the matrix is produced normal to the interface. And, as a consequence, an interfacial contact pressure, P, develops normal to the interface at every point along the length of the fiber, the magnitude of which is given by the equation:

$$P = \frac{\varepsilon_o}{(1+\nu_m)/E_m + (1-\nu_f)E_f} \qquad 2.26$$

where ν_m and ν_f are the Poisson's ratio of matrix and fiber, respectively, and E_m and E_f are the elastic modulus of matrix and fiber, respectively. When the fiber is loaded along its length by a stress $\sigma_f(x)$, it undergoes a Poisson contraction ($\varepsilon_f = \nu_f \sigma_f(x)/E_f$), and this results in a reduction in the fiber-matrix misfit. Following Equation 2.26, a reduction in misfit strains by an amount ε_f ($\varepsilon = \varepsilon_o - \varepsilon_f$) causes a reduction in the interfacial contact pressure. Taking all the above mentioned factors into consideration, Pinchin and Tabor derived an expression to calculate the stress in the fiber $\sigma(x)$ at any distance x from the embedded fiber end:

$$\sigma_f(x) = \frac{\delta E_f}{r_f \nu_f}\left[1 - \exp\left(\frac{-2\nu_f \mu x}{E_f r_f\{(1+\nu_m)/E_m + (1-\nu_f)/E_f\}}\right)\right] \qquad 2.27$$

When $E_f >> E_m$, Equation 2.27 reduces to Equation 23 derived by Takaku and Arridge [54]. An estimate of the magnitude of fiber-matrix misfit can be obtained from the experimental relationship between the fiber pullout stress and the embedded fiber length, and using Equation 2.27.

Based on experimental pullout test results obtained for steel fibers, they concluded that during the process of pullout the frictional resistance markedly decreased. They hypothesized that the observed decrease in pullout load was not due to the wear of the matrix but it was due to the compaction and densification of the cement particles near the fiber surface which caused a non-reversible reduction in the fiber-matrix misfit.

Hsueh [67]

Hsueh [67] modeled progressive debonding of the fiber-matrix interface using shear lag theory. Stresses required to debond the fiber-matrix interface and to pull out a fiber were analyzed as a function of embedded length of fiber. With an assumption that interfacial debonding initiates when the maximum interfacial shear stress exceeds the interfacial shear strength, τ_s, the initial debonding stress, σ_d (i.e., the applied pullout stress σ_d required to initiate debonding), was derived as:

$$\sigma_d = -\tau_s \left(\frac{(2/a)\left[(1+\nu_m)\left\{1+(b^2/a^2-1)(E_m/E_f)\right\}\left\{b^2\ln(b/a)-(b^2-a^2)/2\right\}\right]^{1/2}}{(b^2/a^2-1)(E_m/E_f)\coth(\alpha t)+2/\left\{(\exp(\alpha t)-\exp(-\alpha t)\right\}} \right) \qquad 2.28$$

where, a is fiber radius, b is the outer radius of the coaxial cylinder of the pullout specimen, t is fiber length, ν_m is matrix Poisson's ratio, E_f and E_m are the elastic modulus of fiber and matrix, respectively, and α is defined by:

$$\alpha = \frac{1}{a}\left[\frac{a^2E_f+(b^2-a^2)E_m}{E_f(1+\nu_m)\left\{b^2\ln(b/a)-(b^2-a^2)/2\right\}} \right]^{1/2} \qquad 2.29$$

From the above equation, it can be seen that the initial debonding stress, σ_d, depends upon the length of fiber, t. Also, for a partially debonded fiber with a debond length equal to h, the debonding stress, σ_d, can be obtained by replacing t by t-h in the Equation 2.28.

It was shown that at the debonded interface pullout of the fiber was resisted by the frictional shear stress arising due to the existence of the residual clamping stress, σ_c at the interface. Shrinkage of the matrix or the thermomechanical mismatch between fiber and matrix that take place during fabrication were identified as the phenomena responsible for the presence of a residual clamping stress at the interface. As assumed in other models [54,57], Hsueh [67] also assumed a constant value of residual clamping stress, σ_c, along the entire fiber length. Further, it was demonstrated that the radial compressive stress at the interface decreases due to Poisson's contraction of fiber, and as a result, the interfacial frictional shear stress distribution along the debonded length of fiber becomes nonlinear. With these assumptions, the axial stress distribution, σ_f, in a partially debonded fiber was derived as:

$$\sigma_f = \frac{A_3}{A_2}\{1-\exp(m_2 z)\} + B\{\exp(m_1 z) - \exp(m_2 z)\} + \sigma_d \exp(m_2 z) \qquad 2.30$$

where $z=0$ at the embedded end and is equal to L (fiber length) at the location where the fiber enters the matrix; specimen geometry and material property dependent coefficients A_2, A_3, B, m_1, and m_2 are defined in the reference [67].

Nammur et al. [61] and Naaman et al. [62,63]

The fiber pullout model introduced by Nammur, Naaman and Clark [61] is a cohesive interface type model [106]. A cohesive interface type model assumes that only relative displacements between the fiber and the matrix can activate stress transfer at the interface. Also, in these types of models the interfacial traction is described as a function of the displacement discontinuity, and since there exists a unique relationship between interface traction and interface displacement discontinuity, it is not required to distinguish between the debonded and the bonded interface. In this model, the relationship between the interfacial bond stress versus relative slip between fiber and matrix was assumed to be of the type shown in Figure 2.2.3.

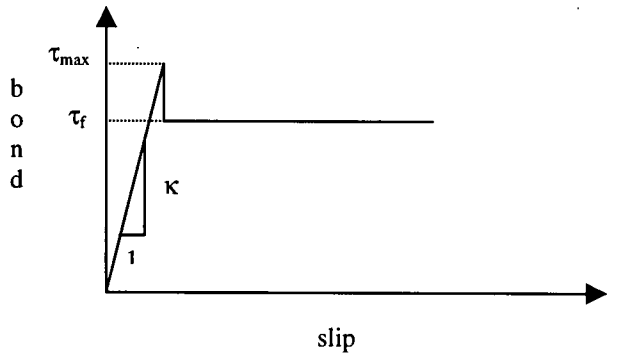

Figure 2.2.3: Interfacial bond stress vs. slip relationship [61]

As can be noticed in the above figure, the bond-slip curve is assumed to be linear elastic up to the point where the bond strength τ_{max} of the interface is attained. In the elastic region, the slope of the bond stress vs. slip curve represents the bond modulus, κ. Beyond the slip corresponding to τ_{max}, a constant frictional shear stress equal to τ_f is assumed to exist at the interface. Furthermore, it was assumed that τ_f cannot exceed τ_{max}. Since the interfacial bond due to chemical adhesion is not slip induced, the application of the bond stress vs. slip relationship assumed in this model is limited to the cases where chemical adhesion is negligible. The other

major limitation of this model is that it assumes a constant value of interfacial shear stress at the debonded front.

Applying the bond stress vs. slip constitutive relationship to a cylindrical fiber-matrix coaxial pullout model, relationships were derived for interfacial shear stress distribution, axial shear stress distribution, and fiber displacement at the various stages of pullout loading. In the interest of brevity these relationships are not included in this review.

Applying shrink-fit theory to the problem of pullout and hypothesizing that the radial misfit between fiber and matrix decreases as a fiber is pulled out of the matrix, Naaman et al. [62,63] modified the previous model developed by Nammur et al. [61]. It was shown that as the fiber pulled out from the matrix, the interfacial frictional shear stress at the debonded interface decreased as a result of the decrease in radial misfit.

Wang, Li and Backer [69]

In this work [69], the authors emphasize the triviality of fiber-matrix interfacial elastic shear bond on the overall pullout response of both high as well as low modulus fibers. They compared the theoretical pullout response for steel fibers embedded in two different types of matrix using the model developed by Gopalaratnam and Shah [56]. With the first kind of matrix, the interfacial fiber matrix bond was considered to be purely frictional, and with the second kind of matrix, both elastic and frictional bonds were assumed to exist. They demonstrated that, for both cases, the theoretical pullout responses predicted by the Gopalaratnam and Shah model [56] were very similar. Commenting on the influence of fiber modulus, they pointed out that for fibers with lower E_f/E_m ratios, the effect of elastic shear stresses on pullout response would be even less. They concluded that for most cases, the pullout analysis could be simplified by neglecting the elastic stress field existing at the fiber-matrix interface.

Further, they developed a model to predict the pullout load versus displacement response of polymeric fibers. For modeling purposes, they assumed a linear elastic constitutive behavior for both polymeric materials studied (nylon and polypropylene). Also, the effect of Poisson's contraction of the fiber, and the effect of the elastic shear stress field were ignored. In the pullout curves reported by the authors, the fiber pullout load increased with the pullout distance. They attributed this increase to an increase in interfacial frictional shear stresses while the fiber pulled out from the matrix. They pointed out that this increase in frictional shear stresses was

due the wear of the fiber surface during the fiber pullout process. Based on this observation they developed a model to predict the pullout response, which took into account the variation of the interfacial frictional bond strength as a function of fiber pullout distance. They assumed the frictional bond strength $\tau(s)$, to be a quadratic function of the slippage distance, s,

$$\tau(s) = a_o + a_1 s + a_2 s^2 \qquad 2.31$$

where a_o, a_1, and a_2 are constants, determined empirically such that the theoretical pullout curves match the experimental curves. However, they also pointed out that an alternative expression based on the theory for fiber-cement friction and wear would be more desirable to represent the τ-s relationship.

2.3 Experimental Studies on the Fiber Pullout Behavior

Interfacial bond defined as the shearing stress at the interface between the fiber and the surrounding matrix allows transfer of stress between the two materials. As discussed in the previous section, the fiber-matrix interface has been modeled and studied extensively because of its important role in composite materials. It is well accepted that the contribution of fiber in increasing the toughness of a composite is primarily governed by the energy dissipation mechanisms associated with the pullout of fibers from the matrix. Because of the importance of the interfacial properties on the overall composite response, various researchers [110-153] have put considerable effort into the investigation of interfacial properties via single fiber pullout tests. Fiber pullout tests are also routinely carried out in other fiber reinforced composites, such as fiber reinforced ceramics [169-177] and fiber reinforced metals [8,178,179]. In addition, because of the dependence of micromechanical properties on the interfacial microstructure, considerable effort has also been put toward the microstructural investigation of cementitious interfaces [160-168]. A brief review of some important experimental fiber pullout studies follows.

Gopalaratnam and Abu-Mathkour [125] investigated the influence of fiber embedded length, fiber diameter and matrix quality on the pullout behavior of steel fibers. They concluded that the average bond strength was inversely related to the embedded length and that the average bond strength increased with an increase in fiber diameter. Additionally, they found that the peak pullout load did not increase with an increase in the matrix compressive strength. Based on this

result they concluded that the frictional bond strength might be unrelated to the matrix compressive strength. Similarly, Gray and Johnston [107] also found no correlation to exist between the matrix compressive strength and the average interfacial bond strength for the case of straight fibers.

Investigating the pullout response of deformed and straight fibers, Naaman and Najm [123] found that for deformed fibers the load increased with matrix strength even beyond the peak pullout load, i.e., in the descending branch, while for smooth fibers the increase was mostly noticeable in the ascending branch. Thus, they concluded that as the matrix strength increases, the bond between the fiber and matrix also increases; however, the debonding rate following the peak load is greater for high strength matrices. They also investigated the influence of various mineral admixtures: micro-silica, fly ash, and latex. They found that micro-silica did not improve the interfacial bond strength. On the other hand, small improvements were obtained with the addition of fly ash. Similarly, addition of latex led to a significant increase in the peak pullout load but had no effect on the post-peak response, suggesting that addition of latex increased the adhesional bond strength but had no effect on the frictional bond strength. Larson and Bayasi [139] also reported that bond strength drastically increased with the addition of latex.

Banthia [131] found that addition of silica fume improved the adhesional bond strength but at the same time made the matrix more brittle. Also, pullout resistance was found to be better at subzero temperatures (-55°C) in comparison to that at normal temperature (22°C). It was also found that the mortar matrices offered a greater resistance to fiber pullout in comparison to cement paste. It was suggested that the sand particles possibly act as tiny crack arresters (blunting and deflecting crack) in the vicinity of the fiber and help arrest debonding of the interfacial crack. Influence of curing temperature on the pullout response was also studied in this investigation.

Pinchin and Tabor [141,146-147] reported that compaction of the concrete surrounding a fiber enhanced the frictional bond, and that the pullout load increased almost linearly with increase in confining pressure. They also reported that pullout load was proportional to the fiber-matrix misfit, defining misfit as the difference between the radius of the wire and that of the hole in the matrix in the absence of the wire. Similar conclusions have been made recently by Geng and Leung [120]. In an earlier study, Geng and Leung [119] found that the post-peak pullout response displayed different trends for fibers with different materials. For instance, for steel

fibers the post-peak load decreased rapidly, for polypropylene fibers the post-peak load decreased slowly and for nylon fibers the post-peak pullout load increased with the sliding distance. Wang et al. [115,116] observed that synthetic fibers like polypropylene and nylon are easily abraded by cement particles during the process of pullout. The severity of surface abrasion of fiber was found to increase with increase in fiber slip and it was accompanied with an increase in the apparent fiber/matrix bond strength.

Gokoz and Naaman [145] reported that the peak pullout load, which is indicative of the elastic bond on the interface, was not sensitive to strain-rate. Banthia and Trottier [127] and Banthia et al. [134] also investigated strain rate sensitivity of bond for straight and deformed fibers. They found that pullout performance for deformed fibers was sensitive to the rate of loading. On the other hand, for straight fibers no definite conclusion could be made with regard to the strain rate sensitivity of the interfacial bond. In particular, for deformed fibers they found that both the peak pullout load and the pullout energies increased with an increase in the rate of loading. They concluded that since steel, cementitious matrices and the fiber-matrix interface all have properties dependent upon the rate of loading, the capability of the fiber to resist pullout largely depends upon the rate at which fiber pullout occurs. In addition, in these studies, cement paste matrices were found to be less sensitive to loading rate in comparison to the mortar matrices. Pacios et al. [138] also investigated the influence of rate of loading on interfacial response between fibers and cementitious matrices. They found that both pullout load and slip increased with increase in the rate of loading.

Naaman and Shah [142] found that the efficiency of bond in the case of pullout of an inclined steel fiber (with respect to loading axis) was at least as good as that of fibers aligned parallel to the loading direction. Ouyang el al. [86] also found that pullout resistance of inclined fibers was generally greater than that of aligned fibers. The maximum inclination of fiber with respect of loading axis investigated in this study was 37^0. On the other hand, Banthia and Trottier [127] investigated a wider range of fiber inclination ($0^0 - 60^0$) and concluded otherwise, stating that the bond efficiency of aligned fibers was greatest, and increasing inclinations of fiber with respect to the loading axis reduced the efficiency of interfacial bond. Maage [140,144] also investigated the influence of fiber inclination and reported that the bond efficiency increased to a maximum and then decreased as the angle between the fiber and the loading direction increased.

Gray and Johnston [107] found that the bond strength depended on the direction of casting, concluding that vertically cast specimens developed a higher interfacial bond strength than horizontally cast specimens. Additionally they found that an increase in the sand-cement ratio in the mortar matrix led to a decrease in interfacial bond for the vertically cast specimens and an increase in bond for the horizontally cast specimens. Burakiewicz [143], on the other hand, reported otherwise, stating that the bond strength was virtually insensitive to vibration and fiber orientation during setting and hardening of the matrix.

Shao et al. [154] studied the processes of matrix cracking and fiber-matrix interfacial debonding using high-sensitivity Moire interferometry techniques. The initiation and propagation of cracking and interfacial debonding were observed during uniaxial tension tests, and fiber stress, interfacial slip, interfacial shear stress, and the matrix strain distribution were calculated from the experimental information. Based on the experimental study, they questioned the validity of the fiber-matrix interfacial shear stress versus slip constitutive relationships assumed in several fiber pullout models [60-63].

Kawamura and Igarashi [149] carried out a fluorescence microscopic study of the interfacial zone between steel fibers and cementitious matrices subjected to pullout load. They reported that progressive debonding of the interface originated from the point where the fiber entered the matrix, as predicted by shear-lag theory based analytical pullout models. A similar conclusion was made by Li et al. [81,82], based on the fluorescence optical microscopic investigation carried out on uniaxial tensile specimens. Kawamura and Igarashi [149] also found silica fume modified cementitious matrices to be less tough in comparison to the matrices without silica fume. Further, they reported that during the propagation of interfacial cracks, local failures around a fiber in the silica fume matrices were limited to smaller regions around the interface because of the presence of denser and more homogeneous bulk phases in the matrix; on the other hand, the toughening mechanisms of non-silica fume matrices were responsible for deflection and branching of cracks due to unhydrated cement particles and $Ca(OH)_2$ crystals. In an another study, Kawamura and Igarashi [151] reported that the maximum pullout load increased with increasing silica fume content (20% replacement) but the drop in load immediately after the maximum load was considerably small. Also, the total work of pullout was considerably greater with the silica fume matrix and authors attributed this to the increase in frictional resistance along the debonded surfaces due to the addition of silica fume. In this study authors also found that the values of microhardness (measured using the ultramicrohardness tester with Vickers

indenter - minimum load=0.1gm) in the bulk cement paste matrix as well as in the interfacial transition zone were increased by the addition of silica fume.

2.4 Mechanical Behavior of Fiber Reinforced Cementitious Composites

Especially since the pioneering work of Romualdi and Batson [180] on steel fiber reinforced concrete, extensive research into the mechanical properties of fiber reinforced cementitious composites has taken place [1-3, 181-184]. Moreover, in recent years, several advancements have been made with regard to matrix, fibers, interfaces and the composite production process. Some examples include [182]: i.) the commercial introduction of a new generation of additives such as superplasticizers that allow high matrix strengths to be readily achieved with little loss in workability; ii.) the increasing use of active or inactive micro-fillers such as silica fume and fly ash and a better understanding of their effect on matrix porosity, strength, and durability; iii.) the increasing availability for use in concrete of fibers of different types and properties which can add significantly to the strength, ductility, and toughness of the resulting composite; iv.) the use of polymer addition or impregnation of concrete which adds to its strength and durability but also enhances the bond between fibers and matrix thus increasing the efficiency of fiber reinforcement; and, v.) innovations in production processes to achieve uniform mixing of high volume fiber fractions with reduced effects on the matrix porosity.

In general, the parameters governing the behavior of fiber reinforced cementitious composites can be classified under three categories. The first category consists of the parameters related to the fibers, such as elastic modulus, tensile strength, ductility, length, diameter, and volume fraction. The second category consists of the parameters related to the matrix such as fracture toughness, elastic modulus, ultimate tensile strength, ultimate tensile strain, and initial flaw size. Finally, the third category consists of the micromechanical parameters related to fiber-matrix interface, such as interfacial bond strength. Traditionally, research on fiber reinforced concrete has focused on studying the dependence of composite behavior on one or two of the aforementioned properties at a time. Typically, these properties have been fiber volume fraction and fiber aspect ratio. Thus, it is important to recognize that fiber volume fraction, for instance, is only one of an array of parameters under our control when designing fiber reinforced cementitious composites. For this reason it is not sufficient to understand the individual influence of each parameter on composite properties. Composite optimization requires

establishing the combined influence of all relevant parameters on composite properties. Through composite optimization, composites with tailored properties can be produced with only moderate volume fraction of fibers. In this regard, development of high-performance cementitious composites, (i.e., composites with an optimized combination of properties, such as quasi-strain hardening behavior, multiple cracking, strength, toughness, energy absorption, stiffness, durability, and corrosion resistance) require an understanding of the fundamental micromechanisms controlling the composite behavior.

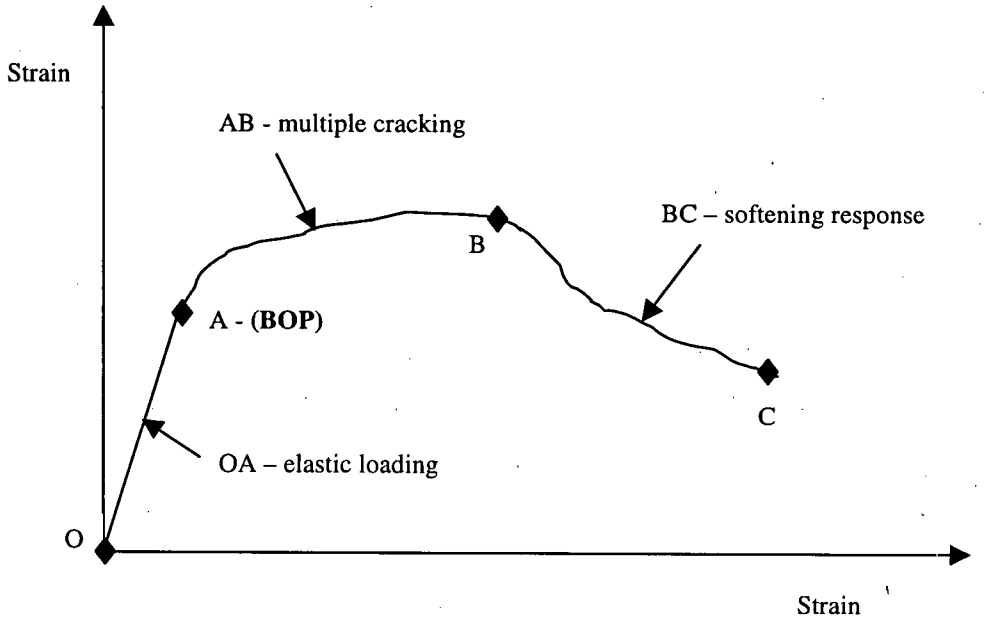

Figure 2.4.1: Stress-strain response for a fiber reinforced cementitious composite showing strain hardening response

Figure 2.4.1 shows the stress-strain response in tension for a fiber reinforced cementitious composite exhibiting multiple cracking. The overall tensile response can be divided into three regions. First, the initial linear region up to the Bend-Over-Point (BOP) represents the elastic loading of the composite (i.e., the region OA). Beyond this region, multiple cracking of the matrix takes place, and the stress-strain curve rises in a non-linear fashion showing a quasi-strain hardening response (i.e., the region AB). Finally, at the end of multiple cracking, strain localization takes place and the stress-strain curve shows a softening response (i.e, region BC). The extent of these stages depends on the properties of the fiber, matrix and interface. So far, considerable research efforts have been put into modeling the tensile behavior of fiber reinforced composites [185-214]. However, as Shah and Ouyang [105] have pointed out, despite the extensive modeling efforts, the phenomenon of crack propagation in fiber reinforced cement

based matrices still remains poorly understood. A brief review of literature describing the conditions leading to quasi strain hardening and multiple cracking behavior is presented below. These solutions generally identify a number of controlling parameters, such as fiber reinforcing parameters, the interfacial fiber-matrix bond, critical fiber volume that lead to quasi strain hardening and multiple cracking.

Aveston et al. [185] proposed an analytical model to predict the conditions required to obtain multiple matrix cracking and crack spacing in the event of multiple cracking. This model is commonly known as the ACK model. The authors suggested that if one of the two constituents (fiber or matrix) of a fibrous composite breaks at a much lower elongation than the other, then provided the non-broken constituent is able to bear the load, a tensile specimen will show continued or multiple fracture of the more brittle phase until the specimen finally breaks when the ultimate strength of the stronger phase is reached. The above statement suggests that if the breaking strain of the matrix is less than that of the fiber then the matrix will be successively fractured into shorter lengths by a process of multiple fracture, until the fiber attains its failure strain. Likewise, if the breaking strain of the fiber is less than that of the matrix, then the fiber will be successively fractured into shorter lengths by a process of multiple fracture, until the matrix attains its failure strain. The condition for multiple cracking of matrix was derived as:

$$\sigma_{fu} V_f \geq \sigma_{mu} V_m + \sigma'_f V_f \qquad 2.32$$

where σ_{fu} and σ_{mu} are fiber and matrix strength, respectively, σ'_f is the fiber stress required to produce a strain equal to the breaking matrix strain, and V_f and V_m are volume fractions of fibers and matrix, respectively. The right hand side of the above equation represents the composite stress at the instant matrix attains failure strain. Thus, the above equation suggests that the fibers are able to sustain the additional load thrown upon them when the matrix fails. The minimum fiber volume fraction required to achieve multiple cracking (i.e., critical fiber volume fraction) can be obtained by using the equality expressed in the above equation. Furthermore, assuming a linear distribution of shear stress in the debonded zone, authors calculated the crack spacing x' as:

$$x' = \left(\frac{V_m}{V_f}\right)\frac{\sigma_{mu} r}{2\tau} \qquad 2.33$$

where σ_{mu} is the matrix fracture stress, r is the fiber radius, and τ is the average fiber-matrix interfacial bond strength. By assuming that the crack spacing at the beginning of multiple cracking is $2x'$, (i.e., sliding occurs along the entire fiber-matrix interface), authors derived the solution for failure strain of matrix, ε_{mu}, from the energy balance as:

$$\varepsilon_{mu} = \left[\frac{12\tau\gamma_m E_f V_f^2}{E_c E_m^2 r V_m} \right]^{1/3} \qquad 2.34$$

where γ_m is the fracture surface work in forming a crack in matrix, E_c is the elastic modulus of composite, E_m is the elastic modulus of the matrix.

Budiansky et al. [186] generalized the ACK model to include the three types of fiber interface conditions: perfectly bonded fibers, debonded sliding fibers and unbonded, sliding fibers. This model is commonly known as the BHE model. Authors obtained distributions of stress and strain in the fiber and matrix based on shear lag analysis. The strain energy release rate of composites was calculated from the obtained stress distributions, and the multiple cracking response was predicted from the energy balance, which equated the strain energy release rate of composites to the sum of energies resulting from debonding and sliding, and the matrix surface energy. For a perfectly bonded fiber, the BHE model predicts the composite stress, σ_{cf}, for multiple cracking as:

$$\frac{\sigma_{cf}}{E_c} = \left(\frac{V_f E_f G_{mc} \rho}{r E_m E_c} \right) \qquad 2.35$$

where

$$\rho = \frac{1}{V_m} \left[\frac{2V_m^{\ 3}}{-6\log(V_f) - 3V_m(3 - V_f)} \frac{6E_c}{E_f(1+\upsilon_m)} \right]^{1/2}$$

where ν_m is Poisson's ratio of the matrix, G_{mc} is the fracture resistance of matrix, E_f, E_m and E_c are the elastic modulus of fiber, matrix and composite, respectively, and V_f and V_m are the volume fraction of fiber and matrix, respectively.

Naaman [187] proposed a solution based on the mechanics of composite materials for predicting conditions required for achieving multiple cracking of matrix. Assuming a three dimensional fiber distribution, he derived equations for predicting the first cracking stress, σ_{cc}, and the

maximum post-cracking stress (or bridging stress), σ_{pc}. The composite tensile stress at first cracking of matrix was derived as:

$$\sigma_{cc} = \sigma_{mu}(1 - V_f) + \alpha_1 \alpha_2 \tau V_f L/d \qquad 2.36$$

where

V_f = volume fraction of fibers

L = fiber length

d = fiber diameter

σ_{mu} = matrix tensile strength

τ = average bond strength at the fiber matrix interface

α_1 = coefficient representing the fraction of bond mobilized at first matrix cracking

α_2 = efficiency factor of fiber orientation in the uncracked state of the composite

The maximum post cracking stress, σ_{pc}, was derived assuming that a critical crack exists across the entire section of the tensile member, the crack is normal to the tensile stress field, and the contribution of the matrix is negligible. Thus, the maximum post cracking stress, σ_{pc} was derived as:

$$\sigma_{pc} = \lambda_1 \lambda_2 \lambda_3 \tau V_f L/d \qquad 2.37$$

where

λ_1 = expected pullout length ratio (equal to 1/4 from probability considerations)

λ_2 = efficiency factor of orientation in the cracked state

λ_3 = group efficiency factor associated with the number of fibers pulling out per unit area

For multiple cracking to occur, the maximum post-cracking stress must be larger than the first cracking stress, i.e.:

$$\sigma_{pc} \geq \sigma_{cc} \qquad 2.38$$

Combining Equations 2.36-38, the minimum fiber volume required to guarantee multiple cracking (i.e., critical fiber volume, $V_{f,crit}$) was obtained as:

$$V_{f,crit} = \frac{1}{1 + \frac{\tau}{\sigma_{mu}} \frac{L}{d} (\lambda_1 \lambda_2 \lambda_3 - \alpha_1 \alpha_2)} \qquad 2.39$$

The above equation depicts that the fiber aspect ratio and the ratio of fiber-matrix interfacial bond strength and matrix tensile strength are influential parameters in controlling the fiber volume fraction required for multiple cracking to occur. Parametric studies conducted using the above equation depict that a higher fiber aspect ratio and a lower interfacial bond strength to matrix tensile strength ratio lead to reduction in critical fiber volume.

Li and Wu [188] assumed a random fiber orientation and used the fracture mechanics based J-integral approach (originally proposed by Marshall and Cox [202]) to derive the condition leading to multiple cracking and quasi-strain hardening. They derived the critical fiber volume fractions as:

$$V_{f,crit} = \frac{12 J_c}{g\tau (L_f / d_f)\delta_o} \qquad 2.40$$

where J_c is the composite crack tip toughness, which may be related to the matrix fracture toughness, K_m, as suggested in Reference [195]. L_f and d_f are fiber length and diameter, respectively. The snubbing factor, g, and interfacial frictional bond strength, τ, are the parameters describing the interaction between fiber and matrix. The snubbing factor accounts for the variation in bridging force across a matrix crack when a fiber is pulled out at an inclined angle. And, finally, δ_o in the above equation represents the crack opening at which the fiber bridging stress reaches a maximum, σ_o, and is given by:

$$\delta_o = \frac{\tau L_f^2}{E_f d_f (1+\eta)} \qquad 2.41$$

where $\eta = (V_f E_f)/(V_m E_m)$, and V_f and E_f are the fiber volume fraction and fiber elastic modulus, respectively, and V_m and E_m are the matrix volume fraction and matrix elastic modulus, respectively.

For a pseudo strain hardening material, the ultimate strength of the composite, σ_{cu} coincides with the maximum bridging stress, σ_o, given by:

$$\sigma_{cu} = \frac{1}{2} g\tau V_f \left(\frac{L_f}{d_f} \right) \qquad 2.42$$

From the viewpoint of composite design, Equation 2.40 is significant, since it provides guidelines to tailor the micromechanical parameters for strain hardening materials such that $V_{f,crit}$

is minimized. In an another article, Li [196] has recommended the following with regard to the tailoring of micromechancial parameters:

Matrix Toughness Tailoring: With a decrease in matrix toughness, J_c, smaller amount of fibers is needed to make the transition from the quasi-brittle failure mode to the strain-hardening failure mode. From the viewpoint of matrix design, in order to tailor the matrix toughness, adjustments can be made to the water/cement ratio, size and type of aggregates, and microfillers such as silica fume.

Interfacial Bond Tailoring: Enhancing the interfacial frictional bond, τ, while still ensuring that fiber fracture does not occur, would assist in lowering the amount of fibers required to achieve multiple cracking. The ductility of fiber reinforced cementitious composites is associated with the inelastic strain generated as a consequence of multiple cracking. Moreover, the composite inelastic strain is a function of the multiple crack density and crack opening. The multiple crack density can be expected to increase with the interfacial bond strength, τ, which controls the stress transfer from the bridging fiber into the matrix material. To improve the interfacial bond strength, several methods can be employed, such as fiber surface modification, fiber deformation, and transition zone modification.

Fiber Length Tailoring: Equation 2.40 depicts that the critical fiber volume fraction, $V_{f,crit}$, is inversely proportional to L_f^3 (since δ_o is proportional to L_f^2), suggesting that fibers with long lengths are preferable. However, difficulty in processing places a limitation on the choice of fiber length.

In addition to the models discussed above, several other micromechanical models have been proposed for predicting cracking behavior in fiber reinforced cementitious composites (including the ones by Leung and Li [190,191], Tjiptobroto and Hansen [200,201], Cox and Evans [203,204], Nemat-Nasser and Hori [205], Marshall, Mai [206], Mori and Mura [207], Yang et al. [208], Hillerborg, Modeer and Peterson [209], Foote, Mai and Cotterell [212], Jenq and Shah [213] and Ouyang, Mobasher and Shah [214]).

Chapter 3

Macromechanical Behavior of Fiber Reinforced Concrete (FRC) & Measurement of Flexural Response of Low Toughness FRC

3.0 Introduction

Cementitious materials have low strain capacity and ductility. The tensile strain capacity and energy absorption capability (i.e., ductility) of these materials can be dramatically improved by inclusion of fibers in the matrix. The extent of improvement obtained due to the addition of fibers depends on the mechanical properties of the fiber and the matrix, and on the nature of interaction between the two. Optimal design of fiber reinforced concretes can be accomplished only when the influence of various material variables on the macromechanical behavior of fiber reinforced concrete composite is properly understood. Therefore, one objective of this research is to experimentally investigate influence of various important material variables on the post-cracking response in flexure and the ensuing toughness of fiber reinforced concretes.

Measured flexural response of fiber reinforced concretes is also influenced by the various test variables [41,42]. One such test variable is stiffness of testing machine. The present ASTM standard (ASTM C1018 [4]) and the JSCE standard (JSCE-SF4 [5]) for evaluating flexural response and toughness of fiber reinforced concretes are appropriate only for fiber reinforced concretes with high toughness [6]. For low toughness fiber reinforced concretes, the measured flexural response based on the aforementioned standards has been found to grossly depend upon the relative stiffness of testing machine [6]. Thus, another major objective of this research is to address the issue of rationally measuring the true flexural response of fiber reinforced concretes with low toughness. ASTM has recently accepted a new test method [7] as a test standard for measurement of flexural performance of fiber reinforced concretes. This method is referred as the Residual Strength Test Method in this chapter. Validity of this method is explored as a part of this research program and the results are reported in this chapter.

3.1 Material Variables Influencing Macromechanical Behavior and Toughness of FRC

This section investigates the influence of various material variables on the macromechanical behavior and toughness of FRC. Important material variables investigated include properties of matrix, volume content of fibers, fiber geometry, fiber aspect ratio, surface properties of fibers, and shrinkage properties of matrix.

Materials and Mixes

The materials and the mixes used in this investigation are given below in Table 3.1.1. CSA Type 10 normal Portland cement was used. Clean river sand with a fineness modulus of 2.3 was used as the fine aggregate, and pea gravel with a maximum size of 10 mm was used as the coarse aggregate. All mixes contained air-entraining agent at a dosage of 0.1ml/kg of cement. For a few other mixes, different mix proportions were used and those will be indicated at appropriate locations in this section. Geometry and mechanical properties of fibers used in this investigation are given in the Table 3.1.2.

Table 3.1.1: Mix Proportions

Cement (kg)	Water (kg)	Sand (kg)	Aggregate (10 mm) (kg)	Air Entraining Agent (ml/kg of cement)
400	200	800	1000	0.1

Table 3.1.2: Description of fibers investigated

Fiber	Material	Geometry	Cross-sectional shape	Length (mm)	Diameter (mm)	f_t ~ (MPa)	E_f $ (GPa)
STL-STR	Stainless Steel	Straight	Circular	40	0.76	1100	210
PP-STR1	Polypropylene	Straight	Oval	40	0.63	450	3.5
PP-STR2	Polypropylene	Straight	Oval	38	0.19	450	3.5
PVA-1	PVA*	Straight	Oval	29	0.42	1100	23
ST-HKD	Steel	Hooked-end	Circular	35	0.55	1115	210
ST-HKD2	Steel	Hooked-end	Circular	30	0.50	1115	210
ST-CR1	Steel	Crimped#	Crescent	38	2.0 x 0.35	1037	210

* PVA - Polyvinyl Alcohol; # Crimp amplitude=1mm and Wave length=7.5mm;
~ f_t – Tensile strength of fiber; $ E_f – Elastic Modulus of fiber

Specimens and Test Methods

Cylinders for compressive strength test: Cylindrical specimen 200 mm long and 100 mm in diameter were used to test the compressive strength of FRC and plain concrete mixes. Cylinders

were tested in compression in a 1000 *kN* compression testing machine as per ASTM C 39 at 7 and 28 days.

Beams for flexural toughness test: Beam specimens conforming to the dimensions recommended in ASTM C1018 – (100 mm x 100 mm x 350 mm) were used for flexural testing of FRC and plain concrete mixes. A pan type concrete mixer (capacity: 0.18 m^3) was used for mixing the concrete and the procedure outlined in ASTM C192 "Method of Making and Curing Concrete Specimens in the Laboratory" [215] was followed. All coarse aggregate and some of the mixing water were first mixed, followed by the addition of fine aggregate, cement, water, pozzolanic admixture in slurry form (when included), air entraining agent and fibers.

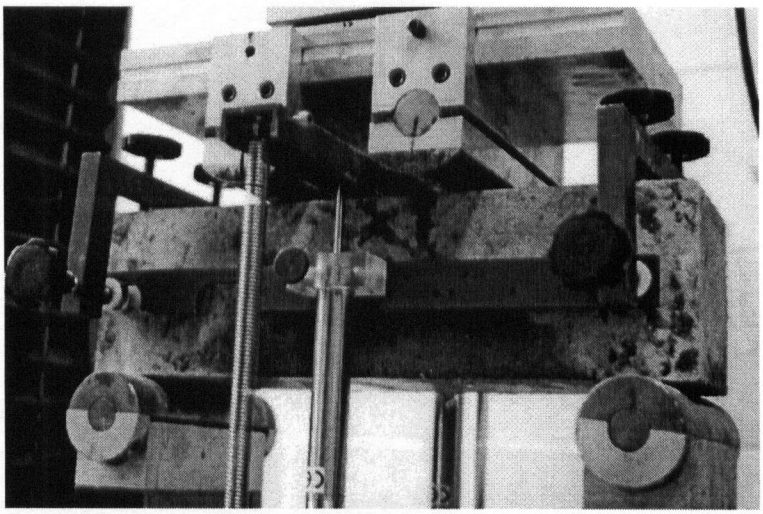

Figure 3.1.1: Test setup for flexural toughness test according to ASTM C 1018 [4]

For flexural tests, a 150-kN capacity floor mounted, Instron electro-mechanical testing machine was used. All operations were controlled by a microprocessor based central processing unit. Two LVDTs mounted on a *Japanese Yoke*, shown in Figure 3.1.1, recorded the net deflection of the beam at the mid-span. With the use of a *Japanese Yoke*, extraneous deflections resulting from settlement of supports, crushing at load points, and load-fixture deformations are eliminated and only the true deflections are recorded [42,44]. The load was applied at a constant cross-head displacement rate of 0.1mm/min. A PC-based data acquisition system was used to digitally record loads and displacements at a frequency of 10 *Hz*. The output signals from the testing machine and LVDTs were acquired by a computer-based high-speed data acquisition system. The data acquisition system comprised a PC-486 computer, a 16 channel A/D conversion board,

and a 16 I/O channel AC and DC conditioner unit in which each channel was equipped with amplifiers with gains of up to 1000. The maximum sampling rate of this data acquisition system is 10 million points per second, i.e., 1 MHz. The software package used for acquiring data was "Quicklog" by Strawberry Inc. The resulting load versus mid-span deflection plots were analyzed for JSCE flexural toughness parameters [5]. The test procedure described above is also referred as the Open-loop Test Method (OLTM) in this thesis.

3.1.1 Mineral Admixtures

Constituents of the binder have a significant influence on the chemistry and microstructure of the matrix in the interfacial regions. Both chemistry and microstructure of matrix are modified to a considerable extent when a portion of cement is replaced by a mineral admixture such as pozzolan. For example, a silica fume modified matrix gives rise to a very densified microstructure at the fiber-matrix interface [105]. It can be expected that the post-cracking response of FRC would be affected as a consequence of the modified interfacial properties brought about by the inclusion of pozzolans. The objective of the following studies was to investigate the influence of matrix modification by pozzolans on the post-cracking response of FRC.

Influence of Matrix Modification by Silica Fume Pozzolan

The influence of pozzolanic modification of the matrix on the post-cracking response of fiber reinforced concrete was investigated. Pozzolan-silica fume was chosen for this purpose; properties of the silica fume used are given in Table 3.1.3. The two mixes investigated contained straight-smooth, stainless steel fibers at a volume fraction of 0.76%. The mix proportion used was - water : binder : sand : aggregate = 0.35 : 1.00 : 1.50 : 1.75. The control mix did not contain silica fume and the silica fume mix contained silica fume at a dosage of 10% by weight of binder as shown in Table 3.1.4. The twenty-eight day compressive strength for the control mix was approximately about 69 MPa and that for the silica fume mix was about 71 MPa.

Table 3.1.3: Properties of Pozzolans

Property	Silica fume	High-Reactivity Metakaoline
Average Particle size, μm	0.1	1.5
Reactive Component (minimum percent by mass)	SiO_2 (97%)	$SiO_2+Al_2O_3+Fe_2O_3$ (95%)
Specific Gravity	2.2	2.5

Five beams were tested for each mix. The average flexural responses for these mixes are compared in Figure 3.1.2. It can be noticed that the post-peak flexural response in the case of mix containing silica fume was relatively inferior in comparison to the mix without silica fume. JSCE toughness parameters [5], namely, "Absolute Toughness (T_{JCI})" and "Flexural Toughness Factor (σ_b)" were calculated from the average flexural response. The Absolute Toughness, T_{JCI} is defined as the area under the load-deflection curve to a deflection of *span/150*. The Flexural Toughness Factor, σ_b, (a measure of the equivalent flexural strength) is defined as:

$$\sigma_b = \frac{T_{JCI}.S}{\delta_{150}.w.d^2} \qquad 3.1$$

where S is beam span, w is beam width, d is beam depth, and δ_{150} *is* $S/150$. The calculated JSCE toughness parameters are given in Table 3.1.4. Apparently, the observed disparity in the flexural performance in the two cases is related to the micromechanics of fiber-matrix interface. The influence of matrix modification by mineral admixtures on fiber pullout response is a subject of investigation in Chapter 4.

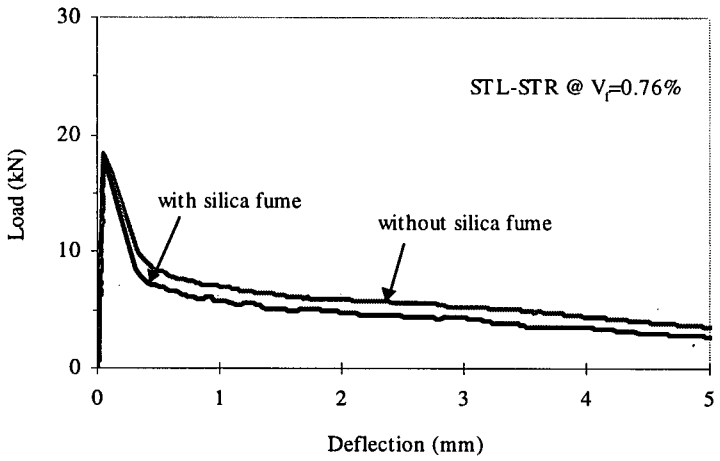

Figure 3.1.2: Comparison of flexural load versus deflection response for fiber reinforced concrete mixes with and without silica fume and containing straight-smooth, stainless steel fiber at a dosage of 0.76%

Table 3.1.4: JSCE Absolute Toughness and Flexural Toughness Factor – Influence of Pozzolan

Fiber Id.	Fiber Description	Binder Type (% weight)	Fiber Volume (%)	MOR (MPa)	Absolute Toughness, T_{JCI} (N-m)	Flexural Toughness Factor, σ_b (MPa)
STL-STR	Straight-smooth, stainless steel	100% CSA Type 10 NPC*	0.76	5.51 (0.51)@	14.9 (1.28)	2.25 (0.19)
SRL-STR	Straight-smooth, stainless steel	90% CSA Type 10 NPC + 10% Silica fume	0.76	5.46 (0.54)	12.5 (0.90)	1.88 (0.14)

* NPC – Normal Portland Cement; @ - Figures in brackets indicate standard deviations

Influence of Pozzolan Type

While the addition of pozzolans densifies the matrix microstructure, it also increases the brittleness of matrix. Increased matrix brittleness is of particular concern when deformed fibers are involved. Increased matrix brittleness can cause crushing and splitting of the matrix and in turn, curtail the ability of fibers to transfer stresses during pullout, thus reducing the overall toughness. In addition to the water/binder ratio, one may anticipate that the type, chemical reactivity, and particle size of the pozzolan used will have a decisive effect on the brittleness of the matrix and on the fiber-matrix bond. The objective of this investigation was to study the influence of various matrix modifications on the flexural toughness performance of steel fiber reinforced concrete. Two types of pozzolanic admixtures were investigated, namely,

i. silica fume, and

ii. high-reactivity metakaolin (HRM)

High-reactivity metakaolin (HRM) is produced by calcining purified kaoline clay in the temperature range of 700 to 800^{o}C. HRM is a poorly crystallized white powder with a high pozzolanic reactivity, which earns it the name *super-pozzolan.* It comprises nearly 95% of (SiO_2+Fe_2O_3+Al_2O_3) and has elongated particles about 1μm in size on average. Physical characteristics and chemical properties of silica fume and HRM investigated are given in Table 3.1.3.

Mix CF (control mix) contained only CSA Type 10 (ASTM Type I) cement as the cementing material. The mix proportion (by weight) for the control mix was: water : cement : fine aggregate : coarse aggregate = 0.35 : 1.0 : 1.5 : 2.25. In Mix SF, on the other hand, 10% of cement was replaced by an equal quantity of silica fume, and in Mix MF, 10% of cement was replaced by an equal quantity of high-reactivity metakaolin. Finally in Mix SMF, a combination of 5% silica fume and 5% high-reactivity metakaolin replaced 10% of cement. In all the mixes, hooked-end steel fibers, 30 mm long and 0.5 mm in diameter were added at 1% by volume.

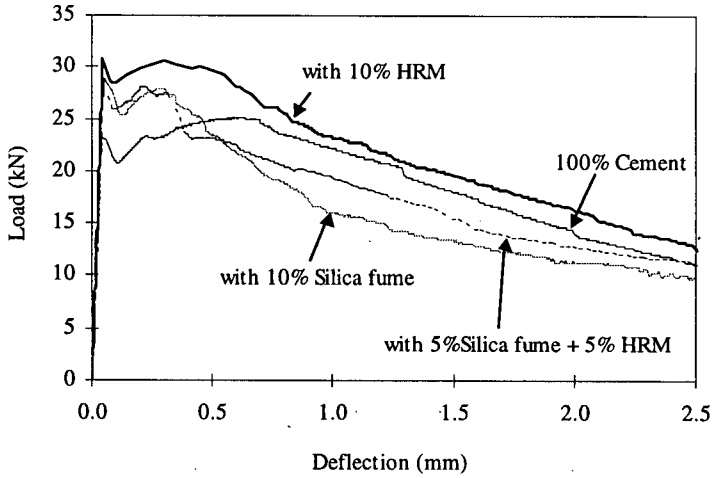

Figure 3.1.3: Comparison of flexural load versus deflection response for fiber reinforced concrete mixes different types of pozzolans

Representative load versus mid-span deflection plots for the various steel fiber reinforced concrete mixes are given in Figure 3.1.3. It can be observed that the post-peak performance of fiber reinforced concrete with HRM was superior to other composites. Silica fume concrete (Mix SF) exhibited a relatively brittle behavior with a steeper drop in load beyond peak. The load-deflection performance of the control, non-pozzolan concrete (Mix CF) and the hybrid-pozzolan concrete (Mix SMF) was between that of concretes with HRM (Mix MF) and silica fume (Mix SF). As expected, at a high fiber volume fraction of 1% used in this investigation,

some pseudo-strain hardening occurred in the post-peak region for all composites. JSCE toughness parameters, shown in Table 3.1.5, also depict the superior performance of concrete containing HRM. Lower JSCE numbers for silica fume concrete (mix SF) are directly related to the relatively steeper drop in the load that occurred after peak, indicating a greater rate of softening and damage in these composites. Visually, one could notice that the silica fume matrix had cracked more extensively, and fibers as a result could not develop adequate mechanical anchorage with the matrix. These fibers then pulled out with minimal straightening of the hooks and absorbed much less energy. For fibers in concrete with high-reactivity metakaolin, on the other hand, the ends had been straightened for a greater number of fibers signifying an increased absorption of energy.

Table 3.1.5: JSCE Absolute Toughness and Flexural Toughness Factor – Influence of Pozzolan Type

Mix Id.	Fiber Description	Binder Type (% weight)	Fiber Volume (%)	MOR# (MPa)	Absolute Toughness, T_{JCI} (N-m)	Flexural Toughness Factor, σ_b (MPa)
CF	Hooked end steel ST-HKD	100% Cement	1.0	7.19 (0.53)@	39.20 (3.8)	5.88 (0.44)
SF	Hooked end steel ST-HKD	90% Cement + 10% Silica fume	1.0	8.37 (0.30)	32.0 (3.36)	4.80 (0.50)
MF	Hooked end steel ST-HKD	90% Cement + 10% HRM	1.0	8.39 (0.82)	41.4 (3.24)	6.40 (0.49)
SMF	Hooked end steel ST-HKD	90% Cement + 5% Silica fume + 5% HRM	1.0	8.39 (0.32)	36.8 (4.30)	5.81 (0.45)

- MOR – Modulus of Rupture; @ - Figures in brackets indicate standard deviation

3.1.2 Fiber Volume Content

To investigate the influence of fiber volume content, three types of fibers were chosen. Fiber types and the corresponding fiber volumes investigated were,

i. Straight-smooth, stainless steel fiber, STL-STR – $V_f = 0.76\%$ and 5.0%

ii. straight, smooth polypropylene fiber, PP-STR1 – $V_f = 1.0\%$ and 5.0%

iii. straight polyvinyl alcohol fiber, PVA-1 – $V_f = 1.0\%$ and 5.0%

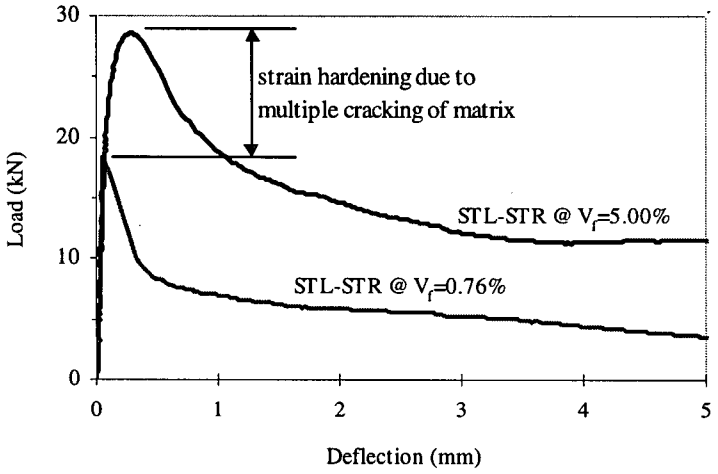

Figure 3.1.4a: Comparison of flexural load versus deflection response for fiber reinforced concrete mixes – Influence of fiber volume, V_f = 0.76% and 5.0% of straight-smooth, stainless steel fiber (STL-STR1)

Five beams were tested for each mix. The average flexural responses for the various mixes are shown in Figures 3.1.4a, b and c. JSCE Flexural Toughness and Flexural Toughness Factor for the various mixes are reported in Table 3.1.6. It can be noticed that the flexural toughness increases with increase in fiber volume. Also, both the prepeak and the postpeak response are a function of properties of fibers incorporated in the matrix. In specimens reinforced with 5% steel and polyvinyl alcohol fibers, considerable multiple cracking of the matrix took place and this gave rise to strain hardening response in the prepeak region. On the other hand, for specimens reinforced with 5% polypropylene fibers, no multiple cracking of the matrix took place. Moreover, the strain hardening response observed in the postpeak region was most likely related to the constitutive behavior of polypropylene fibers.

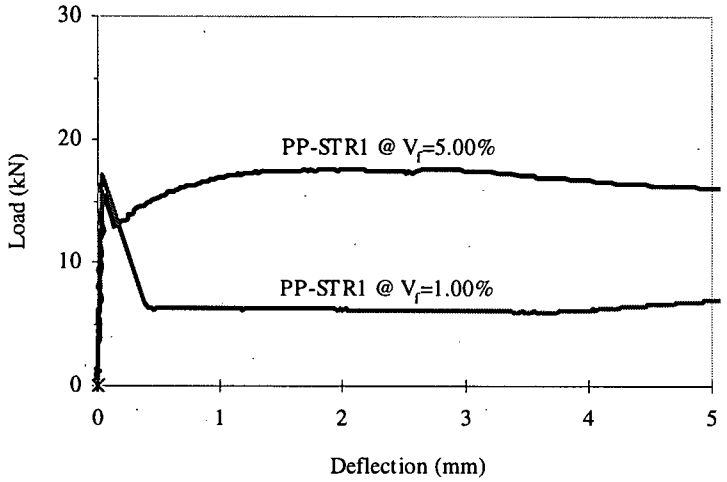

Figure 3.1.4b: Comparison of flexural load versus deflection response for fiber reinforced concrete mixes – Influence of fiber volume, V_f = 1.0% and 5.0% of straight, smooth polypropylene fibers (PP-STR1)

In the specimens reinforced with steel and polypropylene fibers it was also observed that the majority of crack bridging fibers pulled out during crack opening. On the other hand, for specimen reinforced with polyvinyl alcohol fibers, the majority of crack bridging fibers fractured during pullout, which led to relatively steeper drop in post-crack load. High interfacial adhesional bond strength and low transverse shear strength of polyvinyl alcohol fibers could be the possible reasons responsible for fracture of fibers.

Table 3.1.6: JSCE Absolute Toughness and Flexural Toughness Factor – Influence of fiber volume

Fiber Id.	Fiber Description	Fiber Volume (%)	MOR (MPa)	Absolute Toughness, T_{JCI} (N-m)	Flexural Toughness Factor, σ_b (MPa)
STL-STR	Straight-smooth, stainless steel	0.76	5.51 (0.51)	14.9 (1.28)	2.25 (0.19)
		5.0	8.59 (0.73)[@]	42.8 (2.87)	6.43 (0.43)
PP-STR1	Straight, smooth polypropylene	1.0	5.14 (0.55)	7.41 (0.63)	1.11 (0.09)
		5.0	5.19 (0.65)	32.8 (3.25)	4.91 (0.10)
PVA-1	Straight polyvinyl alcohol	1.0	6.21 (0.60)	21.5 (1.29)	3.23 (0.19)
		5.0	6.81 (0.86)	39.0 (1.74)	5.85 (0.26)

[@] - Figures in brackets indicate standard deviations

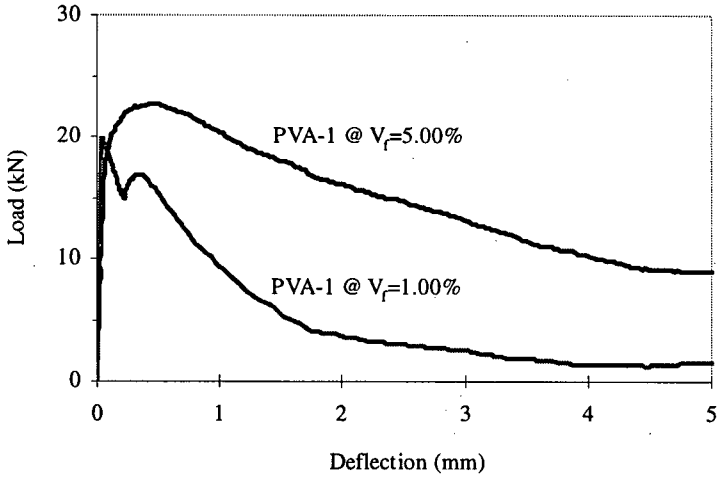

Figure 3.1.4c: Comparison of flexural load versus deflection response for fiber reinforced concrete mixes – Influence of fiber volume, V_f = 1.0% and 5.0% of straight polyvinyl alcohol fibers (PVA-1)

3.1.3 Fiber Aspect Ratio

Fiber aspect ratio is defined as the ratio of fiber length to fiber diameter. The influence of fiber aspect ratio was investigated by comparing the flexural toughness response of concretes reinforced with the following polypropylene fibers, namely:

i. straight, smooth polypropylene fiber, PP-STR1 (L=38 mm, d=0.63 mm, L/d=60)

ii. straight, smooth polypropylene fiber, PP-STR2 (L=38 mm, d=0.19 mm, L/d=200)

Both fibers were virgin polypropylene with an elastic modulus of approximately 3.5 GPa. Five beams were tested for each mix. The average flexural responses for FRC reinforced with these fibers are shown in Figure 3.1.5, and the corresponding JSCE flexural toughness parameters are reported in Table 3.1.7. Two features are apparent in the load versus deflection plots:

- A higher fiber aspect ratio led to an increase in total energy absorption.
- Instability was more pronounced in the case of fibers with lower aspect ratio.

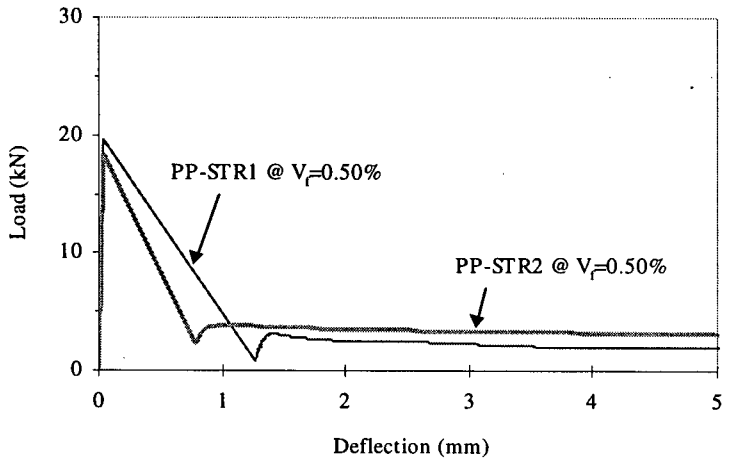

Figure 3.1.5: Comparison of flexural load versus deflection response for fiber reinforced concrete mixes – Influence of fiber aspect ratio, V_f = 0.50% of straight, smooth polypropylene fibers (PP-STR1 and PP-STR2)

Table 3.1.7: JSCE Absolute Toughness and Flexural Toughness Factor – Influence of fiber aspect ratio

Fiber Id.	Fiber Description	Aspect ratio l/d	Fiber Volume (%)	MOR (MPa)	Absolute Toughness, T_{JCI} (N-m)	Flexural Toughness Factor, σ_b (MPa)
PP-STR1	Straight, smooth polypropylene	68	0.50	5.86 (0.83)[@]	3.5 (0.34)	0.52 (0.05)
PP-STR2	Straight, smooth polypropylene	200	0.50	5.49 (0.35)	6.88 (0.61)	1.03 (0.09)

[@] - Figures in brackets indicate standard deviations

3.1.4 Surface Characteristics of Fiber

Influence of surface characteristics of fiber on toughness of FRC was investigated by testing concretes reinforced with the following fibers:

i. straight-smooth, stainless steel fiber, STL-STR; $V_f = 0.76\%$

ii. grease coated, straight-smooth, stainless steel fiber, STL-STR; $V_f = 0.76\%$

iii. straight polyvinyl alcohol fiber, PVA-1; $V_f = 1.0\%$

iv. grease coated, straight polyvinyl alcohol fiber, PVA-1; $V_f = 1.0\%$

Five beams were tested for the each mix mentioned above. Figure 3.1.6a compares the average flexural response for virgin and grease coated steel fibers (STL-STR). The corresponding JSCE toughness parameters are reported in the Table 3.1.8. In the figure, it can be noticed that the prepeak response remained practically unaltered as a result of grease coating of steel fibers. On the other hand, considerable variation in the postpeak flexural response was seen as a result of the grease coating - the postpeak flexural performance of concrete with grease coated steel fibers was inferior in comparison to that of concrete with virgin steel fibers. This variation in performance is possibly related to the reduction in fiber-matrix interfacial coefficient of friction (and hence, reduction in interfacial frictional bond) brought about by the coating of grease.

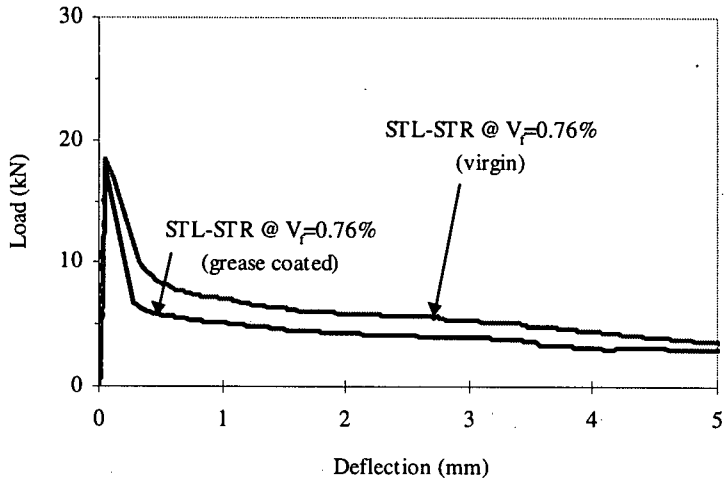

Figure 3.1.6a: Comparison of flexural load versus deflection response for fiber reinforced concrete mixes – Influence of fiber surface characteristics, Steel fiber – STL-STR @ $V_f = 0.76\%$

Table 3.1.8: JSCE Absolute Toughness and Flexural Toughness Factor – Influence of fiber surface characteristics

Fiber Id.	Fiber Description	Fiber Volume (%)	MOR (MPa)	Absolute Toughness, T_{JCI} (N-m)	Flexural Toughness Factor, σ_b (MPa)
STL-STR	Straight, smooth steel	0.76	5.51 (0.51)[@]	14.9 (1.28)	2.25 (0.19)
STL-STR	Grease coated, straight steel	0.76	5.31 (0.43)	10.72 (0.23)	1.61 (0.03)
PVA-1	Straight, smooth PVA	1.00	6.21 (0.60)	21.5 (1.29)	3.23 (0.19)
PVA-1	Greased coated, straight PVA	1.00	5.76 (0.66)	30.31 (1.32)	4.55 (0.20)

[@] - Figures in brackets indicate standard deviations

Figure 3.1.6b compares the average flexural response for virgin and grease coated polyvinyl alcohol fibers (PVA-1), and the corresponding JSCE toughness parameters are reported in Table 3.1.8. In the figure it can be noted that the total energy absorption was superior in the case of grease coated polyvinyl alcohol fibers. Visually, it was noticed that in the concrete reinforced with virgin polyvinyl alcohol fibers, most fibers had fractured during crack opening. On the other hand, in the concrete reinforced with grease coated polyvinyl alcohol fibers, a greater number of fibers had pulled out during crack opening. It appears that a high adhesional bond between fiber and matrix leads to fracture of virgin fibers, and as a result, energy absorption remains low. The coating of grease possibly reduces the adhesional bond between fiber and matrix. Consequently, a greater number of fibers are able to pull out, and in this process they absorb a greater amount of energy relative to the energy absorbed by the concrete specimen reinforced with virgin fibers.

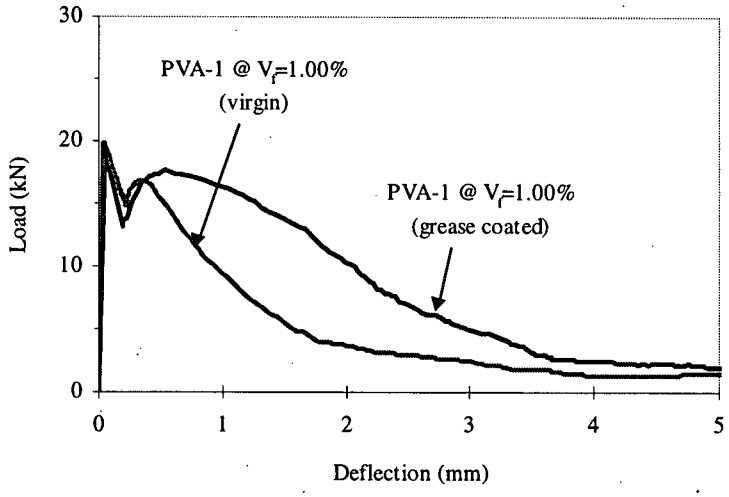

Figure 3.1.6b: Comparison of flexural load versus deflection response for fiber reinforced concrete mixes – Influence of fiber surface characteristics, Polyvinyl alcohol fiber – PVA-1 @ V_f = 1.00%

From the above experimental investigation it can be concluded that the flexural toughness response of fiber reinforced concretes is strongly dependent upon the characteristics of the fiber surface. Dependence of micromechanical properties of interface on characteristics of the fiber surface will be a subject of investigation in Chapters 4-7.

3.1.5 Fiber Geometry

Influence of fiber geometry was investigated by comparing the flexural toughness response of concretes reinforced with three different steel fiber types, namely,

i. Straight-smooth, stainless steel fiber, STL-STL, $V_f = 0.76\%$

ii. hooked-end steel fiber, STL-HKD, $V_f = 0.76\%$

iii. crimped steel fiber, STL-CR1, $V_f = 0.76\%$

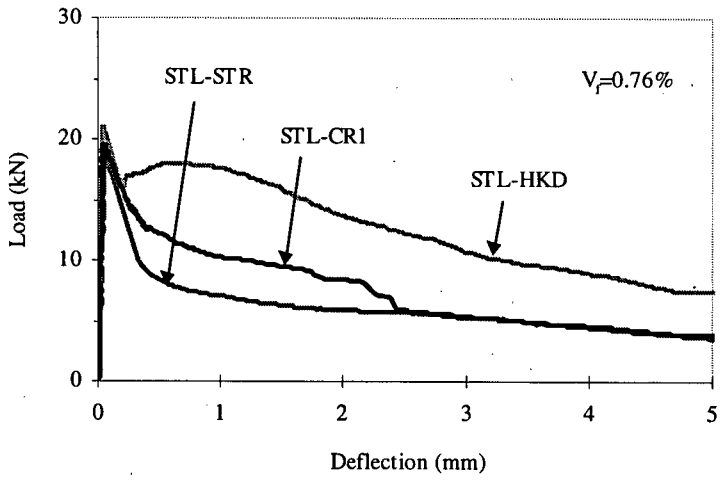

Figure 3.1.7: Comparison of flexural load versus deflection response for fiber reinforced concrete mixes – Influence of fiber geometry

Fiber beam specimens were tested for the each case mentioned above. Flexural load versus deflection responses for fiber reinforced concretes reinforced these fibers are shown in Figure 3.1.7, and the corresponding JSCE flexural toughness parameters are reported in Table 3.1.9. Comparing the performance of the three fibers, it is clear that for stiff fibers like steel, the geometry of the fiber has a considerable influence on flexural toughness response. Concrete specimens reinforced with deformed steel fibers absorbed more energy in comparison to those reinforced with straight-smooth steel fibers. Also, different fiber geometrical configuration gave different degrees of energy absorption. It appears that the main energy absorption mechanism is derived from the cold working of steel that takes place when deformed portions of fibers are

pulled out. For the crimped fiber, it was noticed that considerable matrix damage took place during the process of fiber pullout, and this had an unfavorable influence on the overall energy absorption.

Table 3.1.9: JSCE Absolute Toughness and Flexural Toughness Factor – Influence of fiber geometry

Fiber Id.	Fiber Description	Fiber Volume (%)	MOR (MPa)	Absolute Toughness, T_{JCI} (N-m)	Flexural Toughness Factor, σ_b (MPa)
STL-STR	Straight, smooth steel	0.76	5.51 (0.51)[@]	14.9 (1.28)	2.25 (0.19)
STL-HKD	Hooked-end steel	0.76	6.21 (0.56)	34.1 (1.98)	5.11 (0.30)
STL-CR1	Crimped steel	0.76	5.87 (0.64)	22.7 (1.74)	3.41 (0.26)

[@] - Figures in brackets indicate standard deviations

3.1.6 Shrinkage Properties of Matrix

Shrinkage of cementitious matrix largely depends upon the setting, hardening and curing history of concrete and upon the properties of the matrix. For a given history of setting, hardening and curing, it can be expected that a cementitious matrix containing shrinkage compensating admixtures will experience reduced shrinkage. A type of cementitious matrix that falls under this category is available commercially under the name 'non-shrink grout'. Below, comparison is made for the flexural toughness performance for fiber reinforced concretes with two different kinds of matrix, namely:

i. CSA Type 10 normal Portland cement matrix, and

ii. Non-shrink grout matrix

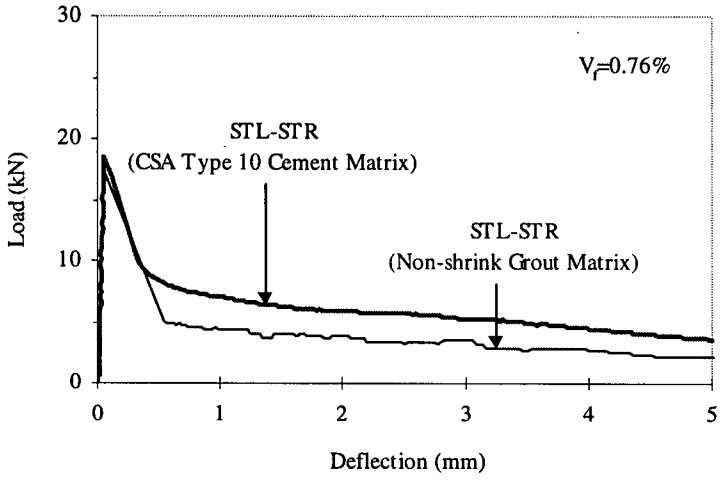

Figure 3.1.8: Comparison of flexural load versus deflection response for fiber reinforced concrete mixes – Influence of shrinkage properties of matrix

Flexural toughness performance of composites reinforced with straight-smooth, stainless steel fibers at V_f=0.76% was investigated. Five beams were tested for each combination of matrix and fiber. Figure 3.1.8 compares the average flexural responses of fiber reinforced concretes for the two types of matrices investigated. The corresponding results are tabulated in the Table 3.1.10. It can be seen that the fiber reinforced concrete specimens with normal Portland cement (CSA Type 10) matrix absorbed more energy in comparison to the non-shrink grout matrix. This behavior is possibly related to the to the higher fiber pullout resistance offered by the normal Portland cement matrix. This aspect is explored from the micromechanical perspective in Chapters 4.

Table 3.1.10: JSCE Absolute Toughness and Flexural Toughness Factor – Influence of matrix shrinkage

Fiber Id.	Fiber Description	Matrix	Fiber Volume (%)	MOR (MPa)	Absolute Toughness, T_{JCI} (N-m)	Flexural Toughness Factor, σ_b (MPa)
STL-STR	Straight, smooth steel	CSA Type 10 Normal Portland Cement	0.76	5.51 (0.51)[@]	14.9 (1.28)	2.25 (0.19)
		Non-shrink Grout	0.76	5.22 (0.60)	9.1 (0.76)	1.36 (0.11)

[@] - Figures in brackets indicate standard deviations

3.2 Characterization of Flexural Toughness of Fiber Reinforced Concretes

Toughness is the most important property of any fiber reinforced concrete. One variable that significantly influences the measured toughness of FRC is the stiffness of testing machine/loading system on which the test is performed. When a loading system applies a load on a test specimen, there is a reactive force on the loading system itself, and due to this reactive force, the loading system deforms and stores energy. The extent of energy built up in the loading system depends upon its stiffness - the softer the testing system, the greater the energy built up in it. At the instant when the beam cracks, a part of the stored energy is suddenly released into the specimen. The specimen absorbs this incoming energy, and as a consequence, the amount of energy absorbed by the specimen from the external load is reduced. If an FRC specimen is inadequately reinforced, the sudden release of energy causes unstable propagation of cracks, thus influencing the post-cracking flexural response.

Unfortunately, the currently available methods of quantifying toughness using a flexural specimen are riddled with ambiguities and considered unacceptable. ASTM C1018 test procedure [4] to characterize flexural toughness of concrete suffers from the above-mentioned problem. Thus, the test procedure is particularly worrisome when concrete reinforced with a low volume fraction of synthetic or other fiber is tested using an open-loop test machine with low stiffness under load control. Under such circumstances, the brittle nature of concrete manifests itself in the post-peak region of the load-displacement curve and two specific features become apparent (Figure 3.2.1):

- Immediately following the peak load, the load drops suddenly in an uncontrolled and unstable manner depending upon the stiffness of the machine. The data-logger even when running at a very high frequency does not usually record any points in this region.
- After the unstable part, the curve attains a stable softening level, during which loads are again functions of the test machine characteristics. If the machine stiffness is too low, the release of energy during the unstable part will be high and the specimen may suffer a greater damage due to the higher incoming energy. If so, the loads during softening will be lower and the post peak load carrying response will be inferior as compared to close-loop testing (high stiffness) where this sudden release of energy and related damage are not allowed to occur (Figure 3.2.1).

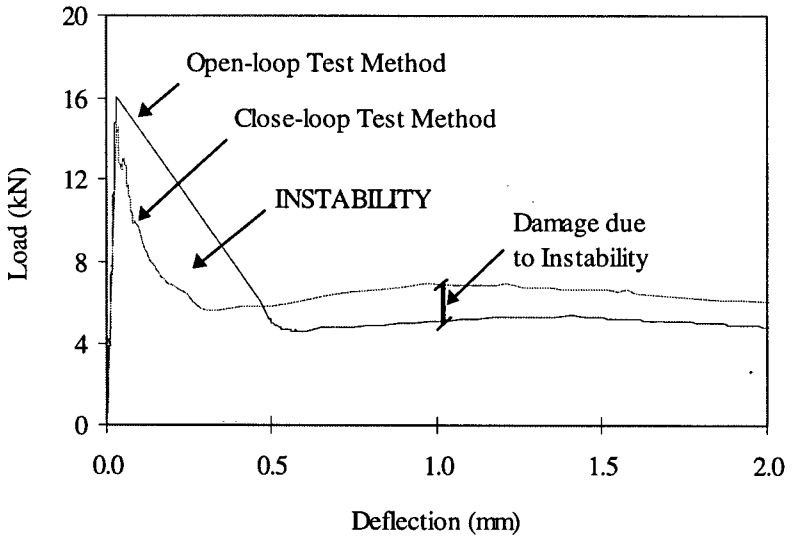

Figure 3.2.1: Comparison of Close-loop Test Method with Open-Loop Test Method for Flexural Tests on Fiber Reinforced Concrete. Notice the large load instability that occurs during at the peak load during an open-loop test, and the related damage [6]

For most fiber reinforced concretes, rather than the pre-peak response, which is not expected to be very different from plain concrete, it is the post-peak response that is of a primary interest. With the above mentioned artifacts in the post-peak load displacement part of the curve, any analysis carried out using the standardized ASTM C1018 technique (or any other technique for that matter) is going to be of limited use and even misleading. One possible solution, naturally, would be to always use a close-loop machine, especially when pronounced instability in the post-peak part of the curve is expected. Unfortunately, close-loop tests are difficult to run and time consuming. These tests are also expensive and necessitate sophisticated and complex instrumentation and data acquisition devices. Since most testing laboratories are equipped only with open-loop test machines, any new methodology developed should be designed such machines and still provide a valid post-peak response.

A new test method, called the Residual Strength Test Method [6,7], has recently been developed which characterizes the softening part of the curve by first loading the specimen in conjunction with a steel plate. Steel plate absorbs the energy released by the machine at the occurrence of matrix cracking, and in this manner, damage to the specimen resulting from the sudden release of energy is minimized. After first cracking, the specimen is unloaded, the steel plate is removed, and the specimen is reloaded. The post-peak response thus obtained on reloading is expected to give the true stress transfer capability (and the toughening capability) of fibers across a crack.

Until this date, no systematic and exhaustive study has been carried out to assess the validity of the Residual Strength Test Method. This aspect has been explored in the following investigation. The major objectives of this investigation are:

- To assess the validity of the Residual Strength Test Method. This is achieved by examining the data obtained from the proposed test method and comparing it with the results obtained from an open-loop test machine with low stiffness and a close-loop test with high stiffness.
- To assess the capability of the Residual Strength Test Method to identify the influence of various fiber characteristics such as type, length, configuration, volume fraction, geometry, and the elastic modulus.

3.2.1 Residual Strength Test Method (RSTM) – Assessment and Calibration

In the Residual Strength Test Method, fiber-reinforced beams are pre-cracked under third-point flexural loading in parallel with a 12 mm thick steel plate as shown in Figure 3.2.2a and b. The steel plate provides the support and absorbs the energy that is released from the machine at the occurrence of the peak load when compliance of specimen changes suddenly. At a net deflection between 0.25 mm and 0.50 mm, the cracked beam is unloaded, residual beam deflection on complete unloading is recorded (relaxation of beam during unloading is monitored by LVDT's), and this is followed by the removal of the steel plate. The cracked beam is then reloaded without the steel plate in four-point bending to obtain the residual load-deflection curve. The loads supported by this beam at 0.5, 0.75, 1.0 and 1.25 mm of beam deflection are then averaged and normalized to obtain Residual Strength, *RS* values by using an elastic analysis. In other words,

$$RS = \frac{L}{bd^2}\left[\frac{P_{0.5} + P_{0.75} + P_{1.0} + P_{1.25}}{4}\right] \qquad 3.2$$

where $P_{0.5}$, $P_{0.75}$, $P_{1.0}$, $P_{1.25}$ correspond to the load values at 0.5, 0.75, 1.0 and 1.25 mm beam deflection, respectively, L is the test span, b is width of the beam and d is the depth of the beam. Notice that the Residual Strength, *RS*, which has the units of stress, is not the true stress in the specimen (which has already cracked and the application of the elastic equation is strictly not valid), but a measure of an approximate "engineering" stress.

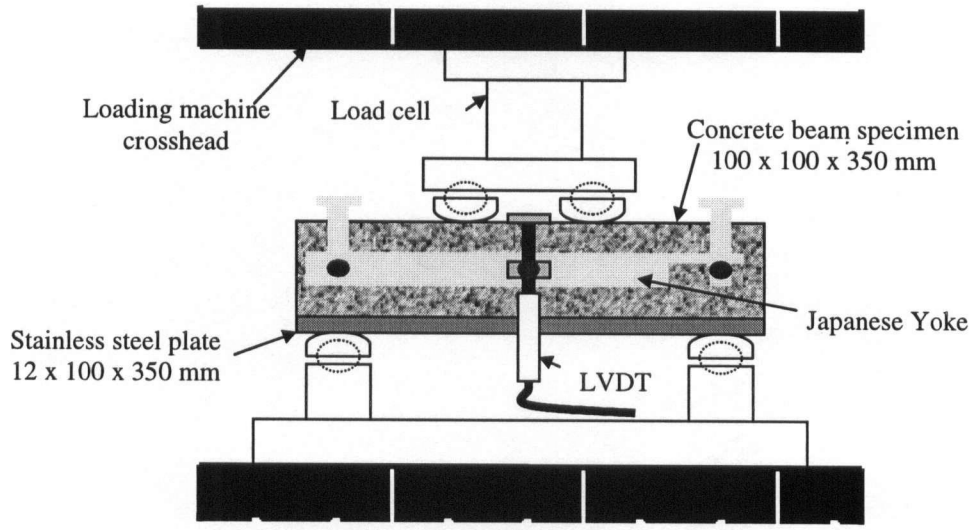

Figure 3.2.2a: Schematic of Residual Strength Test Method experimental setup

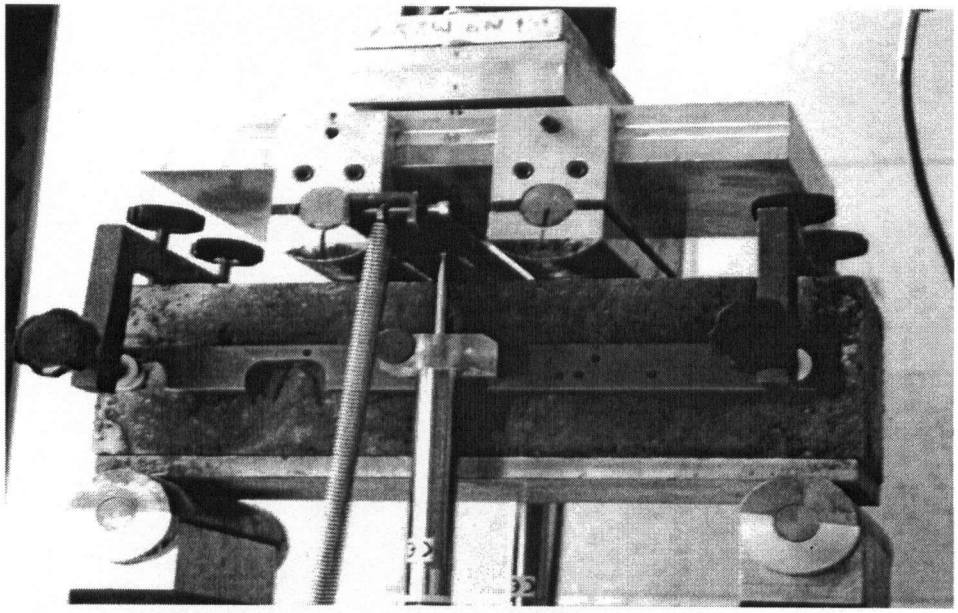

Figure 3.2.2b: Test on a Fiber Reinforced Concrete Beam using the Residual Strength Test Method. Note the steel plate under the beam.

Further, the Residual Strength Index, *RSI* can be calculated as:

$$RSI(\%) = \frac{RS}{MOR} \text{ x } 100 \qquad 3.3$$

where *RS* is the Residual Strength as defined in Equation 3.2, and *MOR* is the modulus of rupture of the material calculated by testing beams (without the steel plate) in accordance with the

ASTM Test Method C 78 [218]. This test procedure, an assessment of which was the principal objective of this investigation, is abbreviated as RSTM.

3.2.1.1 Experimental Procedure

Materials and Mixes

To assess Residual Strength Test Method, three types of polymeric fibers were investigated:

i. Fiber PP1: Fiber PP1 was 100% polypropylene with a special blend of fibers with lengths in the range of 11-20 mm. This fiber was fibrillated.

ii. Fiber PP2: Fiber PP2 was also 100% polypropylene with a length of 19 mm. This was a monofilament fiber.

iii. Fiber NL1: Fiber NL1 was 100% nylon with a length of 19 mm. Like the fiber PP2, this was a monofilament fiber without fibrillation.

Table 3.2.1: Mix Proportions

Cement (kg)	Silica-fume (kg)	Water (kg)	Sand (kg)	Aggregate (10 mm) (kg)	Superplasticizer (ml/100 kg of Cement)
460	51	179	767	893	600

The mix proportions of the concrete matrix are given in Table 3.2.1. The design compressive strength was approximately 70 MPa. A particularly high design compressive strength was chosen to exaggerate the problem of instability. Cement, aggregate and part of the silica fume were first dry mixed in a pan type mixer. The rest of the silica-fume and the superplasticizer were added to water to form a slurry. This slurry was then added to the dry-mix to obtain a workable wet-mix. Lastly, fibers were added gradually to avoid any fiber balling. Fiber addition rates were 0.1, 0.3 and 0.5 percent by volume of the PP1 and PP2 fibers and 0.5 percent by volume of the NL1 fibers.

Six compression cylinders of size 100 mm × 200 mm and 15 beams of size 100 mm × 100 mm × 350 mm were cast for each mix. External vibration was used for consolidating the concrete into the moulds. Specimens were demolded 24 hours after casting and then cured in a tank with lime saturated water for 28 days before testing.

Typical values of the slump, air content and unit weight for the control and 0.5% fiber volume concretes are presented in Table 3.2.2. Notice that there was some drop in the slump values due to fiber reinforcement, but generally the mixes were well workable and in the practical range.

Table 3.2.2: Fresh Properties of Concrete Mixes

Mix	Slump (mm)	Air Content (%)	Unit Weight (kg/m^3)	Compressive Strength (MPa)	
				7 days	28 days
Control Plain	140	1.6	2405	54.5	71.4
FRC - PP1 Fiber*	120	1.5	2402	52.9	71.5
FRC - PP2 Fiber*	110	2.0	2382	54.5	71.8
FRC - NL1 Fiber*	80	1.4	2413	55.2	72.8

*Fiber volume fraction of 0.5%

Test Procedure

Close-loop testing was conducted in a 150 kN MTS machine with a function generator. Figure 3.2.3a shows the experimental test setup and Figure 3.2.3b shows the schematic of the controls.

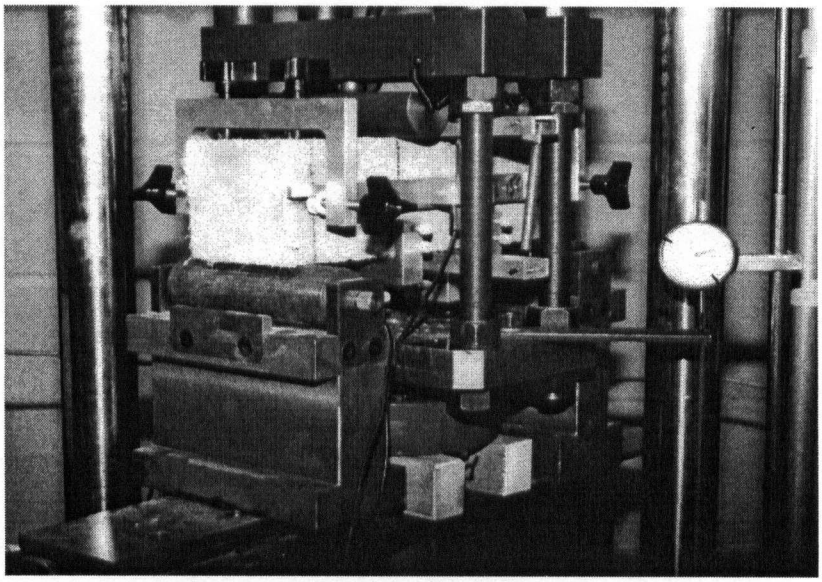

Figure 3.2.3a: Test on a Fiber Reinforced Concrete Beam using the Close-Loop Test Method.

As seen in the Figure 3.2.3a, a crack mouth opening displacement (CMOD) transducer monitored the crack opening displacement and supplied the feed-back signal to the servo-controller. A *Japanese Yoke* [5] was mounted around the specimen to record the net deflections so that the extraneous deflections resulting due to the settlement of supports, crushing at the load points, and the loading fixture deformations were eliminated and only the net deflections were

recorded. Two LVDT were used to record the net deflection of the beam at mid-span and data from these were then averaged. At the start of the program, specimens were tested under control signals first from the CMOD transducer and then from the two LVDTs determine whether the source of feedback signal made any difference to the load-displacement curves. No particular difference was noticeable. The rest of the close-loop tests were then performed under CMOD control, as illustrated in Figure 3.2.3b. In a typical test, the CMOD, the applied load, and the vertical net displacement values were recorded using a digital data acquisition system based on a personal computer. The close-loop Test Method is abbreviated as CLTM.

Note that the Open-loop Test Method (OLTM) has already been described in Section 3.1.

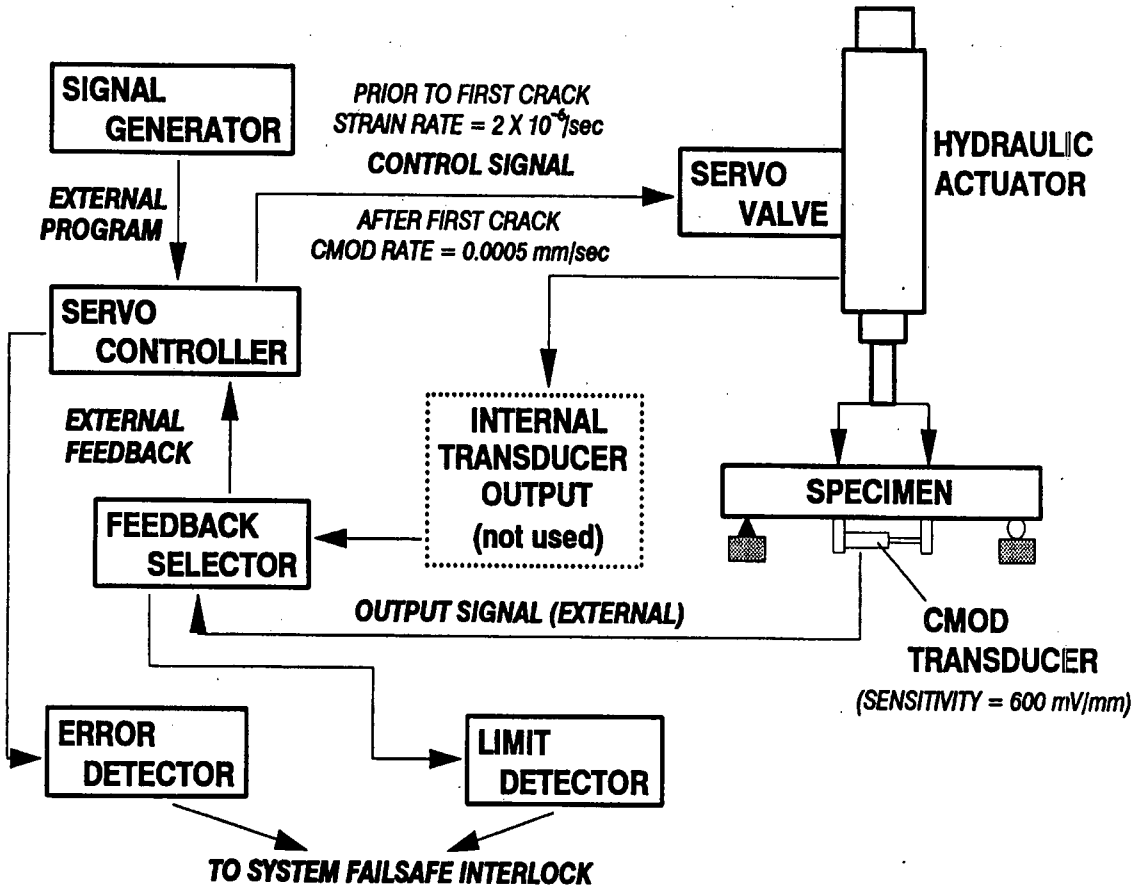

Figure 3.2.3b: Schematic of controls in a flexural Close-loop Test Method

3.2.1.2 Results

The differences between the curves from the close-loop and the open-loop tests were discussed previously and are illustrated in Figure 3.2.1. Typical close-loop and open-loop curves for concrete with PP1 fiber are compared in Figures 3.2.4 and 3.2.5 for 0.1 and 0.3% fiber volume fractions, respectively. The same for FRC with PP2 fibers are compared in Figure 3.2.6 and 3.2.7. In general, for both fiber volume fractions, a large instability region was noticeable immediately after the peak load when the displacement jumped from ~0.04 mm at the peak load, to ~1.0 mm (25 fold) at the end of the instability. This sudden release of energy from the machine in all likelihood created some damage in the specimen, with cracks undergoing a large uncontrolled opening, and the load carrying capacity beyond the instability was affected.

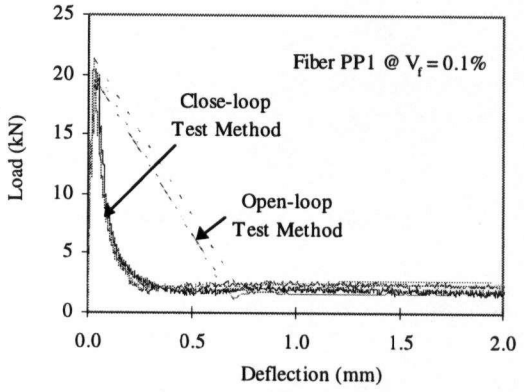

Figure 3.2.4: Comparison of Close-loop and Open-loop curves for concrete with 0.1% of Fibrillated Polypropylene Fiber (PP1)

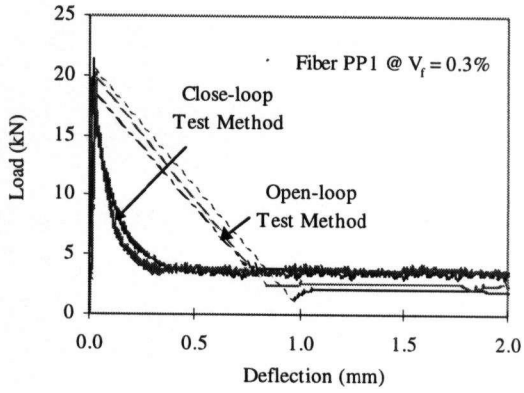

Figure 3.2.5: Comparison of Close-Loop and Open-loop curves for concrete with 0.3% of Fibrillated Polypropylene Fiber (PP1)

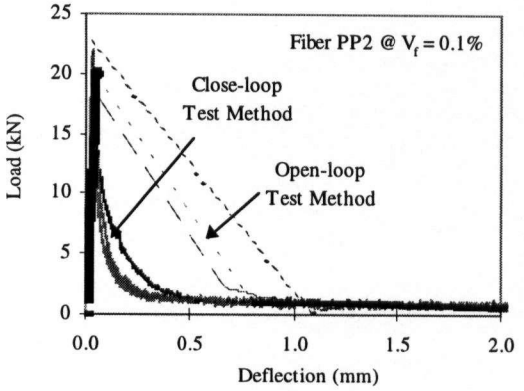

Figure 3.2.6: Comparison of Close-loop and Open-loop curves for concrete with 0.1% of Monofilament Polypropylene Fiber (PP2)

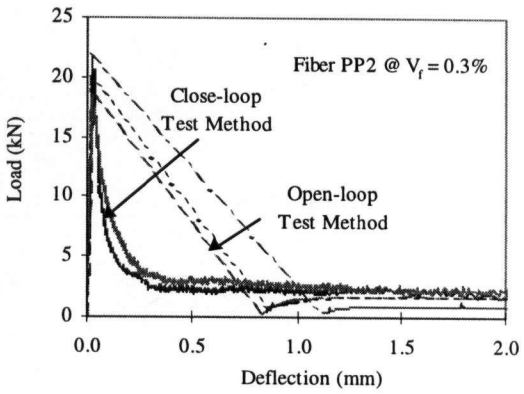

Figure 3.2.7: Comparison of Close-Loop and Open-loop curves for concrete with 0.3% of Monofilament Polypropylene Fiber (PP2)

In Figures 3.2.8-10, the close-loop load-deflection plots for concrete with PP1 fiber are compared with those from the Residual Strength Test Method (RSTM) for fiber volume fractions of 0.1, 0.3 and 0.5%, respectively. The same for FRC with PP2 fibers are compared in Figures 3.2.11-13. The corresponding curves for FRC with NL1 fibers at a fiber volume fraction of 0.5% are compared in Figure 3.2.14. Notice that the curves from the CLTM and RSTM match quite well in the post-peak region. The RSTM curves start at a certain finite displacement, which is the same as the residual displacement in the specimen after the first loading with the steel plate. Notice also that the RSTM curves start at varying initial displacements, indicating that varying levels of damage were induced in these beams during the first loading with the steel plate. These minor variations in the induced damage during the first loading, however, do not appear to alter or influence the load carrying capacity during the second loading.

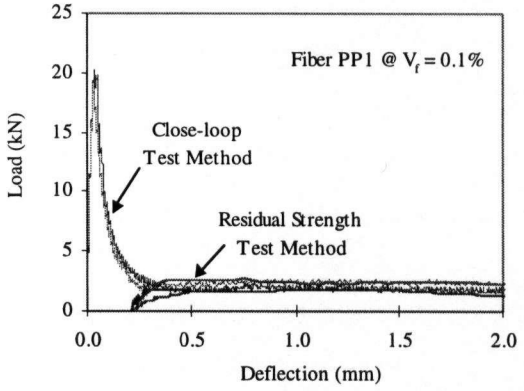

Figure 3.2.8: Comparison of Close-Loop and Residual Strength Test Method Curves for Concrete with 0.1% of Fibrillated Polypropylene Fiber (PP1)

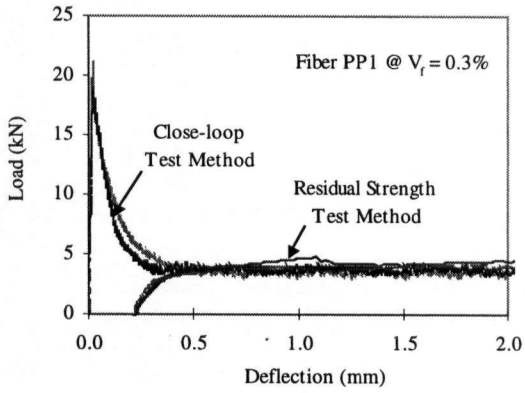

Figure 3.2.9: Comparison of Close-Loop and Residual Strength Test Method Curves for Concrete with 0.3% of Fibrillated Polypropylene Fiber (PP1)

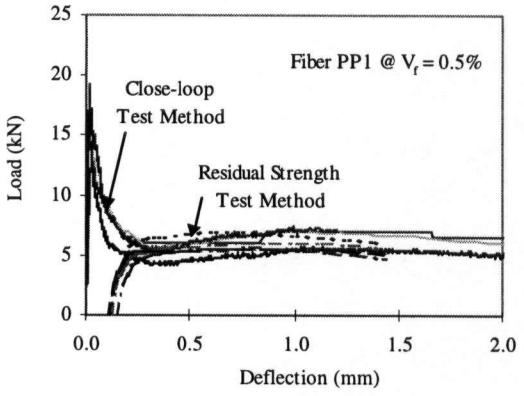

Figure 3.2.10: Comparison of Close-Loop and Residual Strength Test Method Curves for Concrete with 0.5% of Fibrillated Polypropylene Fiber (PP1)

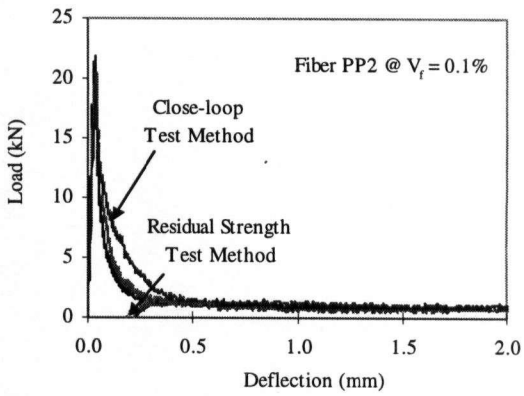

Figure 3.2.11: Comparison of Close-Loop and Residual Strength Test Method Curves for Concrete with 0.1% of Monofilament Polypropylene Fiber (PP2)

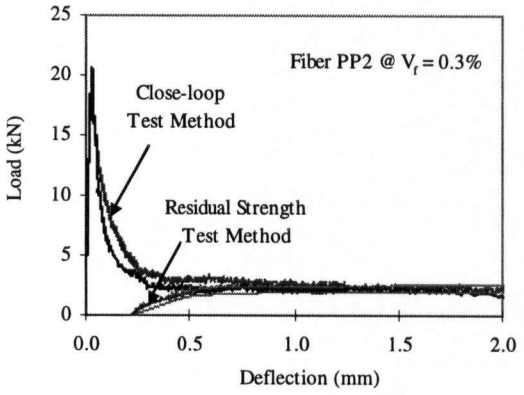

Figure 3.2.12: Comparison of Close-Loop and Residual Strength Test Method Curves for Concrete with 0.3% of Monofilament Polypropylene Fiber (PP2)

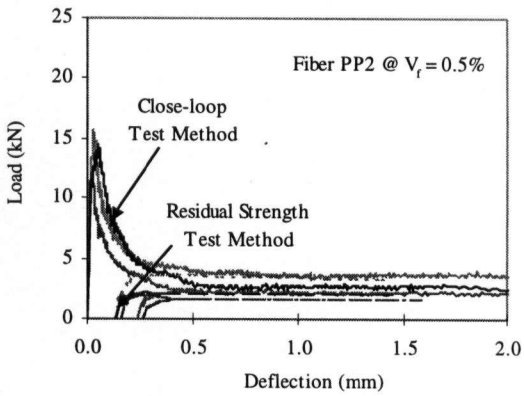

Figure 3.2.13: Comparison of Close-Loop and Residual Strength Test Method Curves for Concrete with 0.5% of Monofilament Polypropylene Fiber (PP2)

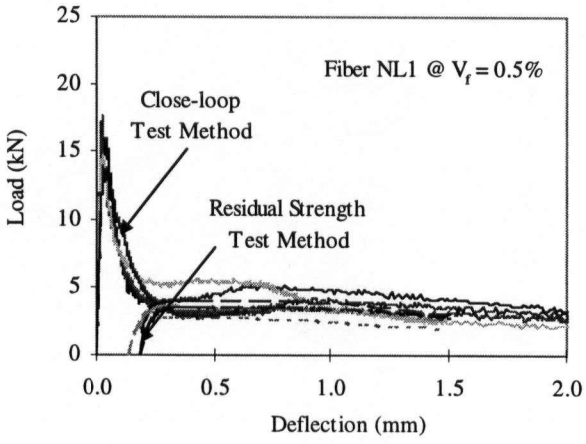

Figure 3.2.14: Comparison of Close-Loop and Residual Strength Test Method Curves for Concrete with 0.5% of Monofilament Nylon Fiber (NL1)

In Table 3.2.3, the Residual Strength (RS) values (Equation 3.2), for the various fibers, are reported. Generally speaking, the RS values obtained using the Open-Loop Test Method were the lowest and those obtained using the close-loop method were the highest. The values from the proposed RSTM were in-between these two extremes, but were closer to values from the close-loop method. This is to be expected, given that substantial damage is induced in the specimen during the open-loop testing. In the RSTM, on the other hand, the presence of the steel plate substantially reduces the damage and the technique more or less imitates close-loop testing. The good agreement between the CLTM and the RSTM data indicates that the proposed method is capable of accurately measuring the capacity of fiber reinforced concrete to carry loads beyond cracking.

Table 3.2.3: Residual Strengths, *RS* for various mixes

Mix/Fiber	V_f (%)	Residual Strength, *RS* (MPa)		
		Open-Loop Test Method (RS_{OLTM})[@]	Close-Loop Test Method (RS_{CLTM})	Residual Strength Test Method (RS_{RSTM})
FRC- PP1 Fiber Fibrillated Polypropylene	0.1	0.61 (0.11)*	0.67 (0.08)	0.63 (0.12)
	0.3	0.78 (0.35)	1.27 (0.02)	1.19 (0.13)
	0.5	--	1.88 (0.21)	1.75 (0.17)
FRC-PP2 Fiber Monofilament Polypropylene	0.1	0.33 (0.06)	0.32 (0.04)	0.31 (0.02)
	0.3	0.4 (0.12)	0.74 (0.09)	0.66 (0.08)
	0.5	--	0.87 (0.24)	0.69 (0.22)
FRC-NL1 Fiber Monofilament Nylon	0.1	--	--	--
	0.3	--	--	--
	0.5	--	1.16 (0.19)	1.02 (0.15)

* Figures in brackets indicate standard deviation;

[@] For the Open-loop Test Method where $P_{0.5}$ and $P_{0.75}$ were in the unstable region, the Residual Strength (*RS*) was calculated by ignoring the load values (in Equation 3.2) falling under the unstable region.

The CLTM results for the various fiber types are further compared with the RSTM results in Figure 3.2.15. Note again a very good match between these techniques at all fiber volume fractions. Notice also that at a certain fiber volume fraction, the CLTM predicts the PP1 fiber to be more effective than the PP2 fiber, and an identical conclusion can be drawn from the RSTM data. Further, the nylon fiber (NL1) is less effective than the PP1 fiber but more effective than the PP2 fiber as per the close-loop data, and an identical conclusion can be drawn from the Residual Strength Test Method. These data indicate very clearly that the RSTM is entirely

capable of distinguishing between not only the various fiber volume fractions of the same fiber type but also between the various fiber types at a given volume fraction.

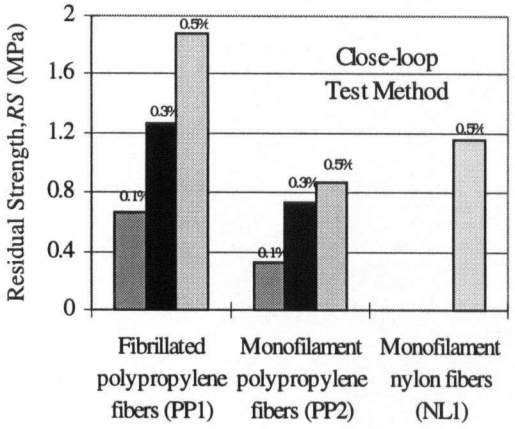

Figure 3.2.15a: Residual Strength for Various Mixes using the Close-Loop Test Method

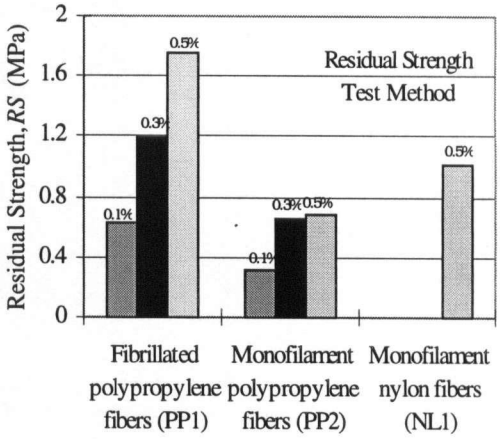

Figure 3.2.15b: Residual Strength for Various Mixes using the Residual Strength Test Method

One way to assess the effectiveness of the RSTM as compared to the CLTM, is to calculate the difference, δ, as:

$$\delta = \left[\frac{RS_{CLTM} - RS_{RSTM}}{RS_{CLTM}} \right] \times 100 \qquad 3.4$$

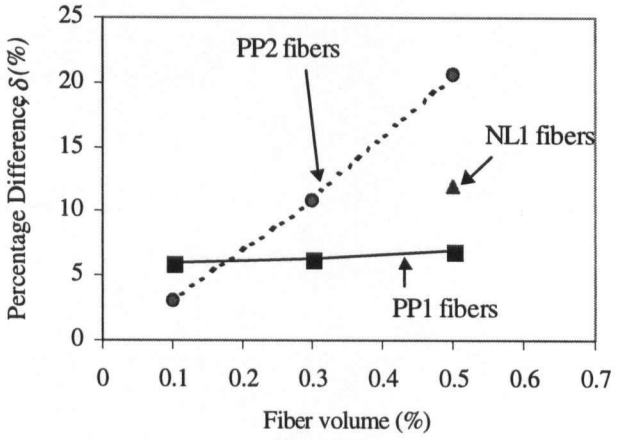

Figure 3.2.16: Percentage Difference (δ) in RS Values between the Close-Loop Test Method and the Residual Strength Test Method

These values of the difference, δ, are plotted in Figure 3.2.16 for the various fiber types. Notice that δ is always positive (i.e., the RSTM always underestimates the capacity) and is in the range of 5-25 percent depending on the fiber type. It also appears that the difference δ is directly related to fiber efficiency; a fiber with lower efficiency indicates a higher δ. This is logical since

a less effective fiber with a poorer pull-out resistance may lead to more damage during the first loading cycle and thus sustain lower loads in the second loading cycle.

3.2.1.3 A Round-Robin Test Program to Validate RSTM

To assess the validity and inter-laboratory reproducibility of the proposed Residual Strength Test Method, a round-robin test program was carried out between the University of British Columbia (UBC), The Ministry of Transportation of Ontario (MTO), and the Technical University of Nova Scotia (TUNS). This section describes the results obtained from this test program.

Twenty-five fiber reinforced concrete beams (100 mm x 10 mm x 350 mm) were cast at UBC with mix details given in Table 3.2.1. Only one fiber volume addition rate of 0.3% was investigated. Fifteen beams were retained at UBC, five beams were sent to MTO and the remaining five to TUNS. The division of tasks for the three laboratories is outlined in Table 3.2.4. All of the tests were performed at the specimen age of 14 days.

Table 3.2.4: Test planning

Institute	ASTM C1018 (Close-loop)	Residual Strength Test Method	ASTM C1018 (Open-loop)
UBC	√	√	√
MTO		√	
TUNS		√	

Results of the open-loop and close-loop tests performed on identical beams at UBC are given in Figure 3.2.17. Notice that although the two test configurations result essentially in identical peak loads, the post-peak load-displacement behaviors are markedly different for the reasons stated earlier. Figure 3.2.18 compares the load-displacement curves recorded in close-loop conditions with those recorded during the second stage loading of the proposed RSTM technique by the three institutes. Notice that for a proper comparison, the starting displacements for the RSTM curves are shifted by the amount of residual displacement in the specimen (considering relaxation) after the first loading with the steel plate. The residual displacement at the end of first loading ranged from 0.25 mm to 0.75 mm and was noticeably different for each of the three laboratories. One would expect that the residual displacement, apart being a function of machine stiffness, is also a function of operator experience. UBC, having had more experience with the test procedure, managed to halt the loading sufficiently rapidly after the creation of the crack in the specimen, and thus had lower residual displacements at the end of the first stage.

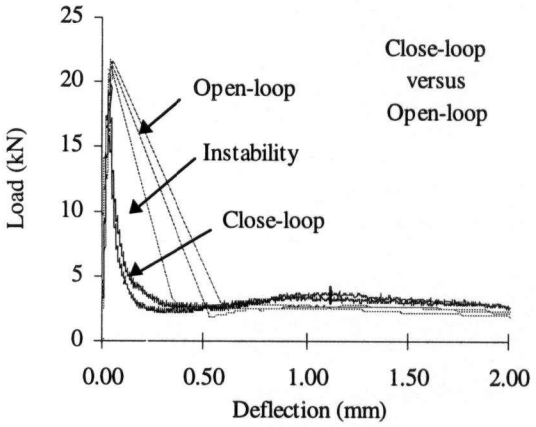

Figure 3.2.17: Comparison of Close-Loop and Open-Loop Curves for Concrete with 0.3% of Fibrillated Polypropylene Fiber (PP1)

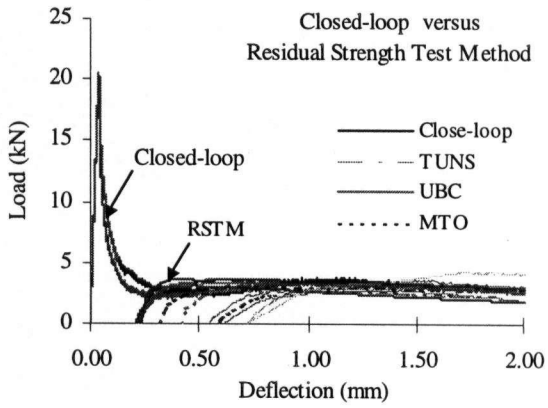

Figure 3.2.18: Comparison of Close-Loop and Residual Strength Test Method Curves for Concrete with 0.3% of Fibrillated Polypropylene Fiber (PP1)

In spite of the variation in the residual displacement from one laboratory to the other, interestingly, the residual load carrying capacity remained relatively unaffected as seen in Figure 3.2.18. As stipulated in the proposed technique, the load-displacement curves were analyzed for Residual Strength, *RS*, which are reported in Table 3.2.5. Notice that the Residual Strength reported by the three laboratories are comparable, and the within batch standard deviations (0.17, 0.08 and 0.18) are not very different from the inter-laboratory standard deviation (0.14). A variation in the residual displacement (and hence, in the extent of damage in the beam) at the onset of the Residual Strength test does not appear to affect the residual strength capacity in any way; the specimens tested at TUNS suffered most damage during the first stage of loading, but also recorded the highest Residual Strength.

Table 3.2.5: Residual Strengths, RS - Canadian Round-Robin Test Program [221]

Residual Strength, *RS* (MPa)				
Open-loop	Close-loop	Residual Strength Test Method		
UBC	UBC	UBC	MTO	TUNS
0.78	0.96	0.97 (0.17)*	0.81 (0.08)	1.03 (0 .18)
		Average=0.94 (0.14)		

* Figures in brackets indicate standard deviation

Thus, from the results obtained from the Canadian Round-Robin Test Program it was concluded that the Residual Strength Test Method is capable of characterizing the contribution of fibers in the post-matrix cracking stage with acceptably low within-batch and inter-laboratory variation.

3.2.1.4 Discussion

In the following, the stress state in the composite (FRC beam + steel plate) at the instant matrix cracking occurs is analyzed (i.e., at the instant beam is unloaded).

The response of a concrete beam to an applied load while supported by a plate is expected to be significantly different from that of the beam loaded without the plate. Assuming that the concrete beam and the steel plate act monolithically (i.e., there is no slip between the two and strain compatibility is maintained), one can show that for the composite beam, the depth of the neutral axis prior to cracking is:

$$\bar{y} = \frac{nbd_p\left(d + \frac{d_p}{2}\right) + bd\left(\frac{d}{2}\right)}{bd + nbd_p} \qquad 3.5$$

where, n = modulus ratio between concrete and steel (~6), d and b = depth and width of concrete beam, and d_p = depth of the steel plate.

The maximum tensile stress carried by the beam at the instant of cracking is given by [219]:

$$\sigma_c = \frac{M_c(d - \bar{y})}{\frac{bd^3}{12} + bd\left(\bar{y} - \frac{d}{2}\right)^2 + nb\frac{d_p^{\,3}}{12} + nbd_p\left(d + \frac{d_p}{2} - \bar{y}\right)^2} \qquad 3.6$$

and the corresponding stress in steel plate is given by [219]:

$$\sigma_s = \frac{nM_c(d + d_p - \bar{y})}{\frac{bd^3}{12} + bd\left(\bar{y} - \frac{d}{2}\right)^2 + nb\frac{d_p^{\,3}}{12} + nbd_p\left(d + \frac{d_p}{2} - \bar{y}\right)^2} \qquad 3.7$$

where, M_c is the moment at cracking. Assuming full compatibility between steel plate and concrete beam (i.e., both steel plate and concrete beam flex about a combined neutral axis) at the instant beam cracks, the maximum tensile stress in concrete, σ_c calculated using Equation 3.6 is given in Table 3.2.6 for the various mixes. Clearly, the maximum stress in concrete attained with the steel plate underneath remains significantly lower than the corresponding modulus of rupture value for the various mixes. This indicates that when the concrete beam is loaded in parallel with the steel plate, at failure it carries peak stresses far below its flexural capacity and

that its compliance is not significantly altered. Moreover, it can also be shown that stresses in concrete and the corresponding damage to the concrete beam will reduce further as the thickness of steel plate is increased.

Table 3.2.6: Maximum concrete stress at peak load with and without steel plate

Mix/Fiber	Modulus of Rupture[$] MOR (MPa)	Concrete beam + Steel Plate		
		Cracking Load[$] P_{cr} (kN)	Deflection at Cracking Load[$] δ_{cr} (mm)	Theoretical Concrete Stress[@] σ_c (MPa)
FRC- PP1 Fiber Fibrillated Polypropylene	5.64 (0.41)[#]	28.3 (5.83)	0.037 (0.0096)	1.60
FRC-PP2 Fiber Monofilament Polypropylene	5.46 (0.64)	26.9 (5.15)	0.036 (0.0092)	1.52
FRC-NL1 Fiber Monofilament Nylon	4.83 (0.52)	34.1 (9.21)	0.038 (0.0086)	1.93

[$] - Data for beams with different V_f (Table 3.2.3) combined for calculating average values and standard deviations reported in the table
[@] - Maximum concrete stress calculated assuming full compatibility between concrete beam and steel plate
[#] - Figures in brackets indicate standard deviation

Note that full compatibility between steel plate and concrete beam is assumed in the above calculations. In reality, however, some slip will occur between the two, which will increase the stress in concrete, and the actual value of maximum concrete stress, σ_c, may be expected to lie somewhere between the theoretical value of σ_c (Table 3.2.6) and the corresponding Modulus of Rupture values.

The exact distribution of the applied load between the concrete beam and the steel plate will depend upon the extent of slip possible between the two. If the two remain monolithic slip, the steel plate will carry a much larger share of the load and the stresses in the concrete as described above will remain low. As the possibility of slip between the two increases, so do the stress in concrete and the portion of the load carried by concrete beam. At the limit, if concrete beam and steel plate act totally independently of each other (i.e., both steel plate and concrete beam flex about their own centroidal axes), the concrete beam will carry nearly all of the applied load with only a very minor portion (< 2%) carried by the plate.

3.2.2 Residual Strength Test Method – Performance of Various Composites

After having established the validity of the test technique, the technique was applied to fiber reinforced concrete carrying various volume fractions of polymeric and steel fibers. Based on the extensive Residual Strength data reported below, it is clear that the technique is highly suitable for characterizing the mechanical response of fiber reinforced composites.

3.2.2.1 Materials, Mixes and Testing

Two sets of beams were cast as described below. In *Set 1*, the objective was to investigate fibrillated and monofilament polymeric fibers at low to medium dosage rates in concrete. In *Set 2*, concretes reinforced with high volume fractions of steel, PVA and deformed polypropylene fibers were investigated. The concrete mix proportions are given in Table 3.2.7. Cement, sand and aggregate were first mixed dry in an Omni-mixer, followed by the addition of water. Lastly, fibers were added gradually to avoid any fiber balling. For each mix, eight beams of size 100 mm x 100 mm x 350 mm were cast using external vibration. In addition, six compression cylinders of size 100 mm x 200 mm were cast for compressive strength determination.

Table 3.2.7: Mix Proportions

Cement (kg)	Water (kg)	Sand (kg)	Aggregate (10 mm) (kg)	Air Entraining Agent (ml/kg of cement)
400	200	1000	800	0.1

Set 1: Polymeric Fibers at Low to Medium Dosages

In the first set, a total of seven different polymeric fibers—five micro-denier and two macro-denier—were investigated. The details of the test program are given in Table 3.2.8. As seen, both the Open-Loop Test Method (OLTM) and the Residual Strength Test Method (RSTM) were employed to characterize the composites (see Sections 3.1 and 3.2 for details). Of the seven fibers investigated, six were of polypropylene and one was of nylon (Table 3.2.8). Further, of the six polypropylene fibers, four were fibrillated (PPF-1 to PPF-4) while the remaining two were monofilament type (PPM-1 and PPM-2). The nylon fiber (NLM-1) was also a monofilament type. All four fibrillated fibers had similar geometrical configurations and were procured from different manufacturers. The two monofilament polypropylene fibers investigated were also procured from different manufacturers. Monofilament PPM-1 fiber was 38 mm long

and had a diameter of 0.19 mm. Monofilament PPM-2 fiber was also 38 mm long but had a diameter of 0.63 mm.

Table 3.2.8: Fibers Investigated in Set 1 and Details of Test Program [220]

Fiber and Mix Id.	Fiber Information	Length (mm)	Test Method									
			$V_f = 0.2\%$		$V_f = 0.4\%$		$V_f = 0.5\%$		$V_f = 0.6\%$		$V_f = 0.8\%$	
			OL$^-$	RS$^+$	OL$^-$	RS$^+$	OL$^-$	RS$^+$	OL$^-$	RS$^+$	OL$^-$	RS$^+$
PPF-1	Fibrillated Polypropylene	38	x	x	x	x	x	x	x	x	x	x
PPF-2	Fibrillated Polypropylene	38	x	x	x	x	x	x	x	x	x	x
PPF-3	Fibrillated Polypropylene	38	-	-	-	-	x	x	-	-	-	-
PPF-4	Fibrillated Polypropylene	38	-	-	-	-	x	x	-	-	-	-
PPM-1	Monofilament Polypropylene	38	-	-	-	-	x	x	-	-	-	-
PPM-2	Monofilament Polypropylene	38	x	x	x	x	x	x	x	x	x	x
NLM-1	Monofilament Nylon	38	x	x	x	x	x	x	x	x	x	x

$^-$ OL - Open-Loop Test Method; $^+$ RS - Residual Strength Test Method

Set 2: Large Diameter Steel and Polymeric Fibers at High Dosages

The four commercially available macro fibers (large diameter) investigated in *Set 2* are described in Table 3.2.9. The mixes and the test program are described in Table 3.2.10. Of the four fibers investigated, one was polypropylene fiber, another was polyvinyl alcohol fiber and the remaining two were deformed steel fibers. One hybrid mix was also investigated, where both polypropylene and steel fibers were combined in the same mix. As in the case of the *Set 1* specimens, both Open-Loop and Residual Strength Test Methods were employed.

Table 3.2.9: Fibers investigated in Set 2

Fiber	Material	Geometry	Cross-sectional shape	Length (mm)	Size			$f_t^{@}$ (MPa)	$E_f^{\$}$ (GPa)
					Diameter (mm)	Amplitude (mm)	Wave length (mm)		
PP-STR	Polypropylene	Straight	Oval	50	0.63	-	-	450	3.5
PVA-1	PVA*	Flattened-ends	Oval	29	0.42	-	-	1100	23
ST-HKD	Steel	Hooked-end	Circular	35	0.55	-	-	1115	210
ST-CR1	Steel	Crimped	Crescent	38	2.0 x 0.35	1.0	7.5	1037	210

* PVA - Polyvinyl Alcohol; @ f_t - tensile strength; $ E_f - Fiber Elastic Modulus

Table 3.2.10: Various Mixes Investigated in Set 2 and Details of Test Program

Fiber and Mix Id.	Fiber Material and Type	Test Method									
		$V_f = 0.76\%$		$V_f = 1.0\%$		$V_f = 1.6\%$		$V_f = 3.0\%$		V_f=PP @ 1.6% + Steel @ 0.25%	
		OL^-	RS^+	OL^-	RS^+	OL^-	RS^+	OL^-	RS^+	OL^-	RS^+
PP-STR	Straight Polypropylene	-	-	-	-	x	x	x	x	-	-
PVA-1	Straight Polyvinyl Alcohol	-	-	x	x	x	x	-	-	-	-
ST-HKD	Hooked-end Steel	X	x	-	-	-	-	-	-	-	-
ST-CR1	Crimped Steel	x	x	-	-	-	-	-	-	-	-
HBRD-1	Hybrid 1.6% PP-STR +0.25% ST-HKD	-	-	-	-	-	-	-	-	x	x

Typical values of slump, V-B time, air content, and unit weights for the mixes in Set 2 are given in Table 3.2.11. Notice that all mixes were adequately workable and the V-B time increased with an increase in the fiber dosage rate. Testing procedures are similar to those described in the Sections 3.1 and 3.2.

3.2.2.2 Results

Compressive Strengths

Twenty-eight day compressive strengths for mixes belonging to *Set 1* are given in Table 3.2.12. Clearly, influence of fiber type and fiber volume on compressive strength was not seen. The twenty-eight day compressive strength for mixes belonging to *Set 2* are given in Table 3.2.13. Again, no influence of fiber type and fiber volume fraction on the compressive strength was noticeable.

Analysis of Flexural Toughness: Specimens from Set 1

In *Set 1* as described, the performance of four fibrillated polypropylene (PPF-1 to PPF-4), two monofilament polypropylene (PPM-1 and PPM-2), and one monofilament nylon (NLM-1) fibers was investigated at fiber volume fractions of up to 0.8%. To illustrate the general performance, the curves for fiber PPF-1 are shown in Figures 3.2.19a-e for an increasing fiber volume fraction from 0.2% to 0.8%. Curves for the other fibers depicted similar qualitative trends and hence are not reproduced in the interest of brevity. In Figures 3.2.19a-e, notice that for concrete mixes with very low fiber volume fractions (V_f=0.2%), considerable instability occurred in the open-loop tests. Even in such cases, the Residual Strength Test Method was able to capture the

toughening due to fiber reinforcement. The instability problem worsened for mixes containing nylon fibers (NLM-1) where even for fiber volume fractions as high as 0.4%, no reading could be recorded in the post-peak region (Figure 3.2.20). Once again the Residual Strength Test Method was able to capture fiber toughening in the case of nylon fiber at all fiber volumes including 0.4%.

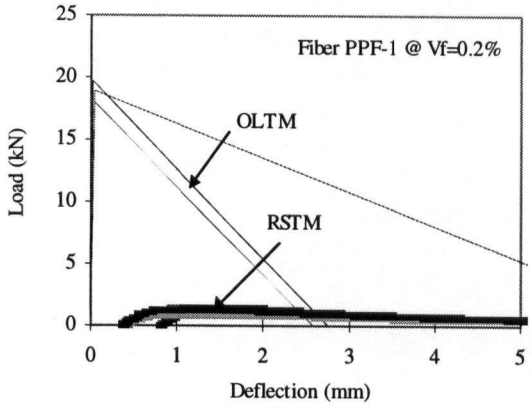

Figure 3.2.19a: Load-Deflection Curves for FRC with PPF-1 Fiber at Dosage Rate of 0.2%

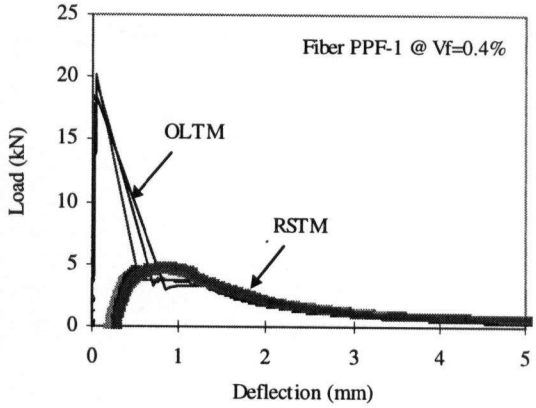

Figure 3.2.19b: Load-Deflection Curves for FRC with PPF-1 Fiber at Dosage Rate of 0.4%

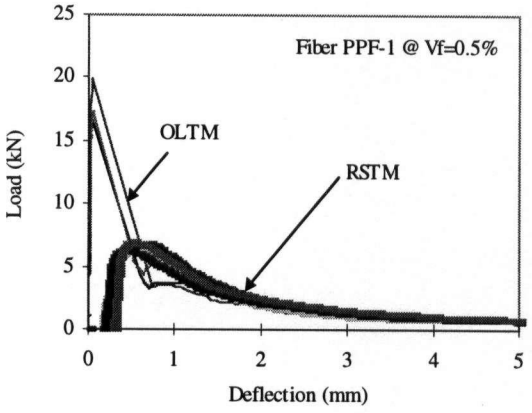

Figure 3.2.19c: Load-Deflection Curves for FRC with PPF-1 Fiber at Dosage Rate of 0.5%

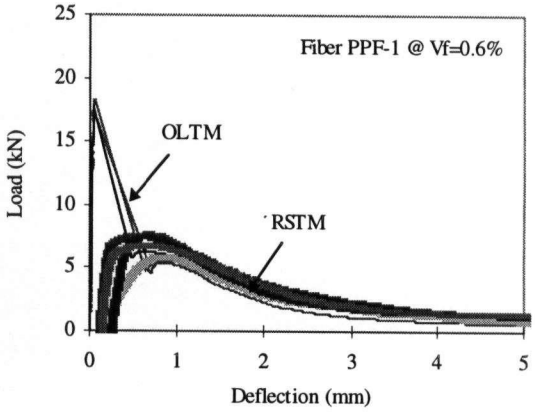

Figure 3.2.19d: Load-Deflection Curves for FRC with PPF-1 Fiber at Dosage Rate of 0.6%

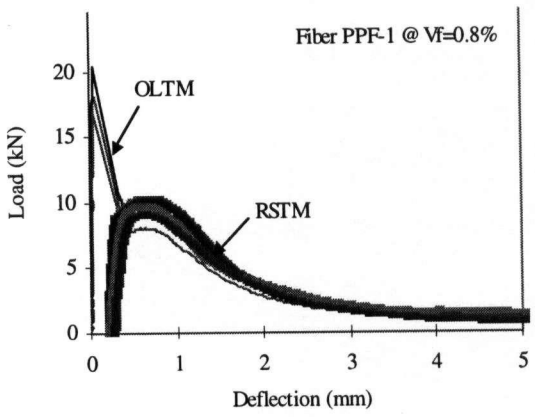

Figure 3.2.19e: Load-Deflection Curves for FRC with PPF-1 Fiber at Dosage Rate of 0.8%

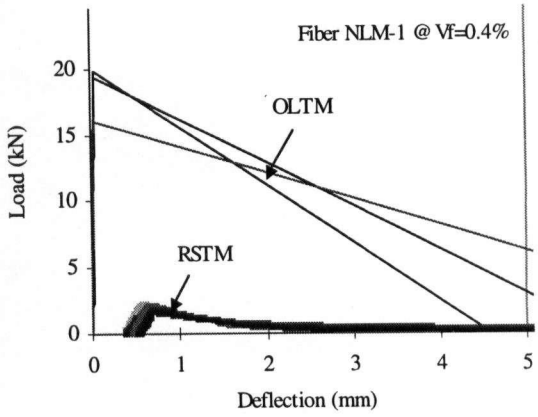

Figure 3.2.20: Load-Deflection Curves for FRC with NLM-1 Fiber at Dosage Rate of 0.4%

As the fiber dosage is increased (Figures 3.2.19a-e), one can notice a decrease in the load instability in the OLTM. One can also notice an increase in the post-peak load carrying capacity as measured by the RSTM and hence a related increase in the Residual Strength (RS) values (Equation 3.2). The RSTM was thus capable of predicting the post–peak toughness performance for composites with a wide range of various fiber volume fractions—both low and high.

The results obtained for all the fibers tested in Set 1 are given in Table 3.2.14, where the modulus of rupture (MOR) from the open-loop test, and the Residual Strength (RS, Equation 3.2) and Residual Strength Index (RSI, Equation 3.3) values from the Residual Strength Test Method are reported. The RS values are plotted in Figure 3.2.21 as a function of fiber volume fraction for the various fibers. The RSI values follow similar trends and hence are not reproduced. As seen clearly in Figure 3.2.21, the Residual Strength, RS, increases almost linearly with an increase in the fiber volume fraction. For the fiber volumes tested, interestingly, Residual Strength, RS did not reach an asymptotic limit as is often expected. The performance of fibrillated fibers PPF-1 and PPF-2 was very similar at various fiber volume fractions. Also, the performance of the other two fibrillated fibers (PPF-3 and PPF-4), which were tested only at a fiber dosage rate of 0.5%, compared well with that of PPF-1 and PPF-2 fibers at the given volume fractions. Monofilament polymeric fibers had inferior performance in comparison to their fibrillated counterparts. Among the two monofilament fibers investigated, the performance of the small diameter fiber PPM-1 was superior to that of the large diameter fiber PPM-2. A small diameter resulted in an increased fiber surface area for a given volume fraction and hence a

greater total frictional resistance during the process of fiber pullout during a test. In general, for the fibrillated fibers, Residual Strength increased by nearly 7 to 8 times when the fiber volume increased from 0.2% to 0.8%; the corresponding increase in the case of the monofilament fibers was only of the order of 5 to 6 times.

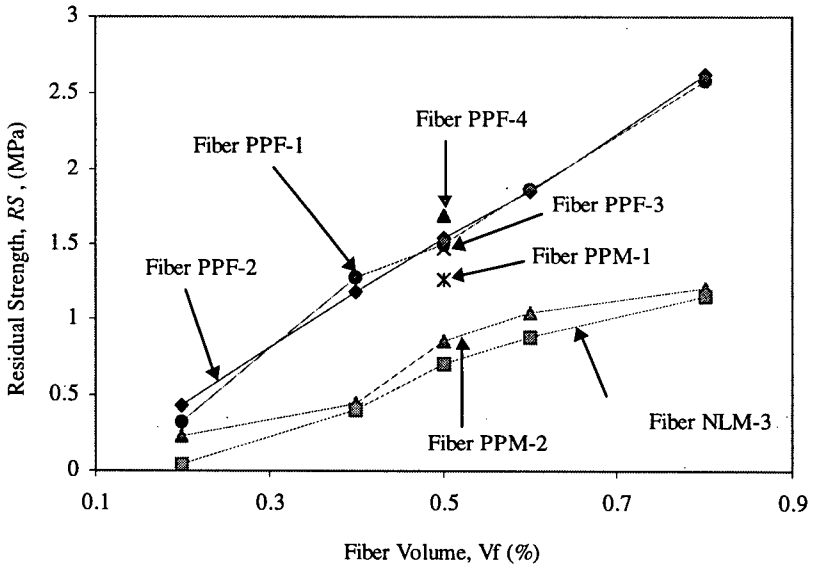

Figure 3.2.21: Residual Strength Values Plotted as a Function of Fiber Volume for Fibers in Set 1

Analysis of Flexural Toughness: Specimens from Set 2

In *Set 2*, performance of eight commercially available large diameter fibers was investigated at high volume fractions equal to or exceeding 0.76%. Given that high volume fractions of fibers were investigated in Set 2, the damage resulting due to instability even in an open-loop test was marginal. The results are compiled in Table 3.2.15. Some illustrative flexural load versus deflection curves for FRC with various fibers are shown in Figures 3.2.22 to 26. In Figure 3.2.22 data for the straight polypropylene fiber (PP-STR) are given at 1.6% by volume. Notice that the Residual Strength values for concrete reinforced with 1.6% of straight polypropylene fiber (PP-STR) were inferior than those for concrete reinforced with even a lower volume fraction of the fibrillated fiber (PPF-1 and PPF-2) (Tables 3.2.14 and 3.2.15). This is most likely due to the large diameter of the PP-STR fiber; a similar trend was observed previously when comparing the PPM-1 fiber with the PPM-2 fiber and the fibrillated fibers (Figure 3.2.21). In Figure 3.2.23, the results for the hybrid mix (HRBD-1) with a combination of the straight polypropylene fiber (PP-STR) at 1.6% by volume and hooked-end steel fiber (ST-HKD) at 0.25% by volume are presented. When Figures 3.2.22 and 3.2.23 are compared, a significant improvement due to the

addition of steel fibers is clearly noticeable. This is also clear from the RS values reported in Table 3.2.15.

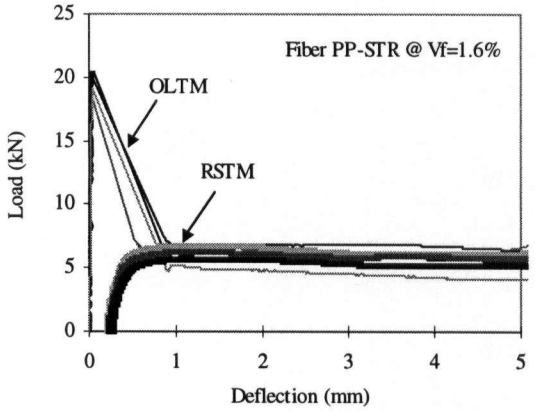

Figure 3.2.22: Load-Deflection Curves for FRC with PP-STR Fiber at a Dosage Rate of 1.6%.

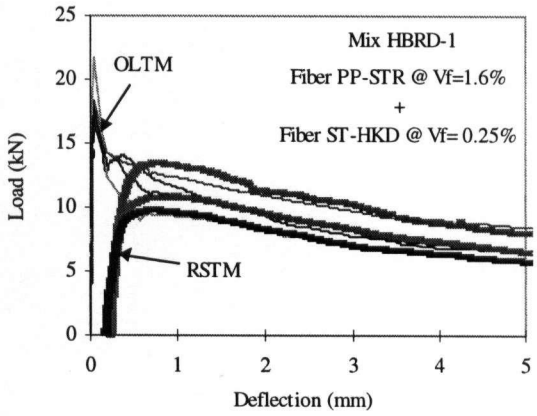

Figure 3.2.23: Load-Deflection Curves for FRC with a Hybrid Combination of PP-STR Fiber @ 1.6% and Steel Fiber (ST-HKD) @ 0.25%.

Finally, in Figures 3.2.24-26, the results for the PVA fiber (PVA-1), the hooked-end steel fiber (ST-HKD) and the crimped steel fiber (ST-CR1), respectively, are presented. Notice that the high modulus PVA fiber performed better than the low modulus polypropylene fibers (Table 3.2.15) and that the instability was minimized due to the higher modulus. Steel fibers with the hooked ends (Figure 3.2.25) gave the highest RS values of all composites tested even at a modest volume fraction of 0.76%. The crimped steel fiber, on the other hand, was not as effective as the hooked-end steel fiber (Figures 3.2.25 and 3.2.26) and this clearly demonstrates the ability of the RSTM to distinguish between steel fibers of various geometries.

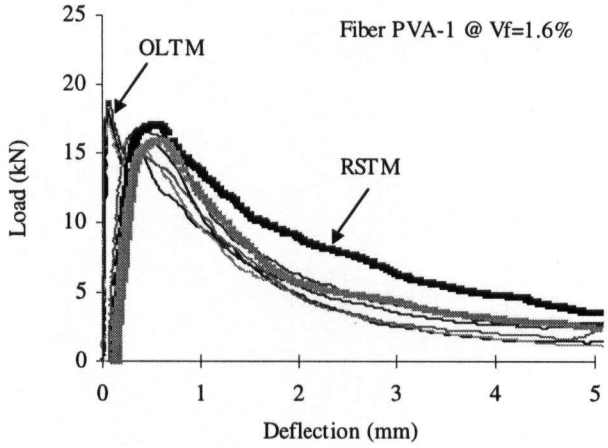

Figure 3.2.24: Load-Deflection Curves for FRC with PVA-1 Fiber at a Dosage Rate of 1.6%.

Table 3.2.11: Fresh properties of Mixes in Set 2

Fiber and Mix Id.	Fiber Material and Type	Fresh Properties															
		V_f = 0.76% of Steel OR 1.0% of PVA				V_f = 1.6%				V_f = 3.0%				V_f=1.6%(PP) + 0.25%(Steel)			
		Slm* (mm)	V-B+ (sec)	AC~ (%)	UW# (kg/m³)	Slm (mm)	V-B (sec)	AC (%)	UW (kg/m³)	Slm (mm)	V-B (sec)	AC (%)	UW (kg/m³)	Slm (mm)	V-B (sec)	AC (%)	UW (kg/m³)
PP-STR	Straight Polypropylene	-	-	-	-	0	21.1	4.8	2368	0	27.8	4.9	2362	-	-	-	-
PVA-1	Straight Polyvinyl Alcohol	50	4.7	4.5	2369	10	8.9	4.2	2389	-	-	-	-	-	-	-	-
ST-HKD	Hooked-end Steel	80	2.9	4.0	2377	-	-	-	-	-	-	-	-	-	-	-	-
ST-CR1	Crimped Steel	90	4.5	4.3	2382	-	-	-	-	-	-	-	-	-	-	-	-
HBRD-1	Hybrid 1.6% PP-STR +0.25% ST-HKD	-	-	-	-	-	-	-	-	-	-	-	-	10	35.1	4.4	2391

*Slm - Slump; +V-B - Vee-Bee; ~AC - Air Content; #UW - Unit Weight

Table 3.2.12: Compressive strengths (28-Day) for Mixes in Set 1

Fiber & Mix Id.	Fiber Information	Compressive Strength (MPa)				
		V_f=0.2%	V_f=0.4%	V_f=0.5%	V_f=0.6%	V_f=0.8%
PPF-1	Fibrillated Polypropylene	37.8 (2.1)#	41.1 (3.3)	38.9 (1.6)	40.44 (4.4)	42.1 (3.1)
PPF-2	Fibrillated Polypropylene	41.3 (3.6)	39.2 (2.7)	40.3 (4.9)	39.8 (4.2)	40.6 (2.2)
PPF-3	Fibrillated Polypropylene	-	-	37.9 (1.1)	-	-
PPF-4	Fibrillated Polypropylene	-	-	38.9 (2.8)	-	-
PPM-1	Monofilament Polypropylene	-	-	39.1 (2.7)	-	-
PPM-2	Monofilament Polypropylene	39.4 (3.5)	39.7 (0.4)	42.1 (4.3)	37.1 (2.1)	39.6 (5.1)
NLM-1	Monofilament Nylon	38.9 (2.9)	40.4 (1.1)	41.9 (3.5)	40.1 (2.2)	37.5 (2.4)

- Figures in brackets indicate standard deviation

Table 3.2.13: Compressive strengths (28-Day) for Mixes in Set 2

Fiber and Mix Id.	Fiber Material and Type	Compressive Strength (MPa)			
		V_f = 0.76% Steel OR 1.0% PVA	V_f = 1.6%	V_f = 3.0%	V_f=1.6 % PP + 0.25% Steel
PP-STR	Straight Polypropylene	-	36.6 (0.9)#	38.9 (3.2)	
PVA-1	Straight Polyvinyl Alcohol	42.6 (4.4)	41.3 (1.2)	-	
ST-HKD	Hooked-end Steel	41.5 (2.7)	-	-	-
ST-CR1	Crimped Steel	42.2 (2.1)	-	-	-
HBRD-1	Hybrid 1.6% PP-STR +0.25% ST-HKD	-	-	-	41.2 (2.6)

- Figures in brackets indicate standard deviation

Table 3.2.14: Detailed Results for Fibers in Set 1

Fiber and Mix Id.	Fiber Volume, Vf														
	Vf = 0.2%			Vf = 0.4%			Vf = 0.5%			Vf = 0.6%			Vf = 0.8%		
	MOR* (MPa)	RS+ (MPa)	RSI+# (%)	MOR (MPa)	RS (MPa)	RSI (%)	MOR (MPa)	RS (MPa)	RSI (%)	MOR (MPa)	RS (MPa)	RSI (%)	MOR (MPa)	RS (MPa)	RSI (%)
PPF-1	5.63 (0.3)~	0.33 (0.07)	5.9 -	5.85 (0.26)	1.27 (0.04)	21.7 -	5.41 (0.48)	1.5 (0.23)	27.7 -	5.37 (0.07)	1.86 (0.10)	34.6 -	5.54 (0.51)	2.58 (0.07)	46.6 -
PPF-2	5.63 (0.50)	0.44 (0.03)	7.8 -	5.57 (0.36)	1.18 (0.12)	21.2 -	5.65 (0.30)	1.54 (0.20)	27.3 -	5.39 (0.10)	1.85 (0.16)	34.3 -	5.77 (0.22)	2.62 (0.11)	45.4 -
PPF-3	- -	- -	- -	- -	- -	- -	5.98 (0.53)	1.46 (0.02)	24.4 -	- -	- -	- -	- -	- -	- -
PPF-4	- -	- -	- -	- -	- -	- -	5.73 (0.23)	1.69 (0.11)	29.5 -	- -	- -	- -	- -	- -	- -
PPM-1	- -	- -	- -	- -	- -	- -	5.46 (0.25)	1.26 (0.35)	23.1 -	- -	- -	- -	- -	- -	- -
PPM-2	6.92 (0.52)	0.23 (0.12)	3.3 -	5.79 (0.20)	0.45 (0.09)	7.8 -	6.03 (0.15)	0.85 (0.11)	14.1 -	5.86 (0.27)	1.04 (0.18)	17.7 -	5.9 (0.14)	1.21 (0.08)	20.5 -
NLM-1	5.04 (0.44)	0.04 (0.02)	0.8 -	5.54 (0.57)	0.41 (0.08)	7.4 -	5.61 (0.14)	0.71 (0.05)	12.7 -	5.10 (0.58)	0.88 (0.14)	17.3 -	5.56 (0.32)	1.15 (0.07)	20.7 -

* Average of three beams

\+ Average of four beams

\# RSI = 100 x RS/MOR

~ Figures in brackets indicate standard deviation

Table 3.2.15: Detailed Results for Fibers in Set 2

Fiber and Mix Id.	Fiber Volume, Vf														
	Vf = 0.76%			Vf = 1.0%			Vf = 1.6%			Vf = 3.0%			Vf = 1.6% (PP) + 0.25% (Steel)		
	MOR* (MPa)	RS** (MPa)	RSI*** (%)	MOR* (MPa)	RS** (MPa)	RSI*** (%)	MOR* (MPa)	RS** (MPa)	RSI*** (%)	MOR* (MPa)	RS** (MPa)	RSI*** (%)	MOR* (MPa)	RS** (MPa)	RSI*** (%)
PP-STR	- -	- -	- -	- -	- -	- -	5.87 (0.21)****	1.83 (0.19)	31.2 -	5.58 (0.24)	2.47 (0.08)	44.3 -	- -	- -	- -
PVA-1	- -	- -	- -	5.96 (0.19)	3.19 (0.65)	53.6 -	5.45 (0.14)	3.88 (0.48)	71.2 -	- -	- -	- -	- -	- -	- -
ST-HKD	6.31 (0.22)	5.74 (0.43)	91.0 -	- -	- -	- -	- -	- -	- -	- -	- -	- -	- -	- -	- -
ST-CR1	5.72 (0.34)	3.27 (0.20)	57.2 -	- -	- -	- -	- -	- -	- -	- -	- -	- -	- -	- -	- -
HBRD-1	- -	- -	- -	- -	- -	- -	- -	- -	- -	- -	- -	- -	5.59 (0.63)	3.34 (0.55)	59.7 -

* Average of four beams

** Average of three beams

*** RSI = 100 x RS/MOR

**** Figures in brackets indicate standard deviation

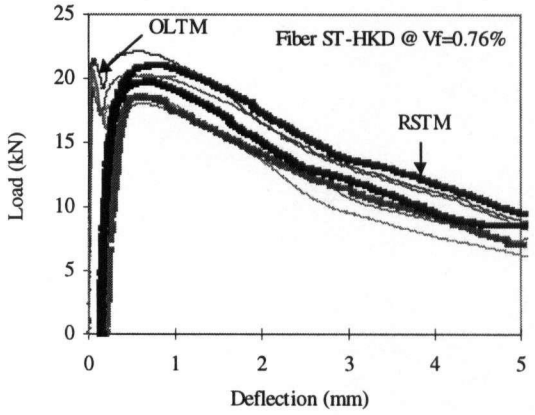

Figure 3.2.25: Load-Deflection Curves for FRC with Steel Fiber ST-HKD at a Dosage Rate of 0.76%.

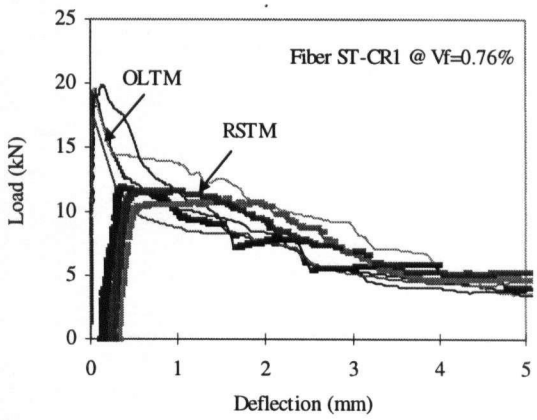

Figure 3.2.26: Load-Deflection Curves for FRC with Steel Fiber ST-CR1 at a Dosage Rate of 0.76%.

3.2.2.3 Discussion

The purpose of the research reported in this section was to make an assessment of the validity of the newly developed Residual Strength Test Method for toughness characterization of fiber reinforced concrete. The Residual Strength Test Method was seen to be highly effective in differentiating between different fiber types, fiber lengths, fiber configurations, fiber volume fractions, fiber geometries and fiber moduli. With respect to the specific composites tested, the following conclusions could be drawn:

- Based on the results from specimens in Set 1, it is clear that at a given fiber volume fraction, fibrillated polypropylene fibers provide better toughening than monofilament polypropylene fibers or the monofilament nylon fibers. In the range of fiber volume fractions investigated (0.2%-0.8%), both the Residual Strengths and the Residual Strength Indices increase almost linearly with the fiber volume fraction. Other parameters remaining the same, performance of FRC with small diameter fibers is better.
- Data from specimens tested in Set 2 indicate that the Residual Strength Test Method equally well predicts the toughening capabilities of steel and other macro-fibers at large volume fractions. The post-peak instability in these composites, however, was minimal. Steel fibers provided very high Residual Strengths, but among the steel fibers the hooked-end steel fiber demonstrated better toughening capability than the crimped steel fiber. Combining polypropylene and steel fibers in the same mix had a synergistic effect and composites with very high Residual Strengths were obtained.

3.3 Conclusions

- Material factors that were found to influence toughness of fiber reinforced concrete include fiber aspect ratio, fiber surface characteristics, fiber geometry, fiber volume content, shrinkage properties of matrix, and mineral admixtures (pozzolans).
- The influence of test machine stiffness on the measured flexural load versus deflection response of fiber reinforced concrete composites has been evaluated. It has been found that the measured flexural response of fiber reinforced cementitious composites, particularly of the ones containing low fiber volume fractions, is greatly influenced by the machine configuration. For machines with open-loop test configuration with low stiffness, the load drops suddenly in an uncontrolled and unstable manner immediately following the peak load, the extent of this instability being dependent upon machine stiffness and loading rate. In addition, after the unstable part, the curve attains a stable softening level, during which loads are functions of the test machine characteristics. For the aforementioned reasons the use of such load versus deflection curves to quantify toughness often translates into meaningless toughness parameters. Unfortunately, the existing standards to characterize toughness make use of such flexural load versus deflection curves, and therefore toughness measures using these standards are highly suspect.
- An evaluation of the Residual Strength Test Method (RSTM) for the measurement of post-cracking performance and flexural toughness of fiber reinforced concrete composites has been carried out. In the test method, a stable narrow crack is first created in the specimen by applying flexural load in parallel with a steel plate under controlled conditions. The plate is then removed, and the specimen is tested in a routine manner in flexure to obtain the post-crack load versus displacement response. In the experimental test program, several fiber reinforced concrete mixes containing a variety of fibers at different volume fractions were evaluated. Results from the test program suggest that the RSTM holds promise in the measurement of post-cracking performance of fiber reinforced concrete composites.
- The Residual Strength Test Method is seen to be highly effective in differentiating between different fiber types, fiber lengths, fiber configurations, fiber volume fractions, fiber geometries and fiber moduli. In particular, the technique is very useful for testing cement-based composites containing fibers at very low dosages.

- It is recommended that proper care must be exercised while removing the steel plate before reloading the cracked specimen. Specimen mishandling may increase the damage and the consequent results.
- The post-peak load-deformation curves obtained from the Residual Strength Test Method correlated well with those obtained from the Close-Loop Test Method for all three types of fibers (PP1, PP2 and NL1 fibers) investigated at various fiber volume fractions up to 0.5%. Slightly lower Residual Strength (RS) values are obtained from the Residual Strength Test Method as compared to the close-loop method. The error is magnified to a small extent for low efficiency fibers. When various fiber types are compared using the close-loop method, fibrillated polypropylene (PP1) is found to be the most effective followed by the nylon (NL1) fiber and the monofilament polypropylene (PP2) fiber. The Residual Strength Test Method was also capable of accurately predicting these important trends.
- At a given fiber volume fraction, fibrillated polypropylene fibers provide better toughening than monofilament polypropylene fibers or the monofilament nylon fibers. In the range of fiber volume fractions investigated (0.2%-0.8%) of these fibers, both the Residual Strengths and the Residual Strength Indices increase almost linearly with increase in fiber volume fraction. Other parameters remaining the same, FRC with smaller diameter fibers have better performance.
- The Residual Strength Test Method equally well predicts the toughening capabilities of steel and other macro-fibers at large volume fractions. The post-peak instability in these composites, however, is minimal. Steel fibers provide very high Residual Strengths, but among the steel fibers, the hooked-end steel fiber demonstrates better toughening capability than the crimped steel fiber. Combining polypropylene and steel fibers in the same mix has a synergistic effect on the toughness of FRC.

Chapter 4

Bond-Slip Performance of Fibers Embedded in Cementitious Matrices

4.0 Introduction

In the previous chapter, it was observed that the energy absorption capability of fiber reinforced concrete was dependent upon the properties of its constituents, i.e., properties of fibers and properties of matrix. It was also noted that the main energy absorption mechanism in fiber reinforced concrete composite is associated with pullout of fibers from the matrix. More specifically, the micromechanical properties of fiber-matrix interface dictate the fiber pullout response and the consequent composite toughening or strengthening. If optimization of composite toughening or composite strengthening is sought, it becomes critical to identify different variables that influence micromechanical properties of the fiber-matrix interface and the consequent fiber pullout response. Therefore, the objective of the present investigation is to shed some light on this important aspect through experimental fiber pullout studies.

4.1 Bond-Slip Performance of Fibers – Influence of Pullout Parameters

Despite numerous micromechanical fiber pullout studies done in the past, the extent of dependence of micromechanical properties (and the consequent fiber pullout response) on the various pullout parameters is not properly understood. The objective of the present investigation is to critically explore this important aspect. In this regard, dependence of experimental fiber pullout response on the following pullout parameters has been explored:

- Fiber elastic modulus
- Fiber length
- Fiber surface roughness
- Matrix shrinkage properties
- Matrix water/cement ratio
- Matrix modification by pozzolan - silica fume

Single fiber pullout tests were performed using the specimen shown in Figure 4.1.1. The specimen preparation is as follows - the specimens are cast in two parts separated by a plastic separator film. The lower part (labeled 'I' in Figure 4.1.1) is cast first with the fiber embedded in it, and is allowed to cure for 24 hours. Once the lower half has hardened, the other half (labeled 'II' in Figure 4.1.1) of the specimen is cast. The assembly is further cured for a period of 28 days. For preparing specimens with fiber lengths longer than the standard specimen size shown in Figure 4.1.1, an attachment is added to the standard mould while casting. Pullout tests were performed in a 150-kN floor mounted testing machine. Load was applied at a cross-arm travel rate of 0.1 mm/min through a 5-kN load cell. Displacements were measured by two LVDTs (Linear Variable Differential Transformers). Loads and displacements were digitally recorded using a 16-bit data acquisition system operating at a frequency of 10 Hz.

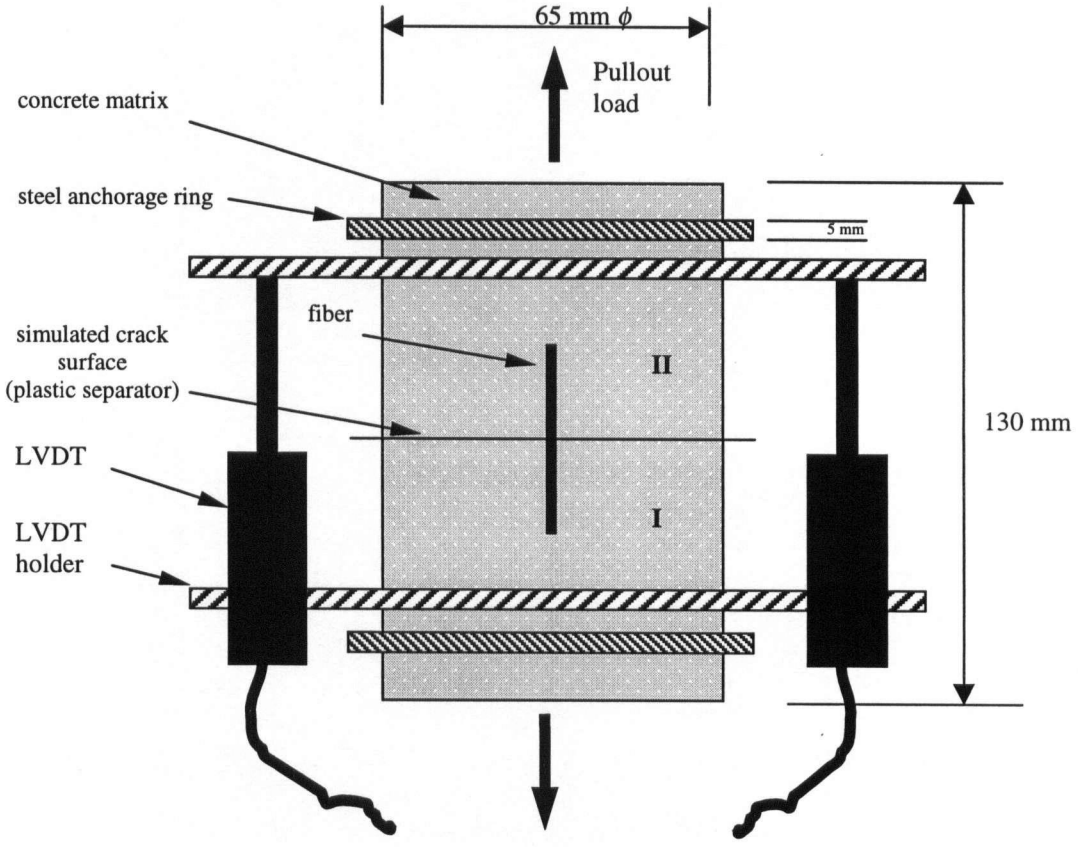

Figure 4.1.1: Schematic of a standard pullout test specimen

Three fiber types were investigated, namely,

i. straight-smooth, stainless steel fiber (fiber diameter - 0.44 mm)

ii. straight, stainless steel fiber with rough surface[1] (fiber diameter - 0.44 mm)

iii. straight, smooth polypropylene fiber (fiber diameter – 0.95 mm)

Matrix types investigated were:

i. normal strength matrix (Concrete matrix, CSA Type 10 Portland Cement)
   - Compressive strength - 36 MPa

ii. high strength matrix (Concrete matrix, CSA Type 10 Portland Cement)
   - Compressive strength - 69 MPa

iii. non-shrink grout matrix (Mortar matrix)
   - Compressive strength - 18 MPa

iv. silica fume modified high strength matrix (Concrete matrix, CSA Type 10 Portland Cement)
   - Compressive strength - 71 MPa

The experimental fiber pullout test results are reported below.

4.1.1 Straight-smooth, Stainless Steel Fibers Embedded in Normal Strength Matrix

The experimental pullout responses of straight-smooth, stainless steel fibers embedded in a normal strength matrix were investigated, and the corresponding results are reported here. The mix proportion used was - water : cement : sand : aggregate = 0.50 : 1.0 : 2.5 : 2.0. Cement used was of CSA Type 10 specification. The above mix proportion gave an average 28-day compressive strength of approximately 36 MPa, as determined by testing five 200 mm x 100 mm ϕ cylinders. Fibers with embedded lengths equal to 15 mm, 30 mm, 60 mm and 90 mm on both sides of the crack were chosen, and for each fiber length, five fibers were tested for pullout. Figure 4.1.2 shows the pullout response of fibers tested. The average pullout curves have also been plotted in the same figure (thick lines). Results from these pullout tests are tabulated in Table 4.1.1. The total pullout energy, E_{total}, was measured by numerical integration of pullout curve.

[1] Straight-smooth stainless steel fibers were sand blasted for about 25 minutes to produce the straight stainless steel fibers with rough surface

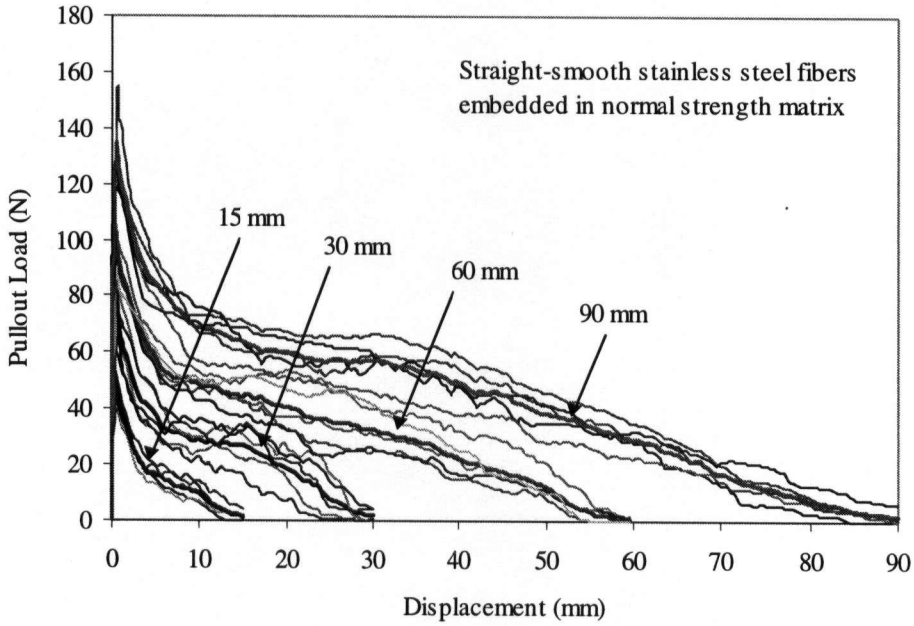

Figure 4.1.2: Pullout response of straight-smooth, stainless steel fibers embedded in normal strength matrix

Table 4.1.1: Experimental pullout test results for straight-smooth, stainless steel fibers embedded in normal strength matrix

Fiber	Matrix	Embedded Fiber Length (mm)	Pullout Response		
			P_{peak} (N)	δ_{peak} (mm)	E_{total} (N-mm)
Straight-smooth, stainless steel	Normal strength	15	51.2 (6.6)#	0.034 (0.011)	226 (32)
		30	95.1 (9.0)	0.120 (0.038)	769 (166)
		60	100.5 (8.3)	0.387 (0.099)	1940 (288)
		90	134.5 (21.3)	0.484 (0.054)	3818 (374)

P_{peak} – Peak load; δ_{peak} – Displacement at peak pullout load; E_{total} – Total pullout energy
- Figures in brackets indicate standard deviation

4.1.1.1 Influence of Fiber Length

In the Table 4.1.1, it can be noticed that increase in fiber length led to an increase in peak pullout load. However, the rate of increase in peak pullout load diminished with increase in fiber length. The peak pullout load reached an asymptote at very long fiber lengths as seen in Figure 4.1.3.

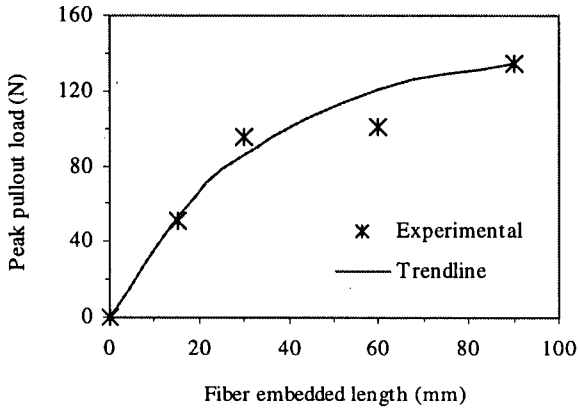

Figure 4.1.3: Embedded fiber length vs. peak pullout load curve for straight-smooth, stainless steel fibers embedded in normal strength matrix

4.1.2 Straight, Stainless Steel Fibers with Rough Surface Embedded in Normal Strength Matrix

The experimental pullout response of straight, stainless steel fibers with a rough surface embedded in a normal strength matrix was investigated and the corresponding results are reported here. The mix proportion used and the concrete compressive strength were same as mentioned in the previous sub-section. Fibers with embedded lengths equal to 15 mm, 30 mm, 60 mm and 90 mm on both sides of the crack were chosen, and for each fiber length five fibers were tested for pullout. Figure 4.1.4 shows the pullout response of the fibers tested. The average pullout curves have also been plotted in the same figure (thick lines). Results from these pullout tests are tabulated in Table 4.1.2.

Table 4.1.2: Experimental pullout test results for straight, stainless steel fibers with rough surface embedded in normal strength matrix

Fiber	Matrix	Embedded Fiber Length (mm)	Pullout Response		
			P_{peak} (N)	δ_{peak} (mm)	E_{total} (N-mm)
Straight, fiber with rough surface	Normal strength	15	105.9 (14.3)#	0.052 (0.019)	450 (145)
		30	116.1 (9.6)	0.123 (0.038)	1160 (228)
		60	127.9 (14.0)	0.546 (0.131)	3201 (557)
		90	135.9 (10.39)	0.591 (0.109)	5916 (1045)

P_{peak} – Peak load; δ_{peak} – Displacement at peak pullout load; E_{total} – Total pullout energy
- Figures in brackets indicate standard deviation

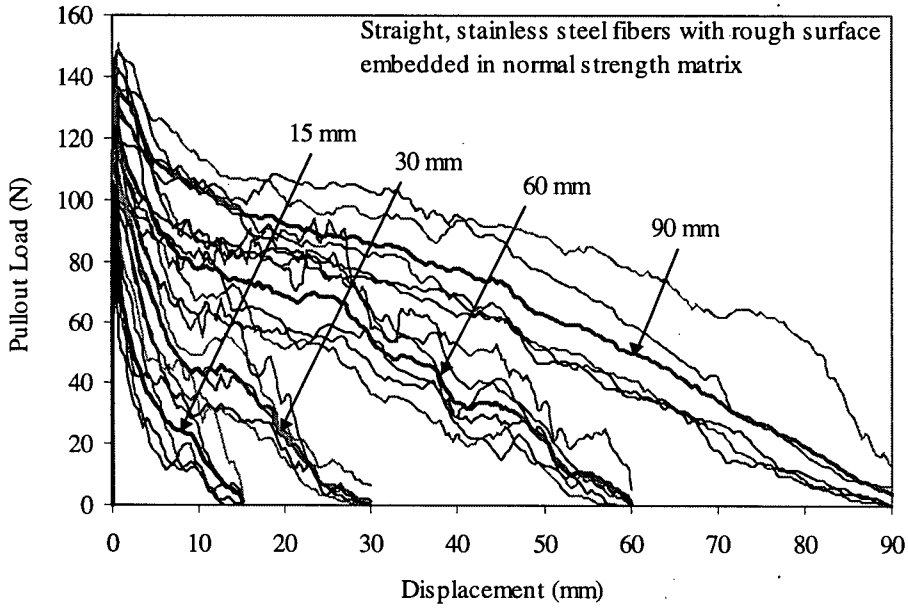

Figure 4.1.4: Pullout response of straight , stainless steel fibers with rough surface embedded in normal strength matrix

4.1.2.1 Influence of Surface Roughness

To study the influence of fiber surface roughness on the fiber pullout response, the pullout curves for 30 mm long smooth and rough fibers are compared in Figure 4.1.5. It can be seen that peak pullout loads were higher for fibers with rough surface. Also, the peak pullout displacement and the total pullout energy were higher for fibers with rough surface (compare Table 4.1.1 and Table 4.1.2). With increase in fiber length, disparity between the peak pullout loads for smooth fiber and rough fiber diminished.

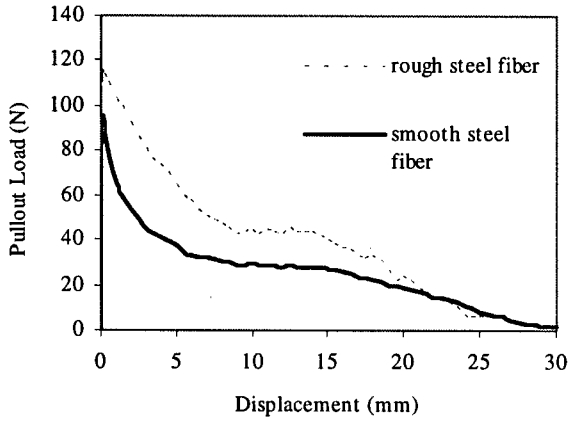

Figure 4.1.5: Comparison of the pullout response of 30 mm long straight-smooth, stainless steel fibers and 30 mm long straight, stainless fibers with rough surface (normal strength matrix)

4.1.2.2 Influence of Fiber Length

For fiber with rough surface, it can be seen that an increase in fiber length led to an increase in the peak pullout load (Figure 4.1.6). However, the rate of increase in peak pullout load diminished with increase in fiber length as seen in Table 4.1.2 and Figure 4.1.6, and reached an asymptotic value. The asymptotic value of pullout load for straight-rough, stainless steel fibers was very close to that obtained for the straight-smooth, stainless steel fibers (compare Figure 4.1.5 and Figure 4.1.6).

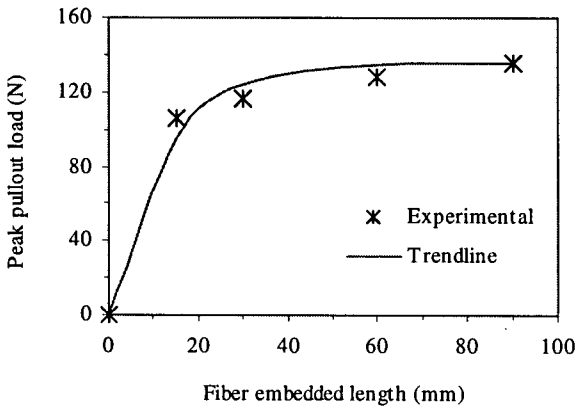

Figure 4.1.6: Embedded fiber length vs. peak pullout load curve for straight, stainless steel fibers with rough surface

4.1.3 Straight-smooth, Stainless Steel Fibers Embedded in Non-Shrink Grout Matrix

The frictional resistance to fiber pullout is dependent upon the normal contact stresses (acting perpendicular to the longitudinal fiber axis) that develop at the fiber-matrix interface. The normal contact stress at the fiber-matrix interface results from matrix shrinkage taking place during the curing, setting and hardening of the matrix. The greater the matrix shrinkage, the higher the magnitude of interfacial normal contact stress and the corresponding frictional resistance. Thus, it can be inferred that a cementitious matrix that experiences less shrinkage will offer lower resistance to fiber pullout. A type of cementitious matrix that undergoes relatively lesser shrinkage is available commercially under the name 'non-shrink grout' (mortar matrix). Fiber pullout response of straight-smooth, stainless steel fibers embedded in non-shrink grout matrix was investigated. The 28-day compressive strength of the non-shrink grout matrix was approximately 18 MPa, as determined by testing five 200 mm x 100 mm ϕ cylinders. Fibers with embedded lengths equal to 15 mm, 30 mm, 60 mm and 90 mm on both sides of the crack

were chosen, and for each fiber length, five fibers were tested for pullout. Figure 4.1.7 shows the pullout response of fibers tested. The average pullout curves have also been plotted in the same figure (thick lines). Results from these pullout tests are tabulated in Table 4.1.3.

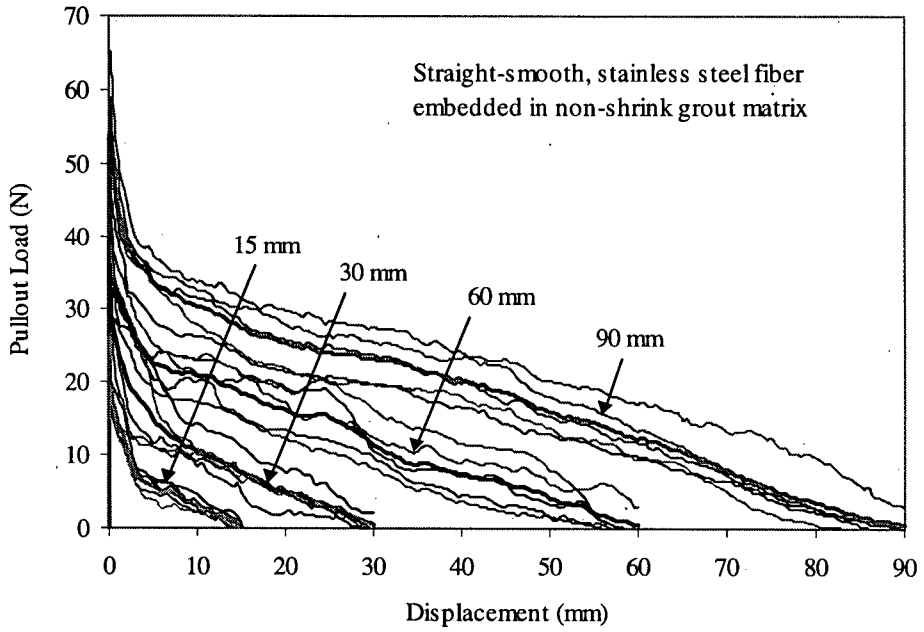

Figure 4.1.7: Pullout response of straight-smooth, stainless steel fibers embedded in non-shrink grout matrix

Table 4.1.3: Experimental pullout test results for straight-smooth, stainless steel fibers embedded in non-shrink grout matrix

Fiber	Matrix	Embedded Fiber Length (mm)	Pullout Response		
			P_{peak} (N)	δ_{peak} (mm)	E_{total} (N-mm)
Straight-smooth, stainless steel	Non-shrink grout	15	26.1 (3.9)#	0.013 (0.003)	83 (12)
		30	36.6 (4.6)	0.044 (0.009)	269 (67)
		60	39.5 (5.8)	0.148 (0.049)	754 (145)
		90	42.5 (5.9)	0.160 (0.057)	1560 (240)

P_{peak} – Peak load; δ_{peak} – Displacement at peak pullout load; E_{total} – Total pullout energy
- Figures in brackets indicate standard deviation

4.1.3.1 Influence of Matrix Shrinkage Behavior

To study the influence of matrix shrinkage on the fiber pullout response, the pullout curves for 30 mm long straight, smooth fibers are compared in the Figure 4.1.8 for the following two types of cementitious matrices:

i. CSA Type 10 normal strength matrix

ii. Non-shrink grout matrix

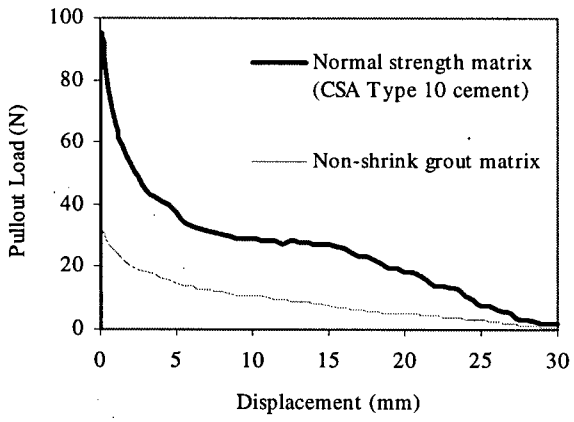

Figure 4.1.8: Pullout response of 30 mm long fibers embedded in normal strength matrix (CSA Type 10 cement) and in non-shrink grout matrix

In the figure, it can be noticed that the peak pullout load attained in the case of non-shrink grout matrix was much lower in magnitude in comparison to that obtained in the case of CSA Type 10 normal strength matrix. Also, the displacement at peak pullout load and the total pullout energy was lower in the case of non-shrink grout matrix.

4.1.3.2 Influence of Fiber Length

It can be seen that increase in fiber length led to an increase in peak pullout load. However, the rate of increase in peak pullout load diminished with increase in fiber length. The peak pullout load reached an asymptote at very long fiber lengths as seen in Figure 4.1.9. The asymptotic value of pullout load obtained in this case ($\cong$ 43 N) was much lower than that obtained in the case of CSA Type 10 normal strength concrete matrix ($\cong$ 135 N).

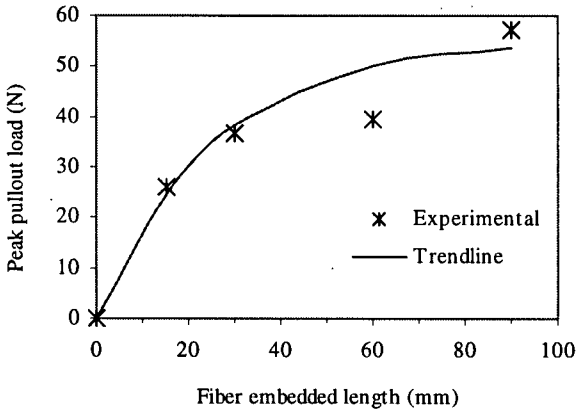

Figure 4.1.9: Embedded fiber length vs. peak pullout load curve for straight-smooth, stainless steel fibers embedded in non-shrink grout matrix

4.1.4 Straight-smooth, Stainless Steel Fibers Embedded in High-Strength Matrix

The experimental fiber pullout response of straight-smooth, stainless steel fibers embedded in a high strength matrix was investigated, and the corresponding results are reported here. The mix proportion used was - water : cement : sand : aggregate = 0.35 : 1.00 : 1.50 : 1.75. Cement used was of CSA Type 10 specification. The above mix proportion gave an average 28-day compressive strength of approximately 69 MPa, as determined by testing five 200 mm x 100 mm ϕ cylinders. Fibers with one-side embedded lengths equal to 30 mm were tested for pullout. Figure 4.1.10 shows the pullout response of the fibers tested. The average pullout curve has also been plotted in the same figure (thick line). Results from these pullout tests are tabulated in Table 4.1.4.

Table 4.1.4: Experimental pullout test results for straight-smooth, stainless steel fibers embedded in high strength matrix

Fiber	Matrix	Embedded Fiber Length (mm)	Pullout Response		
			P_{peak} (N)	δ_{peak} (mm)	E_{total} (N-mm)
Straight-smooth, stainless steel	High strength	30	102.80 (9.95)	0.134 (0.038)	1026 (271)

P_{peak} – Peak load; δ_{peak} – Displacement at peak pullout load; E_{total} – Total pullout energy
- Figures in brackets indicate standard deviation

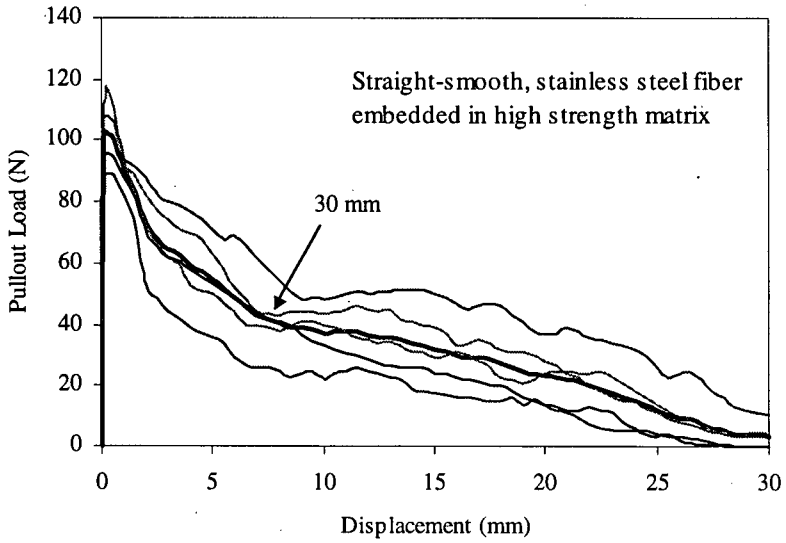

Figure 4.1.10: Pullout response of straight-smooth, stainless steel fibers embedded in high strength matrix

4.1.4.1 Influence of Water/Cement Ratio

To study the influence of water/cement ratio on fiber pullout response, the pullout curves for 30 mm long straight, smooth fibers are compared in Figure 4.1.11 at the following two water/cement ratios:

i. w/c = 0.50

ii. w/c = 0.35

In Figure 4.1.11 it can be seen that the pullout loads in the descending branch of the pullout curve at a w/c ratio of 0.35 are greater in comparison to those at a w/c ratio of 0.50. The post-peak pullout loads are a function of the frictional shear resistance that mobilizes at the fiber-matrix interface. A superior post-peak descending pullout curve obtained at lower w/c ratio (= 0.35) implies that the interfacial frictional resistance was greater at this w/c ratio. Autogeneous shrinkage of matrix associated with the low w/c ratio matrices is one possible reason that may influence the frictional resistance. It must be noted that an enhanced matrix shrinkage leads to an increase in fiber-matrix interfacial contact stress and the consequent interfacial frictional bond. The physical characteristics of the sliding surfaces between the fiber and the matrix is yet another factor that to some extent may influence the interfacial frictional bond.

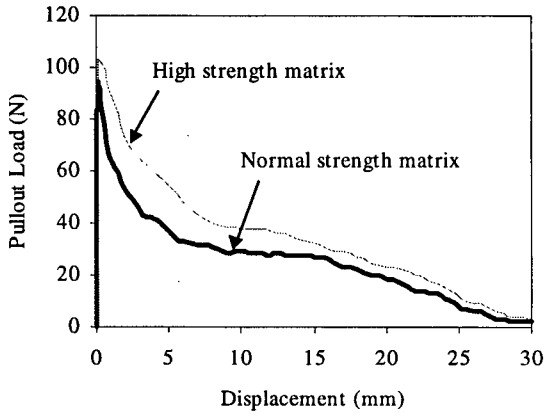

Figure 4.1.11: Pullout response of straight-smooth, stainless steel fibers embedded in normal strength matrix and high strength matrix

4.1.5 Straight-smooth, Stainless Steel Fibers Embedded in Silica-fume Modified High-Strength Matrix

The experimental fiber pullout response of straight-smooth, stainless steel fibers embedded in a silica-fume modified normal strength matrix was investigated and the corresponding results are reported here. The mix proportion used was - water : binder : sand : aggregate = 0.35 : 1.00 : 1.50 : 1.75. The binder contained a mixture of cement (90% by weight) and silica fume (10% by weight). Cement used was of CSA Type 10 specification. The above mix proportion gave an average 28-day compressive strength of about 71 MPa, as determined by testing five 200 mm x 100 mm ϕ cylinders. Fibers with one-side embedded lengths equal to 30 mm were tested for pullout. Figure 4.1.12 shows the pullout response of the fibers tested. The average pullout curve has also been plotted in the same figure (thick line). Results from these pullout tests are tabulated in Table 4.1.5.

Table 4.1.5: Experimental pullout test results for straight-smooth, stainless steel fibers embedded in silica-fume modified high strength matrix

Fiber	Matrix	Embedded Fiber Length (mm)	Pullout Response		
			P_{peak} (N)	δ_{peak} (mm)	E_{total} (N-mm)
Straight-smooth, stainless steel	Silica fume Modified High strength	30	101.9 (4.60)#	0.125 (0.032)	1295 (209)

P_{peak} – Peak load; δ_{peak} – Displacement at peak pullout load; E_{total} – Total pullout energy
- Figures in brackets indicate standard deviation

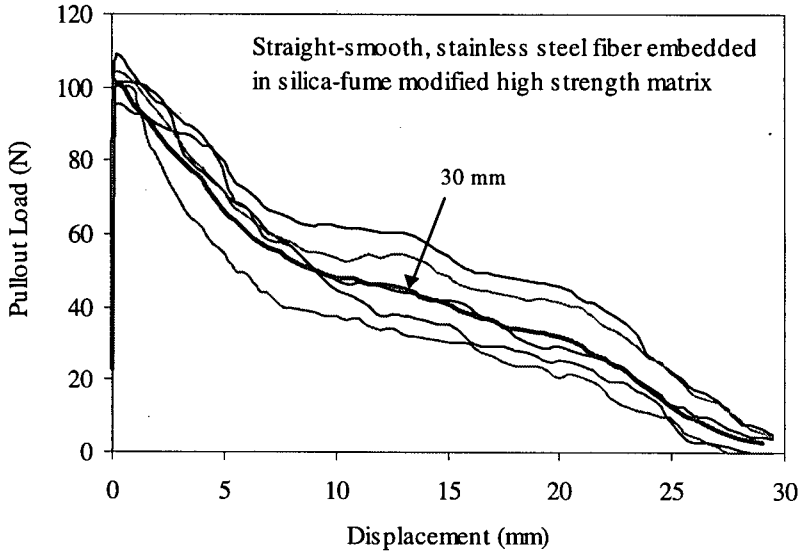

Figure 4.1.12: Pullout response of straight-smooth, stainless steel fibers embedded in silica fume modified high strength matrix

4.1.5.1 Influence of Silica-fume Modification

To study the influence of matrix modification by silica-fume on the fiber pullout response, pullout curves for 30 mm long straight-smooth, stainless steel fibers pulled out from two different types of matrices are compared in Figure 4.1.13. These matrices are:

i. High strength matrix

ii. Silica fume modified high strength matrix

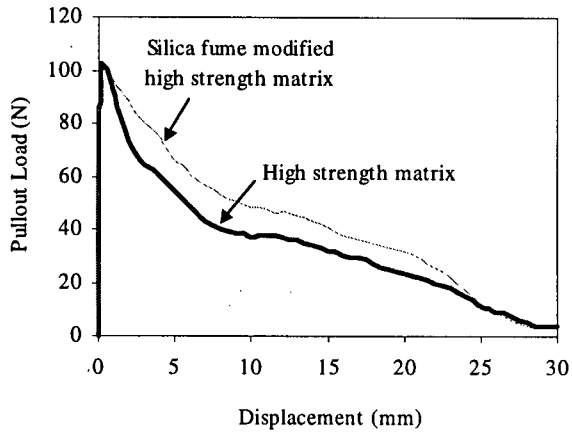

Figure 4.1.13: Pullout response of straight-smooth, stainless steel fibers embedded in high strength matrix and silica fume modified high strength matrix

In Figure 4.1.13, it can be seen that the fiber pullout response was superior in the case of the silica fume modified high strength matrix. Disparity in the fiber pullout response with the above two matrix systems could be the result of one or more of the following factors: chemical nature of the interface, shrinkage behavior of the matrix, and the physical characteristics of the sliding surfaces during fiber pullout.

4.1.6 Straight, Smooth Polypropylene Fibers Embedded in Normal Strength Matrix

The experimental pullout response of straight, smooth polypropylene fibers embedded in a normal strength matrix was investigated and the corresponding results are reported here. The mix proportion used was - water : cement : sand : aggregate = 0.5 : 1.0 : 2.5 : 2.0. Cement used was of CSA Type 10 specification. The above mix proportion gave an average 28-day compressive strength of about 36 MPa, as determined by testing five 200 mm x 100 mm ϕ cylinders. Fibers with embedded lengths equal to 5 mm, 15 mm, 30 mm, and 60 mm on both sides of the crack were chosen, and for each fiber length, five to six fibers were tested for pullout. Figure 4.1.14 shows the pullout response of fibers tested. The average pullout curves have also been plotted in the same figure (thick lines). Results from these pullout tests are tabulated in Table 4.1.6.

Table 4.1.6: Experimental pullout test results for straight, smooth polypropylene fibers embedded in normal strength matrix

Fiber	Matrix	Embedded Fiber Length (mm)	Pullout Response		
			P_{peak} (N)	δ_{peak} (mm)	E_{total} (N-mm)
Straight, smooth polypropylene	Normal strength	5	12.4 (2.00)#	0.047 (0.02)	28 (3)
		15	14.9 (1.25)	0.300 (0.24)	139 (59)
		30	17.6 (1.00)	1.251 (0.89)	306 (46)
		60	22.3 (2.70)	2.983 (1.46)	894 (87)

P_{peak} – Peak load; δ_{peak} – Displacement at peak pullout load; E_{total} – Total pullout energy
- Figures in brackets indicate standard deviation

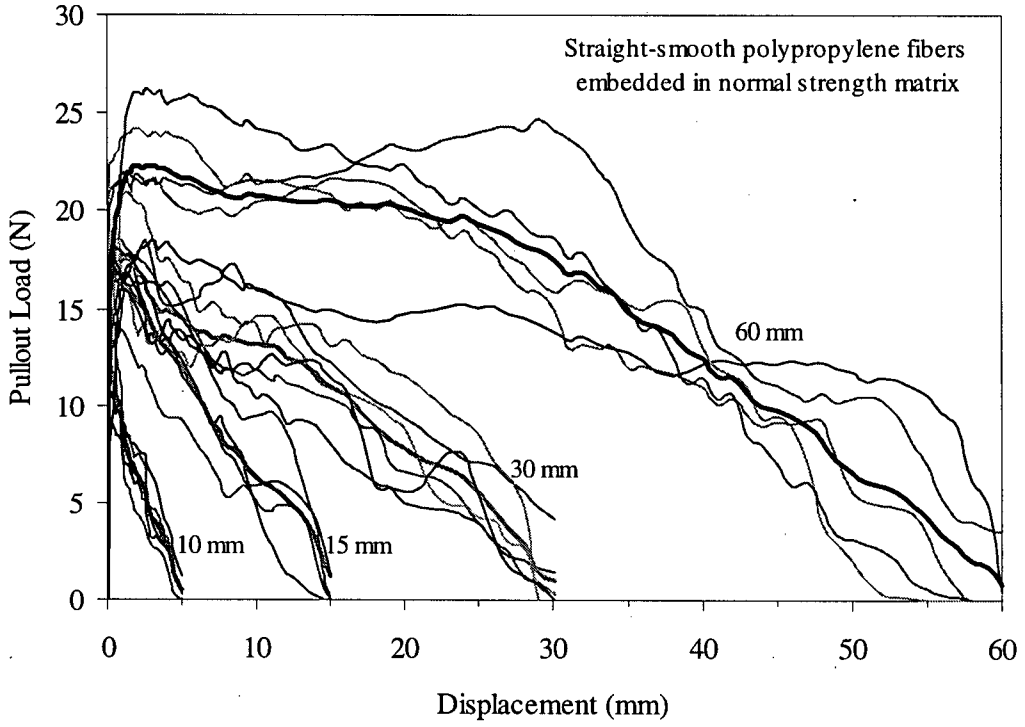

Figure 4.1.14: Pullout response of straight, smooth polypropylene fibers embedded in normal strength matrix

4.1.6.1 Influence of Fiber Length

It can be seen that increase in fiber length led to an increase in peak pullout loads. However, the rate of increase in peak pullout load diminished with increase in fiber length. The peak pullout load reached an asymptote at longer fiber lengths as shown in the Figure 4.1.15. Also, it can be noticed that for any given fiber length, the peak pullout load attained for polypropylene fiber was much lower in comparison to that for steel fiber (compare Figure 4.1.3 and Figure 4.1.15). Furthermore, for polypropylene fibers, the asymptotic value of pullout stress was reached at a much smaller fiber length in comparison to that for steel fibers.

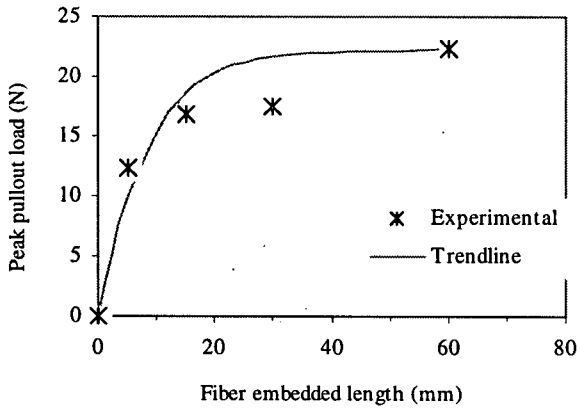

Figure 4.1.15: Embedded fiber length vs. peak pullout load curve for straight, smooth polypropylene fibers

4.2 Conclusions

- Increase in fiber length led to an increase in peak pullout load. However, at long fiber lengths, the peak pullout load reached an asymptote.
- For a given fiber length, an increase in fiber surface roughness increased the peak pullout load. However, disparity between the peak pullout load for a smooth steel fiber and a rough steel fiber decreased with increase in fiber length. The asymptotic value of peak pullout load attained at long fiber lengths in the case of rough steel fiber was very similar to that obtained for smooth steel fiber. The displacement corresponding to peak pullout load and the total energy absorption were also found to increase with increase in surface roughness.
- For a given fiber length, peak pullout loads decreased substantially when steel fibers were pulled out from non-shrink grout matrix. The observed decrease in peak pullout load is likely related to the shrinkage behavior of the non-shrink grout matrix.
- The post-peak pullout response for steel fibers embedded in high-strength matrix was superior in comparison to that for steel fibers embedded in normal strength matrix. This observation implied that frictional resistance in the former was greater.

- For any given fiber length, the peak pullout load attained for polypropylene fiber was much lower in comparison to that for steel fiber. Also, for polypropylene fibers, the asymptotic value of pullout stress was reached at a much smaller fiber length in comparison to that for steel fibers.

Chapter 5

Progressive Debonding Model for Fiber Pullout

5.0 Introduction

Both one-sided and two-sided pullout specimens are commonly used to investigate the fiber-matrix interfacial properties [108]. In a two-sided pullout test specimen, a matrix crack is simulated at the center of the specimen. A single fiber embedded on both sides of the simulated crack provides resistance to the crack opening. Figure 5.0.1 depicts one side of a two-sided pullout test specimen. A fiber of radius a and length $2L$ is embedded at the center of the matrix coaxial cylinder of radius b. The gripping fixtures of the testing machine hold the matrix coaxial cylinders on each side of the simulated crack, and the specimen is subjected to tensile stress in the axial direction (normally at a constant rate of displacement). The pullout load versus displacement response is recorded to yield the pullout curve.

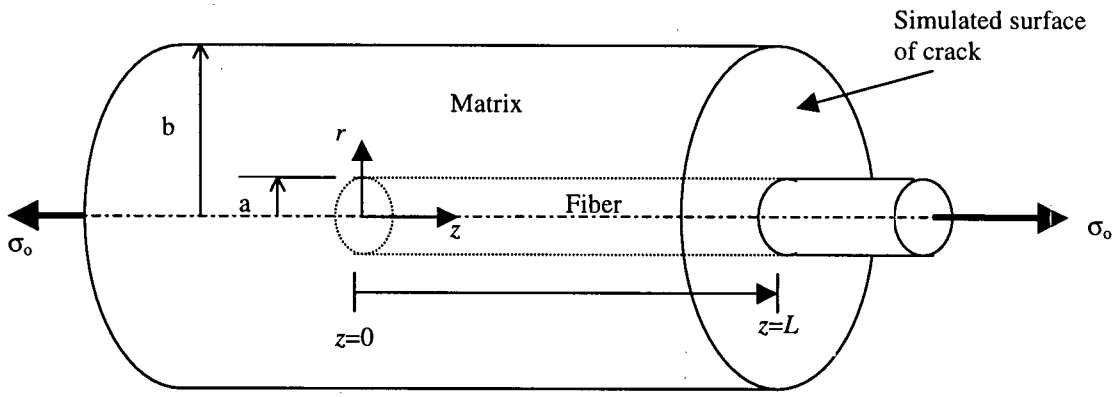

Figure 5.0.1: Single fiber embedded in concrete matrix. Figure depicts one side of a two-sided pullout test specimen

Interpretation of pullout curves is commonly carried out using the analytical models based on the shear-lag analysis [52-78]. The shear-lag analysis assumes that the extensional stresses in the matrix are small relative to those in the fiber and that the shear stresses in the fiber are small

compared to those in the matrix [109]. Some important shear-lag models [53-56,61,67,68] that are widely used to study the interfacial debonding phenomena in the problem of fiber pullout were reviewed in Chapter 2. Table 5.0.1 shows the important features captured by these models. A brief discussion on these models follows.

Table 5.0.1: Various parameters taken into consideration in the theoretical fiber pullout models

Parameter	Greszczuk (53)	Lawrence (55)	Takaku &Arridge (54)	Nammur et al. (61)	Gopalaratnam & Shah (56)	Hsueh (67,68)
Adhesional shear bond	√	√	√	√	√	√
Progressive debonding	×	√	×	√	√	√
Dependence of debond stress on fiber length	×	√	×	×	×	√
Poisson's effect (Non-constant interfacial frictional shear bond)	×	×	√	×	×	√
Evolution of interfacial properties during pullout	×	×	×	×	×	×

× - not considered √ - considered

Models by Greszczuk [53], Takaku and Arridge [54], Lawrence [55], Gopalaratnam and Shah [56], Naamur et al. [61] and Hsueh [67,68] acknowledge the existence of the adhesional shear bond at the bonded interface. Furthermore, these models use a strength based criterion to govern interfacial debonding (i.e., interfacial debonding is assumed to occur when the interfacial shear stress equals the adhsesional shear bond strength of the interface). Greszczuk [53] was the first to derive an interfacial debonding criterion using the shear-lag theory. Progressive debonding was not considered in his analysis, since he postulated that catastrophic debonding would occur with the initiation of debonding. Thus, his solution did not consider the stabilization of the debonding process that may take place due to the existence of frictional shear bond at the debonded interface. For the first time, existence of frictional shear bond at the debonded interface was included in the analysis by Lawrence [55]. Assuming existence of adhesional

bonded interface and a constant frictional shear bond at the debonded interface, Lawrence [55] derived a solution for progressive debonding. Later, Gopalaratnam and Shah [56] and Nammur et al. [61] also developed solutions for progressive debonding with an assumption of a constant frictional shear bond at the debonded interface. Note that the magnitude of the frictional shear bond at the debonded interface is actually dependent upon the interfacial contact stress and the coefficient of friction of the sliding surfaces. Since the interfacial contact stress varies with the fiber axial force and coefficient of friction may vary with the sliding distance, it is not necessary that the frictional shear bond remain constant over the debonded region. Therefore, the assumption of a constant frictional shear bond constitutes a major limitation of the above-mentioned progressive debonding models.

It is also important to include the influence of Poisson's contraction of the fiber in the analysis. This is because Poisson's contraction of the fiber reduces the net contact stress at the interface and, in turn, the frictional shear bond. Models by Lawrence [55], Gopalaratnam and Shah [56], and Naamur et al. [61] do not include the influence of Poisson's effect in the analysis. Neither do these models explicitly include interfacial properties such as coefficient of friction and interfacial contact stress in the analysis. These constitute major limitations of the above mentioned models. It must be noted that the dependence of interfacial frictional bond on the interfacial contact stress and the coefficient of friction warrants explicit inclusions of these parameters into the analysis. Only, the models by Takaku and Arridge [54] and Hsueh [67,68] include both parameters in the analysis. The model by Takaku and Arridge [54] was the first to consider the influence of Poisson's contraction of fiber in the analysis. However, these aspects were considered in the analysis only after the occurrence of complete interfacial debonding (i.e., in the fiber pullout case as explained later). Thus, the influence of Poisson's contraction during progressive debonding remained unaccounted, which constituted a major limitation of this model. The model by Hsueh [54] considers Poisson's effect during progressive debonding, however the analysis and the closed-form solutions presented are complex to use.

During the process of fiber pullout, considerable matrix wear close to the interface is expected to occur. In such a scenario, the interfacial coefficient of friction would diminish with increase in pullout distance. Therefore, to objectively characterize the fiber-matrix interface, variation in the interfacial coefficient of friction with pullout distance must be taken into consideration.

Surprisingly, the existing theoretical fiber pullout models have not addressed this important aspect. In light of this fact, it may be possible to explain why the predictions obtained from the existing pullout models deviate considerably from the experimental results. To appreciate this fact profoundly, in what follows, predictions from the pullout models by Takaku and Arridge [54], Gopalaratnam and Shah [56] and Hsueh [67,68] are compared with the experimental results. Figure 5.0.2 compares the experimental pullout curve for a steel fiber reported by Gopalaratnam and Shah [56] with the predicted responses using the models mentioned above. Note that the fiber diameter was 0.25 mm and the fiber length was 12.5 mm. For making predictions using the models by Takaku and Arridge [54][1] and Hsueh [67,68][2], the fiber length was assumed to be 12 mm, since the source codes were written to accept only integer values for fiber length. In the figure it can be seen that all three theoretical predictions deviate considerably from the experimental curve. The reason for such wide disparity could possibly be attributed to the fact that these models disregard the evolution of interfacial properties during the pullout process.

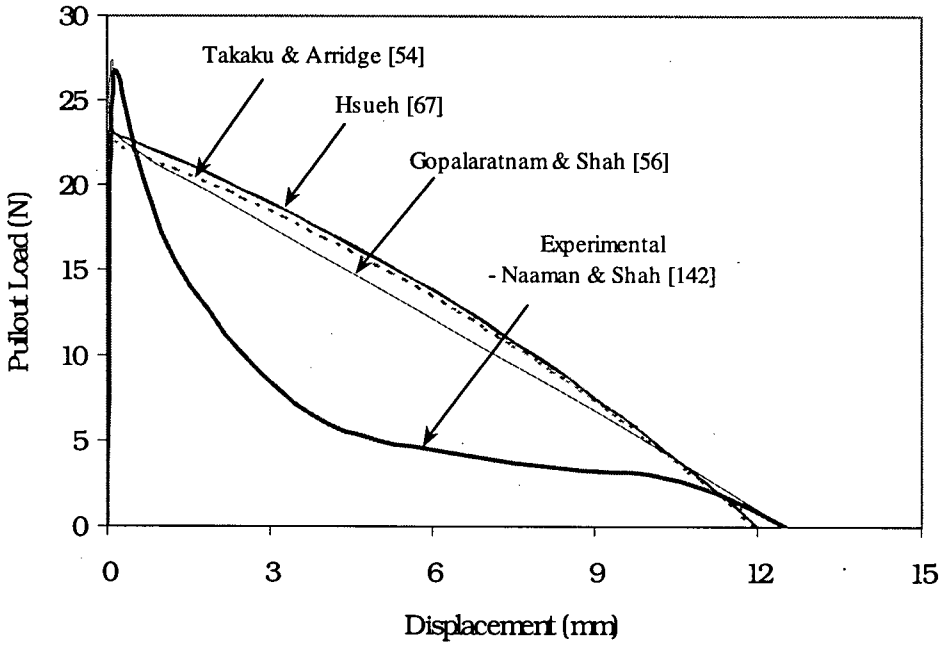

Figure 5.0.2: A comparison between the experimental pullout response for a steel fiber with the predicted responses using the existing pullout models. The experimental pullout response is by Naaman and Shah [142]

[1] The source code for Takaku and Arridge model [54] is attached in Appendix A.
[2] The source code for Hsueh model [67,68] is attached in Appendix B.

The above discussion brings to attention the inadequacy of the existing fiber pullout models, and also the fact that a need exists for a model that realistically captures the physical phenomenon occurring during the process of fiber pullout. A new fiber pullout model is proposed below that considers the evolution of the interfacial coefficient of friction during the process of fiber pullout. Additionally, the proposed model takes into account the following aspects that are either considered or ignored in the earlier models:

- Dependence of the initial debonding stress on the embedded fiber length.
- Radial dependence of the axial stress in the matrix.
- Explicit inclusion of the interfacial properties such as the contact stress and the coefficient of friction.
- Poisson's effect (in the event of a debonded fiber).

5.1 The Proposed Progressive Debonding Model

Consider a fiber of radius a and length L embedded at the center of the matrix coaxial cylinder with inner radius a and outer radius b, as shown in Figure 5.0.1. A cylindrical coordinate system is selected so that the z-axis corresponds to the fiber axial direction and the r-axis corresponds to the radial direction. The embedded end of the fiber is located at $z=0$, and the other end where the fiber exits the matrix is located at $z=L$. The exit-end of the fiber (i.e., at $z=L$) is subjected to the tensile stress, σ_o, as shown in Figure 5.0.1. Both fiber and matrix are assumed to be elastic. Transfer of stress between the fiber and the matrix is via interfacial shear stresses. The entire pullout process can be divided into three stages [106], as shown in Figure 5.1.1:

i. *Stage 1 - Fiber completely bonded along the length of the fiber:* During stage 1, fiber and matrix displacements at the interface remain compatible, and the resistance to fiber pullout is derived from the adhesional shear stresses at the interface. At the end of stage 1, debonding of the interface is initiated at the location where the fiber enters the matrix.

ii. *Stage 2 - Fiber partially bonded along its embedded length:* During stage 2, progressive debonding of the interface is initiated at the location where the fiber exits the matrix. The

adhesional shear stresses at the bonded interface and the frictional shear stresses at the debonded interface resist the fiber pullout. At the end of stage 2, the fiber is completely debonded along its embedded length.

iii. *Stage 3 - Fiber completely debonded over its embedded length and pulling out:* At the end of stage 2, pullout of the fiber is initiated, and thereafter, the interfacial frictional shear stresses resist the pullout of fiber from the matrix.

Analysis for these three stages of the pullout process is presented below.

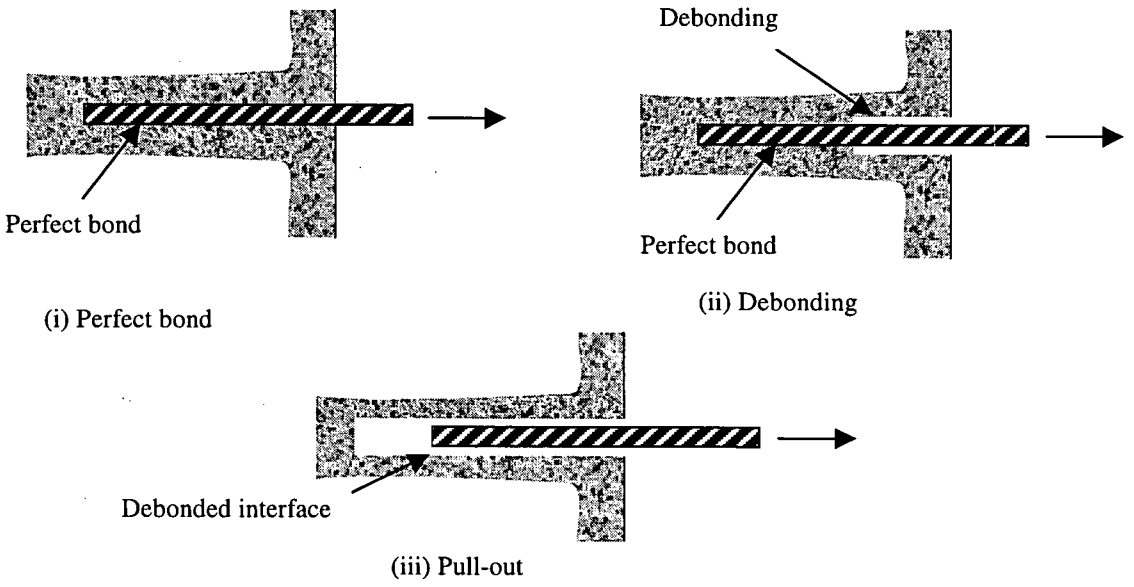

Figure 5.1.1: The principle of a single fiber pullout test – The three stages of pullout process (Stang and Shah [106])

5.1.1 Stage 1: Fiber Completely Bonded Along Its Entire Embedded Length

Consider the case where the fiber is completely bonded to the matrix (i.e., fiber and matrix displacements remain compatible at the interface) over its entire embedded length as shown in Figure 5.1.2. σ_o represents the fiber pullout stress applied at the emerging fiber end. The essence of the formulation presented below is similar to the one presented earlier by Hsueh [67,68] in light of the fact that the analysis takes into consideration the radial dependence of the axial stresses in the matrix. The models by Greszczuk [53], Lawrence [55], Takaku and Arridge [54], Nammur et al. [61] and Gopalaratnam and Shah [56] do not consider the radial dependence of the axial stress in the matrix.

Assuming that the shear force in the matrix decreases linearly in the radial direction with a maximum at the fiber-matrix interface (i.e., at $r=a$) and zero at the free surface of the coaxial cylinder (i.e., at $r=b$), the matrix shear stress, τ_m, at any radial distance, r, can be expressed as:

$$\tau_m = \left[\frac{b-r}{b-a}\right]\frac{a}{r}\tau_a \qquad \text{for } r \geq b \qquad 5.1$$

where τ_a represents the shear stress at the interface, i.e., at $r=a$. The above equation satisfies the equilibrium in the axial direction, approximately, when the fiber diameter, a, is small in comparison to the radial dimension, b and the axial stress gradient in the matrix is small. In the models by Gopalaratnam and Shah [56] and Hsueh [57], the formulation of the stress transfer problem is based on the assumption that the shear stress in the matrix varies inversely with the radial distance (with a maximum at the interface). In the model by Greszczuk [53], the problem formulation is based on the shear deformation of a thin layer of interface. Based on the earlier work by Cox [52], the models by Lawrence [55] and Takaku and Arridge [54] use a rather awakard scheme to define the shear deformation of the matrix material.

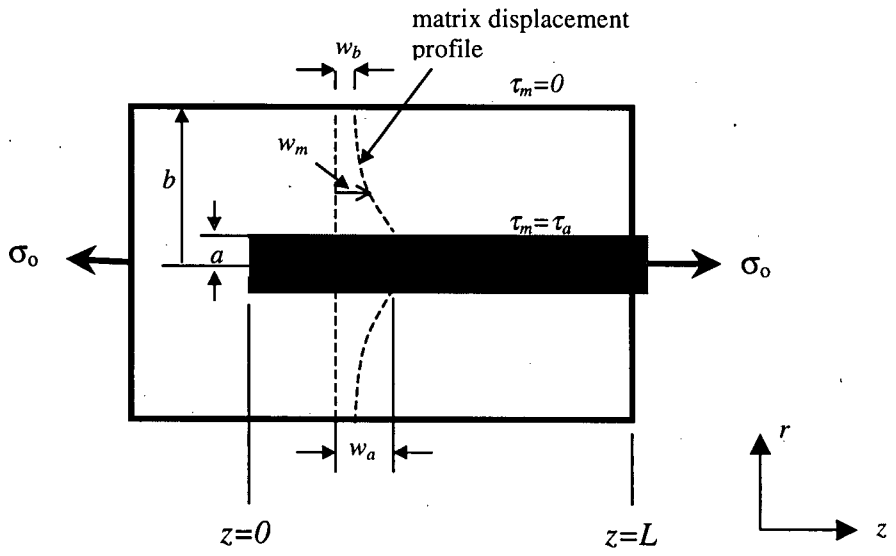

Figure 5.1.2: Fiber completely bonded over its embedded length

If w_m represents the displacement of matrix in the axial direction, the corresponding shear stress in the matrix (ignoring the radial displacements) is given by:

$$\tau_m = \frac{E_m}{2(1+\upsilon_m)} \frac{dw_m}{dr} \tag{5.2}$$

Combining Equations 5.1 and 5.2, and integrating:

$$\frac{\tau_a a}{(b-a)} \int_a^b \frac{(b-r)}{r} dr = \frac{E_m}{2(1+\upsilon_m)} \int_{w_a}^{w_b} dw_m \tag{5.3}$$

where w_a and w_b are the axial displacement in the matrix at $r=a$ and $r=b$, respectively. Solving the above equation, the interfacial shear stress, τ_a, can be written as:

$$\tau_a = \frac{E_m (w_b - w_a)}{2(1+\upsilon_m) a \left[\frac{b}{(b-a)} \log\left(\frac{b}{a}\right) - 1 \right]} \tag{5.4}$$

Combining 5.1 and 5.4, the shear stress in the matrix, τ_m, at any radial distance, r, is given by:

$$\tau_m = \frac{E_m (w_b - w_a)(b-r)}{2(1+\upsilon_m) r \left[b \log\left(\frac{b}{a}\right) - (b-a) \right]} \tag{5.5}$$

Combining Equations 5.2 and 5.5 and integrating, the axial displacement in the matrix, w_m, can be written as:

$$w_m = w_a + \frac{w_b - w_a}{b \log\left(\frac{b}{a}\right) - (b-a)} \left[b \log\left(\frac{r}{a}\right) + a - r \right] \tag{5.6}$$

Ignoring the Poisson's effect (i.e., treating the problem as one-dimensional), the axial stress in the matrix, σ_m, (in the z direction) is given by:

$$\sigma_m = E_m \frac{dw_m}{dz} \tag{5.7}$$

Combining Equations 5.6 and 5.7, the axial stress in the matrix at any radial distance, r, is given by:

$$\sigma_m = \frac{E_m}{E_f}\sigma_f + \frac{\sigma_b - \frac{E_m}{E_f}\sigma_f}{\left[b\log\left(\frac{b}{a}\right) - (b-a)\right]}\left[b\log\left(\frac{r}{a}\right) + a - r\right] \tag{5.8}$$

The above equation describes the radial dependence of the axial stress in the matrix. As mentioned earlier, the models presented in the References 53, 55, 54, 61 56 do not consider the radial dependence of the axial stress in the matrix.

The condition for mechanical equilibrium between the external applied stress, σ_0, and the internal stress distribution at any section can be written as:

$$\sigma_f + \frac{2}{a^2}\int_a^b \sigma_m r\, dr = \sigma_0 \tag{5.9}$$

Combining Equations 5.8 and 5.9, the axial stress in the matrix, $\sigma_{m=b}$ is obtained as:

$$\sigma_b = \frac{\sigma_o}{\eta} - \left[\frac{\gamma + \alpha - \gamma\eta\alpha}{\gamma\eta}\right]\sigma_f \tag{5.10}$$

where,

$$\alpha = \frac{E_m}{E_f}$$

$$\gamma = \frac{a^2}{b^2 - a^2}$$

$$\eta = \frac{2}{a^2\left[b\log\left(\frac{b}{a}\right) - (b-a)\right]}\left\{b\left[\frac{b^2}{2}\log\left(\frac{b}{a}\right) - \frac{(b^2-a^2)}{4}\right] + \frac{a(b^2-a^2)}{2} - \frac{(b^3-a^3)}{3}\right\}$$

Now, considering the equilibrium between the axial stress in the fiber and the interfacial shear stress:

$$\frac{d\sigma_f}{dz} = -\frac{2\tau_a}{a} \qquad 5.11$$

Combining Equations 5.4 and 5.11:

$$\frac{d\sigma_f}{dz} = -\theta\, E_m (w_b - w_a) \qquad 5.12$$

where

$$\theta = \left\{a^2(1+\upsilon_m)\left[\frac{b}{(b-a)}\log\left(\frac{b}{a}\right) - 1\right]\right\}^{-1}$$

Differentiating the above equation:

$$\frac{d^2\sigma_f}{dz^2} = -\theta\, E_m\left[\frac{dw_b}{dz} - \frac{dw_a}{dz}\right] \qquad 5.13$$

From which we obtain:

$$\frac{d^2\sigma_f}{dz^2} = -\theta E_m\left[\frac{\sigma_b}{E_m} - \frac{\sigma_f}{E_f}\right] \qquad 5.14$$

Substituting for σ_b from Equation 5.10 in Equation 5.14:

$$\frac{d^2\sigma_f}{dz^2} - \left[\frac{\theta}{\gamma\eta}(\gamma+\alpha-\gamma\eta\alpha)+\alpha\theta\right]\sigma_f = -\frac{\theta}{\eta}\sigma_o \qquad 5.15$$

The above equation is a second order linear differential equation and it dictates the stress transfer between the fiber and the matrix for a bonded interface.

5.1.1.1 Fiber Axial Stress Distribution, σ_f

The solution to the above differential equation represents the axial stress distribution over the embedded fiber length ($z \le L$) prior to debonding and at initiation of debonding. With boundary conditions, $\sigma_f = \sigma_o$ at $z=L$ and $\sigma_f = 0$ at $z=0$, the solution of the differential equation becomes:

$$\sigma_f = \frac{\sigma_o}{\gamma+\alpha-\gamma\eta\alpha+\alpha\eta}\left[(\alpha-\gamma\eta\alpha+\alpha\eta)\frac{\sinh(\beta z)}{\sinh(\beta L)} - \gamma\frac{\sinh[\beta(L-z)]}{\sinh(\beta L)} + \gamma\right] \qquad 5.16$$

where, $\beta = \left[\frac{\theta}{\gamma\eta}(\gamma+\alpha-\gamma\eta\alpha)+\alpha\theta\right]^{1/2}$

For any fiber pullout stress, σ_o, that is less than or equal to the initial fiber debonding stress, σ_d, Equation 5.16 represents the fiber axial stress distribution, σ_f.

5.1.1.2 Interfacial Shear Stress Distribution, τ_a

The interfacial shear stress, τ_a distribution can be obtained by combining Equations 5.11 and 5.16:

$$\tau_a = \frac{-a\beta\sigma_o}{2(\gamma+\alpha-\gamma\eta\alpha+\alpha\eta)}\left[(\alpha-\gamma\eta\alpha+\alpha\eta)\frac{\cosh(\beta z)}{\sinh(\beta L)}+\gamma\frac{\cosh[\beta(L-z)]}{\sinh(\beta L)}\right] \quad 5.17$$

For any fiber pullout stress, σ_o, that is less than or equal to the initial fiber debonding stress, σ_d, Equation 5.17 represents the interfacial shear stress distribution, τ_a along the embedded fiber length.

5.1.1.3 Fiber Displacement, U_b

Fiber displacements, U_b, when the fiber is completely bonded over its embedded length is obtained by integrating the strains along the fiber length:

$$U_b = \frac{\sigma_o}{E_f(\gamma+\alpha-\gamma\eta\alpha+\alpha\eta)}\int_0^L\left[(\alpha-\gamma\eta\alpha+\alpha\eta)\frac{\sinh(\beta z)}{\sinh(\beta L)}-\gamma\frac{\sinh[\beta(L-z)]}{\sinh(\beta L)}+\gamma\right]dz \quad 5.18$$

Solving:

$$U_b = \frac{\sigma_o}{E_f(\gamma+\alpha-\gamma\eta\alpha+\alpha\eta)}\left[(\alpha-\gamma\eta\alpha+\alpha\eta-\gamma)\frac{\cosh(\beta L)-1}{\beta\sinh(\beta L)}+\gamma L\right] \quad 5.19$$

For a two-sided pullout test, fiber displacement is given by:

$$U_b = \frac{2\sigma_o}{E_f(\gamma+\alpha-\gamma\eta\alpha+\alpha\eta)}\left[(\alpha-\gamma\eta\alpha+\alpha\eta-\gamma)\frac{\cosh(\beta L)-1}{\beta\sinh(\beta L)}+\gamma L\right] \quad 5.20$$

where, the total fiber length is equal to $2L$ and embedded fiber length on each side of the pullout specimen is equal to L.

5.1.1.4 Debonding Criterion and Initial Debonding Stress, σ_d

Using the maximum shear stress as the debonding criterion, the applied pullout stress, σ_d, required to initiate debonding can be obtained from Equation 5.17 by putting $\tau_a=\tau_s$ at $z=L$ (τ_s=shear strength of the interface). Thus, the debonding criterion can be written as:

$$\sigma_d = -\frac{2\tau_s(\gamma+\alpha-\gamma\eta\alpha+\alpha\eta)}{a\beta}\left[\frac{(\alpha-\gamma\eta\alpha+\alpha\eta)\cosh(\beta L)+\gamma}{\sinh(\beta L)}\right]^{-1} \qquad 5.21$$

Thus, σ_d, in the above equation represents the fiber pullout stress, σ_o, at which interfacial debonding initiates. The above equation also depicts dependence of the initial debonding stress on fiber length. On plotting σ_d as a function of L, it can be seen that with increase in the fiber length, the initial debonding stress increases and attains an asymptotic value at long fiber lengths. Some earlier works on the problem of fiber pullout [54,55,68,93,176] also demonstrate the dependence of the initial debonding stress on the embedded fiber length.

5.1.2 Stage 2: Fiber Partially Debonded Along Its Embedded Length

Takaku and Arridge [54] assume fiber and matrix to be held together in a shrink-fit configuration [224] to derive a differential equation of stress transfer for a debonded interface. However, they reserve the application of this equation to the case of a completely debonded fiber (i.e., stage 3). In the following, the application of their analysis is extended to the case of a partially debonded fiber.

After the inception of interfacial debonding, a debonded zone of length l_d is created as shown in Figure 5.1.3. During partial debonding, fiber pullout is resisted by the adhesional shear stresses acting at the bonded interface of length L-l_d, and the frictional shear stresses acting at the debonded interface of length l_d. The interfacial frictional shear stress at the debonded zone is mobilized because of the existence of the interfacial contact pressure resulting due to matrix shrinkage [1,106]. The fiber axial stress, σ_f, at the junction of the bonded and the debonded zone is termed here as the progressive debonding stress, σ_d, and as a first approximation, σ_d for any debond length, l_d, can be obtained by replacing L by L-l_d in Equation 5.21.

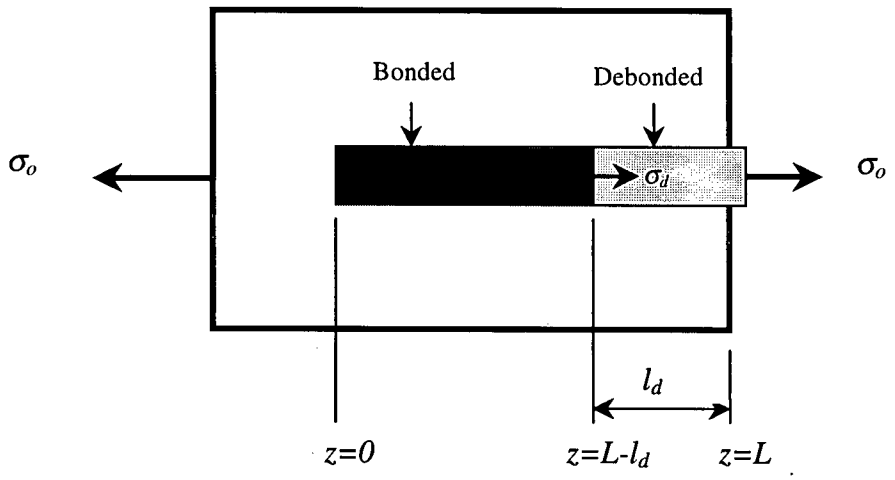

Figure 5.1.3: Fiber partially debonded along its embedded length

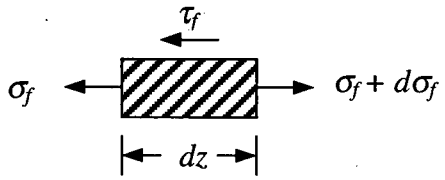

Figure 5.1.4: Free body diagram for a fiber element of length dz

Over the debonded interface, transfer of stress between fiber and encapsulating matrix takes place through interfacial frictional shear stresses, τ_f. Equilibrium between the fiber axial stress, σ_f, and the interfacial frictional shear stress, τ_f, is given by (Figure 5.1.4):

$$\frac{d\sigma_f}{dz} = -\frac{2\tau_f}{a} \tag{5.22}$$

From Coulomb's Law, we obtain:

$$\frac{d\sigma_f}{dz} = -\frac{2\tau_f}{a} = -\frac{2\mu\sigma_{cp}}{a} \tag{5.23}$$

where μ is the interfacial coefficient of friction, and σ_{cp} is the contact pressure between fiber and matrix at the interface after the fiber has undergone Poisson's contraction.

In a shrink-fit configuration [224], the radial fiber-matrix misfit mobilizes radial contact pressure at the fiber-matrix interface. The fiber-matrix misfit is the difference between the fiber radius and the matrix hole radius after shrinkage in the absence of fiber. The fiber-matrix misfit is also equal to the sum of the increase in the inner radius of the matrix cylinder and the decrease in the radius of the fiber in the presence of radial contact pressure. For an unstressed fiber, the relationship between the interfacial contact pressure, σ_c, and the radial fiber-matrix misfit, δ_r, can be written as [224]:

$$\sigma_c = -\frac{\delta_r}{\frac{a}{E_m}\left[\frac{a^2+b^2}{b^2-a^2}+\upsilon_m\right]+\frac{a}{E_f}\left[1-\upsilon_f\right]} \tag{5.24}$$

Due to the Poisson's effect, the radial fiber-matrix misfit and the interfacial contact pressure decreases when fiber is stressed in the axial direction. For an axially stressed fiber, reduction in fiber-matrix misfit is given by:

$$\Delta a = a\upsilon_f \frac{\sigma_f}{E_f} \tag{5.25}$$

where σ_f is the fiber axial stress. The resultant contact pressure, σ_{cp}, at the interface can be obtained by substituting δ_r-Δa for δ_r and a-Δa ($\equiv a$) for a in the Equation 5.24:

$$\sigma_{cp} = -\frac{(\delta_r - \Delta a)}{\frac{a}{E_m}\left[\frac{a^2+b^2}{b^2-a^2}+\upsilon_m\right]+\frac{a}{E_f}\left[1-\upsilon_f\right]} \qquad 5.26$$

Substituting for Δa in the above equation:

$$\sigma_{cp} = \frac{-\delta_r}{\frac{a}{E_m}\left[\frac{a^2+b^2}{b^2-a^2}+\upsilon_m\right]+\frac{a}{E_f}\left[1-\upsilon_f\right]} + \frac{\upsilon_f \sigma_f}{\frac{E_f}{E_m}\left[\frac{a^2+b^2}{b^2-a^2}+\upsilon_m\right]+\left[1-\upsilon_f\right]} \qquad 5.27$$

Thus, when tensile stress in the fiber is σ_f, the resultant contact pressure, σ_{cp}, at the interface is given by:

$$\sigma_{cp} = \sigma_c + \omega\sigma_f \qquad 5.28$$

where $\omega = \dfrac{\upsilon_f}{\frac{E_f}{E_m}\left[\frac{a^2+b^2}{b^2-a^2}+\upsilon_m\right]+\left[1-\upsilon_f\right]}$

Since Takaku and Arridge [54] developed their model for stiff fibers, the constant ω was defined differently in their model.

Substituting for σ_{cp} in the equation of stress transfer (Equation 5.23):

$$\frac{d\sigma_f}{dz} = -\frac{2\mu}{a}\left[\sigma_c + \omega\sigma_f\right] \qquad 5.29$$

Rearranging:

$$\frac{d\sigma_f}{dz}+\frac{2\mu}{a}\omega\sigma_f=-\frac{2\mu}{a}\sigma_c \qquad 5.30$$

The above equation is a first order linear differential equation, and it dictates stress transfer between fiber and matrix over a debonded interface. This equation was first derived by Takaku and Arridge [54], and was applied to the case of a completely debonded fiber. In the following, the application of this equation is extended to the case of a partially debonded fiber.

5.1.2.1 Fiber Axial Stress Distribution, σ_f

The solution of the above differential equation represents the axial stress, σ_f over the debonded fiber length (i.e., $L \geq z \geq L\text{-}l_d$). With the boundary condition, $\sigma_f=\sigma_d$ at $z=L\text{-}l_d$, the solution is obtained as:

$$\sigma_f=-\frac{\sigma_c}{\omega}+\left[\sigma_d+\frac{\sigma_c}{\omega}\right]e^{\frac{2\omega\mu(L-l_d)}{a}}e^{\frac{-2\omega\mu z}{a}} \qquad 5.31$$

The fiber axial stress, σ_f, along the bonded region ($z \leq L\text{-}l_d$) can be obtained by replacing L by $L\text{-}l_d$ and σ_o by σ_d in Equation 5.16.

5.1.2.2 Interfacial Frictional Shear Stress Distribution, τ_f

From Coulomb's law, the distribution of interfacial frictional shear stress, τ_f over the debonded fiber length can be obtained as:

$$\tau_f=\mu\sigma_{cp}=\mu(\sigma_c+\omega\sigma_f) \qquad 5.32$$

The above equation depicts that the dependence of interfacial frictional shear stress, τ_f, on fiber axial stress, σ_f. Substituting for σ_f, the interfacial frictional shear stress, τ_f, over the debonded region ($L \geq z \geq L\text{-}l_d$) is obtained as:

$$\tau_f = \mu\omega\left[\sigma_d + \frac{\sigma_c}{\omega}\right] e^{\frac{2\omega\mu(L-l_d)}{a}} e^{\frac{-2\omega\mu z}{a}} \qquad 5.33$$

The interfacial shear stress, τ_a, along the bonded region ($z \le L\text{-}l_d$) can be obtained by replacing L by $L\text{-}l_d$ and σ_o by σ_d in Equation 5.17.

5.1.2.3 Pullout Stress versus Debond Length Relationship, σ_o *vs.* l_d

The relationship between the fiber pullout stress, σ_o, and the debond length, l_d, is obtained by using Equation 5.31 at $z=L$:

$$\sigma_o = -\frac{\sigma_c}{\omega} + \left[\sigma_d + \frac{\sigma_c}{\omega}\right] e^{\frac{-2\mu\omega l_d}{a}} \qquad 5.34$$

Note that the fiber pullout stress, σ_o, is equal to the initial debonding stress, σ_d, when the debond length is equal to zero, i.e., $\sigma_o=\sigma_d$ when $l_d=0$.

5.1.2.4 Fiber Displacement versus Debond Length Relationship, U_{pd} *vs.* l_d

The total fiber displacement, U_{pd}, can be obtained by integrating the fiber strains along the embedded fiber length:

$$U_{pd} = \frac{\sigma_d}{E_f(\gamma+\alpha-\gamma\eta\alpha+\alpha\eta)} \int_0^{L-l_d} \left\{(\alpha-\gamma\eta\alpha+\alpha\eta)\frac{\sinh(\beta z)}{\sinh[\beta(L-l_d)]} - \gamma\frac{\sinh[\beta(L-l_d-z)]}{\sinh[\beta(L-l_d)]} + \gamma\right\} dz$$

$$+ \frac{1}{E_f} \int_{L-l_d}^{L} \left\{-\frac{\sigma_c}{\omega} + \left[\sigma_d + \frac{\sigma_c}{\omega}\right] e^{\frac{2\omega\mu(L-l_d)}{a}} e^{\frac{-2\omega\mu z}{a}}\right\} dz \qquad 5.35$$

Solving:

$$U_{pd} = \frac{\sigma_d}{E_f(\gamma+\alpha-\gamma\eta\alpha+\alpha\eta)}\left[(\alpha-\gamma\eta\alpha+\alpha\eta-\gamma)\frac{\cosh[\beta(L-l_d)]-1}{\beta\sinh[\beta(L-l_d)]}+\gamma(L-l_d)\right] - \frac{\sigma_c l_d}{E_f\omega} - \frac{a}{2E_f\mu\omega}\left[\sigma_d+\frac{\sigma_c}{\omega}\right]\left[e^{\frac{-2\mu\omega l_d}{a}}-1\right] \quad 5.36$$

and, for a two-sided pullout problem, the total fiber displacement, U_{pd}, assuming debonding occurs symmetrically, can be derived as:

$$U_{pd} = \frac{2\sigma_d}{E_f(\gamma+\alpha-\gamma\eta\alpha+\alpha\eta)}\left[(\alpha-\gamma\eta\alpha+\alpha\eta-\gamma)\frac{\cosh[\beta(L-l_d)]-1}{\beta\sinh[\beta(L-l_d)]}+\gamma(L-l_d)\right] - \frac{2\sigma_c l_d}{E_f\omega} - \frac{2a}{2E_f\mu\omega}\left[\sigma_d+\frac{\sigma_c}{\omega}\right]\left[e^{\frac{-2\mu\omega l_d}{a}}-1\right] \quad 5.37$$

where the total fiber length is equal to $2L$, and the embedded length on each side of the pullout specimen is equal to L.

5.1.2.5 Bond and Frictional Components of Pullout Stress, $\sigma_{o,bond}$ and $\sigma_{o,fric}$

At any debond length l_d, the fiber pullout stress, σ_o, is a summation of two components – the one arising due to the adhesional shear bond ($\sigma_{o,bond}$) and the other arising due to the frictional shear bond ($\sigma_{o,fric}$). That is:

$$\sigma_o = \sigma_{o,bond} + \sigma_{o,fric} \quad 5.38$$

From the above solution, the two components of pullout stress are obtained as:

$$\sigma_{o,bond} = \sigma_d; \qquad \sigma_{o,fric} = \left[e^{\frac{-2\mu\omega l_d}{a}}-1\right]\sigma_d + \frac{\sigma_c}{\omega}\left[e^{\frac{-2\mu\omega l_d}{a}}-1\right] \quad 5.39$$

5.1.2.6 Catastrophic Debonding

The interfacial debonding process becomes catastrophic when the fiber pullout stress, σ_o begins to drop with an increase in debond length, l_d. Thus, the condition for catastrophic debonding can be written as:

$$\frac{d\sigma_o}{dl_d} \leq 0 \tag{5.40}$$

The above condition will be satisfied when the difference between the increase in the frictional component of the pullout stress (i.e., $\sigma_{o,fric}$) and the decrease in the adhesional component of the pullout stress (i.e., $\sigma_{o,bond}$) with increase in l_d is equal to or less than zero. That is:

$$\left|\frac{d\sigma_{o,fric}}{dl_d}\right| \leq \left|\frac{d\sigma_{o,bond}}{dl_d}\right| \tag{5.41}$$

Let the debond length at which the debonding process turns catastrophic be represented by $l_{d,cat}$. With the mechanical properties of constituent materials, interfacial properties, fiber length and fiber radius all known, the length of debond zone, l_d, at which the debonding process will turn catastrophic can be obtained by satisfying the equality expressed by the Equation 5.40. Substituting for σ_o in Equation 5.40, we obtain the slope of σ_o vs. l_d curve as:

$$\frac{d\sigma_o}{dl_d} = \left\{-\frac{2\mu\omega x_1}{a x_2} - \frac{\beta x_4}{x_2} + \frac{\beta x_1 x_3}{x_2^2} - \frac{2\mu\sigma_c}{a}\right\} e^{\frac{-2\mu\omega l_d}{a}} \tag{5.42}$$

where

$$x_1 = \frac{-2\tau_s(\gamma+\alpha-\gamma\eta\alpha+\alpha\eta)}{a\beta}\sinh[\beta(L-l_d)]$$

$$x_2 = (\alpha-\gamma\eta\alpha+\alpha\eta)\cosh[\beta(L-l_d)]+\gamma$$

$$x_3 = (\alpha-\gamma\eta\alpha+\alpha\eta)\sinh[\beta(L-l_d)]$$

$$x_4 = \frac{-2\tau_s(\gamma+\alpha-\gamma\eta\alpha+\alpha\eta)}{a\beta}\cosh[\beta(L-l_d)]$$

At the instant that catastrophic debonding occurs, the slope of the σ_o vs. l_d curve will be zero. Therefore, the debond length, $l_{d,cat}$, at which debonding process becomes catastrophic can be obtained by equating the right hand side of the Equation 5.42 to zero. The peak pullout load and the fiber displacement corresponding to peak pullout load can be obtained by substituting the calculated value of catastrophic debond length, $l_{d,cat}$, into Equation 5.34 and Equation 5.37, respectively.

5.1.3 Stage 3: Fiber Completely Debonded and Pulling Out

Consider the case when the fiber is completely debonded along its embedded length, and let p_d be the rigid body displacement of the fiber as shown in Figure 5.1.5. In this case, transfer of stress between the fiber and the encapsulating matrix takes place entirely through the interfacial frictional shear bond. The governing differential equation of stress transfer for the pullout case has been derived by Takaku and Arridge [54]:

$$\frac{d\sigma_f}{dz}+\frac{2\mu}{a}\omega\sigma_f = -\frac{2\mu}{a}\sigma_c \qquad 5.43$$

Solving this equation, Takaku and Arridge [54] derived a solution for the fiber axial stress distribution, σ_f. However, their solution implicitly assumed that the coefficient of friction remain constant during the fiber pullout process (i.e., μ is independent of p_d). This limitation is

relaxed in the analysis proposed below. Based on the energy considerations, a procedure to calibrate interfacial properties is proposed in the next section; this procedure effectively describes the dependence of the coefficient of friction, μ on the fiber pullout distance, p_d.

The work of Takaku and Arridge [54] is further extended here and closed-form solutions are derived for the interfacial frictional shear stress distribution, τ_f, the fiber pullout stress, σ_o, and the fiber displacement, U_{p_d}.

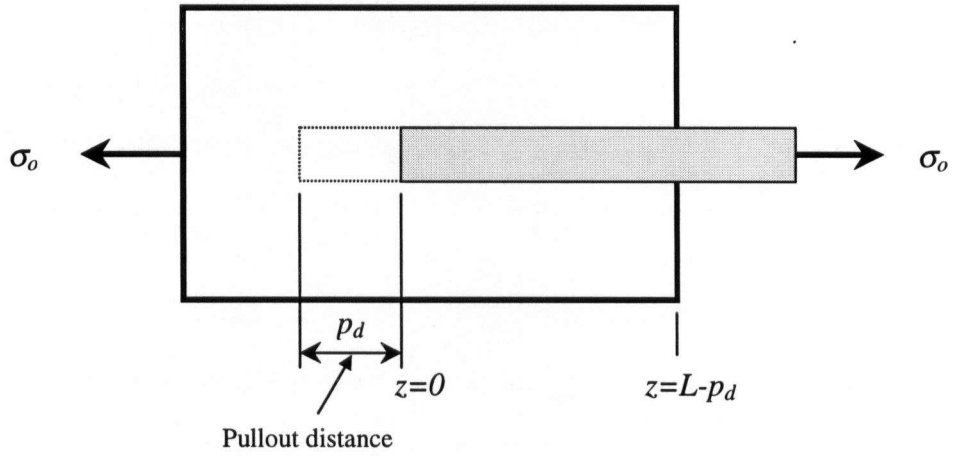

Figure 5.1.5: Fiber completely debonded over its length and pulling out

5.1.3.1 Fiber Axial Stress Distribution, σ_f

The solution of the above differential equation (Equation 5.43) represents the axial stress along the embedded length of a completely debonded fiber. With the boundary condition, $\sigma_f = 0$ at $z=0$, the solution is obtained as:

$$\sigma_f = -\frac{\sigma_c}{\omega}\left[1 - e^{\frac{-2\omega\mu z}{a}}\right] \qquad 5.44$$

where $0 \leq z \leq L\text{-}p_d$. In the above equation note that μ is a function of p_d.

5.1.3.2 Interfacial Frictional Shear Stress Distribution, τ_f

Following Coulomb's law, the interfacial frictional shear stress, τ_f, over the embedded length can be obtained as follows:

$$\tau_f = \mu\sigma_{cp} = \mu(\sigma_c + \omega\sigma_f) \tag{5.45}$$

Substituting for σ_f, the interfacial frictional shear stress, τ_f is obtained as:

$$\tau_f = \mu\,\sigma_c\, e^{\frac{-2\omega\mu z}{a}} \tag{5.46}$$

where $0 \leq z \leq L\text{-}p_d$.

In the above equation note that μ is a function of p_d. This equation depicts that interfacial frictional shear stress varies along the embedded length of fiber, with a minimum at the exit fiber end and a maximum at the embedded fiber end. It can also be noted that during stage 2, when l_d=L, Equation 5.33 reduces to Equation 5.46.

5.1.3.3 Fiber Pullout Stress, σ_o

The relationship between fiber pullout stress, σ_o, and pullout distance, p_d, can be obtained from Equation 5.44:

$$\sigma_o = -\frac{\sigma_c}{\omega}\left[1 - e^{\frac{-2\omega\mu(L-p_d)}{a}}\right] \tag{5.47}$$

The fiber pullout stress, σ_o, at p_d=0, termed here as the initial frictional pullout stress, σ_{if}, can be written as:

$$\sigma_{if} = -\frac{\sigma_c}{\omega}\left[1 - e^{\frac{-2\omega\mu L}{a}}\right] \tag{5.48}$$

In the above equations note that μ is a function of p_d.

5.1.3.4 Fiber Displacement, U_{p_d}

The total fiber displacement, U_{p_d}, is obtained by integrating the fiber strains along the total fiber length:

$$U_{p_d} = p_d - \frac{\sigma_c}{E_f \omega}\int_0^{L-p_d}\left[1-e^{\frac{-2\omega\mu z}{a}}\right]dz - \frac{\sigma_c}{E_f \omega}\int_{L-p_d}^{L}\left[1-e^{\frac{-2\omega\mu(L-p_d)}{a}}\right]dz \qquad 5.49$$

Solving:

$$U_{p_d} = p_d - \frac{\sigma_c}{E_f \omega}\left[(L-p_d)+\frac{a}{2\mu\omega}\left\{e^{\frac{-2\mu\omega(L-p_d)}{a}}-1\right\}+p_d\left\{1-e^{\frac{-2\mu\omega(L-p_d)}{a}}\right\}\right] \qquad 5.50$$

For a two-sided pullout problem, the fiber displacement, U_{p_d}, is given by:

$$U_{p_d} = p_d - \frac{2\sigma_c}{E_f \omega}\left[(L-p_d)+\frac{a}{2\mu\omega}\left\{e^{\frac{-2\mu\omega(L-p_d)}{a}}-1\right\}+p_d\left\{1-e^{\frac{-2\mu\omega(L-p_d)}{a}}\right\}\right] \qquad 5.51$$

where total fiber length is $2L$ and embedded length of fiber on each side of the pullout specimen is L. In the above equations note that μ is a function of p_d.

5.1.4 Calibration of Interfacial Parameters - σ_c, μ and τ_s

Interfacial contact stress, σ_c: When the fiber is axially loaded, the resultant contact stress, σ_{cp}, is given by Equation 5.28:

$$\sigma_{cp} = \sigma_c + \omega\sigma_f$$

where σ_f is the axial fiber stress, σ_c is the interfacial contact stress for an unloaded fiber, and ω is a constant. This equation depicts that with an increase in axial fiber stress the interfacial contact stress decreases due to Poisson's effect (note that σ_c is negative). For fibers with long lengths, a critical value of fiber axial stress will be reached such that the contact between fiber and matrix will disappear and the resultant contact stress, σ_{cp}, will become zero. When this happens, the interfacial debonding will continue without requiring any increase in the applied pullout stress. From the asymptotic value of fiber pullout stress, $\sigma_o = \sigma_{o,asymptotic}$, obtained from the peak pullout stress verses embedded fiber length plot, the interfacial contact stress, σ_c, can be calculated as:

$$\sigma_c = -\omega \sigma_{o,asymptotic} \tag{5.52}$$

Interfacial coefficient of friction, μ: During the process of fiber pullout, gradual abrasion and wear of the interface layer takes place. As a consequence, the interfacial coefficient of friction is expected to decrease with increase in the pullout displacement. Based on the energy considerations of the problem of fiber pullout, a method is proposed below to determine variation in coefficient of friction as a function of fiber pullout displacement. Work of fiber pullout, W_p, when fiber pullout displacement increases from p_{d1} to p_{d2} can be written as:

$$W_p = \pi a^2 \int_{p_{d1}}^{p_{d2}} \sigma_o \, dp_d \tag{5.53}$$

where σ_o is the fiber pullout stress given by Equation 5.47. Substituting for σ_o in Equation 5.53 we obtain:

$$W_p = -\pi a^2 \int_{p_{d1}}^{p_{d2}} \frac{\sigma_c}{\omega} \left[1 - e^{\frac{-2\omega\mu(L-p_d)}{a}} \right] dp_d \tag{5.54}$$

Within a small displacement domain (p_{d1} to p_{d2}), the coefficient of friction, μ, can be assumed to remain constant, and the above equation can be solved as:

$$W_p = -\frac{\pi a^2 \sigma_c}{\omega}\left\{ p_{d2} - p_{d1} - \frac{a}{2\omega\mu} e^{\frac{-2\omega\mu L}{a}} \left[e^{\frac{-2\omega\mu p_{d2}}{a}} - e^{\frac{-2\omega\mu p_{d1}}{a}} \right] \right\} \qquad 5.55$$

To obtain W_p from the experimental pullout curve, the relationship between the total pullout displacement and the rigid body displacement of the fiber must be known. As a first approximation, the rigid body displacement of the fiber, p_d is taken equal to Δ-Δ_{peak}, where, Δ is the total pullout displacement, and Δ_{peak} is the total pullout displacement corresponding to the peak pullout load. With W_p and σ_c known, the coefficient of friction, μ, can be calculated from the above non-linear equation. This equation depicts the dependence of coefficient of friction, μ, on the pullout displacement, p_d.

Adhesional bond strength, τ_s: For very small fiber lengths, the peak pullout stress is governed by the Equation 5.21. Differentiating Equation 5.21 with respect to fiber embedded length we obtain:

$$\frac{d\sigma_d}{dL} = \frac{-2\tau_s(\gamma+\alpha-\gamma\eta\alpha+\alpha\eta)}{a\beta}\left\{ \frac{[(\alpha-\gamma\eta\alpha+\alpha\eta)\cosh(\beta L)+\gamma]\beta\cosh(\beta L)}{[(\alpha-\gamma\eta\alpha+\alpha\eta)\cosh(\beta L)+\gamma]^2} \right. \qquad 5.56$$

$$\left. - \frac{\beta(\alpha-\gamma\eta\alpha+\alpha\eta)\sinh^2(\beta L)}{[(\alpha-\gamma\eta\alpha+\alpha\eta)\cosh(\beta L)+\gamma]^2} \right\}.$$

At $L = 0$ the above equation simplifies to:

$$\left(\frac{d\sigma_d}{dL}\right)_{L=0} = -\frac{2\tau_s}{a} \qquad 5.57$$

Rearranging the above equation we obtain:

$$\tau_s = -\frac{a}{2}\left(\frac{d\sigma_d}{dL}\right)_{L=0} \qquad 5.58$$

Thus, substituting the initial slope of the experimental maximum pullout stress versus embedded fiber length plot in the above equation, the interfacial adhesional shear strength, τ_s, can be calculated.

5.2 Conclusions

- An analytical model for the problem of fiber pullout is proposed in this chapter. The proposed model is unique because of its ability to take into consideration the evolution of the interfacial properties during the pullout process. The proposed model captures the essential features of the pullout process, including the progressive interfacial debonding and the Poisson's effect in the event of a debonded fiber. Analysis is divided into three stages, and for the each stage, closed-form solutions are derived for the fiber axial load distribution, the interfacial shear stress distribution and the fiber displacement. Complete pullout response can be predicted using the proposed progressive debonding model.

- During stage 1, fiber and matrix displacements at the interface remain compatible, and the resistance to fiber pullout is derived from the adhesional shear stresses mobilized at the interface. Closed-form solutions are derived for the fiber axial stress distribution and the interfacial shear stress distribution along the fiber length, the fiber displacement, and the initial debonding stress (i.e., the fiber pullout stress required to initiate interfacial debonding). The closed-form solution for the initial debonding stress is derived based on a maximum shear stress criterion. This solution indicates that, among other factors, the initial debonding stress depends upon fiber length and fiber elastic properties. At the end of stage 1, interfacial debonding initiates at the location where the fiber enters the matrix.

- During stage 2, the fiber is partially bonded along its embedded length. The adhesional shear stresses at the bonded interface and the frictional shear stresses at the debonded interface resist the fiber pullout. The influence of Poisson's contraction of fiber is taken into consideration in the analysis. It is shown that for any debond length, the fiber pullout stress is a summation of two components – the one arising due to the adhesional shear bond and the other arising due to the frictional shear bond. Closed-form solutions are derived for fiber axial stress distribution over the bonded and the debonded interfaces, interfacial adhesional shear stress distribution over the bonded interface, interfacial frictional shear stress

distribution over the debonded interface, fiber pullout stress versus debond length relationship, and fiber displacement versus debond length relationship.

- It is demonstrated that debonding process becomes catastrophic at the instant when the fiber pullout stress begins to drop with increase in debond length. This condition is satisfied when the difference between change in the frictional component of pullout stress and the adhesional component of pullout stress resulting due to change in debond length becomes equal to zero. A closed-form solution is derived to calculate the catastrophic debond length, given the mechanical properties of constituent materials, the interfacial properties and the geometry of the pullout specimen. Closed-form solutions are also derived to calculate the peak pullout stress and the displacement corresponding to the peak pullout stress.
- During stage 3, the fiber is completely debonded along its embedded length and fiber pullout is initiated. Frictional shear stresses existing over the debonded interface resist pullout of fiber from the matrix. Closed-form solutions are derived for fiber axial stress distribution, interfacial frictional shear stress distribution, fiber pullout stress, and fiber displacement at different stages of pullout process.
- A procedure to calibrate interfacial properties is described in this chapter. It is shown that interfacial contact stress can be calculated using the asymptotic value of pullout stress on the peak pullout stress versus embedded length plot. It is recognized that the coefficient of friction may decrease with increase in pullout displacement. Based on the energy considerations, a method is proposed to calculate the coefficient of friction as a function of pullout displacement. The adhesional bond strength can be calculated from the initial slope of the peak pullout stress versus embedded fiber length plot.

Chapter 6

Progressive Debonding Model for Fiber Pullout: Validation

6.0 Introduction

In the previous chapter, an analytical model to study progressive debonding of fiber-matrix interfaces and fiber pullout response was proposed. Validation of this model is achieved in the present chapter. For this purpose, experimental fiber pullout data from Chapter 4 are used. Theoretical predictions are also made for the pullout data found in the literature.

6.1 Calibration of Interfacial Properties and Validation of Model

In order to use the proposed model, calibration of three interfacial properties, namely, σ_c, μ and τ_s, is required. A procedure for calibrating interfacial properties was described in the previous chapter. Clearly, these parameters will depend upon the properties of the constituents involved. For instance, it can be expected that matrices with different shrinkage behavior will yield different values of σ_c, and also that fibers having different surface roughness characteristics will yield different values of μ. In this regard, the experimental pullout curves presented in Chapter 4 are meaningful, since fibers and matrices with different properties led to different pullout curves suggesting dependence of pullout response on interfacial properties. The pullout data of Chapter 4 are used here to calibrate the interfacial properties and to validate the proposed Progressive Debonding Model. Validity of the proposed model is also confirmed by comparing the model predictions with the pullout data found in the literature.

6.1.1 Source Code for Progressive Debonding Model

To theoretically predict fiber pullout response using the proposed Progressive Debonding Model, a source code is written in C programming language. This source code is attached in Appendix C.

6.1.2 Straight-smooth, Stainless Steel Fiber Embedded in Normal Strength Matrix

In Section 4.1.1, experimental pullout curves for straight-smooth, stainless steel fibers embedded in a normal strength matrix were presented. Here, those data are used to calibrate the interfacial properties. The elastic modulus of fiber and matrix are taken as 210 GPa and 30 GPa, respectively. The fiber radius, a and the outer radius of matrix cylinder, b are taken as 0.22 mm and 22 mm, respectively.

Substituting the asymptotic value of pullout stress from the pullout stress versus embedded length plot in Equation 5.52, the magnitude of the interfacial contact stress, σ_c, is obtained as -29.3 MPa.

The coefficient of friction versus pullout distance relationship was calculated from Equation 5.55. In this equation, the interval between p_{d1} and p_{d2} was chosen as 0.5 mm, and the area under the pullout curve, W_p lying between p_{d1} and p_{d2} was calculated as:

$$W_p = \frac{\left(P_{p_{d1}} + P_{p_{d2}}\right)}{2} * \left(p_{d1} - p_{d2}\right) \qquad 6.1$$

where P_{pd1} and P_{pd2} are the pullout load values corresponding to the pullout distances p_{d1} and p_{d2}, respectively. Equation 5.55 is a non-linear equation, and it was solved for μ using the *Mathcad PLUS 6.0 Professional Edition* software. The coefficient of friction versus pullout distance curves obtained using Equation 5.55 for fibers of different lengths are plotted in Figure 6.1.1. In the figure, it can be noted the coefficient of friction, μ, decreases exponentially with increase in pullout distance. The evolution law for the coefficient of friction can be described by the following equation:

$$\mu = (\mu_i - \mu_{ss})\, e^{-cp_d} + \mu_{ss} \qquad 6.2$$

where,

μ_i - initial coefficient of friction

μ_{ss} - steady state value of coefficient of friction attained at large pullout distances

c - a constant that governs the rate at which coefficient of friction decays with increase in pullout distance

The following values of μ_i, μ_{ss} and c gave an appropriate data fit describing variation in coefficient of friction with increase in pullout distance: $\mu_i = 0.12$, $\mu_{ss} = 0.035$ and $c = 0.7$.

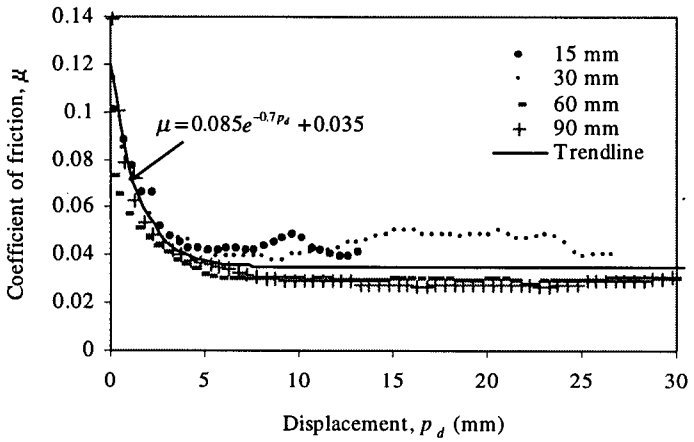

Figure 6.1.1: Coefficient of friction versus pullout displacement curves for straight-smooth, stainless steel fibers embedded in normal strength matrix

Substituting these values in Equation 6.2, the evolution law for coefficient of friction, μ can thus be written as $\mu = 0.085\, e^{-0.7 p_d} + 0.035$. Note that the observed decrease in coefficient of friction is attributable to matrix wear and consequent smoothening of interface layer as the fiber pulls out of the matrix. It can be readily appreciated that the evolution law for coefficient of friction, μ, may take different forms depending upon the age of matrix, matrix porosity/air content, size of voids, and loading rate.

On substituting the initial slope of maximum pullout stress versus fiber embedded length curve in Equation 5.58, the magnitude of adhesional bond strength, τ_s, is obtained as -2.4 MPa. It must be noted that a more precise prediction of adhesional bond strength can be obtained by testing fibers of even smaller embedded length.

Using the above values of interfacial properties, the theoretical pullout response is predicted for a straight-smooth, stainless steel fiber with 30 mm embedded length (Section 4.1.1). Figure 6.1.2 compares the experimental pullout curves with the theoretical. A good correspondence between the theoretical prediction and the experimental curves is noticeable in the figure.

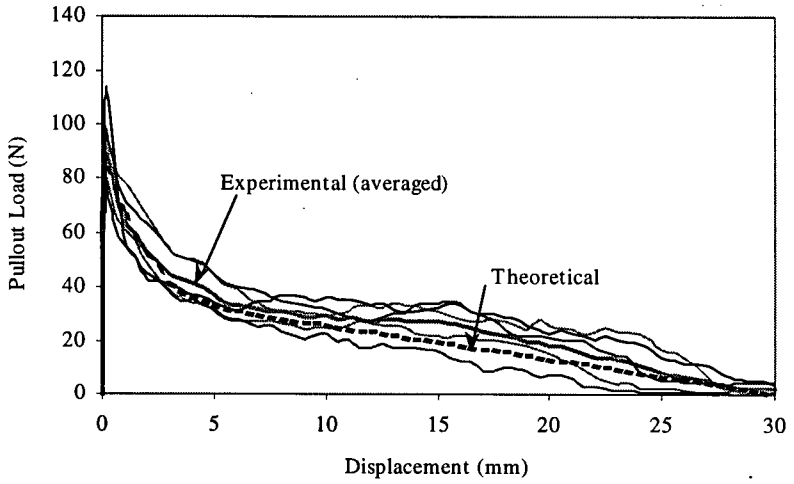

Figure 6.1.2: Comparison of experimental and theoretical pullout response – straight-smooth, stainless steel fiber fiber (embedded length – 30 mm) embedded in normal strength matrix

Theoretically predicted peak pullout load and the displacement corresponding to peak pullout load are compared with experimental values in the Table 6.1.1. Model predicted results agree well with the experimental ones.

Table 6.1.1: Theoretical and experimental peak pullout load and displacement corresponding to peak pullout load for a straight-smooth, stainless steel fiber embedded in normal strength matrix

Fiber	Embedded Fiber Length (mm)	Fiber Diameter (mm)	Matrix	P_{peak} (N)		δ_{peak} (mm)	
				Experi-mental	Model	Experi-mental	Model
Straight-smooth, stainless steel	30	0.44	Normal strength	95.10	89.16	0.120	0.099

P_{peak} – Peak pullout load; δ_{peak} – Displacement at peak pullout load

6.1.3 Straight, Stainless Steel Fibers with Rough Surface Embedded in Normal Strength Matrix

In Section 4.1.2, experimental pullout curves for straight, stainless steel fibers with a rough surface embedded in a normal strength matrix were presented. Here, those data are used to calibrate the interfacial properties. The elastic modulus of fiber and matrix are taken as 210 GPa and 30 GPa, respectively. The fiber radius, a and the outer radius of matrix cylinder, b are taken as 0.22 mm and 22 mm, respectively. Substituting the asymptotic value of pullout stress from the pullout stress versus embedded length plot in Equation 5.52, the magnitude of interfacial

contact stress, σ_c, is obtained as -29.5 MPa. Coefficient of friction versus pullout distance curves obtained using Equation 5.55 are plotted in Figure 6.1.3 for fibers of different lengths. The magnitudes of μ_i and μ_{ss} are obtained as 0.26 and 0.068, respectively, thus indicating that even for rough steel fiber the coefficient of friction, μ, decreases with increase in pullout distance. However, for rough steel fiber, both the initial coefficient of friction, μ_i and the steady-state coefficient of friction, μ_{ss}, are greater than those for straight-smooth, stainless steel fibers. The decay rate for coefficient of friction, characterized by the constant c, is found to be independent of a fiber's surface roughness. Substituting these values in Equation 6.2, the evolution law for coefficient of friction, μ, can thus be written as $\mu = 0.192\, e^{-0.7 p_d} + 0.068$. Note that this evolution law is different than that obtained for smooth steel fiber, and this suggests the dependence of interfacial coefficient of friction on fiber surface roughness. Superior interlocking between fiber and matrix probably is responsible for greater values of the coefficient of friction in the case of rough steel fibers.

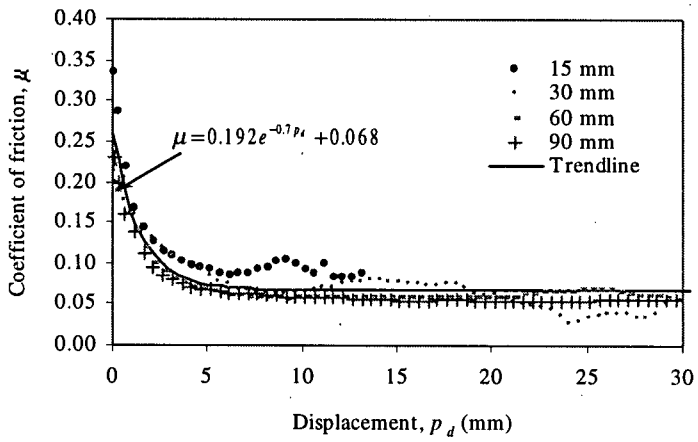

Figure 6.1.3: Coefficient of friction versus pullout displacement curves for straight, stainless steel fibers with rough surface embedded in normal strength matrix

Using these values of interfacial properties, the theoretical pullout response is predicted for a fiber with 30 mm embedded length (Section 4.1.2). Figure 6.1.4 compares the model prediction with the experimental pullout curves. A good correspondence between the model prediction and the experimental curves is distinctly noticeable in the figure.

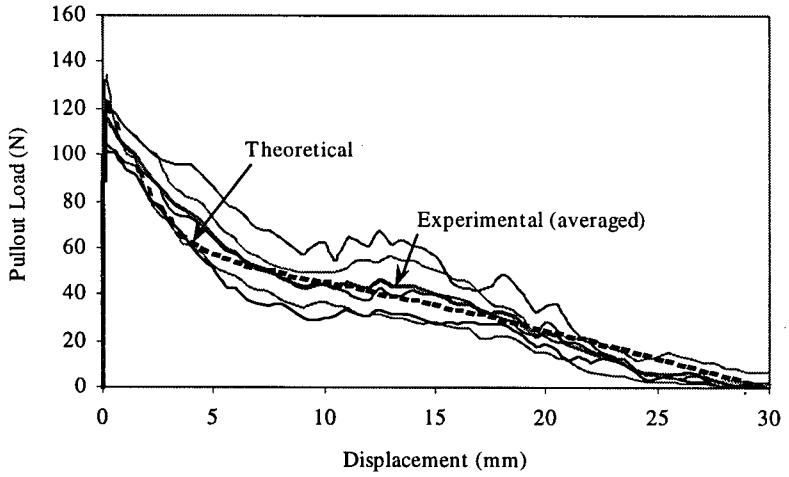

Figure 6.1.4: Comparison of experimental and theoretical pullout response - straight, stainless steel fiber with rough surface (embedded length – 30 mm) embedded in normal strength matrix

Model predictions for the peak pullout load and the displacement corresponding to peak pullout load are compared with the experimental values in Table 6.1.2. Model predicted values agree well with the experimental ones.

Table 6.1.2: Theoretical and experimental peak pullout load and the displacement corresponding to peak pullout load for a steel fiber with rough surface embedded in normal strength matrix

Fiber	Embedded Fiber Length (mm)	Fiber Diameter (mm)	Matrix	P_{peak} (N)		δ_{peak} (mm)	
				Experi-mental	Model	Experi-mental	Model
Straight, stainless steel fiber with rough surface	30	0.44	Normal strength	116.1	122.04	0.120	0.156

P_{peak} – Peak pullout load; δ_{peak} – Displacement at peak pullout load

6.1.4 Straight-smooth, Stainless Steel Fibers Embedded in Non-Shrink Grout Matrix

In Section 4.1.3, experimental pullout curves for straight-smooth, stainless steel fibers embedded in non-shrink grout matrix were presented. Here, those data are used to calibrate the interfacial properties. The elastic modulus of fiber and matrix are taken as 210 GPa and 30 GPa, respectively. The fiber radius, a and the outer radius of matrix cylinder, b were taken as 0.22 mm and 22 mm, respectively. Substituting the asymptotic value of pullout stress from the pullout stress versus embedded length plot in the Equation 5.52, the magnitude of interfacial

contact stress, σ_c, is obtained as -11.7 MPa. Clearly, the magnitude of interfacial contact stress obtained with non-shrink grout matrix is much smaller than that obtained with normal strength matrix. This decrease is directly attributable to the reduced shrinkage of non-shrink grout matrix. Elastic modulus of fiber and matrix are taken as 210 GPa and 30 GPa, respectively. The fiber radius, a and the outer radius of matrix cylinder, b were taken as 0.22mm and 22 mm, respectively. Coefficient of friction versus pullout displacement curves obtained using Equation 6.55 are plotted in the Figure 6.1.5 for fibers of different lengths. It can be noted that coefficient of friction, μ, decreases with increase in pullout distance, and that the evolution law for coefficient of friction can be described by the equation $\mu = 0.085\, e^{-0.7 p_d} + 0.035$. This evolution law for coefficient of friction, μ, is same as that obtained for a straight-smooth, stainless steel fiber embedded in a normal strength matrix. On substituting the initial slope of maximum pullout stress versus fiber embedded length curve in Equation 5.58, the magnitude of adhesional bond strength, τ_s, is obtained as -1.3 MPa. Using these values of interfacial properties, theoretical pullout response is predicted for a fiber with 30 mm embedded length (Section 4.1.3). Figure 6.1.6 compares the theoretical pullout curve with the experimental ones. A good correspondence between the theoretical prediction and the experimental curves is distinctly noticeable in the figure.

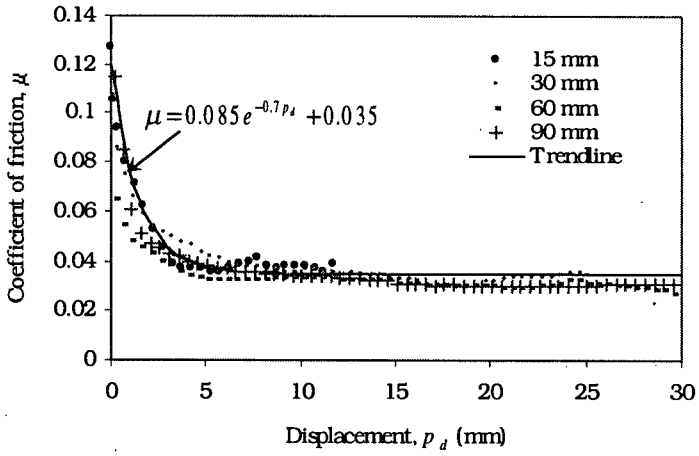

Figure 6.1.5: Coefficient of friction versus pullout displacement curves for straight-smooth, stainless steel fibers embedded in non-shrink grout matrix

Model predictions for the peak pullout load and the displacement corresponding to peak pullout load are compared with the experimental values in Table 6.1.3. Model predicted values compared well with the experimental ones.

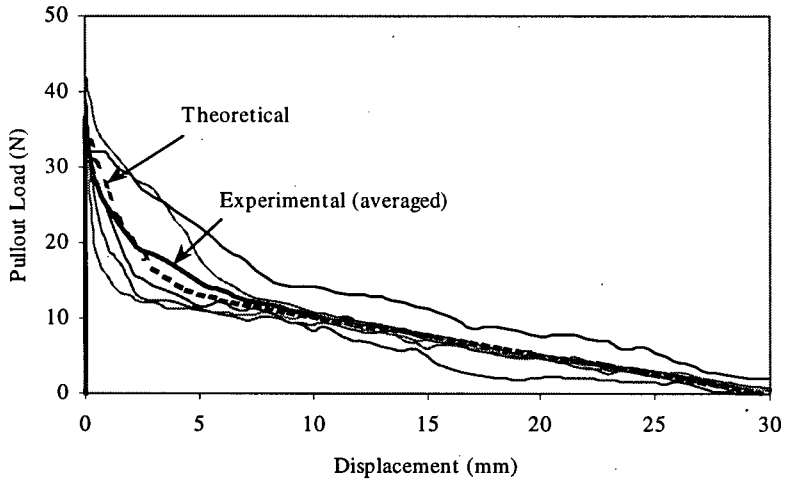

Figure 6.1.6: Comparison of experimental and theoretical pullout response – straight-smooth, stainless steel fiber (embedded length – 30 mm) embedded in non-shrink grout matrix

Table 6.1.3: Theoretical and experimental peak pullout load and the displacement corresponding to peak pullout load for a straight-smooth, stainless steel fiber embedded in non-shrink grout matrix

Fiber	Embedded Fiber Length (mm)	Fiber Diameter (mm)	Matrix	P_{peak} (N)		δ_{peak} (mm)	
				Experi-mental	Model	Experi-mental	Model
Straight-smooth, stainless steel	30	0.44	Non-shrink Grout	36.6	35.6	0.044	0.039

P_{peak} – Peak pullout load; δ_{peak} – Displacement at peak pullout load

6.1.5 Straight, Smooth Polypropylene Fibers Embedded in Normal Strength Matrix

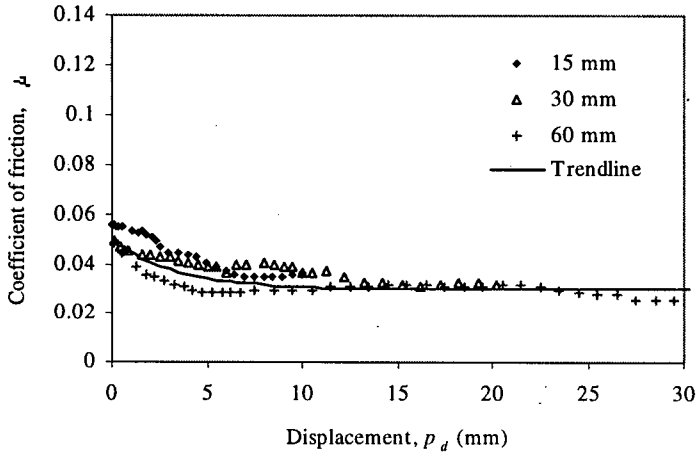

Figure 6.1.7: Coefficient of friction versus pullout displacement curves for straight, smooth polypropylene fibers embedded in normal strength matrix

In Section 4.1.6, experimental pullout curves for straight, smooth polypropylene fibers embedded in normal strength matrix were presented. Here, those experimental pullout data are used to calibrate the interfacial properties. The elastic modulus of fiber and matrix are taken as 3.5 GPa and 30 GPa, respectively. The fiber radius, a and the outer radius of matrix cylinder, b are taken as 0.475 mm and 47.5 mm, respectively. Substituting the asymptotic value of pullout stress from the pullout stress versus embedded length plot in the Equation 5.52, the magnitude of interfacial contact stress, σ_c, is obtained as -11.0 MPa. This value of interfacial contact stress, σ_c, is smaller than that obtained for stainless steel fibers embedded in a similar type of matrix. Since interfacial frictional bond and interfacial contact stress, σ_c, are related by Equation 5.46, it can be concluded that magnitude of interfacial frictional bond will also be lower in the case of polypropylene fibers. The coefficient of friction versus pullout distance curves obtained using Equation 5.55 for fibers of different lengths are plotted in the Figure 6.1.7. It can be noted that the coefficient of friction, μ, decreases with increase in pullout distance, and that the evolution law for coefficient of friction can be described by the equation $\mu = 0.02\, e^{-0.3 p_d} + 0.03$. Note that this evolution law is different than that obtained for steel fibers embedded in a similar type of matrix. On substituting the initial slope of the maximum pullout stress versus fiber embedded length curve in Equation 5.58, the magnitude of adhesional bond strength, τ_s is obtained as -0.61 MPa. Using these values of interfacial properties, theoretical pullout response is predicted for a fiber with 15 mm embedded length. Figure 6.1.8 compares the model prediction with the

experimental pullout curves, and it can be seen that model prediction agrees well with the experimental ones.

Model predictions for the peak pullout load and the displacement corresponding to peak pullout load are compared with the experimental values in Table 6.1.4. The predicted peak pullout load agrees well with the experimental value, however, the experimental displacement at peak pullout load is much greater than the predicted value.

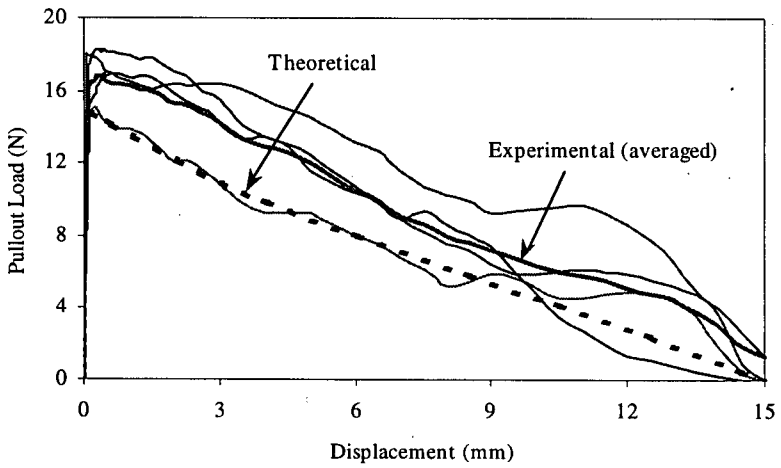

Figure 6.1.8: Comparison of experimental and theoretical pullout response - straight, smooth polypropylene fiber (embedded length – 15 mm) embedded in normal strength matrix

Table 6.1.4: Theoretical and experimental peak pullout load and the displacement corresponding to peak pullout load for a straight, smooth polypropylene fiber embedded in normal strength matrix

Fiber	Embedded Fiber Length (mm)	Fiber Diameter (mm)	Matrix	P_{peak} (N)		δ_{peak} (mm)	
				Experi-mental	Model	Experi-mental	Model
Straight-smooth, polypropylene	15	0.95	Normal strength	16.84	14.90	0.300	0.106

P_{peak} – Peak pullout load; δ_{peak} – Displacement at peak pullout load

6.1.6 Pullout Data Found in the Literature

Naaman and Shah [142]

Figure 6.1.9 compares the experimental fiber pullout response reported by Naaman and Shah [142] for a steel fiber and the theoretical prediction based on the proposed Progressive

Debonding Model. Length of fiber was 12.7 mm and diameter of fiber was 0.25 mm. The elastic modulus of fiber and matrix are taken as 210 GPa and 30 GPa, respectively. The outer radius of matrix cylinder, b is taken as 12.5 mm. Following interfacial properties are assumed to obtain the theoretical prediction:

τ_s = -2.4 MPa

σ_c= -29.3 MPa

$\mu = 0.085\, e^{-0.7 p_d} + 0.035 \quad (\mu_i = 0.12 \text{ and } \mu_{ss} = 0.035)$

It can be seen that very good agreement between the theoretical prediction from the progressive debonding model and the experimental response is obtained. Note that, interfacial properties assumed here to make theoretical prediction are same as the ones used previously to predict pullout response of straight, smooth steel fibers embedded in normal strength matrix (Section 6.1.2). For comparison, the predictions obtained from the other theoretical models are also shown in the same figure.

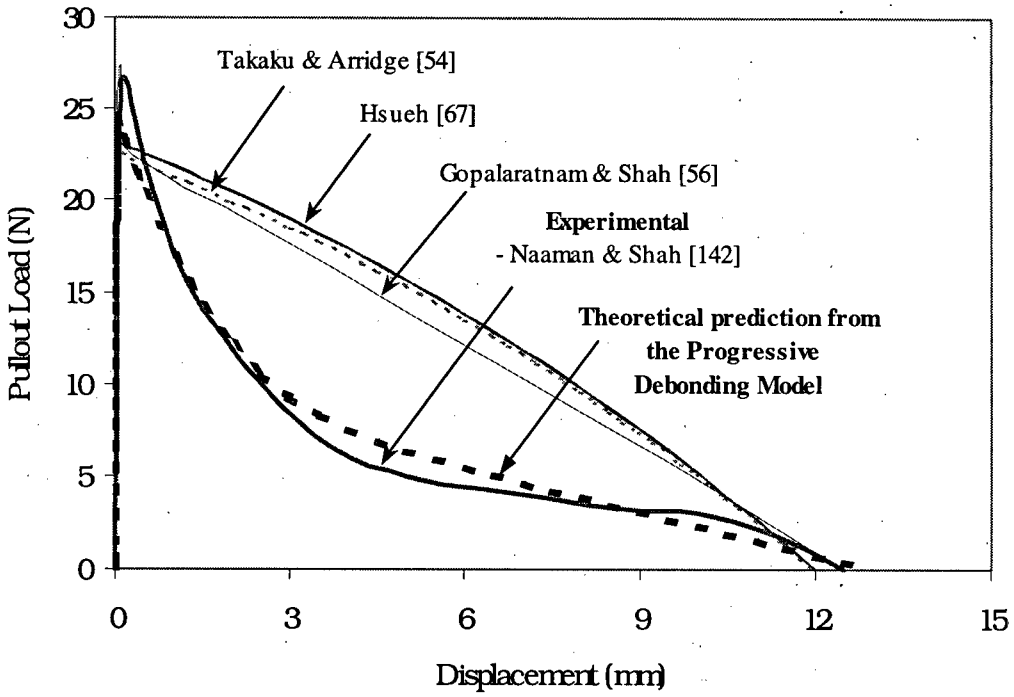

Figure 6.1.9: Comparison of experimental and theoretical pullout response for a straight, smooth steel fiber. Experimental curve is by Naaman and Shah [142]

Mallikarjuna, Fafard and Banthia [225]

Table 6.1.5 compares the peak pullout loads predicted by the proposed Progressive Debonding Model and the Finite Element Analysis results obtained by Mallikarjuna et al. [225]. Theoretical predictions are obtained for fibers with three different diameters – 0.50, 0.75 and 1.00 mm. In all cases the embedded fiber length is 18 mm. The elastic modulus of fiber and matrix are taken as 210 GPa and 30 GPa, respectively. The following interfacial properties are assumed to obtain theoretical predictions:

τ_s = -2.4 MPa

σ_c= -29.3 MPa

$\mu = 0.085\, e^{-0.7 p_d} + 0.035 \quad (\mu_t = 0.12 \text{ and } \mu_{ss} = 0.035)$

Table 6.1.5: Comparison of peak pullout loads as predicted by (i) the proposed progressive debonding model, and (ii) finite element analysis, Mallikarjuna, et al. (225)

Fiber	Embedded Fiber Length (mm)	Fiber Diameter (mm)	Peak pullout load, P_{peak} (N)	
			Finite Element Analysis	Proposed Progressive Debonding Model
Straight-smooth, steel	18	0.50	77.7	75.8
		0.75	119.5	124.0
		1.00	159.6	172.9

Very good agreement is obtained between the two results. Agreement is better for smaller diameter fibers, and disparity between the two result decreases with decrease in fiber diameter.

Wang, Li and Backer [69]

Figure 6.1.10 compares the experimental fiber pullout response reported by Wang et al. [69] for a straight, smooth polypropylene fiber and the theoretical prediction based on the proposed Progressive Debonding Model. Length and diameter of fiber are 50 mm and 0.508 mm, respectively. The elastic modulus of fiber and matrix are taken as 3.5 GPa and 30 GPa, respectively. The outer radius of matrix cylinder, b is taken as 25 mm. The following interfacial properties are assumed to obtain theoretical prediction:

τ_s = -0.61 MPa

σ_c= -14.0 MPa

$\mu = 0.02\, e^{-0.3 p_d} + 0.03 \quad (\mu_t = 0.05 \text{ and } \mu_{ss} = 0.03)$

In the figure, a good agreement between the theoretical and the experimental response is noticeable.

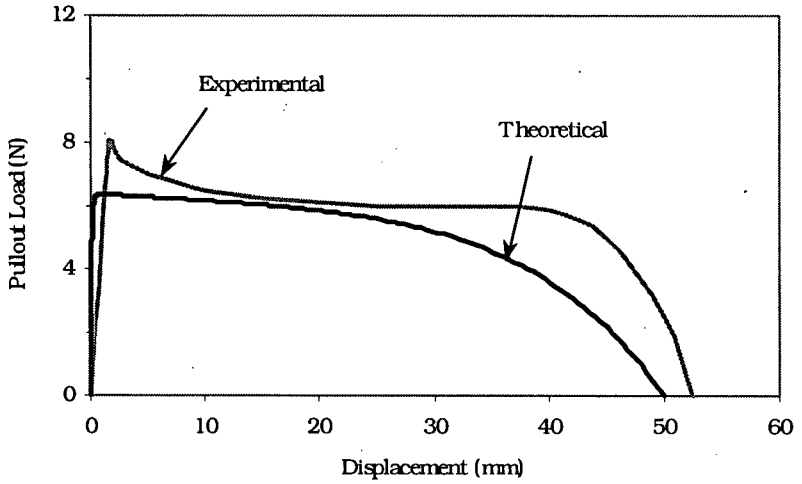

Figure 6.1.10: Comparison of experimental and theoretical pullout response for a straight, smooth polypropylene fiber. Experimental curve is by Wang, Li and Backer [69]

6.2 Conclusions

- The main objective of this chapter was to validate the proposed Progressive Debonding Model. Theoretical predictions from the proposed model compare well with the experimental pullout data presented in Chapter 4 and the pullout data found in literature. Good agreement between the theoretical and the experimental results thus validates the proposed model.
- The evolution law for the coefficient of friction indicates that coefficient of friction decays exponentially with increase in fiber pullout distance. This observation is found to be valid for both steel as well as polypropylene fibers. Smoothening of the interface (due to matrix wear) with increase in pullout distance appears to be responsible for this behavior.
- A comparison between the evolution laws for the coefficient of friction for rough steel fiber and a smooth steel fiber indicates that the coefficient of friction values for the former are greater than for the latter. A superior interlocking mechanism between fiber and matrix in the case of rough steel fibers appears to be the reason for higher values of coefficient of friction in the case of rough steel fibers. This observation depicts the dependence of interfacial frictional bond on fiber's surface roughness.

- A comparison between the evolution laws for the coefficient of friction for the smooth polypropylene fibers and the smooth steel fibers indicates that the coefficient of friction values for the former are smaller than for the latter. This may be attributable to the following two reasons: the smoother surface of the polypropylene fibers and the hydrophobic nature of polypropylene material. The hydrophobic property of polypropylene will prevent penetration of the matrix into the fine cavities on the fiber surface. As a result, a good interlocking mechanism between fiber and matrix will not be established, and the coefficient of friction will remain low.
- A comparison between the evolution laws for the coefficient of friction for the smooth polypropylene fibers and the smooth steel fibers indicates that the coefficient of friction decays from the initial value to a steady-state value at a faster rate for the steel fibers.
- The magnitude of the interfacial contact stress obtained with a Portland cement matrix (CSA Type 10) is found to be greater than that obtained with a non-shrink grout matrix. This observation depicts the dependence of interfacial contact stress and interfacial frictional bond on shrinkage properties of the matrix.
- For polypropylene fibers embedded in a normal strength matrix, the interfacial contact stress is found to be smaller than that for steel fibers embedded in a similar type of matrix. This observation depicts the dependence of interfacial contact stress and interfacial frictional bond on the elastic properties of constituents.

Chapter 7

Progressive Debonding Model for Fiber Pullout: Parametric Studies

7.0 Introduction

In the Chapter 4, it was experimentally observed that fiber pullout response depends upon various factors, such as fiber-matrix interfacial properties, mechanical properties of constituents and physical dimensions of the fiber. From the viewpoint of optimization of toughness/strength, it is critical to identify the relative importance of these factors, given the dependence of composite properties on fiber pullout response. Thus, the objective of this chapter is to systematically investigate influence of various factors on the progressive debonding behavior and fiber pullout response. This objective has been achieved by conducting parametric studies using the proposed Progressive Debonding Model.

7.1 Parametric Studies

The influence of the following factors on progressive debonding and pullout response has been investigated:

- Adhesional bond strength, τ_s
- Interfacial contact stress, σ_c
- Interfacial coefficient of friction, μ

Important results obtained from parametric studies are reported below.

7.1.1 Influence of Adhesional Bond Strength, τ_s

The influence of adhesional bond strength, τ_s, on progressive debonding and fiber pullout response is investigated in this section. For this purpose, parametric studies are carried out on two fibers with different elastic moduli. The first fiber has an elastic modulus of 210 GPa and the same for the second fiber is 3.5 GPa.

7.1.1.1 Fiber Elastic Modulus, E_f = 210 GPa

Parametric studies are carried out for three different values of adhesional bond strength, τ_s: -1 MPa, -5 MPa and -10 MPa. Assumed values of the other interfacial properties are: σ_c = -15.0

MPa and $\mu = 0.065\, e^{-0.7 p_d} + 0.035$ (μ_i=0.1 and μ_{ss}=0.035). Mechanical properties of fiber are assumed as: E_f=210 GPa (elastic modulus) and, ν_f=0.30 (Poisson's ratio), and the same for matrix are assumed as 30 GPa and 0.20, respectively. Total fiber length, L, is taken as 50 mm (i.e., one side embedded length=25 mm), and fiber diameter is taken as d=1.0 mm. The assumed value of b (the outer radius of matrix cylinder) is 50 mm. Note that an elastic modulus of 210 GPa corresponds to that of steel.

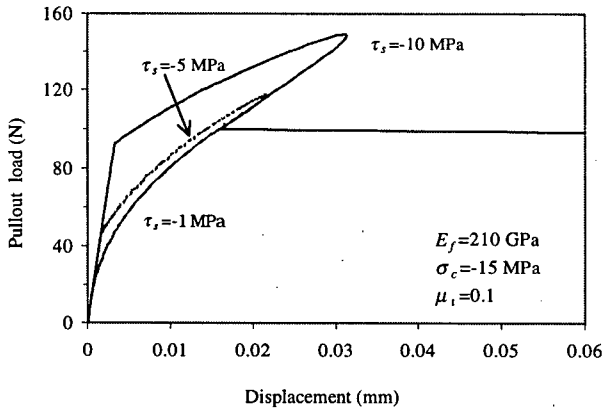

Figure 7.1.1a: Influence of adhesional bond strength on pullout response (E_f=210 GPa)

Figure 7.1.1a compares the fiber pullout response for three different values of adhesional bond strength, τ_s. The initial linear part of the pullout curves seen in the figure depicts elastic loading of fibers. In the linear region of the pullout curve, the maximum interfacial shear stress remains below the interfacial adhesional bond strength, τ_s, therefore, the interface along the entire embedded length remains fully bonded. On further loading, the pullout load increases in a non-linear fashion until the peak pullout load is attained. In this region interfacial debonding initiates and continues in a progressive fashion, i.e., pullout load increases with increase in debond length. Also, over the debonded interface, interfacial frictional shear stresses are mobilized. The pullout load during progressive debonding increases because the rate at which the frictional component of pullout load increases with change in debond length is greater than the corresponding rate at which adhesional component of the pullout load decreases, i.e., $d\sigma_{o,fric}/dl_d \geq d\sigma_{o,bond}/dl_d$ (Equation 5.41). At the peak pullout load, the rate of increase in the frictional component of pullout load becomes equal to the rate of decrease in adhesional component of the pullout load.

On further loading, the remaining intact portion of the interface debonds catastrophically, i.e., no increase in pullout load is required to further debond the interface. Thus, pullout load drops in this region, which is accompanied by decrease in pullout displacement. The pullout load in this region drops because the rate at which frictional component of pullout load increases due to change in debond length is smaller than the corresponding rate at which the adhesional component of the pullout load decreases. The theoretically predicted decrease in pullout displacement is not observed in the experiments since pullout tests are normally carried out at a constant rate of pullout displacement. In Figure 7.1.1a it can also be noticed that no catastrophic debonding occurs when τ_s = -1 MPa.

In Figure 7.1.1b, the pullout load at initial debonding and the peak pullout load are plotted as a function of adhesional bond strength, τ_s. Both the pullout load at initial debonding and the peak pullout load increase with increase in adhesional bond strength. However, the rate of increase of the former is greater than that of the latter. In Figure 7.1.1c, pullout displacement at the peak pullout load is plotted as a function of adhesional bond strength, τ_s. In the figure it can be seen that pullout displacement at the peak pullout load increases with increase in adhesional bond strength, τ_s.

After initial debonding, further debonding requires the applied pullout load to overcome the interfacial frictional shear stresses at the debonded interface and adhesional shear stresses at the bonded interface. As a result, the pullout load required to further debond the interface depends upon the extent of prior debonding. Figure 7.1.1d shows variation in pullout load as a function of debond length for the case when τ_s = -5 MPa. In the same figure, components of pullout load, (i.e., the adhesional and the frictional components) are also plotted. The following points can be noted in the figure:

- Interfacial debonding initiates at the surface where the fiber enters the matrix. At initiation of debonding the fiber pullout load (i.e., the initial debonding load) is equal to the adhesional component of pullout load, since the frictional component of pullout load is equal to zero.
- With increase in debond length, fiber pullout load continues to increase until debond length corresponding to the peak pullout load is attained. Upon further debonding, fiber pullout load begins to decrease; With increase in debond length, the adhesional component of pullout load decreases, on the other hand, the frictional component of pullout load increases.

- The peak pullout load on the pullout load vs. debond length curve corresponds to the point when slope of the curve becomes zero. This condition is satisfied when slope of the adhesional component of pullout load vs. debond length curve is equal and opposite in sign to that of the frictional component of pullout load vs. debond length curve. The debond length corresponding to this point is termed the catastrophic debond length, $l_{d,cat}$ (Section 5.1.2.6), since the debonding process turns catastrophic upon further debonding.

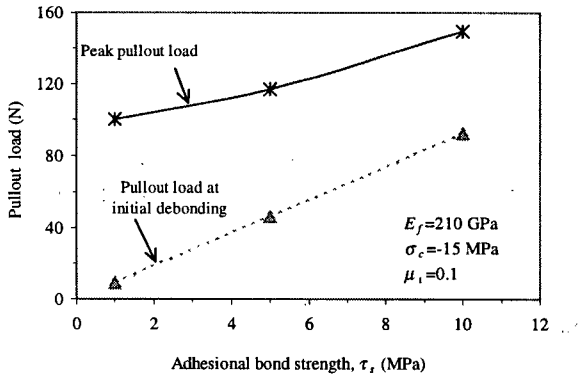

Figure 7.1.1b: Influence of adhesional bond strength on the pullout load at initial debonding and the peak pullout load (E_f=210 GPa)

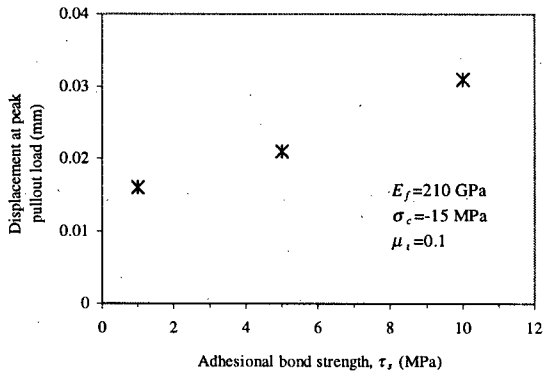

Figure 7.1.1c: Influence of adhesional bond strength on displacement at the peak pullout load (E_f=210 GPa)

Figure 7.1.1e shows pullout load and its components as a function of debond length at different values of adhesional bond strength, τ_s. From this figure, the following important observations can be made:

- The pullout load corresponding to any given debond length increases with increase in adhesional bond strength, τ_s. However, at complete debonding, the magnitude of pullout load is independent of adhesional bond strength, τ_s.
- Prior to complete debonding, the adhesional component of pullout load increases with increase in adhesional bond strength; on the other hand, the frictional component of pullout load decreases with increase in adhesional bond strength.
- Catastrophic debonding takes place at τ_s = -5.0 MPa and -10 MPa; on the other hand, at τ_s = -1.0 MPa, the debonding process is completely stable, i.e., pullout load continues to increase until the fiber is completely debonded.
- For a given fiber length, catastrophic debond length, $l_{d,cat}$, decreases with increase in the adhesional bond strength, τ_s.

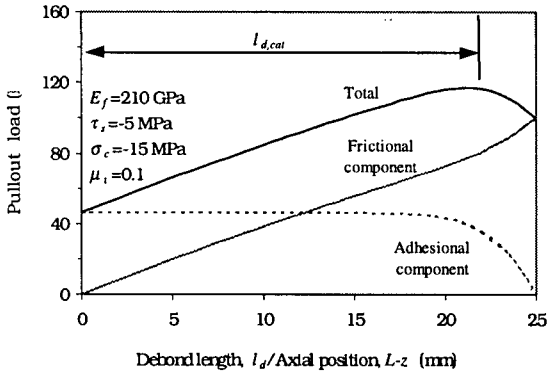

Figure 7.1.1d: Variation in pullout load and pullout load components as a function of debond length (E_f=210 GPa)

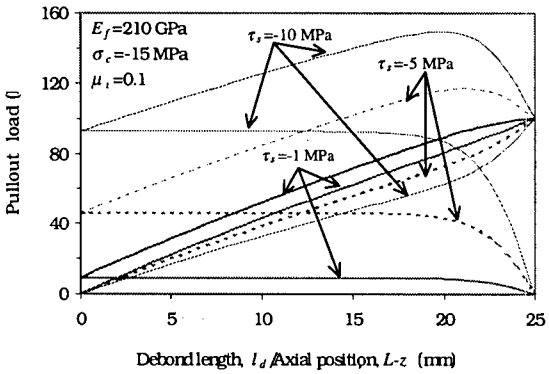

Figure 7.1.1e: Variation in pullout load and its components as a function of debond length at different values of adhesional bond strength, τ_s (E_f=210 GPa)

Figure 7.1.1f shows the variation in axial load distribution in the fiber at initiation of debonding for different values of adhesional bond strength, τ_s. In the figure, it can be seen that fiber axial load increases with increase in adhesional bond strength, τ_s. It can also be noticed that fiber axial load is a maximum at the loaded end of the fiber. Axial load decreases hyperbolically towards the embedded end of fiber and it vanishes near the center of the embedded fiber length. A similar trend can be seen for the interfacial shear stress distribution along the embedded fiber length at initiation of debonding, Figure 7.1.1g.

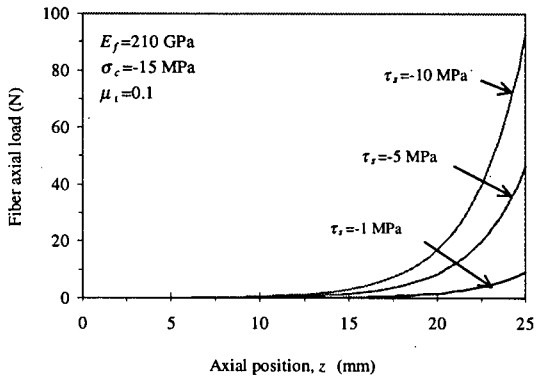

Figure 7.1.1f: Axial load distribution in fiber at initial debonding (E_f=210 GPa)

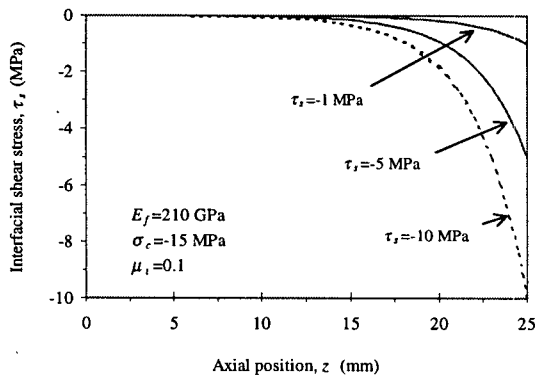

Figure 7.1.1g: Interfacial shear stress distribution at initial debonding (E_f=210 GPa)

Figure 7.1.1h shows the variation in axial load distribution at completion of debonding for different values of adhesional bond strength, τ_s. In the figure it can be seen that the axial load distribution along the fiber length is independent of adhesional bond strength, τ_s, at completion of interfacial debonding. It can also be noticed that fiber axial load is maximum at the loaded fiber end and it decreases almost linearly to a value of zero at the embedded fiber end. Figure

7.1.1i shows the interfacial shear stress distribution at completion of interfacial debonding. In this figure it can be seen that interfacial shear stress is maximum at the embedded fiber end, and it gradually decreases towards the exit fiber end. Poisson's contraction of the fiber is responsible for the observed interfacial shear stress distribution along the embedded length of fiber. Comparison of Figures 7.1.1g and 7.1.1i clearly depicts that the axial load distributions at initiation of debonding and at completion of debonding are very different.

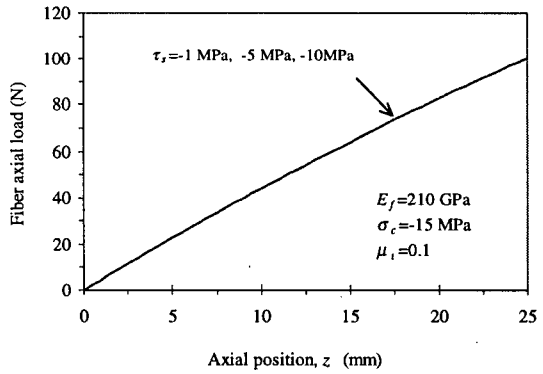

Figure 7.1.1h: Axial load distribution at completion of debonding (E_f=210 GPa)

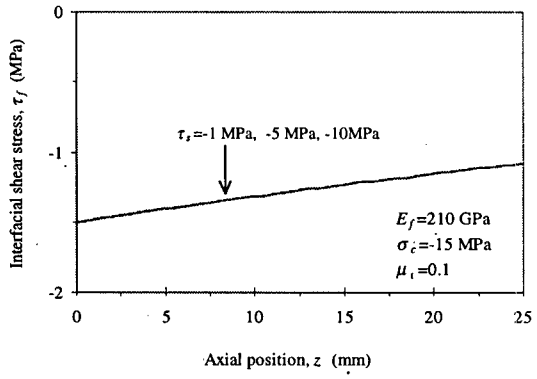

Figure 7.1.1i: Interfacial shear stress distribution at completion of debonding (E_f=210 GPa)

7.1.1.2 Fiber Elastic Modulus, E_f = 3.5 GPa

Parametric studies are carried out for three different values of adhesional bond strength, τ_s: -1 MPa, -5 MPa and -10 MPa. Assumed values of other interfacial properties are: σ_c = -15.0 MPa and $\mu = 0.02\,e^{-0.3p_d} + 0.03$ (μ_i =0.05 and μ_{ss} =0.03). Mechanical properties of fiber are assumed as: E_f=3.5 GPa (elastic modulus) and, ν_f=0.35 (Poisson's ratio), and the same for matrix are assumed as 30 GPa and 0.20, respectively. Total fiber length, L, is taken as 50 mm (i.e., one side embedded length=25 mm), and fiber diameter is taken as d=1.0 mm. The assumed value of b (the outer radius of matrix cylinder) is 50 mm. Note that an elastic modulus of 3.5 GPa corresponds to that of polypropylene.

Figure 7.1.2a compares the pullout response of fibers with E_f = 3.5 GPa at three different values of adhesional bond strength, τ_s. In this figure, it can be seen that the difference between the pullout responses at three different values of adhesional strength, τ_s, is relatively insignificant. At τ_s =-1 MPa the debonding process is completely stable. On the other hand, the debonding process turns catastrophic at τ_s=-5 MPa and –10 MPa; however, the load drop during

catastrophic debonding is very small and not noticeable in the figure.

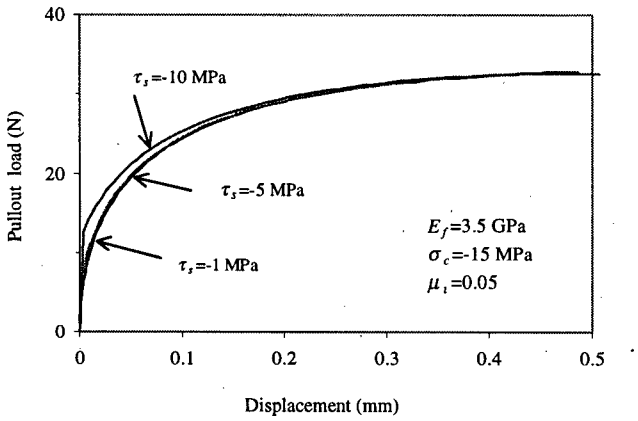

Figure 7.1.2a: Influence of adhesional bond strength on pullout response (E_f=3.5 GPa)

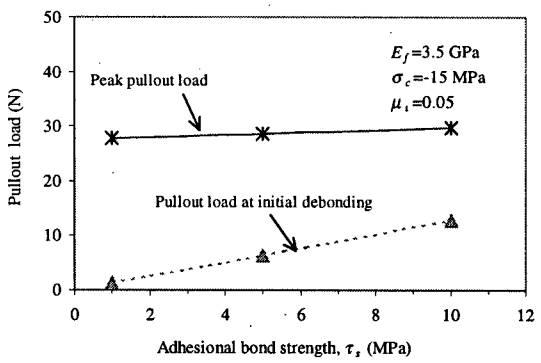

Figure 7.1.2b: Influence of adhesional bond strength on pullout load at initial debonding and maximum pullout load (E_f=3.5 GPa)

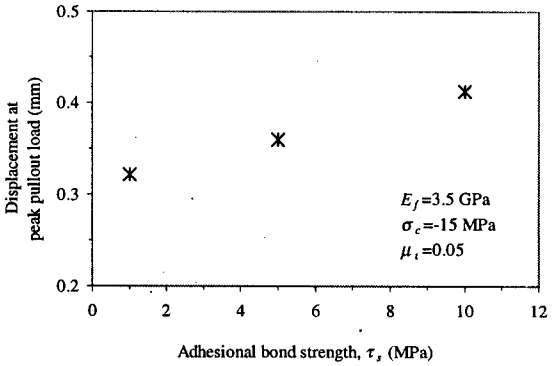

Figure 7.1.2c: Influence of adhesional bond strength on pullout displacement corresponding to peak pullout load (E_f=3.5 GPa)

In Figure 7.1.2b, the pullout load at initial debonding and the peak pullout load are plotted as a function of adhesional bond strength, τ_s. Both the pullout load at initial debonding and the peak pullout load increase with increase in adhesional bond strength; however, the rate of increase of the latter is smaller than that of the former. Comparing Figures 7.1.1b and 7.1.2b it can also be noted that for any given adhesional bond strength, the initial debonding load for low modulus fibers is much smaller than that for high modulus fibers. Moreover, disparity between the two increases with increase in adhesional bond strength. It can also be noted that when adhesional bond strength increases from –1 MPa to –10 MPa, peak pullout load increases by about 49% for high modulus fiber, on the other hand, peak pullout load increases only by about 7% for low modulus fibers.

In Figure 7.1.2c, displacement at the peak pullout load is plotted as a function of adhesional bond strength, τ_s. In the figure, it can be seen that the displacement at peak pullout load increase with increase in adhesional bond strength, τ_s. Comparing Figures 7.1.1c and 7.1.2c it can be noted that at any given adhesional bond strength, the displacement at peak pullout load for low modulus fibers is much greater than for high modulus fibers.

Figure 7.1.2d shows variation in pullout load as a function of debond length for the case when τ_s = -5 MPa. In the same figure, components of pullout load (i.e., the adhesional component and the frictional component) are also plotted. It can be noted that variation in the pullout load and its components with increase in debond length is similar to that for high modulus fibers.

Figure 7.1.2e shows pullout load and its components as a function of debond length at different values of adhesional bond strength, τ_s. From this figure, the following important observations can be made:

- Pullout load corresponding to any given debond length increases with increase in adhesional bond strength, τ_s. However, at complete debonding, magnitude of pullout load is independent of adhesional bond strength, τ_s.
- Prior to complete debonding, the adhesional component of pullout load increases with increase in adhesional bond strength. On the other hand, the frictional component of pullout load decreases with increase in adhesional bond strength.
- In Figures 7.1.1e and 7.1.2e it can be seen that when adhesional bond strength is increased from -1 MPa to -10 MPa, the increase in the peak pullout load for high modulus fibers is about 49%. On the other hand, the same for low modulus fibers is only about 7%. The reason for this disparity is that for low modulus fibers, much of the increase in the adhesional component of pullout load obtained with increase in adhesional bond strength is compensated by the corresponding decrease in the frictional component of pullout load. From the viewpoint of optimization of interfacial properties, this observation is significant, since it demonstrates that efficiency of low modulus fibers cannot be improved substantially by solely increasing adhesional bond strength.

- Catastrophic debonding takes place at τ_s = -5.0 MPa and -10 MPa. On the other hand, at τ_s = -1.0 MPa the debonding process is completely stable, i.e., pullout load continues to increase until the fiber is completely debonded.
- Other parameters remaining same, catastrophic debond length, $l_{d,cat}$ decreases with increase in the adhesional bond strength, τ_s. Also, the catastrophic debond length is greater for low modulus fibers in comparison to its high modulus counterparts.

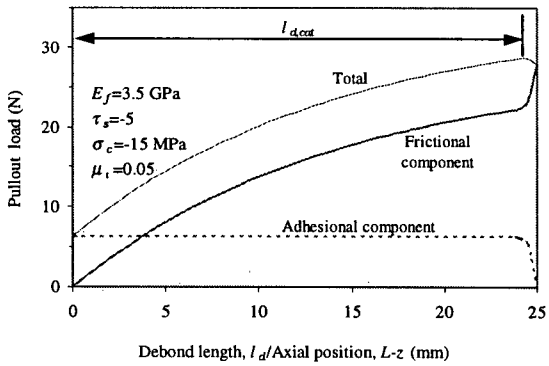

Figure 7.1.2d: Variation in pullout load and pullout load components as a function of debond length (E_f=3.5 GPa)

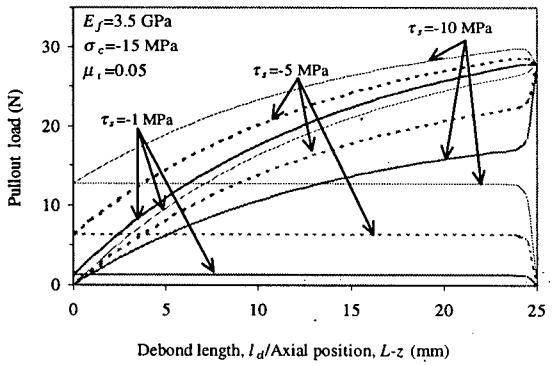

Figure 7.1.2e: Variation in pullout load and its components as a function of debond length at different values of adhesional bond strength, τ_s (E_f=3.5 GPa)

Figure 7.1.2f shows the axial load distribution in the fiber at the initiation of debonding for different adhesional bond strengths, τ_s. In the figure, it can be seen that the fiber axial load increases with increase in adhesional bond strength, τ_s. It can also be noticed that axial load in the fiber is maximum at the loaded fiber end and it decreases very rapidly along the embedded fiber length. Thus, for low modulus fibers only a very small length of the fiber is mobilized in the stress transfer process prior to initiation of interfacial debonding. Comparing Figures 7.1.1f and 7.1.2f it can be seen that prior to initiation of interfacial debonding, the rate of decrease in axial load along the embedded fiber length for low modulus fibers is very rapid in comparison to that for high modulus fibers. This means that prior to initiation of interfacial debonding, the length of fiber mobilized in the stress transfer process is longer for high modulus fibers in comparison to that for low modulus fibers. Observations similar to those above can be made for the interfacial shear stress distribution along the embedded fiber length of low modulus fibers (Figure 7.1.2g).

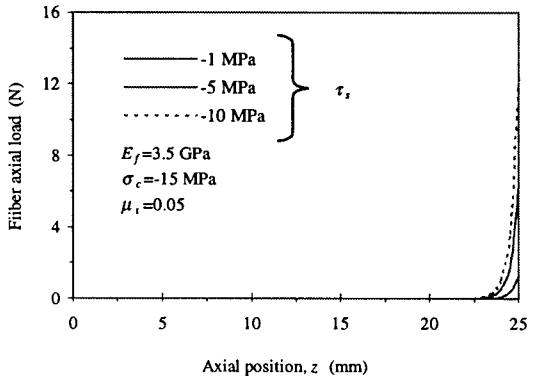

Figure 7.1.2f: Fiber Axial load distribution in fiber at initial debonding (E_f=3.5 GPa)

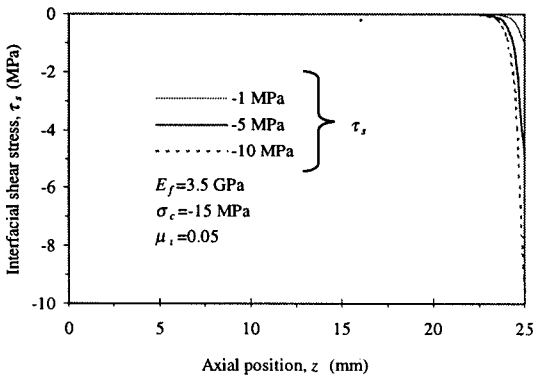

Figure 7.1.2g: Interfacial shear stress distribution at initial debonding (E_f=3.5 GPa)

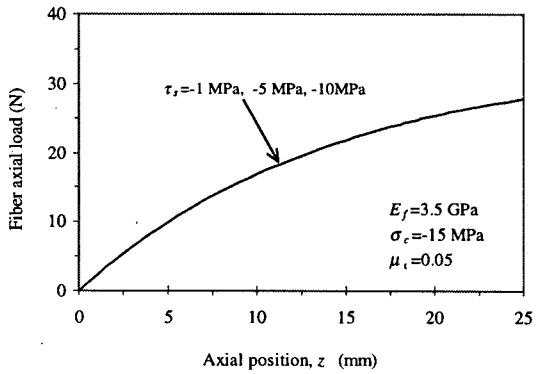

Figure 7.1.2h: Fiber axial load distribution at completion of debonding, (E_f=3.5 GPa)

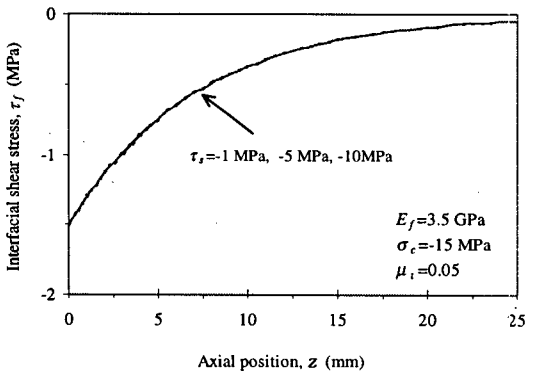

Figure 7.1.2i: Interfacial shear stress distribution at completion of debonding, (E_f=3.5 GPa)

Figure 7.1.2h shows the variation in axial load distribution at completion of debonding for different values of adhesional bond strength, τ_s. In the figure, it can be seen that axial load distribution along the fiber length is independent of adhesional bond strength, τ_s (at completion of interfacial debonding). It can also be noticed that fiber axial load is a maximum at the loaded fiber end and it decreases to a value of zero at the embedded fiber end. Comparison of Figures 7.1.2f and 7.1.2h clearly depicts that the axial load distributions at initiation of debonding and at completion of debonding are very different. In the former case only a part of the fiber is axially loaded, whereas in the latter case, the whole fiber is axially loaded. Figure 7.1.2i shows the interfacial shear stress distribution at completion of interfacial debonding. It can be seen that interfacial shear stress is a maximum at the embedded fiber end, and it decreases towards the exit fiber end. Poisson's contraction of the fiber is responsible for the observed variation in shear stress distribution along the embedded length of fiber. Comparing Figures 7.1.1i and 7.1.2i it

can also be seen that for low modulus fibers, the rate at which interfacial shear stress decays is more rapid in comparison to that for high modulus fibers.

7.1.2 Influence of Interfacial Contact Stress, σ_c

The influence of interfacial contact stress, σ_c, on progressive debonding and fiber pullout response is investigated below. For this purpose, parametric studies are carried out on two fibers with different elastic moduli. The first fiber has an elastic modulus of 210 GPa and the same for the second fiber is 3.5 GPa.

7.1.2.1 Fiber Elastic Modulus, E_f = 210 GPa

Parametric studies are carried out for three different values of interfacial contact stress, σ_c: -5 MPa, -15 MPa and -30 MPa. Assumed values of other interfacial properties are: τ_s = -1.0 MPa and $\mu = 0.065\, e^{-0.7 p_d} + 0.035$ (μ_i =0.1 and μ_{ss} =0.035). Mechanical properties of fiber are assumed as: E_f=210 GPa (elastic modulus) and, ν_f=0.30 (Poisson's ratio), and the same for matrix are assumed as 30 GPa and 0.20, respectively. Total fiber length, L, is taken as 50 mm (i.e., one side embedded length=25 mm), and fiber diameter is taken as d=1.0 mm. The assumed value of b (the outer radius of matrix cylinder) is 50 mm. Note that an elastic modulus of 210 GPa corresponds to that of steel.

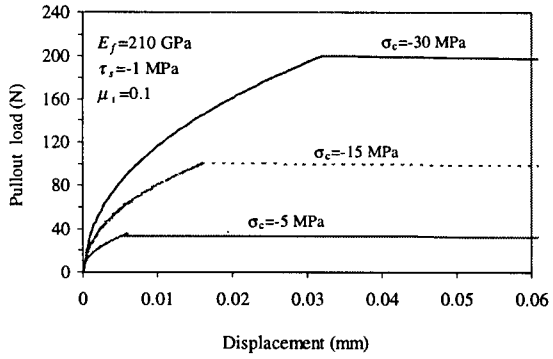

Figure 7.1.3a: Influence of interfacial contact stress on pullout response (E_f=210 GPa)

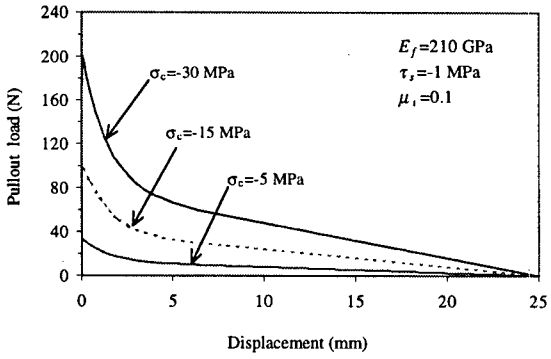

Figure 7.1.3b: Influence of interfacial contact stress on pullout response (E_f=210 GPa)

The prepeak part of pullout curves and the complete pullout curves for different values of interfacial contact stress, σ_c are shown in Figures 7.1.3a and 7.1.3b, respectively. In the former figure it can be noticed that the prepeak pullout curves become nonlinear at very small values of pullout loads. It can also be noticed that both the peak pullout load and the displacement at peak

pullout load increase with increase in interfacial contact stress, σ_c. In the latter figure it can be noticed that the postpeak pullout response varies greatly at different values of interfacial contact stress, σ_c, and in general, postpeak pullout loads increase with increase in interfacial contact stress, σ_c. In other words, energy absorbed during the process of fiber pullout increases with an increase in interfacial contact stress, σ_c.

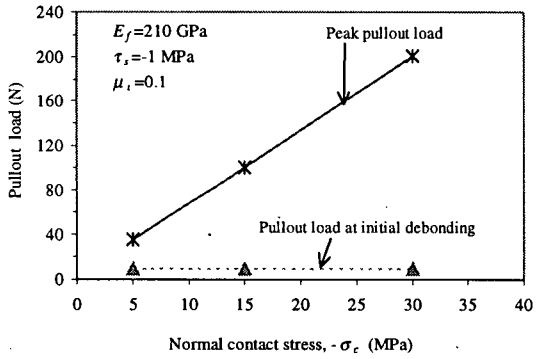

Figure 7.1.3c: Influence of interfacial contact stress on pullout load at initial debonding and peak pullout load (E_f=210 GPa)

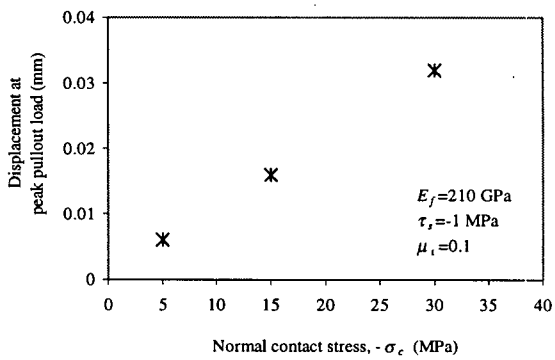

Figure 7.1.3d: Influence of interfacial contact stress on pullout displacement at the peak pullout load (E_f=210 GPa)

In Figure 7.1.3c, the pullout load at initial debonding and the peak pullout load are plotted as a function of interfacial contact stress, σ_c. In this figure it can be seen that the peak pullout load increases and the pullout load at initial debonding remains unchanged with increase in interfacial contact stress, σ_c. In Figure 7.1.3d, displacement at the peak pullout load is plotted as a function of interfacial contact stress, σ_c. In the figure, it can be seen that pullout displacement at peak pullout load increases with increase in interfacial contact stress, σ_c.

Given the dependence of pullout performance on interfacial contact stress, σ_c, two approaches can be used for improving fiber efficiency:

- Using a matrix that shrinks more during curing, setting and hardening, so that a higher value of contact stress, σ_c, is generated at the interface.
- Intelligently designing the fiber such that interfacial contact stress, σ_c, increases during the process of fiber pullout.

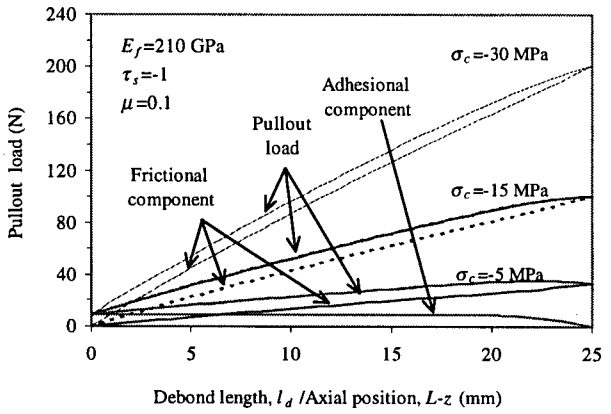

Figure 7.1.3e: Variation in pullout load and its components as a function of debond length (E_f=210 GPa)

Figure 7.1.3e shows pullout load and its components as a function of debond length at different values of interfacial contact stress, σ_c. From this figure, the following important observations can be made:

- Pullout load corresponding to any given debond length increases with increase in interfacial contact stress, σ_c.
- Prior to complete debonding, the frictional component of pullout load increases with increase in interfacial contact stress, σ_c. On the other hand, the adhesional component of pullout load is not affected by change in interfacial contact stress, σ_c.

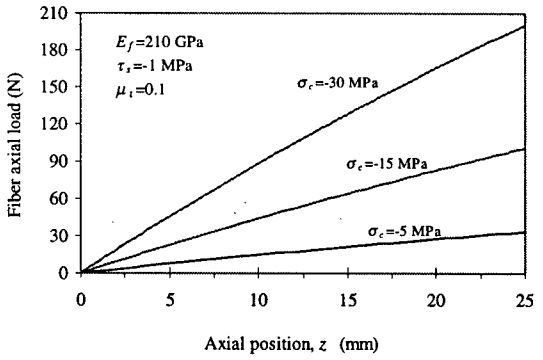

Figure 7.1.3f: Fiber axial load distribution at completion of debonding (E_f=210 GPa)

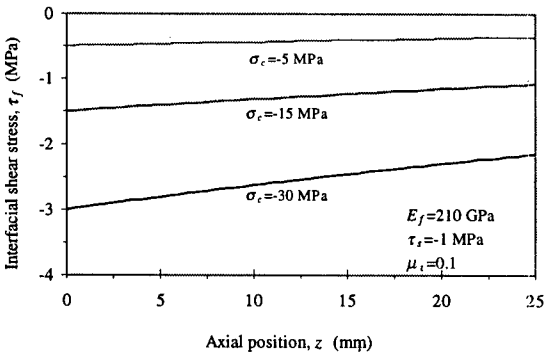

Figure 7.1.3g: Interfacial shear stress distribution at completion of debonding (E_f=210 GPa)

Figure 7.1.3f shows the variation in axial load distribution at completion of debonding for different values of interfacial contact stress, σ_c. In the figure, it can be seen that axial load along the embedded fiber length increases with increase in interfacial contact stress, σ_c. It can also be

noticed that the fiber axial load is maximum at the loaded fiber end and it decreases almost linearly to a value of zero at the embedded fiber end. Figure 7.1.3g shows the interfacial shear stress distribution at completion of interfacial debonding. From this figure two observations can be made. First, interfacial shear stress increases with increase in interfacial contact stress, σ_c. Secondly, for any given value of interfacial contact stress, σ_c, the interfacial shear stress is maximum at the embedded fiber end and it gradually decreases towards the exit fiber end. Poisson's contraction of the fiber is responsible for the observed interfacial shear stress distribution along the embedded length of fiber.

7.1.2.2 Elastic Modulus, E_f = 3.5 GPa

Parametric studies are carried out for three different values of interfacial contact stress, σ_c: -5 MPa, -15 MPa and -30 MPa. Assumed values of other interfacial properties are: τ_s = -1.0 MPa and $\mu = 0.02\, e^{-0.3 p_d} + 0.03$ (μ_i =0.05 and μ_{ss} =0.03). Mechanical properties of fiber are assumed as: E_f=3.5 GPa (elastic modulus) and ν_f=0.35 (Poisson's ratio), and the same for matrix are assumed as 30 GPa and 0.30, respectively. Total fiber length, L, is taken as 50 mm (one side embedded length=25 mm), and fiber diameter is taken as d=1.0 mm. The assumed value of b (the outer radius of matrix cylinder) is 50 mm. Note that an elastic modulus of 3.5 GPa corresponds to that of polypropylene.

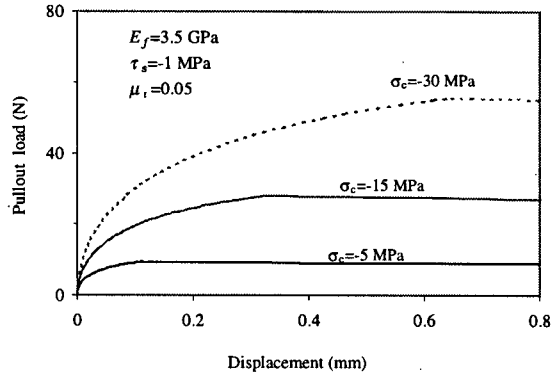

Figure 7.1.4a: Influence of interfacial contact stress on prepeak pullout response (E_f=3.5 GPa)

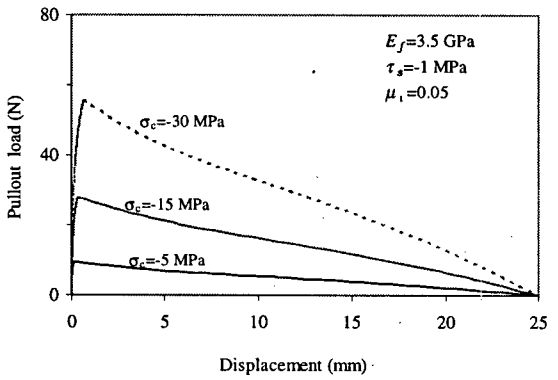

Figure 7.1.4b: Influence of interfacial contact stress on pullout response (E_f=3.5 GPa)

The prepeak part of pullout curves and the complete pullout curves for different values of interfacial contact stress, σ_c, are shown in Figures 7.1.4a and 7.1.4b, respectively. In the former figure, it can be noticed that the prepeak pullout curves become nonlinear at very small values of pullout loads. It can also be noticed that both the peak pullout load and the displacement at peak

pullout load increase with increase in interfacial contact stress, σ_c. In the latter figure it can be noticed that the postpeak pullout response varies greatly at different values of interfacial contact stress, σ_c, and in general, postpeak pullout loads increase with increase in interfacial contact stress, σ_c. In other words, energy absorbed during the process of fiber pullout increases with increase in interfacial contact stress, σ_c.

Given the dependence of pullout performance on interfacial contact stress, σ_c, two approaches can be used for improving fiber efficiency as outlined in the previous sub-section (Section 7.1.2.1).

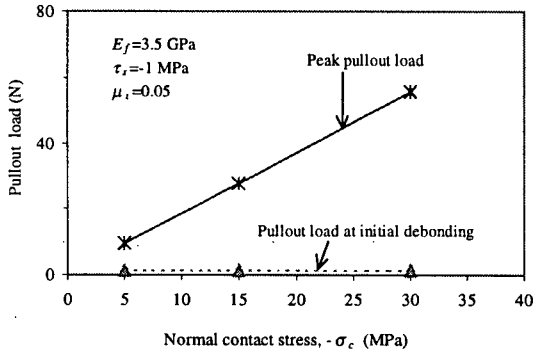

Figure 7.1.4c: Influence of interfacial contact stress on pullout load at initial debonding and peak pullout load (E_f=3.5 GPa)

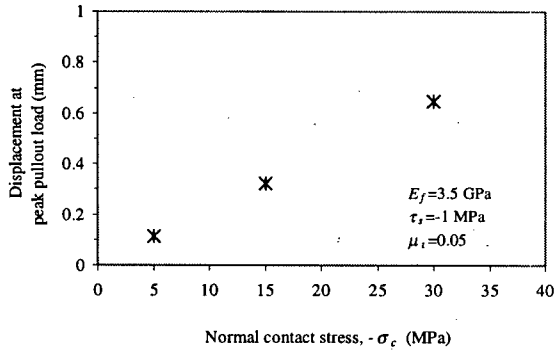

Figure 7.1.4d: Influence of interfacial contact stress on pullout displacement at the peak pullout load (E_f=3.5 GPa)

In Figure 7.1.4c, the pullout load at initial debonding and the peak pullout load are plotted as a function of interfacial contact stress, σ_c. In this figure it can be seen that the peak pullout load increases and the pullout load at initial debonding remains unchanged with increase in interfacial contact stress, σ_c. In Figure 7.1.4d, displacement at the peak pullout load is plotted as a function of interfacial contact stress, σ_c. In this figure, it can be seen that the displacement at the peak pullout load increases with increase in interfacial contact stress, σ_c. Comparing Figures 7.1.3d and 7.1.4d it can be noticed that at any given interfacial contact stress, σ_c, the displacement at the peak pullout load for low modulus fibers is much greater than that for their high modulus counterparts.

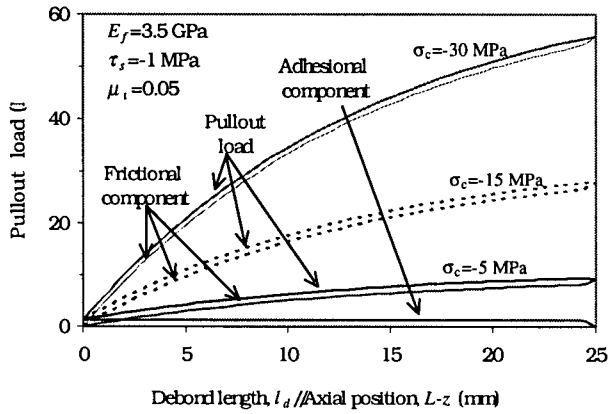

Figure 7.1.4e: Variation in pullout load and its components as a function of debond length (E_f=3.5 GPa)

Figure 7.1.4e shows pullout load and its components as a function of debond length at different values of interfacial contact stress, σ_c. In the figure, it can be seen that the pullout load corresponding to any given debond length increases with increase in interfacial contact stress, σ_c. It can be also seen that the frictional component of pullout load increases with increase in interfacial contact stress, σ_c. On the other hand, the adhesional component of pullout load is not affected by change in interfacial contact stress, σ_c.

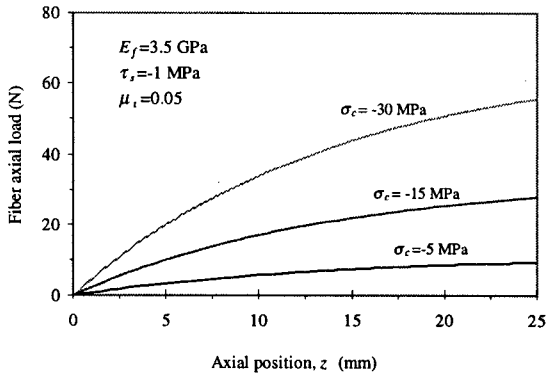

Figure 7.1.4f: Fiber axial load distribution at completion of debonding (E_f=3.5 GPa)

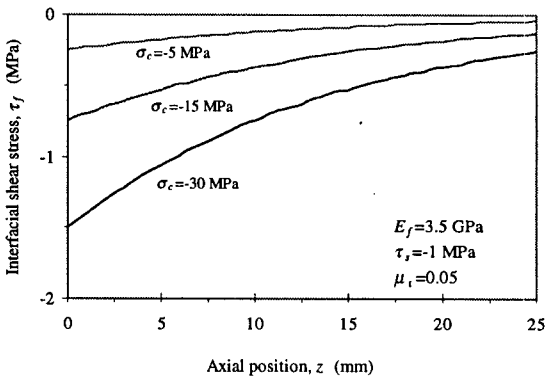

Figure 7.1.4g: Interfacial shear stress distribution at completion of debonding (E_f=3.5 GPa)

Figure 7.1.4f shows the variation in axial load distribution at completion of debonding for different values of interfacial contact stress, σ_c. In the figure, it can be seen that axial load along the embedded fiber length increases with increase in interfacial contact stress, σ_c. It can also be noticed that the fiber axial load is maximum at the loaded fiber end and it decreases to a value of

zero at the embedded fiber end. Figure 7.1.4g shows the interfacial shear stress distribution at completion of interfacial debonding. From this figure, two observations can be made. First, interfacial shear stress increases with increase in interfacial contact stress, σ_c, and secondly, for any given value of interfacial contact stress, σ_c, the interfacial shear stress is maximum at the embedded fiber end and it decreases towards the exit fiber end. Poisson's contraction of the fiber is responsible for the observed interfacial shear stress distribution along the embedded fiber length. Comparison of Figures 7.1.3g and 7.1.4g also indicates that for low modulus fibers the rate of decay of interfacial shear stress along the embedded length is more rapid in comparison to that for their high modulus counterparts.

7.1.3 Influence of Interfacial Coefficient of Friction, μ

The influence of the interfacial coefficient of friction, μ, on progressive debonding and fiber pullout response is investigated below. For this purpose parametric studies are carried out on two fibers with different elastic moduli. The first fiber has an elastic modulus of 210 GPa and the same for the second fiber is 3.5 GPa.

7.1.3.1 Fiber Elastic Modulus, E_f = 210 GPa

Parametric studies are carried out by varying the initial coefficient of friction, μ_i. The three chosen values of μ_i are: 0.1, 0.25 and 0.50, and the corresponding evolution laws for the coefficients of friction selected are: $\mu = 0.065\, e^{-0.7 p_d} + 0.035$, $\mu = 0.215\, e^{-0.7 p_d} + 0.035$, and $\mu = 0.465\, e^{-0.7 p_d} + 0.035$, respectively. Assumed values of the other interfacial properties were: τ_s = -1.0 MPa and σ_c = -15.0 MPa. Mechanical properties of the fiber are assumed as: E_f=210 GPa (elastic modulus), and, ν_f=0.30 (Poisson's ratio), and the same for the matrix are assumed as 30 GPa and 0.20, respectively. Total fiber length, L, is taken as 50 mm (i.e., one side embedded length=25 mm), and fiber diameter is taken as d=1.0 mm. The assumed value of b (the outer radius of matrix cylinder) is 50 mm. Note that an elastic modulus of 210 GPa corresponds to that of steel.

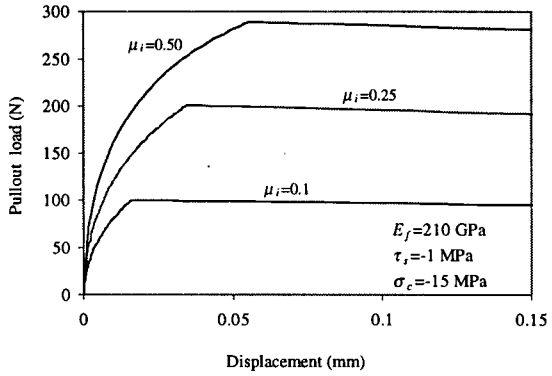

Figure 7.1.5a: Influence of interfacial coefficient of friction on pullout response (E_f=210 GPa)

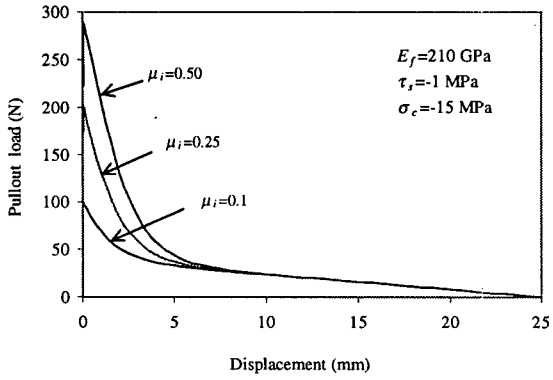

Figure 7.1.5b: Influence of interfacial coefficient of friction on pullout response (E_f=210 GPa)

The prepeak part of the pullout curves and the complete pullout curves for different values of interfacial coefficient of friction, μ_i, are shown in Figures 7.1.5a and 7.1.5b, respectively. In the former figure, it can be noticed that the prepeak pullout curves become nonlinear at very small values of pullout loads, and also that both the peak pullout load and the displacement at peak pullout load increase with increase in interfacial coefficient of friction, μ_i. In the latter figure, it can be noticed that the postpeak pullout response varies greatly at different values of interfacial coefficient of friction, μ_i, and in general, postpeak pullout loads increase with increase in interfacial coefficient of friction. In other words, energy absorbed during the process of fiber pullout increases with increase in interfacial coefficient of friction.

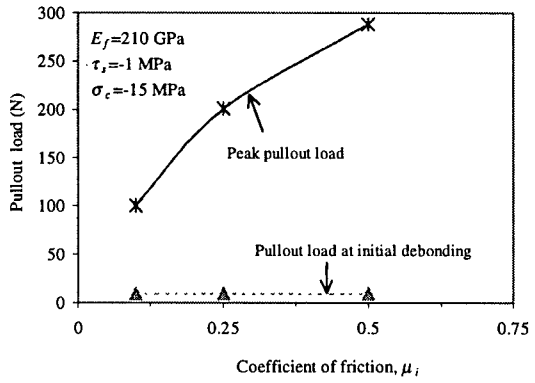

Figure 7.1.5c: Influence of interfacial coefficient of friction on pullout load at initial debonding and peak pullout load (E_f=210 GPa)

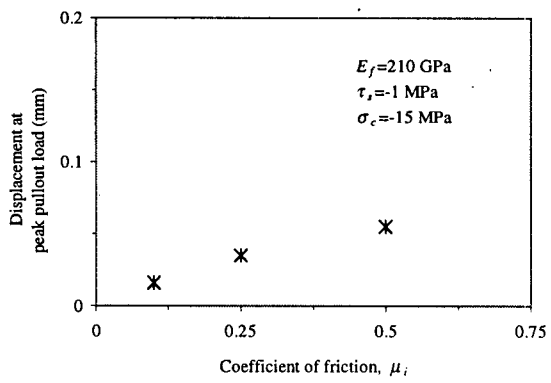

Figure 7.1.5d: Influence of interfacial coefficient of friction on pullout displacement at the peak pullout load (E_f=210 GPa)

In Figure 7.1.5c, the pullout load at initial debonding and the peak pullout load are plotted as a function of interfacial coefficient of friction, μ_i. In this figure, it can be seen that the peak pullout load increases with increase in interfacial coefficient of friction, μ_i. From the viewpoint

of optimization of interfacial properties, this observation is important, since it demonstrates that efficiency of high modulus fibers can be significantly improved by increasing the coefficient of friction.

In the Figure 7.1.5d, the displacement at the peak pullout load is plotted as a function of interfacial coefficient of friction, μ_i. In this figure it can be seen that the displacement at the peak pullout load increases with increase in the interfacial coefficient of friction, μ_i.

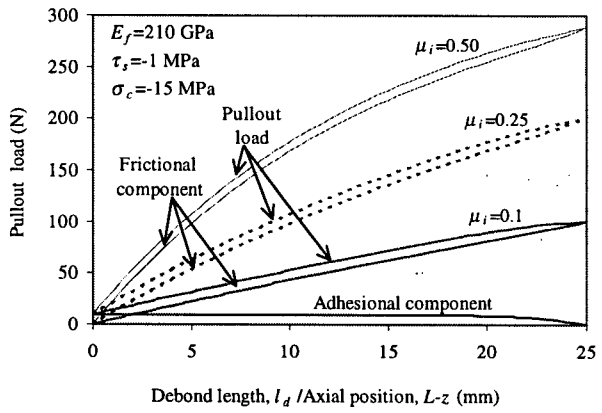

Figure 7.1.5e: Variation in pullout load and its components as a function of debond length (E_f=210 GPa)

Figure 7.1.5e shows pullout load and its components as a function of debond length at different values of interfacial coefficient of friction, μ_i. From this figure, the following important observations can be made:

- Pullout load corresponding to any given debond length increases with increase in interfacial coefficient of friction, μ_i.
- Prior to complete debonding, the frictional component of pullout load increases with increase in interfacial coefficient of friction, μ_i. On the other hand, the adhesional component of pullout load is not affected by a change in interfacial coefficient of friction, μ_i.

Figure 7.1.5f shows the variation in axial load distribution at completion of debonding for different values of interfacial coefficient of friction, μ_i. In the figure, it can be seen that the axial load along the embedded fiber length increases with increase in interfacial coefficient of friction, μ_i. It can also be noticed that the fiber axial load is maximum at the loaded fiber end and it decreases to a value of zero at the embedded fiber end. Figure 7.1.5g shows the interfacial shear

stress distribution at completion of interfacial debonding. In the figure it can be noticed that interfacial shear stress increases with increase in interfacial coefficient of friction, μ_i. Also, for any given value of interfacial coefficient of friction, μ_i the interfacial shear stress is maximum at the embedded fiber end and it decreases towards the exit fiber end. It can also be noticed that the rate of decay of interfacial shear stress along the embedded fiber length increases with increase in interfacial coefficient of friction, μ_i. Poisson's contraction of fiber is responsible for the observed interfacial shear stress distribution along the embedded length of fiber.

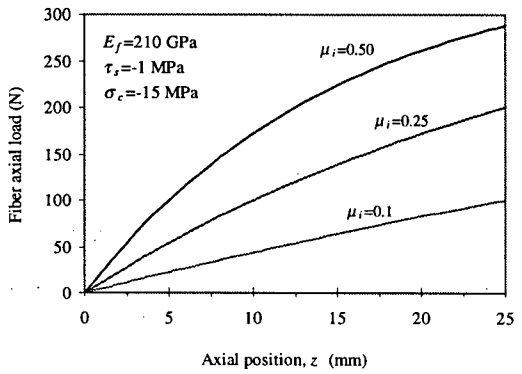

Figure 7.1.5f: Fiber axial load distribution at completion of debonding (E_f=210 GPa)

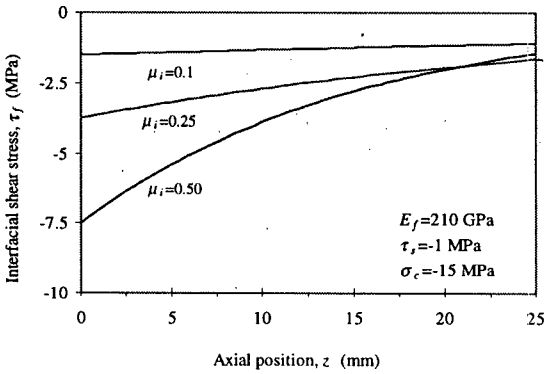

Figure 7.1.5g: Interfacial shear stress distribution at completion of debonding (E_f=210 GPa)

7.1.3.2 Fiber Elastic Modulus, E_f = 3.5 GPa

Parametric studies are carried out by varying the initial coefficient of friction, μ_i. The three chosen values of μ_i are: 0.05, 0.25 and 0.50, and the corresponding evolution laws for coefficient of friction selected are: $\mu = 0.02\, e^{-0.3 p_d} + 0.03$, $\mu = 0.22\, e^{-0.3 p_d} + 0.03$, and $\mu = 0.47\, e^{-0.3 p_d} + 0.03$, respectively. Assumed values of the other interfacial properties were: τ_s = -1.0 MPa and σ_c = -15.0 MPa. Mechanical properties of the fiber are assumed as: E_f=3.5 GPa (elastic modulus), and, ν_f=0.35 (Poisson's ratio), and the same for matrix are assumed as 30 GPa and 0.30, respectively. Total fiber length, L, is taken as 50 mm (i.e., one side embedded length=25 mm), and fiber diameter is taken as d=1.0 mm. The assumed value of b (the outer radius of matrix cylinder) is 50 mm. Note that an elastic modulus of 3.5 GPa corresponds to that of polypropylene.

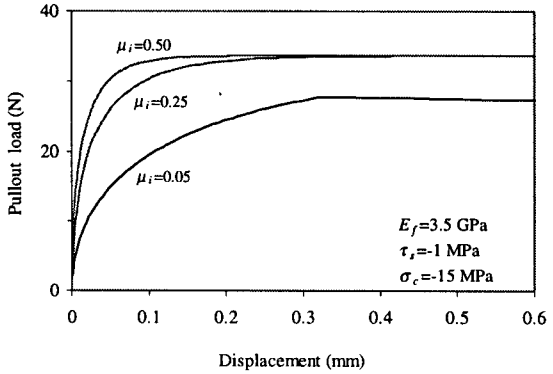

Figure 7.1.6a: Influence of interfacial coefficient of friction on prepeak pullout response (E_f=3.5 GPa)

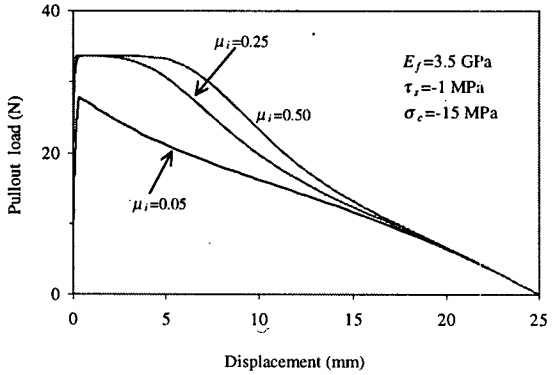

Figure 7.1.6b: Influence of interfacial coefficient of friction on pullout response (E_f=3.5 GPa)

The prepeak part of pullout curves and the complete pullout curves for different values of interfacial coefficient of friction, μ_i, are shown in Figures 7.1.6a and 7.1.6b, respectively. In the former figure, it can be noticed that the prepeak pullout curves become nonlinear at very small values of pullout loads. Also, increase in interfacial coefficient of friction, μ_i, beyond a certain value does not produce any increase in peak pullout load. From Figure 7.1.6b, it can be observed that the total pullout energy does not increase significantly with increase in coefficient of friction.

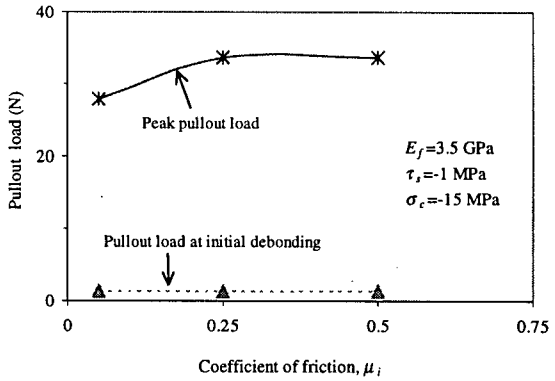

Figure 7.1.6c: Influence of interfacial coefficient of friction on pullout load at initial debonding and peak pullout load (E_f=3.5 GPa)

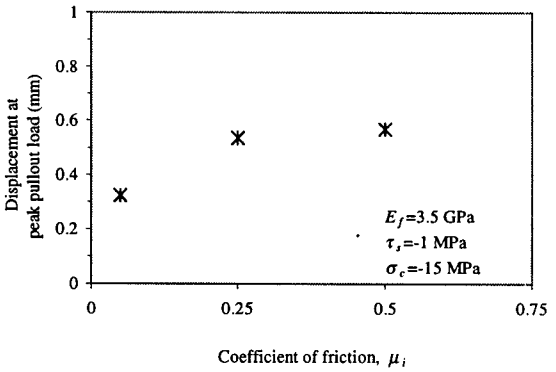

Figure 7.1.6d: Influence of interfacial coefficient of friction on pullout displacement at the peak pullout load (E_f=3.5 GPa)

In Figure 7.1.6c, the pullout load at initial debonding and the peak pullout load are plotted as a function of interfacial coefficient of friction, μ_i. In this figure, it can be seen that the peak pullout load initially increases, and then it becomes constant with increase in interfacial coefficient of friction, μ_i. From the viewpoint of optimization of interfacial properties, this observation is important, since it demonstrates that the efficiency of low modulus fibers cannot

be significantly improved by solely increasing the coefficient of friction. In Figure 7.1.6d, displacement at the peak pullout load is plotted as a function of interfacial coefficient of friction, μ_i, and it can be seen that the displacement at the peak pullout load increases at a decaying rate with increase in interfacial coefficient of friction, μ_i.

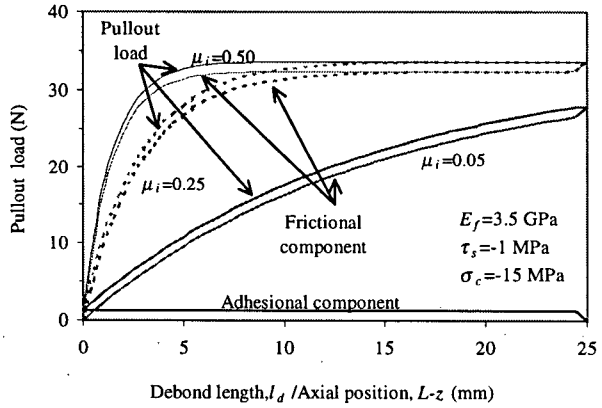

Figure 7.1.6e: Variation in pullout load and its components as a function of debond length (E_f=210 GPa)

Figure 7.1.6e shows pullout load and its components as a function of debond length at different values of interfacial coefficient of friction, μ_i. In this figure, it can be seen that in the lower range of coefficient of friction, μ_i ($\cong$ 0.05 to 0.25), pullout load corresponding to any given debond length increases with increase in interfacial coefficient of friction, μ_i. On the other hand, in the higher range of coefficient of friction, μ_i ($\cong$ 0.25 to 0.50), pullout loads at smaller debond lengths (l_d < 10 mm) increase with increase in coefficient of friction, μ_i, while the difference between pullout loads due to increase in coefficient of friction vanishes at longer debond lengths.

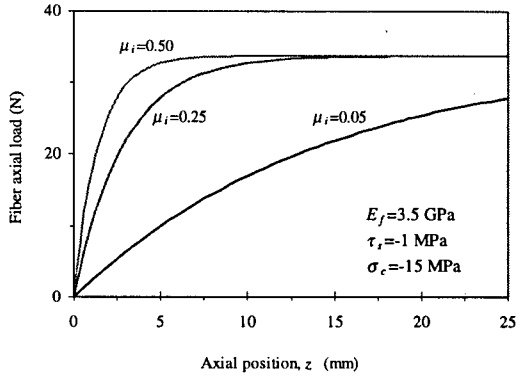

Figure 7.1.6f: Fiber axial load distribution at completion of debonding (E_f=3.5 GPa)

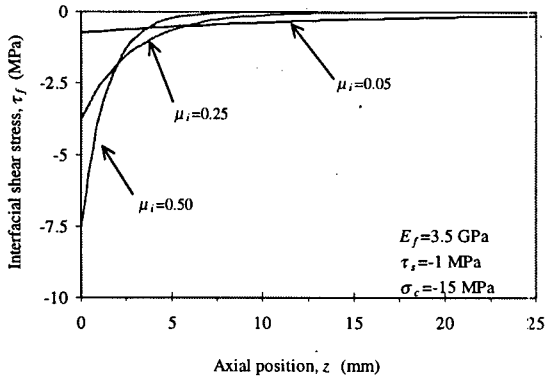

Figure 7.1.6g: Interfacial shear stress distribution at completion of debonding (E_f=3.5 GPa)

Figure 7.1.6f shows variation in axial load distribution at completion of debonding for different values of interfacial coefficient of friction, μ_i. It can be noticed that the fiber axial load is maximum at the loaded fiber end and it decreases to a value of zero at the embedded fiber end. In the figure, it can also be seen that at large values of interfacial coefficient of friction, μ_i, axial load remains constant along the major portion of embedded fiber length. Figure 7.1.6g shows the interfacial shear stress distribution at completion of interfacial debonding for different values of interfacial coefficient of friction, μ_i. In this figure, it can be noticed that the peak value of interfacial shear stress increases with increase in interfacial coefficient of friction, μ_i. Also, for any given value of interfacial coefficient of friction, μ_i, the interfacial shear stress is maximum at the embedded fiber end and it decreases towards the exit fiber end. Moreover, the rate of decrease in shear stress increases with increase in the interfacial coefficient of friction, μ_i. Another very interesting feature that can be seen in this figure is that when μ_i=0.5, the interfacial shear stress distribution along a major part of embedded fiber length is smaller than the same at μ_i = 0.05 and 0.25. Poisson's contraction of fiber is responsible for the observed interfacial shear stress distribution along the embedded fiber length. Comparison of Figures 7.1.5g and 7.1.6g also indicates that for low modulus fibers, the interfacial shear stress along the embedded length decays more rapidly in comparison to their high modulus counterparts.

7.2 Conclusions

- Prior to initial debonding pullout curve is linear and the stress transfer between fiber and matrix is purely elastic via adhesional shear stresses.
- After initial debonding, further debonding (i.e., progressive debonding) requires the applied pullout load to overcome the interfacial frictional shear stresses at the debonded interface and adhesional shear stresses at the bonded interface. As a result, the pullout load required to further debond the interface depends upon the extent of prior debonding. During progressive interfacial debonding, the pullout curve becomes nonlinear. Pullout load during progressive debonding increases because the rate of increase in the frictional component of pullout load with increase in debond length is greater than the corresponding rate at which the adhesional component of the pullout load decreases. At the peak pullout load, the rate of increase in the frictional component of pullout load becomes equal to the rate of decrease in the bond component of the pullout load. Beyond the peak pullout load, the remaining bonded portion of interface debonds catastrophically.

- Both the pullout load at initial debonding and the peak pullout load increase with increase in adhesional bond strength. For low modulus fibers (3.5 GPa) these increases are much smaller relative to high modulus fibers. This is because, for low modulus fibers much of the increase in the bond component of pullout load obtained with increase in adhesional bond strength is compensated by the corresponding decrease in the frictional component of pullout load. From the viewpoint of optimization of interfacial properties, this observation is important, since it demonstrates that efficiency of low modulus fibers cannot be improved significantly by solely increasing adhesional bond strength.
- Prior to complete debonding, the bond component of pullout load increases with increase in adhesional bond strength. On the other hand, the frictional component of pullout load decreases with increase in adhesional bond strength.
- Other parameters remaining the same, debond length at catastrophic debonding decreases with increase in adhesional bond strength. The interfacial debonding process is completely stable at very low values of adhesional bond strength for both the high modulus and the low modulus fibers.
- Prior to initiation of debonding, the rates of decrease in axial load and interfacial shear stress along the embedded fiber length for low modulus fibers are much more rapid in comparison to those for high modulus fibers. As a result, for low modulus fibers, only a very small embedded length of the fiber is mobilized in the stress transfer process prior to initiation of debonding. On the other hand, for high modulus fibers, a relatively longer fiber length is mobilized in the stress transfer process prior to initiation of debonding.
- For a given set of interfacial properties, catastrophic debond length decreases with increase in fiber elastic modulus, i.e., the higher the fiber modulus, the smaller is the catastrophic debond length.
- At completion of debonding and during fiber pullout interfacial shear stress is maximum at the embedded fiber end and it decreases towards the exit fiber end. Poisson's contraction of the fiber in the radial direction reduces the resultant contact stress at the interface and, hence, the interfacial shear stress. Because low modulus fibers undergo higher Poisson's contraction, interfacial shear stresses along the fiber length decrease at a faster rate in comparison to those for high modulus fibers.
- The peak pullout load increases with increase in interfacial contact stress, and this is because the frictional component of pullout load increases with increase in interfacial contact stress. Also, pullout loads on the post peak descending branch of the pullout curve increase with

increase in interfacial contact stress. Thus, the energy absorbed during the process of fiber pullout also increases with increase in interfacial contact stress. The above observations are valid for fibers of different modulus.

- The magnitude of interfacial shear stresses mobilized over the debonded interface increases with increase in interfacial contact stress. Also, for any given value of interfacial contact stress, the interfacial shear stress is maximum at the embedded fiber end and it decreases towards the exit fiber end. These observations are true for both high modulus as well as low modulus fibers. For a given set of interfacial properties, the rate of decrease of interfacial shear stress along the embedded length is greater for low modulus fiber.
- Given the dependence of pullout performance on interfacial contact stress, two approaches can be applied to improve fiber efficiency – i). using a matrix that shrinks more during curing, setting and hardening such that a higher value of interfacial contact stress is generated at the interface, and ii). intelligently designing fiber such that interfacial contact stress increases during the process of fiber pullout.
- The peak pullout load for high modulus fibers increases with increase in interfacial coefficient of friction. From the viewpoint of optimization of interfacial properties, this observation is important, since it demonstrates that efficiency of high modulus fibers can be significantly improved by increasing the coefficient of friction. On the other hand, for low modulus fibers, the peak pullout load initially increases and then it becomes constant with increase in interfacial coefficient of friction. Again, from the viewpoint of optimization of interfacial properties, this observation is important, since it demonstrates that efficiency of low modulus fibers cannot be significantly improved by solely increasing the coefficient of friction.
- The magnitude of interfacial shear stresses over the debonded interface increases with increase in interfacial coefficient of friction. For any given value of interfacial coefficient of friction, the interfacial shear stress is maximum at the embedded fiber end and it decreases towards the exit fiber end. The interfacial shear stress along the fiber length decreases more rapidly with increases in the interfacial coefficient of friction. These observations are true for both high modulus as well as low modulus fibers.

Chapter 8

Conclusions

Principal conclusions drawn from this research can be grouped into the following categories:

Macromechanical Behavior of FRC & Toughness Characterization

- Important material factors that influence post-cracking response (strengthening/toughness) of fiber reinforced concrete include fiber aspect ratio, fiber surface characteristics, fiber geometry, fiber volume content, shrinkage properties of matrix, and properties of mineral admixtures such as pozzolans.
- The measured flexural load versus deflection response of fiber reinforced cement-based composites, particularly of the ones containing low fiber volume fractions of steel or synthetic fibers is greatly affected by the machine configuration. For machines with an open-loop test configuration and low stiffness, the applied flexural load drops suddenly in an uncontrolled and unstable manner immediately following the peak load – the extent of this instability is a function of the machine stiffness and the rate of loading. Beyond the zone of instability, the flexural load versus deflection plot attains a stable softening level, during which loads are functions of the test machine characteristics. For the aforementioned reasons, the use of such load versus deflection curves to quantify toughness translates into meaningless toughness parameters. Unfortunately, the existing standards to characterize toughness (for example, ASTM C1018 [4] and JSCE SF4 [5]) allow the use of such flexural load versus deflection curves.
- Assessment of a new toughness characterization technique termed the Residual Strength Test Method (RSTM) has been made. In this technique, a stable narrow crack is first created in the specimen by applying flexural load in parallel with a steel plate under controlled conditions. The plate is then removed, and the specimen is tested in a routine manner in flexure to obtain the post-crack load versus displacement response. Post-peak flexural response obtained using this technique correlates very well with those obtained with relatively stiffer test configurations such as closed-loop test machines. A good agreement between the flexural response obtained from the aforementioned methods seems to validate

the Residual Strength Test Method. The Residual Strength Test Method is simple, and can be carried out easily in any commercial laboratory equipped with a test machine with low stiffness.

- The Residual Strength Test Method is seen to be effective in differentiating between different fiber types, fiber lengths, fiber configurations, fiber volume fractions, fiber geometries and fiber moduli. In particular, the technique is extremely useful for testing cement-based composites containing fibers at very low dosages (< 0.5% by volume).

Bond-Slip Performance of Fibers Embedded in Cementitious Matrices

- The maximum pullout load is influenced by the embedded fiber length. With increases in fiber length, the maximum pullout load increases, attaining an asymptote at long fiber lengths. The aforementioned observation is found to be valid for fibers with different elastic moduli.
- For a given fiber length and diameter, the maximum pullout load increases with increase in fiber surface roughness. Additionally, for a fiber of a given length, the displacement corresponding to the maximum pullout load and the total energy absorption increase with increase in surface roughness. The disparity between the maximum pullout loads for a smooth steel fiber and a rough steel fiber decreases with increase in fiber length. In particular, the asymptotic value of maximum pullout load attained at long fiber lengths in the case of rough steel fibers is approximately similar to that for smooth steel fibers.
- The maximum pullout load is also influenced by the shrinkage properties of the matrix – for a fiber of given length and diameter, the maximum pullout load with non-shrink grout matrix is substantially lower than that obtained with normal portland cement matrix. This observation is valid for fibers of different length, and therefore, the asymptotic value of pullout stress attained in the case of non-shrink grout matrix is much lower in comparison to that with normal portland cement matrix.
- For a given type of matrix and fiber length, steel fibers attained a greater peak pullout load in comparison to polypropylene fibers. In addition, for polypropylene fibers, the asymptotic value of pullout stress is attained at much smaller fiber length in comparison to that with steel fibers.

Progressive Debonding Model for Fiber Pullout

- To understand the mechanics of interaction between fibers and matrices, a shear-lag model is proposed to study the problem of fiber pullout. The proposed model is unique because of its ability to take into consideration the evolution of the interfacial properties during the pullout process. The analysis of the problem can be divided into three stages:

  - During stage 1, the fiber remains completely bonded along its embedded length, and the displacements at the fiber-matrix interface are compatible. Analysis is based on the shear-lag theory with the maximum shear stress as the criterion for fiber-matrix interfacial debonding. During this stage, resistance to fiber pullout is derived through the interfacial adhesional shear stress. Closed-form solutions are derived for the fiber axial stress distribution, the interfacial shear stress distribution, the fiber displacement, and the initial debonding stress. The closed-form solution for the initial debonding stress depicts that the initial debonding stress primarily depends upon the elastic properties of the fiber and the fiber length.

  - During stage 2, the fiber is partially bonded along its embedded length. The adhesional shear stresses at the bonded interface and the frictional shear stresses at the debonded interface resist the fiber pullout. Interfacial friction is modeled using the Coulomb's law and the Poisson's effect along the debonded interface is modeled by considering the fiber and the matrix to be held together in a shrink-fit configuration. It has been shown that for any interfacial debond length, the fiber pullout stress is a summation of the two components – the one arising due to the adhesional shear bond and the other arising due to the frictional shear bond. Closed-form solutions are derived for the fiber axial stress distribution, the interfacial shear stress distribution, the fiber pullout stress versus debond length relationship, and the fiber displacement versus debond length relationship.

  - The interfacial debonding process becomes catastrophic at the instant when the fiber pullout stress begins to drop with increase in debond length. This condition is satisfied when the difference between the change in the frictional component of pullout stress and the change in adhesional component of pullout stress occurring due to increase in debond length minimizes. Closed-form solutions are derived for the catastrophic debond length, the peak pullout stress and the displacement corresponding to peak pullout stress.

  - During stage 3, the fiber is completely debonded along its embedded length and fiber pullout is initiated. Frictional shear stresses existing over the debonded interface resist

pullout of the fiber from the matrix. Closed-form solutions are derived for the fiber axial stress distribution, the interfacial frictional shear stress distribution, the pullout stress and the fiber displacement.

- Using the proposed progressive debonding model it is possible to predict the complete pullout response. Theoretical predictions from the proposed model compare well with the experimental pullout data.

- A procedure to calibrate interfacial properties from experimental pullout data is established. It is shown that interfacial contact stress can be calculated using the asymptotic value of pullout stress on the peak pullout stress versus embedded length plot. The adhesional bond strength can be calculated from the initial slope of the peak pullout stress versus embedded length plot. Based on energy considerations, a method is proposed to calculate the coefficient of friction as a function of pullout distance. The evolution law for coefficient of friction depicts that interfacial coefficient of friction decays exponentially with increase in fiber pullout distance. This observation is found to be valid for fibers of different elastic modulus. Smoothening of the interface as a result of the matrix wear during fiber pullout appears to be the reason for this behavior.

- Prior to the initial debonding, the stress transfer between fiber and matrix is purely elastic (i.e., via adhesional shear stresses) and the corresponding pullout curve is linear. After the initial debonding, further debonding (i.e., progressive debonding) requires the applied pullout load to overcome the interfacial frictional shear stresses at the debonded interface and adhesional shear stresses at the bonded interface. As a result, the pullout load required to further debond the interface depends upon the extent of prior debonding. During progressive interfacial debonding, the pullout curve becomes nonlinear. Pullout load during progressive debonding increases because the rate of increase in the frictional component of the pullout load with increase in debond length is greater than the corresponding rate at which the adhesional component of the pullout load decreases. At the peak pullout load, the rate of increase in the frictional component of pullout load becomes equal to the rate of decrease in the bond component of the pullout load. Consequently, beyond the peak pullout load, the remaining bonded portion of interface debonds catastrophically.

- Both the pullout load at initial debonding and the peak pullout load increase with increase in adhesional bond strength. For the low modulus fibers ($\cong$3.5 GPa) these increases are not as significant relative to those obtained in the case of high modulus fibers. This is because for

low modulus fibers much of the increase in the bond component of the pullout load obtained with increase in the adhesional bond strength is compensated by the corresponding decrease in the frictional component of the pullout load. From the viewpoint of optimization of the interfacial properties, this observation is important, since it demonstrates that efficiency of low modulus fibers cannot be improved significantly solely by increasing the adhesional bond strength.

- For a given debond length, the bond component of pullout load increases and the frictional component of pullout load decreases with increase in adhesional bond strength. The other parameters remaining constant, the debond length at the occurrence of catastrophic debonding decreases with increase in the adhesional bond strength.

- Prior to initiation of debonding, the rates of decrease in axial load and interfacial shear stress along the embedded fiber length are greater for low modulus fibers in comparison to high modulus fibers. Consequently, for low modulus fibers, only a very small embedded fiber length is mobilized in the stress transfer process. On the other hand, for high modulus fibers, a relatively longer fiber length is mobilized in the stress transfer process.

- For a completely debonded interface, interfacial frictional shear stress is maximum at the embedded fiber end and it decreases towards the exit fiber end. Poisson's contraction of fiber in the radial direction reduces the resultant contact stress at the interface and the consequent interfacial frictional shear stress. Because the low modulus fibers undergo a higher Poisson's contraction, the interfacial frictional shear stresses along the fiber length decrease at a greater rate in comparison to those in the case of high modulus fibers.

- The peak pullout load increases with increase in interfacial contact stress. This is because the frictional component of pullout load increases with increase in interfacial contact stress. Also, pullout loads on the post-peak descending branch of the pullout curve increase with increase in interfacial contact stress. Energy absorbed during the process of fiber pullout also increases with increase in interfacial contact stress. The above observations are valid for fibers of different moduli.

- The magnitude of interfacial shear stresses mobilized over the debonded interface increases with an increase in interfacial contact stress. Also, for any given value of interfacial contact stress, the interfacial shear stress is maximum at the embedded fiber end and it decreases towards the exit fiber end. These observations are true for both high modulus as well as low

modulus fibers. For a given set of interfacial properties, the rate of decrease in interfacial shear stress along the embedded length is greater for low modulus fiber.

- Given the dependence of pullout performance on interfacial contact stress, two approaches can be used to improve fiber efficiency – i). using a matrix that shrinks more during curing, setting and hardening such that a higher value of interfacial contact stress is generated at the interface, and ii). intelligently designing fiber such that interfacial contact stress increases during the process of fiber pullout.
- The peak pullout load for high modulus fibers increases with increase in interfacial coefficient of friction. From the viewpoint of optimization of the interfacial properties this observation is important, since it demonstrates that efficiency of high modulus fibers can be significantly improved by increasing the coefficient of friction. However, the above is not the case with low modulus fibers.

Recommendations for Future Studies

- In the current research program, fiber pullout response under static loading was investigated. However, the micromechanical properties of the interface and the mechanical properties of the constituents, (i.e., fiber and matrix) may be expected to depend upon the rate of loading. In such a scenario, fiber pullout response will be a function of the rate of loading. It is recommended that studies be carried out to investigate the influence of loading rate on fiber pullout response. In this context, it will be worthwhile to examine:
  - The influence of matrix modification by mineral admixtures, such as silca-fume, fly-ash, high reactivity metakaoline, etc.
  - The influence of matrix modification by chemical admixtures, such as air entraining agents, high-range water-reducing admixtures, etc.
  - The influence of polymer viscoelasticity in the case of polymeric fibers.
- Fiber-matrix interfacial properties are expected to change as a result of the treatment of fiber surface with chemical coatings such as Organo-functional silanes. It is recommended that studies be carried out to investigate the extent of dependence of fiber pullout response on different chemical coatings.

- Fibers with extremely good interfacial bond with matrix may fracture during the pullout process. This appears to be the case with polyvinyl alcohol fibers (fiber PVA-1). Thus, for polyvinyl alcohol fibers, improved pullout efficiency may be expected with reduction in interfacial bond. This reduction can possibly be achieved either through the application of appropriate chemical coating on fiber surface or through a change in the chemical properties of the base polymer. Studies are recommended in this context.

- It is recommended that studies be carried out to understand the influence of fiber inclination and ductility of fiber material on the pullout response. Also there is need to model the pullout response for these scenarios.

- In the current research, sensitivity of fiber pullout response on the interfacial contact stress was observed. It was seen that the interfacial contact stress was dependent upon the shrinkage properties of the matrix. However, the interfacial contact stress may also depend upon any external confining stress applied to the fiber reinforced cementitious composite. It is recommended that further studies be carried out to investigate and characterize the influence of external confining stresses on fiber pullout response.

- In addition to the initial water/cement ratio, the shrinkage behavior of cementitious matrix is highly dependent upon the environmental conditions existing during setting, hardening and curing of matrix. Since the fiber-matrix interfacial properties and the pullout response are strongly dependent upon the shrinkage behavior of cementitious matrix (as seen in this study), it becomes important to diligently control the environmental parameters while producing fiber reinforced cementitious composites. Now, what constitute optimal environmental conditions remains to be investigated. Detailed investigations are recommended to explore this aspect.

Bibliography

[1]. Bentur, A. and Mindess, S., "*Fiber Reinforced Cementitious Composites*," Elsevier Applied Science, London, 1990.

[2]. Balaguru, P. N. and Shah, S. P., "*Fiber-Reinforced Cement Composites*," McGraw-Hill, Inc., New York, 1992.

[3]. Hannant, D. J., "*Fiber Cements and Fiber Concretes*," John Wiley & Sons, Chichester, 1978.

[4]. ASTM C 1018-94b, "Standard Test Method for Flexural Toughness and First-Crack Strength of Fiber reinforced Concrete (Using Beam With Third-Point Loading)", *American Society of Testing and Materials*, Philadelphia, 1994, pp. 506-513.

[5]. JSCE-SF4 Standard, "Method of Test for Flexural Strength and Flexural Toughness of Fiber Reinforced Concrete", *Japan Society of Civil Engineers*, 1984, pp. 58-66.

[6]. Banthia, N., Dubey, A., and Bell, L., "The True Stress Transfer Capability of Polymeric Fibers Across a Crack: Quest for a Stable Test," Proceedings of the *Asia-Pacific Specialty Conference on Fibre Reinforced Concrete, Singapore*, Aug 1997.

[7]. ASTM C1399-98, "Standard Test Method for Obtaining Average Residual Strength of Fiber Reinforced Concrete," *American Society of Testing and Materials*, Philadelphia, 1999.

[8]. Piggott, M. R., "Failure Processes in the Fibre-Polymer Interphases," *Composites Science and Technology*, V. 42, 1991, pp. 57-76.

[9]. Kasperkiweicz, J. and Skarendahl, A., "Toughness Estimation in FRC Composites", CIB Report 4:90, ISRN CBI R –90/4—SE, *Swedish Cement and Concrete Research Institute*, 100 44 Stockholm, 1990, pp. 52.

[10]. CUR-Recommendation N° 10, "Design Calculation and Performance of Industrial Floors in Steel Fiber Reinforced Concrete" (in Dutch), 1987.

[11]. Belgian Standard NBN B15-238, "Tests on Fiber Reinforced Concrete – Bending Test on Prismatic Specimens" (in Dutch), 7 pp., 1992.

[12]. Spanish AENOR UNE 83-510-89, "Determination of the Toughness Index and First-crack Strength" (in Spanish), 4 pp., 1989.

[13]. DBV, "Basis for Evaluation of Steel Fiber Reinforced Concrete for Use in Industrial Floor" (in German), pp. 258-272, 1991.

[14]. DBV, "Technology of Steel Fiber Reinforced Concrete and Steel Fiber Shotcrete (in German), pp. 3-18, 1992.

[15]. DBV, "Basis for Dimensioning SFRC in Tunnel Construction" (in German), pp. 19-43, 1992.

[16]. RILEM Technical Committee 49 TFR, "Testing Method for Fibre Reinforced Cement-Based Composites", *Materiaux et Constructions*, No. 102, 1984, pp. 441-456.

[17]. ACI Committee 544, "Measurement of Properties of Fiber Reinforced Concrete", *ACI Materials Journal*, pp. 583-593, 1988.

[18]. Barr, B., "The Fracture Characteristics of FRC Materials in Shear", in *Fibre Reinforced Concrete – Properties and Applications, ACI SP-1-5(28)*, S. P. Shah and G. B. Batson (eds.), 1987, pp. 27-53.

[19]. Barr, B. and Hasso, E. B. D., "A Study of Toughness Indices", *Magazine of Concrete Research*, V. 37, No. 132, 1985, pp. 162-174.

[20]. Barr, B. and Hasso, E. B. D., "The Precision of Toughness Indices Based on Multiples of First-crack Deflections", *ACI Materials Journal*, 1985, pp. 870-876.

[21]. Barr, B. and Hasso, E. B. D., "Fracture of GRC Materials", *International Journal of Cement Composites and Light Weight Concrete*, V. 4, No. 3, 1982, pp. 163-171.

[22]. Barr, B., Liu, K., and Dowers, R. C., "A Toughness Index to Measure the Energy Adsorption of Fibre Reinforced Concrete", *International Journal of Cement Composites and Lightweight Concrete*, V. 4, No. 4, 1982, pp. 221-227.

[23]. French Standard AFNOR P19-409, "Steel Fibre Concrete – Bending Tests" (in French), 8 pp., 1993.

[24]. Wang, Y. and Backer, S., "Toughness Determination of Fiber Reinforced Concrete", *The International Journal of Cement Composites and Lightweight Concrete*, V. 11, No. 1, 1989, pp. 11-19.

[25]. Ward, R. J. and Li, V. C., "Dependence of Flexural Behavior of Fibre Reinforced Mortar on Material Fracture Resistance and Beam Size", *ACI Materials Journal*, V. 87, No. 6, 1990, pp. 627-637.

[26]. Shah, S. P., Daniel, J. I., and Ludiridja, D., "Toughness of Glass Fibre Reinforced Concrete Panels Subjected to Accelerated Aging", *PCI Journal*, V. 32, No. 5, 1987, pp. 82-89.

[27]. Mobasher, B. and Shah, S. P., "Test Parameters for Evaluating Toughness of Glass Fiber Reinforced Concrete Panels, *ACI Materials Journal*, 1989, pp. 448-458.

[28]. Banthia, N. P. and Trottier, J. -F., "Test Methods for Flexural Toughness Characterization of Fibre Reinforced Concrete: Some Concerns and A Proposition", ACI Materials Journal, Col. No. 92(1), 1995, pp. 48-57.

[29]. Norwegian Concrete Association, Publication No. 7, "Guidelines for Shotcrete, Oslo, June 1993.

[30]. EFNARC, European Specification for Sprayed Concrete, Final Draft Published by the European Federation of National Associations of Specialist Contractors and Material Suppliers to the Construction Industry (EFNARC), Hampshire, U. K., pp. 31, 1996.

[31]. Johnston, C. D., "Definition and Measurement of Flexural Toughness parameters for Fibre Reinforced Concrete," *Cement, Concrete and Aggregate*, CCAGDP, V. 4, No. 2, Winter 1982, pp. 53-60.

[32]. Johnston, C. D., "Methods of Evaluating Performance of Fibre-Reinforced Concrete", in Fiber-Reinforced Cementitious Materials, S. Mindess and J. Skanly (eds.), *Materials Research Society Symposium Proceedings*, 211, pp. 15-25, Materials Research Society, Pittsburgh, 1991.

[33]. Johnston, C. D. and Gray, R. J., "Flexural Toughness and First-Crack Strength of Fibre-Reinforced Concrete Using ASTM C 1018," *Proceedings, Third International Symposium on Developments in Fibre Reinforced Cement and Concrete*, RILEM, Paper 5.1, 1986.

[34]. Johnston, C. D. and Skarendahl, A., "Comparative Flexural Performance Evaluation of Steel Fibre-Reinforced Concretes According to ASTM C 1018 Shows Importance of Fibre Parameters," RILEM, *Material and Structures*, V. 25, No. 148, 1992, pp. 191-200.

[35]. Johnston, C. D. and Authors, "Discussion of Reference 56, *ACI Materials Journal*, V. 89, No. 3, 1992, pp. 304-309.

[36]. Johnston, C. D., "Effects of Testing Rate and Age on ASTM C 1018 Toughness Parameters and Their Precision for Steel Fibre-Reinforced Concrete," *Cement Concrete and Aggregate*, CCAGDP, V. 15, No. 1, pp. 50-58, 1991.

[37]. Johnston, C. D., "Effects on Flexural Performance of Sawing Plain Concrete and Sawing and Other Methods of Altering the Degree of Fiber Alignment in Fibre-Reinforced Concrete," *Cement Concrete and Aggregate*, CCAGDP, V. 11, No. 1, 1989, pp. 23-29.

[38]. Johnston, C. D., "Deflection Measurement Considerations in Evaluating FRC Performance Using ASTM C 1018", *Testing of Fiber Reinforced Concrete, ACI SP-155*, D. J. Stevens (ed.), 1995, pp. 1-22.

[39]. Chen, L., Mindess, S., Morgan, D. R., Shah, S. P., Johnston, C. D., and Pigeon, M. "Comparative Toughness Testing of Fiber Reinforced Concrete", *Testing of Fiber Reinforced Concrete, ACI SP-155*, D. J. Stevens (ed.), 1995, pp. 41-75.

[40]. Chen, L., Mindess, S., and Morgan, D. R., "First Crack Strength and Flexural Toughness of Steel Fibre Reinforced Concrete," *ASCE Materials Journal*, V. 6, No. 4, 1994, pp. 529-541.

[41]. Gopalaratnam, V. S. and Gettu, R., "On the Characterization of Flexural Toughness in Fiber Reinforced Concretes", *International Journal of Cement and Concrete Composites*, 1995.

[42]. Gopalaratnam, V. S., Shah, S. P., Batson, G. B., Criswell, M. V., Ramakrishnan, V., and Wecharatna, M., "Fracture Toughness of Fiber Reinforced Concrete", *ACI Materials Journal*, V. 88, No. 4, 1991, pp. 339-353.

[43]. Banthia N. and Trottier, J. -F., "Concrete Reinforced with Deformed Steel Fibers", Part II: Toughness Characterization, *ACI Materials Journal*, V. 92, No. 2, 1995, pp. 146-154.

[44]. Banthia, N. and Trottier, J. -F., "Test Methods for Flexural Toughness Characterization of Fiber Reinforced Concrete: Some Concerns and a Proposition", *ACI Materials Journal*, V. 92, No. 1, 1995.

[45]. Trottier, J. -F. and Banthia, N. P., "Toughness Characterization of Steel-Fiber Reinforced Concrete, *Journal of Civil Engineering Materials*, ASCE, V. 6, No. 2, 1994, pp. 264-289.

[46]. Khajuria, A., El-Shakra, Z. M., Gopalaratnam, V. S., and Balaguru, P. "Influence of Test Control on the Load-Deflection Behavior of FRC", *Fiber Reinforced Concrete – Developments and Innovations, ACI SP-142*, J. I. Daniel and S. P. Shah (eds.), 1994, pp. 167-180.

[47]. El-Shakra, Z. M. and Gopalaratnam, V. M., "Deflection Measurement and Toughness Evaluations for FRC", Cement and Concrete Research, V. 26, No. 6, 1993, pp. 1455-1466.

[48]. Chen, L., "Flexural Toughness of Fiber Reinforced Concrete," *Ph.D. Thesis*, Department of Civil Engineering, The University of British Columbia, Vancouver, Canada, 1995.

[49]. Balaguru, P., Narahari, R., and Patel, M., "Flexural Toughness of Steel Fiber Reinforced Concrete", *ACI Materials Journal*, V. 89, No.6, 1992, pp. 541-546.

[50]. Ramakrishnan, V., Wu, G. Y., and Hosalli, G., "Flexural Behavior of Fiber Reinforced Concretes", *Transportation Research Record*, No. 1226, 1989, pp. 69-77.

[51]. Skjolsvold, O. and Hammer, T. A., "Toughness Testing of Fibre Reinforced Shotcrete", in Sprayed Concrete, Proceedings of Modern Use of Wet Meix Sprayed Reinforced Shotcrete for Underground Support," R. Kompen, O. A. Opsahl and K. R. Berg (eds.), Fagernes, Norway, 1993, pp. 67-77.

[52]. Cox, H. L., "The Elasticity and Strength of Paper and Other Fibrous Materials," *British Journal of Applied Physics*, V. 3, March 1952, pp. 72-79.

[53]. Greszczuk, L. B., "Theoretical Studies of the Mechanics of the Fiber-Matrix Interface in Composites," *Interfaces in Composites, ASTM STP 452,* American Society for Testing and Materials, Philadelphia, 1969, pp. 42-58.

[54]. Takaku, A., and Arridge, R. G. C., "The Effect of Interfacial Radial and Shear Stress on Fibre Pull-Out in Composite Materials," *Journal of Physics D: Applied Physics*, V. 6, 1973, pp. 2038-2047.

[55]. Lawrence, P., "Some Theoretical Considerations of Fibre Pull-out From an Elastic Matrix," *Journal of Material Science*, V. 7, No, 1, Jan. 1972, pp. 1-6.

[56]. Gopalaratnam, V. S., and Shah, S. P., "Tensile Fracture of Steel Fiber Reinforced Concrete," *ASCE Journal of Engineering Mechanics Division*, V. 113, No. 5, 1987, pp. 635-652.

[57]. Pinchin, D. J., and Tabor, D., "Inelastic Behavior in Steel Wire from Portland Cement Mortar," *Journal of Material Science*, V. 13, 1978, pp. 1261-1266.

[58]. Bartos, P., "Analysis of Pull-Out Tests on Fibers Embedded in Brittle Matrices," *Journal of Materials Science*, V. 15, 1980, pp. 3122-3128.

[59]. Laws, V., "Micromechanical Aspects of the Fibre-Cement Bond," *Composites*, April 1982, pp. 145-151.

[60]. Nammur, G. Jr., and Naaman, A. E., "Bond Stress Model for Fiber Reinforced Concrete Based on Bond Stress-Slip Relationship," *ACI Materials Journal*, V. 86, Jan-Feb. 1989, pp. 45-57.

[61]. Nammur, G. Jr., Naaman, A. E., and Clark, S. K., "Analytical Prediction of the Pull-Out Behavior of Steel Fibers in Cementitious Matrices," *Cement Based Composites: Bonding in Cementitious Composites*, Symposia Proceedings, V. 114, Materials Research Society, Pittsburgh, 1988, pp. 217-224.

[62]. Naaman, A. E., Namur, G. G., Alwan, J. M. and Najm, H. S., "Fiber Pullout and Bond Slip I: Analytical Study," *Journal of Structural Engineering*, V. 117, No. 9, 1991, pp. 2769-2790.

[63]. Naaman, A. E., Namur, G. G., Alwan, J. M. and Najm, H. S., "Fiber Pullout and Bond Slip II: Experimental Validation," *Journal of Structural Engineering*, V. 117, No. 9, 1991, pp. 2791-2800.

[64]. Stang, H., Li, Z. and Shah, S. P., "The Pullout Problem-The Stress Versus Fracture Mechanical Approach," *Journal of Engineering Mechanics, ASCE*, V. 116, No. 10, 1990, pp. 2136-2150.

[65]. Gopalaratnam, V. S., and Cheng, J., "On the Modelling of Inelastic Interfaces in Fibrous Composites," *Cement Based Composites: Bonding in Cementitious Composites*, Symposia Proceedings, V. 114, Materials Research Society, Pittsburgh, 1988, pp. 225-231.

[66]. Hsueh, C. H., "Elastic Load Transfer From Partially Embedded Axially Loaded Fiber to Matrix," *Journal of Material Science Letters*, V. 7, No. 5, 1988, pp. 497-500.

[67]. Hsueh, C. H., "Interfacial Debonding and Fiber Pullout Stresses of Fiber-Reinforced Composites," *Materials Science and Engineering*, A123, 1990, pp. 1-11.

[68]. Hsueh, C. H., "Interfacial Debonding and Fiber Pullout Stresses of Fiber Reinforced Composites II: Non-constant Interfacial Bond Strength," *Materials Science and Engineering*, A 125, 1990, pp. 67-73.

[69]. Wang, Y., Li, V. C., and Backer, S., "Modelling of Fibre Pull-Out from a Cement Matrix," *The International Journal of Cement Composites*, 1988, pp. 143-149.

[70]. Kim, J. K., Baillie, C. and Mai, Y. W., "Interfacial Debonding and Fiber Pullout Stresses, Part I: Critical Comparison of Existing Theories with Experiments," *Journal of Materials Science*, V. 27, 1991, pp. 3143-3154.

[71]. Yue, C. Y. and Cheung, W. L., "Interfacial Properties of Fibrous Composites - Part I & Part II," *Journal of Materials Science*, V. 27, 1991, pp. 3173-3191.

[72]. Banbaji, J., "On a More Generalized Theory of the Pullout Test from an Elastic Matrix, Part I-Theoretical Considerations & Part II-Application to a Polypropylene-Cement System," *Composites Science and Technology*, V. 32, 1988, pp. 183-207.

[73]. Bazant, Z. P. and Desmorat, R., "Size Effect in Fiber or Bar Pullout with Interface Softening Slip," *Journal of Engineering Mechanics*, V. 120, No. 9, 1994, pp. 1945-1962.

[74]. Leung, C. K. Y. and Li, V. C., "Applications of a Two-way Debonding Theory to Short Fibre Composites," *Composites*, V. 21, No. 4, 1990, pp. 305-317.

[75]. Rajagopalan, K. and Parameswaran, V. S., "A Study of the Mechanics of Fibre Debonding in Concrete with Micro-reinforcement," *Materiaux Et Constructions*, V. 8, No. 46, 1975, pp. 305-314.

[76]. Cordes, R. D., and Daniel I. M., "Determination of Interfacial Properties from Observations of Progressive Fiber Debonding and Pullout," *Composites Engineering*, V. 5, No. 6, 1995, pp. 633-648.

[77]. Chanvillard, G., and Aitcin, P. C., "Micromechanical Modeling of the Pull-Out Behavior of Wiredrawn Steel Fibers from Cementitious Matrices, in *Fiber Reinforced Cementitious Materials*, S. Mindess and J. Skalny, eds., V. 211, Materials Research Society, 1991, pp. 1436-1445.

[78]. Stang, H., Li, Z. and Shah, S. P., "The Pullout Problem-The Stress Versus Fracture Mechanical Approach," *Journal of Engineering Mechanics, ASCE*, V. 116, No. 10, 1990, pp. 2136-2150.

[79]. Stang, H. and Shah, S. P., "Fracture Mechanical Interpretation of the Fiber/Matrix Debonding Process in Cementitious Composites," in *Fracture Toughness and Fracture Energy of Composites*, ed. F. H. Wittmann, Elsevier 1986, pp. 513-523.

[80]. Shah, S. P. and Jenq, Y. S., "Fracture Mechanics of Interfaces," *Symposium Proceedings, Materials Research Society*, V. 114, 1987, pp. 205-216.

[81]. Li, S. H., Shah, S. P., Li, Z. and Mura, T., "Prediction and Verification of Interface Debonding for Fiber Reinforced Cementitious Materials," *ASTM SP 156-8.*

[82]. Li, S. H., Shah, S. P., Li, Z. and Mura, T., "Micromechanical Analysis of Multiple Fracture and Evaluation of Debonding Behavior for Fiber Reinforced Composites," *International Journal of Solids and Structures*, V. 30, No. 11, 1993, pp. 1429-1459.

[83]. Li. Z., Mobasher, B. and Shah, S. P., "Characterization of Interfacial Properties in Fiber-Reinforced Cementitious Composites," *Journal of American Ceramic Society*, V. 74, No. 9, 1991, pp. 2156-2164.

[84]. Li. Z., Mobasher, B. and Shah, S. P., "Evaluation of Interfacial Properties in Fiber Reinforced Cementitious Composites," *Fracture Processes in Concrete, Rock and Ceramics*, eds. J. G. M. van Mier, J. G. Rots and A. Baker, RILEM, E & F. N. Spon., London, 1991, pp. 317-326.

[85]. Morrison, J. K., Shah, S. P. and Jenq, Y. S., "Analysis of Fiber Debonding and Pullout in Composites," *Journal of Engineering Mechanics, ASCE*, V. 114, No. 2, 1988, pp. 277-294.

[86]. Ouyang, A., Pacios, A. and Shah, S. P., "Pullout of Inclined Fibers from Cementitious Matrices," *Journal of Engineering Mechanics*, V. 120, No. 12, 1994, pp. 2641-2659.

[87]. Bowling, J. and Groves, G. W., "The Debonding and Pullout of Ductile Wires from a Brittle Matrix," *Journal of Material Science*, V. 14, 1979, pp. 431-442.

[88]. Kim, J. K., Baillie, C. and Mai, Y. W., "Interfacial Debonding and Fiber Pullout Stresses, Part II: A New Model Based on the Fracture Mechanics Approach," *Journal of Materials Science*, V. 27, 1991, pp. 3155-3166.

[89]. Zhou. L. M., Kim, J. K. and Mai, Y. W., "Micromechanical Characterization of Fibre/Matrix Interfaces," *Composites Science and Technology*, V. 48, 1993, pp. 227-236.

[90]. Gurney, C. and Hunt, J., "Quasi-static Crack Propagation," *Philosophical Transactions, Royal Society of London*, V. 299, Ser. A, 1967, pp. 508-524.

[91]. Atkinson, C., Avila, J., Betz, E. and Smelser, R. E., "The Rod Pullout Problem, Theory and Experiment," *Journal of Mechanics and Physics of Solids*, V. 30, No. 3, 1982, pp. 97-120.

[92]. Gao, Y. C., Mai, Y. W. and Cotterell, B., "Fracture of Fiber Reinforced Materials," *Journal of Applied Mathematics and Physics*, V. 39, 1988, pp. 550-572.

[93]. Wells, J. K. and Beaumont, P. W. R., "Debonding and Pullout Processes in Fibrous Composites," *Journal of Material Science*, V. 20, 1985, pp. 1275-1284.

[94]. Hutchinson, J. W. and Jensen, H. M., "Models of Fiber Debonding and Pullout in Brittle Composites with Friction," *Mechanics of Materials*, V. 9, 1990, pp. 139-163.

[95]. Mandel, J. A., Wie, S. and Said, S., "Studies of the Properties of the Fiber-Matrix Interface in Steel Fiber Reinforced Mortar, *Materials Journal, ACI*, V. 84, No.2, 1987, pp. 530-562.

[96]. Wei, S., Mandel, J. A. and Said, S., "Study of the Interface Strength in Steel Fiber Reinforced Cement Based Composites, *Materials Journal, ACI*, V. 86, No.2, 1987, pp. 597-605.

[97]. Wang, C., "Fracture Mechanics of Single-Fibre Pull-out Test," *Journal of Material Science*," V. 32, 1997, pp. 483-490.

[98]. Shannag, J. M., Brincker, R. and Hansen, W., "Interfacial (Fiber-Matrix) Properties of High-Strength Mortar (150 MPa) from Fiber Pullout," *ACI Materials Journal*, V. 93, No. 5, 1996, pp. 480-486.

[99]. Stang, H., "The Fibre Pullout Problem: An Analytical Investigation," *Series R, No. 204*, Department of Structural Engineering, Technical University of Denmark, Lyngby, Denmark, 1985.

[100]. Muki, R. and Sternberg, E., "Elastostatic Load Treansfer to a Half-Space From a Partially Embedded Axially Loaded Rod," *International Journal of Solids and Structures*, V. 6, No. 1, 1970, pp. 69-90.

[101]. Freund, L. B., "The Axial Force Needed to Slide a Circular Fiber Along a Hole in an Elastic Material and Implications for Fiber Pull-out," *European Journal of Mechanics*, A/Solids, V. 11, No. 1, 1992, pp. 1-19.

[102]. Tsai, K. H. and Kim K. S., "The Micromechanics of Fiber Pullout," *Journal of Mechanics of Physics of Solids*, V. 144, No. 7, 1996, pp. 1147-1177.

[103]. Marotzke, C, "The Elastic Stress Field Arising in the Single Fiber Pullout Test," *Composites Science and Technology*, V. 50, 1994, pp. 393-405.

[104]. Bartos, P., "Review Paper: Bond in Fibre Reinforced Cements and Concretes," *The International Journal of Cement Composites*, V. 3, No. 3, 1981, pp. 159-177.

[105]. Shah, S. P. and Ouyang C. S., "Mechanical Behavior of Fiber Reinforced Cement Based Composites," *Journal of American Ceramic Society*, V. 74, No. 11, 1991, pp. 2727-2738, 2947-2953.

[106]. Stang, H. and Shah, S. P., "Micromechanics of the Interfaces in Fibre Reinforced Cement Materials," *Interfacial Transition Zone in Concrete*, eds. J. C. Maso, RILEM Report 11, E & FN Spon, London, 1996, pp. 75-100.

[107]. Gray, R. J. and Johnston, C. D., "The Measurement of Fiber-Matrix Interfacial Bond Strength in Steel-Fibre-Reinforced Cementitious Composites," *Testing and Test Methods of Fibre Cement Composites*, RILEM Symposium 1978, The Construction Press, Lancaster, pp. 317-328.

[108]. Gray, R. J., "Experimental Techniques for Measuring Fibre/Matrix Interfacial Bond Shear Strength," *International Journal of Adhesion and Adhesives*, V. 3, No. 4, 1983, pp. 197-202.

[109]. Gray, R. J., "Analysis of the Effect of Embedded Fibre Length on Fibre Debonding and Pull-out from an Elastic Matrix," *Journal of Material Science*, V. 19, 1984, pp. 861-870.

[110]. Gray, R. J., "The Effect of Matrix Composition on Fibre/Matrix Interfacial Bond Shear Strength in Fibre-Reinforced Mortar," *Cement and Concrete Research*, V. 14, 1984, pp. 285-296.

[111]. Morton, J. and Groves, G. W., "Cracking of Composites Consisting of Discontinuous Ductile Fibers in a Brittle Matrix-Effects of Fiber Orientation," *Journal of Materials Science*, V. 9, 1974, pp. 1436-1445.

[112]. Brandt, A. M., "On the Optimal Direction of Short Metal Fibers in Brittle Matrix Composites," *Journal of Materials Science*, V. 20, 1985, pp. 3831-3841.

[113]. Baggott, R. and Gandhi, D., "Multiple Cracking in Aligned Polypropylene Fibre Reinforced Cement Composites," *Journal of Materials Science*, V. 16, 1981, pp. 65-74.

[114]. Bowling, J. and Groves, G. W., "The Debonding and Pull-out of Ductile Wires from a Brittle Matrix," *Journal of Material Science*, V. 114, 1979, pp. 431-442.

[115]. Wang, Y., Backer, S. and Li, V. C., "An Experimental Study of Synthetic Fibre Reinforced Cementitious Composites," *Journal of Material Science*, V. 22, 1987, pp. 4281-4291.

[116]. Wang, Y., Li, V. C. and Backer, S., "Analysis of Synthetic Fiber Pull-out From a Cement Matrix," *Cement Based Composites: Bonding in Cementitious Composites*, Symposia Proceedings, V. 114, Materials Research Society, Pittsburgh, 1988, pp. 159-165.

[117]. Wang, Y., Backer, S. and Li, V. C., "A Special Technique for Determining the Critical Length of Fibre Pull-out From a Cement Matrix," *Journal of Material Science Letters*, V. 7, 1988, pp. 842-844.

[118]. Li, V. C., Wang, Y. and Backer, S., "Effects of Inclining Angle, Bundling and Surface Treatment on Synthetic Fiber Pull-Out from a Cement Matrix," *Composites*, V. 21, No. 2, 1990, pp. 132-140.

[119]. Geng, Y. and Leung, C., "Damage Evolution of Fiber/Mortar Interface During Fiber Pullout," *Materials Research Society, Symposium Proceedings*, V. 370, 1995, pp. 519-536.

[120]. Geng, P. and Leung, C. K. Y., "Damage-Based Modeling of Fiber Pullout under Variable Compressive Stress," *Journal of Engineering Mechanics*, V. 123, No. 4, 1997, pp. 342-349.

[121]. Leung, C. K. Y. and Geng, Y., "Effect of Lateral Stresses on Fiber Debonding and Pullout," *Composites Engineering*, V. 5, No. 10-11, 1995, pp. 1331-1348.

[122]. Rossi, P. and Chanvillard, G., "New Geometry of Steel Fiber for Reinforced Concrete," *High Performance Fiber Reinforced Cement Composites*, H.W. Reinhardt and A.E. Naaman, eds., E. & F. N. Spon, London, 1992, pp. 129-139.

[123]. Naaman, A. E. and Najm. H., "Bond-Slip Mechanisms of Steel Fibers in Concrete," *ACI Materials Journal*, V. 88, No. 2, Sept.-Oct. 1991, pp. 135-145.

[124]. Mindess, S., "Tests to Determine the Mechanical Properties of the Interfacial Zone," *Interfacial Transition Zone in Concrete*, eds. J. C. Maso, RILEM Report 11, E & FN Spon., London, 1996, pp. 47-63.

[125]. Gopalaratnam, V. S. and Abu-Mathkour, H. J., "Investigation of the Pull-out Characteristics of Steel Fibers from Mortar Matrices," *Proceedings, International Symposium on Fibre Reinforced Concrete*, Madras, 1987, pp. 2.201-2.211.

[126]. Banthia, N., Yan, N., Chan, C., Yan, C. and Bentur, A., "Bond-Slip Mechanisms in Steel Micro-Fiber Reinforced Cement Composites," *Materials Research Society, Symposium Proceedings*, V. 370, 1995, pp. 539-548.

[127]. Banthia, N. and Trottier, J.-F., "Concrete Reinforced with Deformed Steel Fibers, Part I: Bond-Slip Mechanisms," *ACI Materials Journal*, V. 91, No. 5, Sept.-Oct. 1994, pp. 435-446.

[128]. Banthia, N. and Trottier, J. -F., "Strain-Rate Sensitivity of Fiber-Matrix Bond," *Proceedings of Canadian Symposium on Cement and Concrete, Ottawa*, 1993, pp. 603-618.

[129]. Banthia, N. and Trottier, J. -F., "Deformed Steel Fiber-Cementitious Matrix Bond Under Impact," *Cement and Concrete Research*, V. 21, No. 1, 1991, pp. 158-168.

[130]. Banthia, N. and Trottier, J. -F., "Effects of Curing Temperature and Early Freezing on the Pull-Out Resistance of Steel Fibers from a Cementitious Matrix," *Cement and Concrete Research*, V. 19, No. 5, 1989, pp. 727-736.

[131]. Banthia, N., "Study of Some Factors Affecting the Fiber-Matrix Bond in Steel Fiber Reinforced Concrete," *Canadian Journal of Civil Engineering*, V. 17, No. 4, 1990, pp. 610-620.

[132]. Banthia, N., Trottier, J.-F., Pigeon, M. and Krishnadev, M. R., "Deformed Steel Fiber Pull-Out: Material Characteristics and Metallurgical Process," *Proceedings: International Workshop on Fiber Reinforced Concrete*, Mainze, 1991.

[133]. Banthia, N. and Trottier, J. -F., "Micromechanics of Steel Fiber Pull-out, Rate Sensitivity at Low Temperatures," *Cement and Concrete Composites*, V. 14, 1992, pp. 119-130.

[134]. Banthia, N., Trottier, J. F. and Pigeon, M., "Fiber Pullout Mechanisms: Effects of Fiber Geometry, Loading Rate and Sub Zero Temperatures, *Proceedings of the International Conference on Recent Developments in Fibre Reinforced Cements and Concretes*, Cardiff, 1989, pp. 136-145.

[135]. Banthia, N., Trottier, J. F., Pigeon, M. and Krishnadev, M. R., "Deformed Steel Fiber Pullout: Material Characteristics and Metallurgical Processes," *High Performance Fiber Reinforced Cement Composites, RILEM*, eds. H. W. Reinhardt and A. E. Naaman, E & FN Spon., London, 1992, pp. 456-46.

[136]. Banthia, N. and Yan C., "Bond-slip Characteristics of Steel Fibers in High Reactivity Metakaoline (HRM) Modified Cement-Based Matrices," *Cement and Concrete Research*, 1997.

[137]. Krishnadev, M. R., Berrada, S., Banthia, N. and Trottier, J. -F., "Deformed Steel Fiber Pull-Out Mechanics: Influence of Steel Properties," in *Fiber Reinforced Cement and Concrete*, RILEM, R. N. Swamy, ed., E. & F. N. Spon, London, 1992, pp. 390-399.

[138]. Pacios, A., Ouyang, C. and S. P. Shah, "Rate effect on Interfacial Response Between Fibres and Matrix," *Materials and Structures*, V. 28, 1995, pp. 83-91.

[139]. Larson, B. K. and Bayasi, Z., "Carbon Fiber-Cement Adhesion in Carbon Fiber Reinforced Cement," *MS Thesis*, Department of Chemical Engineering, Michigan State University, East Lansing, 1988.

[140]. Maage, M., "Fibre Bond and Friction in Cement and Concrete," *Testing and Test Methods of Fibre Cement Composites*, RILEM Symposium 1978, The Construction Press, Lancaster, pp. 329-336.

[141]. Pinchin, D. J. and Tabor, D., "Interfacial Contact Pressure and Frictional Stress Transfer in Steel Fibere Cement," *Testing and Test Methods of Fibre Cement Composites*, RILEM Symposium 1978, The Construction Press, Lancaster, pp. 337-344.

[142]. Naaman, A. E. and Shah, S. P., "Pull-Out Mechanisms in Steel Fiber Reinforced Concrete," *Journal of the Structural Division*, ASCE, Aug. 1976, pp. 1537-1548.

[143]. Burakiewicz, A., "Testing of Fibre Bond Strength in Cement Matrix," *Testing and Test Methods of Fibre Cement Composites*, RILEM Symposium 1978, The Construction Press, Lancaster, pp. 355-365

[144]. Maage, M., "Interaction Between Steel Fibre and Cement Based matrixes," *Materials and Structures, Research and Testing* (RILEM), V. 10, No. 59, 1977, pp. 297-301.

[145]. Gokoz, U. N. and Naaman, A. E., "Effect of Strain-rate on the Pullout Behaviour of Fibres in Mortar," *International Journal of Cement Composites*, V. 3, 1981, pp. 187-202.

[146]. Pinchin, P. J. and Tabor, D., "Interfacial Phenomena in Steel Fiber Reinforced Cement I: Structure and Strength on Interfacial Region," *Cement and Concrete Research*, V. 8, No. 2, 1978, pp. 15-24.

[147]. Pinchin, D. J. and Tabor, D., "Interfacial Phenomena in Steel Fibre Reinforced Cement II: Pull-Out Behavior of Steel Wires," *Cement and Concrete Research*, V. 8, 1978, 139-150.

[148]. Beaumont, P. W. R. and Aleszka, J. C., "Cracking and Toughening of Concrete and Polymer-Concrete Dispersed with Short Steel Wires," *Journal of Materials Science*, V. 13, 1978, 1749-1769.

[149]. Kawamura, M. and Igarashi, S., "Fluorescence Microscopic Study of Fracture Process of the Interfacial Zone Between a Steel Fiber and the Cementitious Matrix under Pullout Loading," *ACI Special Publication, SP 156-10*, pp. 173-190.

[150]. Igarashi, S. I. and Kawamura, M., "Effects of the Addition of Silica Fume and Fine Aggregate on the Fracture Toughness for the Steel Fiber-Matrix Interfacial Zone," *RILEM Proceedings: Fracture Processes in Concrete, Rock and Ceramics*, J. G. M. van Mier, J. G. Rots, and A. Bekker, eds., E. & F. N. Spon, London, 1991, pp. 307-315.

[151]. Kawamura, M. and Igarashi, S., "Fracture Toughness for Steel Fiber-Cement Paste Interface Zone, *Journal of Materials in Civil Engineering*, V. 4, No. 3, 1992, pp. 227-239.

[152]. Laws, V., Lawrence, P. and Nurse, R. W., "Reinforcement of Brittle Material by Glass Fibers," *Journal of Physics D: Applied Physics,* V. 6, No. 19B, 1973, pp. 523-537.

[153]. Mobasher, B. and Shah, S. P., "Interaction Between Fibers and the Cement Matrix in Glass Fiber Reinforced Concrete," *ACI Special Publication No. SP-124*, ACI, Detroit, MI, 1990.

[154]. Shao, Y. S., Li, Z. and Shah, S. P., "Matrix Cracking and Interface Debonding in Fiber-Reinforced Cement-Matrix Composites," *Advanced Cement Based Materials*, V. 1, No. 2, 1993, pp. 55-66.

[155]. Stang, H., "Micromechanical Parameters, Fracture Processes and Application of Fiber Reinforced Concrete," in *Fracture of Brittle Disordered Materials: Concrete, Rock and Ceramics*, eds. G. Baker and B. L. Karihaloo, 1995, pp. 131-148.

[156]. Naaman, A. E., Moavenzadeh, F. and McGarry, F. J., "Probabilistic Analysis of Fiber Reinforced Concrete," *Journal of Engineering Mechanics*, ASCE, V. 100, 1974, pp. 397-413.

[157]. Bowling, J. and Groves, G. W., "Large Work of Fracture Values in Wire Reinforced, Brittle-Matrix Composites," *Journal of Material Science Letters*, V. 10, 1975, pp. 170-172.

[158]. Kelly, A. and Zweben, C., "Poisson Contraction in Aligned Fibre Composites Showing Pull-out," *Journal of Material Science Letters*, V. 11, 1976, pp. 582-587.

[159]. Kelley, A., "Interface Effects and the Work of Fracture of a Fibrous Composite," *Proceedings of Royal Society, London*, V. 319, 1970, pp. 95-116.

[160]. Barnes, B. D., Diamond, S. and Dolch, W. L., "The Contact Zone Between Portland Cement Paste and Glass Aggregate Surfaces," *Cement and Concrete Research*, V. 8, 1978, pp. 233-244.

[161]. Baggott, R. and Abdel-Monem, A. E. S., "Aspects of Bond in High Volume Fraction Steel Fibre Reinforced Calcium Silicates," *High Performance Fiber Reinforced Cement Composites, RILEM*, eds. H. W. Reinhardt and A. E. Naaman, E & FN Spon., London, 1992, pp. 444-455.

[162]. Al Kalaf, M. N. and Page, C. L., "Steel/Mortar Interfaces: Microstructure Features and Mode of Failure," *Cement and Concrete Research*, V. 8, No. 2, 1978, pp. 233-243.

[163]. Bentur, A. and Older, I., "Development and Nature of Interfacial Microstructure," *Interfacial Transition Zone in Concrete*, eds. J. C. Maso, RILEM Report 11, E & FN Spon, London, 1996, pp. 18-43.

[164]. Peled, A., Yankelevsky, D. and Bentur, A., "Bonding and Interfacial Microstructure in Cement Matrices Reinforced by Woven Fabric," *Materials Research Society Symposium Proceedings*, V. 370, Materials Research Society, 1995, pp. 549-558.

[165]. Rice, E. K., Vondran, G. L. and Kunbarge, H. O., "Bonding of Fibrillated Polypropylene Fibers to Cementitious materials," *Materials Research Society Symposium Proceedings*, V. 114, Materials Research Society, 1988, pp. 145-152.

[166]. Bentur, A., Mindess, S. and Diamond, S., "Pullout Processes in Steel Fibre Reinforced Cement," *Materiaux Et Constructions*, 1985, pp. 29-37.

[167]. Bentur, A., Diamond, S. and Mindess, S., "The Microstructure of the Steel Fibre-Cement Interface," *Journal of Materials Science*, V. 20, 1985, pp. 3610-3620.

[168]. Chen, Z. Y. and Wang, N. Z., "Strengthening the Interfacial Zone Between Steel Cement Paste," in Proceedings of 2nd *International Symposium on Brittle Matrix Composites*, Cedzyna, Poland, eds. A. M. Brandt and I. H. Marshall, Elsevier, Essex, U. K., 1989, pp. 342.

[169]. Marshall, D. B. and Oliver, W. C., "Measurement of Interfacial Mechanical Properties in Fiber-Reinforced Ceramic Composites," *Journal of American Ceramic Society*, V. 70, No. 8, 1987, pp. 542-548.

[170]. Singh, R., "Influence of Interfacial Shear Stress on First-Matrix Cracking Stress in Ceramic-Matrix Composites," *Journal of American Ceramic Society*, V. 73, No. 10, 1990, pp. 2930-2927.

[171]. Cao, H. C., Beschoff, E., Ruhle, M., Evans, A. G., Marshall, D. B. and Brennan, J. J., "Effect of Interfaces on the Properties of Fiber-Reinforced Ceramics," *Journal of American Ceramic Society*, V. 73, No. 6, 1990, pp. 1692-1699.

[172]. Evans, A. G., He, M. Y. and Hutchinson J. W., "Interface Debonding and Fiber Cracking in Brittle Matrix Composites," *Journal of American Ceramic Society*, V. 72, No. 12, 1989, pp. 2300-2303.

[173]. Thouless, M. D., Sbaizero, O., Sigl, L. S. and Evans, A. G., "Effect of Interface Mechanical Properties on Pullout in a Sic-Fiber-Reinforced Lithium Aluminum Silicate Glass-Ceramic," *Journal of American Ceramic Society*, V. 72, No. 4, 1989, pp. 525-32.

[174]. Thouless, M. D. and Evans, A. G., "Effects of Pullout on the Mechanical Properties of Ceramic-Matrix Composites," *Acta Metall*, V. 36, No. 3, 1988, pp. 517-522.

[175]. Fuller, E. R., Butler, Jr. E. P., and Carter, W. C., "Determination of Fiber-Matrix Interfacial Properties of Importance to Ceramic Composite Toughening," *Proceedings of NATO Advanced Research Workshop on Toughening Mechanisms in Quasi-Brittle Materials*, Ed. S. P. Shah, Kluwer Publishers, Boston, MA, 1990.

[176]. Bright, J. D., Shetty, D. K., Griffin, C. W. and Limaye, S. Y., " Interfacial Bonding and Friction in SiC-reinforced Ceramic and Glass Matrix Composites," *Journal of American Ceramic Society*, V. 72, No. 10, 1989, pp. 1891-1898.

[177]. Evans, A. G., Zok, F. W., and Davis, J., "The Role of Interfaces in Fiber-Reinforced Brittle Matrix Composites," *Composites Science and Technology*, V. 42, 1991, pp. 3-24.

[178]. Clyne, T. W., and Watson, M. C., "Interfacial Mechanics in Fibre-Reinforced Metals," *Composites Science and Technology*, V. 42, 1991, pp. 25-55

[179]. Desarmot G. and Favre, J. –P., "Advances in Pull-out Testing and Data Analysis," *Composites Science and Technology*, V. 42, 1991, pp. 151-187.

[180]. Romualdi, J. P. and Batson, G. B., "Mechanics of Crack Arrest in Concrete," *ASCE Journal of Engineering Mechanics*, V. 89, 1963, 147-168.

[181]. Reinhardt, H. W. and Naaman, A. E. (eds.), "*High Performance Fiber Reinforced Cement Composites*," RILEM, V. 15, E & FN SPON, London, 1992.

[182]. Naaman A. E. and Reinhardt, H. W., "High Performance Fiber Reinforced Cement Composites 2 (HPFRCC2)," *Proceedings of the Second International Workshop on High Performance Fiber Reinforced Cement Composites*, E & FN SPON, London, 1995.

[183]. Banthia, N. and Mindess, S. (eds.), "Fiber Reinforced Concrete – Modern Developments," The University of British Columbia, Vancouver, 1995.

[184]. Banthia, N., Bentur, A., and Mufti, A. (eds.), "*Fiber Reinforced Concrete – Present and Future*," The Canadian Society for Civil Engineering, Montreal, 1998.

[185]. Aveston, J., Cooper, G. A., and Kelly, A., "Single and Multiple Fracture," The Properties of Fiber Composites, *Conference Proceedings of National Physical Laboratory*, IPC, Science and Technology Press, Ltd., 1971, pp. 14-24.

[186]. Budiansky, B, Hutchinson J. W., and Evans, A. G., "Matrix Fracture in Fiber-Reinforced Ceramics," *Journal of Mechanics and Physics of Solids*, V. 34, 1986, pp. 167-189.

[187]. Naaman, A. E., "High Performance Fiber Reinforced Cement Composites," *Proceedings of the IABSE Symposium on Concrete Structures for the Future*, Paris, France, 1987, pp. 371-376.

[188]. Li, V. C. and Wu, H. C., "Conditions for Pseudo Strain-Hardening in Fiber Reinforced Brittle Matrix Composites," *Journal of Applied Mechanics Review*, V. 4, No. 1, 1992, pp. 41-57.

[189]. Li, V. C., "Post-crack Scaling Relations for Fiber Reinforced Cementitious Composites," *ASCE Journal of Materials in Civil Engineering*, V. 4, No. 1, 1992, pp. 41-57.

[190]. Li, V. C. and Leung, C. K. Y., "Theory of Steady State and Multiple Cracking of Random Discontinuous Fiber Reinforced Brittle Matrix Composites," *ASCE Journal of Engineering Mechanics*, V. 118, No. 2, 1993, pp. 37-48.

[191]. Leung, C. K. and Li, V. C., "First-Cracking Strength of Short Fiber-Reinforced Ceramics," *Ceramic Engineering Science Proceedings*, V. 10, 1989, pp. 1164-1178.

[192]. Li, V. C., "From Micromechanics to Structural Engineering - The Design of Cementitious Composites for Civil Engineering Applications," *JSCE Journal of Structural Mechanics and Earthquake Engineering*, V. 10, No. 2, 1993, pp. 37-48.

[193]. Li, V. C., Stang, H., and Krenchel, H., "Micromechanics of Crack Bridging in Fiber Reinforced Concrete," *Journal of Materials and Structures*, V. 26, 1993, pp. 486-494.

[194]. Li, V. C., Wu, H. C., Maalej, M. M., Mishra, D. K., and Hashida, T., "Tensile Behavior of Engineered Cementitious Composite with Discontinuous Random Steel Fibers," *Journal of American Ceramic Society*, 1995.

[195]. Li, V. C., Mishra, D. K., and Wu, H. C., "Matrix Design for Pseudo-Strain-Hardening Fibre Reinforced Cementitious Composites," Materials and Structures, V. 28, 1995, pp. 586-595.

[196]. Li, V. C., "Engineered Cementitious Composites (ECC) – Tailored Composites Through Micromechanical Modeling," *Fiber Reinforced Concrete – Present and Future*, The Canadian Society for Civil Engineering, Montreal, 1998.

[197]. Stang, H., "Evaluation of Properties of Fiber Composite Materials, in High Performance Fiber Reinforced Cement Composites, *RILEM Proceedings 15, E & FN SPON*, London, 1992.

[198]. Stang, H., "Micromechanical Parameters, Fracture Processes and Application of Fiber Reinforced Concrete," in *Fracture of Brittle Disordered Materials: Concrete, Rock and Ceramics*, eds. G. Baker and B. L. Karihaloo, E & FN SPON, London, 1995, pp. 131-148.

[199]. Stang, H., Li, V. C. and Krenchel, H., "Design and Structural Applications of Stress-Crack Width Relations in Fibre Reinforced Concrete," *Materials and Structures*, V. 28, 1995, pp. 210-219.

[200]. Tjiptobroto, P and Hansen, W., "Tensile Strain Hardening and Multiple Cracking in High-Performance Cement Based Composites," *ACI Materials Journal*, V. 90, No. 1, 1993.

[201]. Tjiptobroto, P and Hansen, W., "A Fracture Model for Fiber Reinforced Concrete," *ACI Materials Journal*, V. 90, No. 2, 1993.

[202]. Marshall, D. B. and Cox, B. N., "A J-Integral for Calculating Steady State Matrix Cracking Stress in Composites," *Mechanics of Materials*, V. 7, 1988, pp. 127-133.

[203]. Marshall, D. B., Cox, B. N. and Evans, A. G., "The Mechanics of Matrix Cracking in Brittle Fiber Matrix Composites," *Acta. Metallurgica*, V. 33, No. 11, 1985, pp. 2013-2021.

[204]. Marshall, D. B. and Cox, B. N., "Tensile Fracture of Brittle-Matrix Composites: Influence of Fiber Strength," *Acta Metallurgica*, V. 35, 1987, pp. 2607-2617.

[205]. Nemat-Nasser, S. and Hori, M., "Toughening by Partial or Full Bridging of Cracks in Ceramics and Fiber-Reinforced Composites," *Mechanics of Materials*, V. 6, 1986, pp. 245-259.

[206]. Mai, Y. W., "Failure Characterization of Fiber Reinforced Cement Comosites with R-curve Characteristics," in *Toughening Mechanisms in Quasi-Brittle Materials*, Eds. S. P. Shah, Kluwer Academic Publishers, Dordrecht, Netherlands, 1991, pp. 467-505.

[207]. Mori, T. and Mura, T., "An Inclusion Model for Crack Arrest in Fiber-Reinforced Materials," *Mechanics of Materials*, V. 3, 1984, pp. 193-198.

[208]. Yang, C. C., Tsai, B., Mura, T., Shibata, S., and Mori, T., "Crack Arrest b Strong Long Fibers in a Brittle-Matrix Composite," *Composite Engineering*, V. 1, No. 2, 1991, pp. 113-125.

[209]. Hillerborg, A., Modeer, M. and Petersson, P. E., "Analysis of Crack Formation and Crack Growth in Concrete by Means of Fracture Mechanics and Finite Elements," *Cement Concrete Research*, V. 6, No. 773-782, 1976.

[210]. Jenq, Y. S. and Shah, S. P., "A Two-Parameter Fracture Model for Concrete," *ASCE Journal of Engineering Mechanics Division*, V. 111, No. 4, 1985, 1227-1241.

[211]. Bazant, Z., "Size Effect in Blunt Fracture of Concrete, Rock and Metal," *ASCE Journal of Engineering Mechanics*, V. 110, No. 4, 1984, pp. 518-535.

[212]. Foote, R. M., Mai, Y. –W. and Cotterell, B., "Crack Growth Resistance Curves in Strain Softening Materials," *Journal of Mechanics and Physics of Solids*, V. 34, No. 6, 1986, pp. 593-607.

[213]. Ouyang, C. and Shah, S. P., "Geometry Dependent R-Curve for Quasi-Brittle Materials," *Journal of American Ceramic Society*, V. 74, No. 11, 1991, 2831-2836.

[214]. Ouyang, C, Mobasher, B., and Shah, S. P., "An R-Curve Approach for Fracture of Quasi-Brittle Materials," *Engineering Fracture Mechanics*, V. 37, No. 4, 1990, pp. 901-913.

[215]. ASTM C 192, "Method of Making and Curing Concrete Testing Specimens in the Laboratory," *American Society of Testing and Materials*, Philadelphia, 1991, pp. 111-113.

[216]. Dubey, A. and Banthia, N., "Choosing an Appropriate Pozzolan For High Performance Fiber Reinforced Concrete," Proceedings of the *Asia-Pacific Specialty Conference on Fibre Reinforced Concrete,* Singapore, Aug 1997.

[217]. Dubey, A. and Banthia, N., "Influence of High-Reactivity Metakaoline (HRM) and Silica Fume on the Flexural Toughness of High Performance Steel Fiber Reinforced Concrete," *Materials Journal, American Concrete Institute*, Jun 1998.

[218]. ASTM C 78, ""*American Society of Testing and Materials*, Philadelphia, 1994, pp. 506-513.

[219]. Banthia, N. and Dubey, A., "Measurement of Flexural Toughness of Fiber Reinforced Concrete Using a Novel Technique Part 1: Assessment and Calibration," Accepted *Materials Journal, American Concrete Institute*, Jun 1998.

[220]. Banthia, N. and Dubey, A., "Measurement of Flexural Toughness of Fiber Reinforced Concrete Using a Novel Technique Part 2: Performance of Various Composites," Accepted *Materials Journal, American Concrete Institute*, Jun 1998.

[221]. Banthia, N., Dubey, A., Yan, C., Bakht, B. and Mufti, A., "Residual Strength Index (RSI) Test For Fiber Reinforced Concrete: Results of Canadian Round Robin Test Program, *Technical Report,* The University of British Columbia, Vancouver, 1996.

[222]. Dubey, A. and Banthia, N., "High-Performance Fiber Reinforced Concrete: Optimizing Interfacial Properties for High-Modulus and Low-Modulus Fibers," *ACI Spring Convention*, Chicago, 1999.

[223]. Dubey, A. and Banthia, N., "Progressive Debonding Model for Fiber Pullout," Submitted to *Journal of Material Science*, 1999.

[224]. Timoshenko, S., "*Strength of Materials, Part II – Advanced Theory and Problems*," Robert E. Krieger Publishing Company, Malabar, Florida, USA.

[225]. Mallikarjuna, M., Fafard, M., and Banthia, N., "A New Three-Dimensional Interface (Contact) Element for Fiber Pull-out Behavior in Composites," *Computers and Structures*, V. 44, No. 4, 1992, pp. 753-764.

Appendix A

```
/*    SOURCE CODE FOR THE FIBER PULLOUT MODEL     */
/*    BY TAKAKU AND ARRIDGE [REFERENCE 54]        */


#include <stdio.h>
#include <float.h>
#include <math.h>
#include <stdlib.h>
#include <memory.h>

#define TT 200
#define N  3


main ()
{
 FILE *input_file;
 FILE *STRS_DISTR;
 FILE *STRS_DISTR2;
 FILE *PO_DISP;
 FILE *PO_DISP2;
 FILE *DEBLEN_DEBSTRSS;
 FILE *DEBLEN_DEBSTRSS2;
 FILE *PO_STRESSvsDL;
 FILE *PO_STRESSvsDL2;
 FILE *TEST;
 FILE *TESTIN;



int L, dl, zz, parts, pdist;

double a, b, Poss_m, Poss_f, Em, Ef, ABS, mu, contact_stress,
Initial_debonding_stress, row, alpha, eps1, eps2,
eps3, eps4, epsilon, theta1, theta2, theta, beta1, beta, cnstnt1, cnstnt2,
mega,
deb_len, deb_pos, Fiber_area, z, zzz, debond_length, omega1, LL, PDS, FD1,
FD2, FAS1, FAS2, FAS3, pd, pullout_distance, FDP1, FDP2, FDP3, FASP1, FASP2,
zero_stress, l_cata, l_cata1, l_cata3, xxxx, yyyy, zzzz, wwww,
alphaa_ta, alpha_ta, sigma_o_peak, U_d;

float Pullout_Bond_component[TT] [N], Pullout_Friction_component[TT] [N],
Fiber_disp_2sides[TT] [N], Pullout_Load[TT] [N],
Fiber_axial_stress[TT] [N], Interfacial_shear_stress[TT] [N],
Fiber_axial_load[TT] [N], Fiber_axl_load_bond_compo[TT] [N],
Fiber_axl_load_frictional_compo[TT] [N], ISS[TT], Fiber_displacement[TT],
Fiber_displacement2[TT], Progressive_dbnd_stress[TT],
Progressive_POstress[TT], PO_LD_Bond[TT], PO_LD_Fric[TT],
Progressive_POload[TT];

input_file = fopen("inp","r");
STRS_DISTR = fopen("stress","w");       /* stress distribution in fiber */
STRS_DISTR2 = fopen("stress2", "w");
PO_DISP = fopen("disp","w");          /* pullout stress and fiber displacement
*/
PO_DISP2 = fopen("disp2", "w");
TESTIN = fopen("in", "w");
```

```
/* read the input file */ /*   ABS  -  Adhesional Bond Strength    */
  fscanf(input_file, "%lf  %lf  %lf  %lf  %lf  %lf  %d   %lf %lf %lf ", &a,
  &b,  &Poss_f, &Poss_m, &Em, &Ef, &L, &ABS, &mu, &contact_stress);


  /*  ------------------------------------------------------ */
  /*  Fiber completely bonded along its length               */
  /*  ------------------------------------------------------ */

  fprintf(PO_DISP, "Deb Len   Dbnd Strs   PO Strs   Fib Disp   Progr PO Ld
  Bnd PO Ld   Fric PO Ld\n");
  fprintf(PO_DISP2, "Deb Len   Dbnd Strs   PO Strs   Fib Disp2   Progr PO Ld
  Bnd PO Ld   Fric PO Ld\n");
  fprintf(STRS_DISTR, "Dbnd Strs  Deb Lt  Deb Pos  Axl Pos  Axl Strs  Shr
  Strs  Axl Lod  Bnd Ld  Fric Ld \n");


  omega=Poss_f*Em/(Ef*(1+Poss_m));
  Fiber_area = 3.14*a*a;
  alphaa_ta=(2*3.14159*Em)/(a*Ef*(1+Poss_m)*log(b/a));
  alpha_ta=sqrt(alphaa_ta);
  deb_len=0.0;
  deb_pos=0.0;
  dl=deb_len;
  zero_stress=0.0;
  Initial_debonding_stress=-2*ABS*tanh(alpha_ta*L)/(a*alpha_ta);
  Progressive_dbnd_stress[dl]=Initial_debonding_stress;
  Progressive_dbnd_stress[dl]=Initial_debonding_stress;
  Progressive_POstress[dl] = zero_stress;
  Progressive_POload[dl]=0.0;
  PO_LD_Bond[dl]=0.0;
  PO_LD_Fric[dl]=0.0;
  Fiber_displacement[dl]=zero_stress/(Ef*a*cosh(alpha_ta*L));
  Fiber_displacement2[dl] = 2*Fiber_displacement[dl];
  fprintf(PO_DISP, "%7.2lf   %7.2lf   %7.2lf   %7.5lf       %7.2lf
  %7.2lf      %7.2lf\n", deb_len, Progressive_dbnd_stress[dl],
  Progressive_POstress[dl], Fiber_displacement[dl], Progressive_POload[dl],
  PO_LD_Bond[dl], PO_LD_Fric[dl]);
  fprintf(PO_DISP2, "%7.2lf   %7.2lf   %7.2lf   %7.5lf       %7.2lf
  %7.2lf      %7.2lf\n", deb_len, Progressive_dbnd_stress[dl],
  Progressive_POstress[dl], Fiber_displacement2[dl], Progressive_POload[dl],
  PO_LD_Bond[dl], PO_LD_Fric[dl]);


  deb_len=0.0;
  deb_pos=0.0;
  dl=deb_len;
  Initial_debonding_stress=-2*ABS*tanh(alpha_ta*L)/(a*alpha_ta);
  Progressive_dbnd_stress[dl]=Initial_debonding_stress;
  Progressive_POstress[dl] = Initial_debonding_stress;
  Progressive_POload[dl]=Progressive_POstress[dl]*Fiber_area;
  PO_LD_Bond[dl]=Progressive_dbnd_stress[dl]*Fiber_area;
  PO_LD_Fric[dl]=Progressive_POload[dl]-PO_LD_Bond[dl];
```

```
Fiber_displacement[dl]=Initial_debonding_stress/(Ef*(row+alpha-
row*epsilon*alpha+alpha*epsilon))*((alpha-row*epsilon*alpha+alpha*epsilon-
row)*(cosh(beta*L)-1)/(beta*sinh(beta*L))+row*L);
Fiber_displacement2[dl] = 2*Fiber_displacement[dl];
fprintf(PO_DISP, "%7.2lf   %7.2lf   %7.2lf   %7.5lf       %7.2lf
%7.2lf      %7.2lf\n", deb_len, Progressive_dbnd_stress[dl],
Progressive_POstress[dl], Fiber_displacement[dl], Progressive_POload[dl],
PO_LD_Bond[dl], PO_LD_Fric[dl]);
fprintf(PO_DISP2, "%7.2lf   %7.2lf   %7.2lf   %7.5lf       %7.2lf
%7.2lf      %7.2lf\n", deb_len, Progressive_dbnd_stress[dl],
Progressive_POstress[dl], Fiber_displacement2[dl], Progressive_POload[dl],
PO_LD_Bond[dl], PO_LD_Fric[dl]);



/*  ------------------------------------------------------ */
/*  Fiber completely debonded along its length             */
/*  ------------------------------------------------------ */

parts=4;
for(pdist=0; pdist<=parts*L; ++pdist)
{
 pullout_distance=pdist;
 pd=pullout_distance/parts;
  /* L_new=L-pout_dist; */
 Progressive_dbnd_stress[pdist]=0.0;

/* calculate progressive pullout stress and fiber displacement */
Progressive_POstress[pdist]=-contact_stress/omega*(1-exp(-2*mu*omega*(L-
pd)/a));
Progressive_POload[pdist]=Progressive_POstress[pdist]*Fiber_area;
PO_LD_Fric[pdist]=Progressive_POload[pdist];
PO_LD_Bond[pdist]=0.0;
FDP1=contact_stress/(Ef*omega);
FDP2=a/(2*mu*omega)*(exp(-2*mu*omega*(L-pd)/a)-1);
FDP3=pd*(1-exp(-2*mu*omega*(L-pd)));
Fiber_displacement[pdist]=pd-FDP1*((L-pd)+FDP2+FDP3);
Fiber_displacement2[pdist] = pd-FDP1*(2*(L-pd)+2*FDP2+FDP3);
fprintf(PO_DISP, "%7.2lf   %7.2lf   %7.2lf   %7.5lf       %7.2lf
%7.2lf      %7.2lf\n", pd, Progressive_dbnd_stress[pdist],
Progressive_POstress[pdist], Fiber_displacement[pdist],
Progressive_POload[pdist], PO_LD_Bond[pdist], PO_LD_Fric[pdist]);
fprintf(PO_DISP2, "%7.2lf   %7.2lf   %7.2lf   %7.5lf       %7.2lf
%7.2lf      %7.2lf\n", pd, Progressive_dbnd_stress[pdist],
Progressive_POstress[pdist], Fiber_displacement2[pdist],
Progressive_POload[pdist], PO_LD_Bond[pdist], PO_LD_Fric[pdist]);


/* calculate fiber axial stress distribution & interfacial shear stress
   distribution over the debonded zone of the partially debonded fiber
   */

for(zz=0; zz<=parts*(L-pd); ++zz)
{
 zzz=zz;
 z=zzz/parts;
```

```
    FASP1=contact_stress/omega;
    FASP2=exp(-2*omega*mu*z/a);
    Fiber_axial_stress[zz] [3]=-FASP1*(1-FASP2);
    Interfacial_shear_stress[zz] [3]=mu*contact_stress*FASP2;
    Fiber_axial_load[zz] [3] = Fiber_axial_stress[zz] [3] * Fiber_area;
    Fiber_axl_load_bond_compo[zz] [3] = Progressive_dbnd_stress[pdist] *
    Fiber_area;
    Fiber_axl_load_frictional_compo[zz] [3] = Fiber_axial_load[zz] [3] -
    Fiber_axl_load_bond_compo[zz] [2];
    fprintf(STRS_DISTR, "%7.2lf  %7.2lf  %7.2lf  %7.2lf  %7.2lf  %7.2lf
    %7.2lf  %7.2lf  %7.2lf \n", Progressive_dbnd_stress[pdist], pd, z, z,
    Fiber_axial_stress[zz] [3], Interfacial_shear_stress[zz] [3],
    Fiber_axial_load[zz] [3], Fiber_axl_load_bond_compo[zz] [3],
    Fiber_axl_load_frictional_compo[zz] [3]);

  }


  }
}
```

Appendix B

```
/*     SOURCE CODE FOR THE PULLOUT MODEL BY HSUEH [REFERENCES 67 & 68]     */


#include <stdio.h>
#include <float.h>
#include <math.h>
#include <stdlib.h>
#include <memory.h>
#include <malloc.h>

#define TT 200

main ()
{
 FILE *input_file;
 FILE *STRS_DISTR;
 FILE *PO_DISP;
 FILE *DEBLEN_DEBSTRSS;
 FILE *PO_STRESSvsDL;
 FILE *TEST;
 FILE *TESTIN;
 FILE *AREA;


int Debnd_stress, L, Counter, zz, dl, ITER, incr, steps, zx, zy, zzyy, zxpo,
rad, bb;

double a, b, Poss_m, Poss_f, Em, Ef, ISS, Alpha, z, LZ, DS_Num, DS_Numerator,
DS_Denominator, Initial_debonding_stress, pullout_strs,
Pullout_stress[200], Fiber_axial_stress[200],  FAS1, FAS2, FAS3,
Interfacial_shear_stress[200], IS3, ISS1, ISS2, ISS3, FD1, FD2, FD3,
Difference, pullout_stress, Fiber_disp[200], alph, ppp, x, y, log_ba,
increment,
DST_Num, DST_Numerator, DST_Denominator, debond_stress_current [200],
deb_len, bl, D, denom, A1, A2, A3[200], mu, stress_pout[200], stress_shrnk,
A1A2, m1, m2, B[200], SP1, SP2a, SP2b, SP2c, SP2, SP3a, SP3b, SP3c, SP3, xx,
xy, xz, xxz, xxzz, m1d, m2d, m1m2, m1m2d, ub1, ub2,ub2a, ub2b, ub2c, ub[200],
LDEB1, LDEB2, US1, US2, US3, US4, US[200], USSS, A3a, A3b, m1dexp, m2dexp,
po_len, emb_len, debond_stress_current3, stress_pout3[200],
USP1, USP2, USP3, USP4, USP[200], UP3[200], m1z, m2z, AS1, AS2, AS3, mmz1,
mmz2, ISSS1, ISSS2, ISSS3, deb_pos, steer, zzz, debond_stress_current01,
pullout_strs01, ISSb1, ISSb2, ISSb3, ISb3, EMBD_LEN, m1m2z, POS, embd_len_po,
separation, deb_component, fric_component, Total_bond_load,
shrnk_strss_net[200], mm2dexp, row, modulus_ratio, eps1, eps2, eps3, eps4,
epsilon, theta1, theta2, theta, beta1, beta, DSC1, DSC2, DSC3, DSC[200],
matrix_stress_b, matrix_stress, rad1, k;

float Pullout_Bond_component[TT], Pullout_Friction_component[TT],
Fiber_disp_2sides[TT], Fiber_area, Pullout_Load_Bond_component[200],
Pullout_Load_Friction_component[200], Pullout_Load[TT],
Fiber_axial_load[TT], Fiber_axl_load_bond_compo[TT],
Fiber_axl_load_frictional_compo[TT], area1[TT];


input_file = fopen("inpt1","r");
STRS_DISTR = fopen("stress","w");    /* stress distribution in fiber */
```

```
PO_DISP = fopen("disp","w");     /* pullout stress and fiber displacement */
DEBLEN_DEBSTRSS = fopen("dbsdbl","w");  /* debond length versus debond stress
*/
PO_STRESSvsDL = fopen("posdl","w");    /* pullout stess vs debond length  */
TEST = fopen("testout", "w");
TESTIN = fopen("in", "w");
AREA = fopen("area", "w");

/* read the input file */
fscanf(input_file, "%lf  %lf  %lf  %lf  %lf  %lf  %d   %lf %lf %lf ", &a, &b,
&Poss_f, &Poss_m, &Em, &Ef, &L, &ISS, &mu, &stress_shrnk);
fprintf(TESTIN, "%lf  %lf  %lf  %lf  %lf  %lf  %d   %lf  \n", a, b, Poss_f,
Poss_m, Em, Ef, L, ISS, mu);

/*  fprintf(DEBLEN_DEBSTRSS, "Debond Length       Debond Stress \n");  */
/*  fprintf(AREA, "pdist  pd  area \n");  */

row=a*a/(b*b-a*a);
modulus_ratio=Em/Ef;
eps1=2/(a*a*(b*log(b/a)-(b-a)));
eps2=(0.5*b*b*b*log(b/a)-b*(b*b-a*a)/4);
eps3=0.5*a*(b*b-a*a);
eps4=(b*b-a*a)/3;
epsilon=eps1*(eps2+eps3-eps4);
theta1=a*a*(1+Poss_m);
theta2=(b/(b-a))*log(b/a)-1;
theta=1/(theta1*theta2);
beta1= (theta*(row+modulus_ratio-
row*epsilon*modulus_ratio)/(row*epsilon))+modulus_ratio*theta;
beta=pow(beta1,0.5);

Fiber_area = 3.14*a*a;

/* calculate the initial debonding stress (which is same as the fiber pull-
out test) */
log_ba = log(b/a);
alph=(a*a*Ef+(b*b-a*a)*Em)/(Ef*(1+Poss_m)*(b*b*log_ba-(b*b-a*a)));
Alpha = pow(alph,0.5)/a;
     /*  fprintf(TEST, "%7.2lf  %7.2lf \n",log_ba, alph);  */
    /*   fprintf(TEST, "%7.2lf %7.2lf  %7.2lf \n",log_ba, alph, Alpha);  */
DS_Num = ((1+Poss_m)*(1+(b*b/(a*a)-1)*(Em/Ef))*(b*b*log_ba-(b*b-a*a)/2));
DS_Numerator = (2/a) * pow(DS_Num,0.5);
DS_Denominator = (((b*b/(a*a)-1)*(Em/Ef))/tanh(Alpha*L))+ 2/(exp(Alpha*L)-
exp(-Alpha*L));
Initial_debonding_stress = -ISS * DS_Numerator/DS_Denominator;
```

```
/* ------------------------------------------------------------------------
*/
/*   FIBER COMPLETELY BONDED ALONG ITS ENTIRE LENGTH
*/
/* ------------------------------------------------------------------------
*/

/* Calculate pullout stress vs displacement relationship when fiber is
elastically bonded to the matrix throughout the embedded fiber length */
   /* NOTE: Initial debonding stress will be same as the fiber pullout test
*/
/* Also calculate the axial stress distribution in fiber and the interfacial
shear stress distribution for pullout load less than or equal to debonding
load */
fprintf(STRS_DISTR, "CTR   PO Strs   Deb Lt    Deb Pos    Axl Pos    Axl Strs
Shr Strs     Axl Ld    Bnd Ld     Fric Ld\n");

 Counter=0;
 pullout_strs=0;
 incr=100;
 steps=(Initial_debonding_stress/100);

 for(ITER=1; ITER <= steps+2; ++ITER)
 {
   dl=0;
   Counter=Counter+1;
   Pullout_stress[ITER] = pullout_strs;
   Pullout_Friction_component[dl]=0.0;
   Pullout_Bond_component[dl]=Pullout_stress[ITER];
   Pullout_Load[ITER] = Pullout_stress[ITER] * Fiber_area;
   Pullout_Load_Friction_component[dl] = 0.0;
   Pullout_Load_Bond_component[dl] = Pullout_Bond_component[dl] * Fiber_area;

   for(zz=0; zz<=2*L; ++zz)
   {
       deb_len=0.0;
       deb_pos=0.0;
       z = 0.5*zz;
       LZ = L-z;
       debond_stress_current[dl] = Initial_debonding_stress;
       /* calculate axial stress distribution in fiber */
      FAS1 = (a*a*Ef*pullout_strs)/(a*a*Ef+(b*b-a*a)*Em);
      FAS2 = ((b*b/(a*a))-1) * (Em/Ef) * (exp(Alpha*z)-exp(-
      Alpha*z))/(exp(Alpha*L)-exp(-Alpha*L));
        FAS3 = (exp(-Alpha*(L-z)) - exp(Alpha*(L-z)))/(exp(Alpha*L) - exp(-
      Alpha*L));
      Fiber_axial_stress[zz] = FAS1*(1+FAS2+FAS3);
      Fiber_axial_load[zz] = Fiber_axial_stress[zz] * Fiber_area;
      Fiber_axl_load_bond_compo[zz]= Fiber_axial_load[zz];
      Fiber_axl_load_frictional_compo[zz]=0.0;


 /* calculate interfacial shear stress distribution   */
 ISS1 = ((b*b/(a*a))-1) * (Em/Ef) * (exp(Alpha*z) + exp(-
Alpha*z))/(exp(Alpha*L)-exp(-Alpha*L));
 ISS2 =  (exp(-Alpha*(L-z)) + exp (Alpha*(L-z)))/(exp(Alpha*L) - exp(-
Alpha*L));
```

```
  IS3  =  ((1+Poss_m)*(1+(b*b/(a*a)-1)*(Em/Ef))*(b*b*log_ba-(b*b-a*a)/2));
  ISS3 = (2/a)* pow(IS3, 0.5);
  Interfacial_shear_stress[zz] = -pullout_strs*((ISS1+ISS2)/ISS3);
  /*  fprintf(TEST, "ISS1=%7.11f  ISS2=%7.21f    ISS3=%7.21f
 ISS[z=%7.21f]=%7.21f\n", ISS1, ISS2, ISS3, z,
 Interfacial_shear_stress[zz][dl]);   */
  fprintf(STRS_DISTR, "%d    %7.21f    %7.21f    %7.21f    %7.21f    %7.21f
%7.21f     %7.21f     %7.21f     %7.21f \n", Counter, pullout_strs, deb_len,
 deb_pos, z,
  Fiber_axial_stress[zz], Interfacial_shear_stress[zz], Fiber_axial_load[zz],
 Fiber_axl_load_bond_compo[zz], Fiber_axl_load_frictional_compo[zz]);

matrix_stress_b = pullout_strs/epsilon - (row+modulus_ratio-
 row*epsilon*modulus_ratio)*Fiber_axial_stress[zz]/(row*epsilon);
bb=b;
for(rad=1; rad<=bb; ++rad)
{
 k=rad;
 rad1=log(k/a);
 matrix_stress=modulus_ratio*Fiber_axial_stress[zz] + matrix_stress_b-
modulus_ratio*Fiber_axial_stress[zz]*(b*rad1+a-rad)/(b*log(b/a)-(b-a));
 fprintf(DEBLEN_DEBSTRSS, "PO STRS=%7.21f   zz=%d   rad=%d
matrix_stress_b=%7.21f   matrix_stress=%7.21f    \n", pullout_strs, zz, rad,
matrix_stress_b, matrix_stress);
}


   }

     /*  calculate fiber displacement */
    FD1 = (a*a*pullout_strs)/(a*a*Ef+(b*b-a*a)*Em);
    FD2 = (((b*b/(a*a))-1)*(Em/Ef)-1)/Alpha;
    FD3 = (exp(Alpha*L)+exp(-Alpha*L)-2)/(exp(Alpha*L)-exp(-Alpha*L));
    Fiber_disp[ITER] = FD1 * (L + FD2*FD3);
    Fiber_disp_2sides[ITER] = 2*Fiber_disp[ITER];
       /*    fprintf(PO_DISP, "%7.21f  %7.21f  %7.21f  %7.21f  \n",
pullout_strs, FD1, FD2, FD3);   */
      /*   fprintf(PO_DISP, "FD1=%7.21f  FD2=%7.21f  FD3=%7.21f\n", FD1,
FD2, FD3);  */
    fprintf(PO_DISP, "%d    %7.21f    %7.21f     %9.61f     %9.61f     %7.21f
%7.21f    %7.21f      %7.21f      %7.21f     %7.21f\n", ITER, deb_len,
debond_stress_current[dl], Fiber_disp[ITER], Fiber_disp_2sides[ITER],
          Pullout_stress[ITER], Pullout_Bond_component[dl],
Pullout_Friction_component[dl], Pullout_Load[ITER],
Pullout_Load_Bond_component[dl], Pullout_Load_Friction_component[dl]);

  if(ITER<steps+1)
    pullout_strs = pullout_strs + incr;
  else
    pullout_strs = Initial_debonding_stress;
       /*  fprintf(PO_DISP,"ITR=%d \n", ITER);   */

 }
```

```
/* ------------------------------------------------------------------------
*/
/*  FIBER PARTIALLY DEBONDED ALONG ITS LENGTH
*/
/* ------------------------------------------------------------------------
*/

/*  Calcualte pullout stress vs displacement relationship
                          when fiber-matrix are partially bonded  */

/*  Calcualte debonding stress (debond_stress_current [dl] for each debond
length  */
   for(dl=0; dl<=2*L; ++dl)
   {
     if(dl < 2*L)
     {
      deb_len = 0.5*dl;
      bl = L - deb_len;
    /*  Counter = Counter+1;  */
      DST_Num = ((1+Poss_m)*(1+(b*b/(a*a)-1)*(Em/Ef))*(b*b*log_ba-(b*b-
a*a)/2));
      DST_Numerator = (2/a) * pow(DST_Num,0.5);
      DST_Denominator = (((b*b/(a*a)-1)*(Em/Ef))/tanh(Alpha*(L-deb_len)))+
      2/(exp(Alpha*(L-deb_len))-exp(-Alpha*(L-deb_len)));
      debond_stress_current [dl]  = -ISS * DST_Numerator/DST_Denominator;

      DSC[dl]=0.0;
      DSC1=2*(row+modulus_ratio-
      row*epsilon*modulus_ratio+modulus_ratio*epsilon)/(a*beta);
      DSC2=(modulus_ratio-
      row*epsilon*modulus_ratio+modulus_ratio*epsilon)/tanh(beta*(L-
      deb_len));
      DSC3= 2*row/(exp(beta*(L-deb_len))-exp(-beta*(L-deb_len)));
      DSC[dl]=-ISS*DSC1/(DSC2+DSC3);
  /*    fprintf(DEBLEN_DEBSTRSS, "%7.2lf          %7.2lf   %7.2lf
      Alpha=%7.2lf  row=%7.2lf   beta=%7.2lf  epsilon=%7.2lf \n", deb_len,
      debond_stress_current [dl], DSC[dl], Alpha, row, beta, epsilon);    */


     }
     else
     {
       deb_len = 0.5*dl;
       bl = L - deb_len;
       debond_stress_current [dl] = 0.0;
       fprintf(DEBLEN_DEBSTRSS, "%7.2lf         %7.2lf \n", deb_len,
      debond_stress_current [dl]);
     }
   }

      D = ((b*b+a*a)/(b*b-a*a)) + Poss_m  +  (Em*(1-Poss_f)/Ef);
      denom = (1+Poss_m)* (b*b*log_ba - (b*b-a*a)/2);
      A1 = a*(1-b*b/(a*a))*D/(2*mu*Poss_m*denom);
      A2 = ((1-b*b/(a*a))*(Em*Poss_f/(Ef*Poss_m))-1)/denom;
      A1A2 = (A1*A1-4*A2);
      m1 = (-A1 + pow(A1A2,0.5))/2;
      m2 = (-A1 - pow(A1A2,0.5))/2;
```

```
/*        fprintf(TEST, "D=%7.2lf  A1=%7.2lf  A2=%7.2lf   m1=%7.2lf
      m2=%7.2lf   \n",D, A1, A2, m1, m2);
      fprintf(TEST, "deb_len      m1       m2    (m1+m2)*deb_len   debond
      stress current                    SP1                       SP2
      SP3   Pullout Stress\n");   */


   /* Caluclate pullout stress (partial debond pullout stress) for various
    debond lengths   */

   fprintf(PO_STRESSvsDL, "Debond length    Debond stress     Pullout stress
    \n");
    /*   fprintf(STP, "SP1, SP2a, SP2b SP2c, SP2, SP3a, SP3c, SP3 Pullout
    stress  \n");   */

   ITER=ITER-1;
   for(dl=0; dl<=2*L; ++dl)
   {
    Counter=Counter+1;
    deb_len = 0.5*dl;
     m1m2 = m1+m2;
     m1d = m1*deb_len;
     m2d = m2*deb_len;
     m1m2d = (m1+m2)* deb_len;
       SP1 = debond_stress_current[dl]*(m1-m2)*exp(m1m2d);
        /* fprintf(TEST, "%7.2lf   %7.2lf %7.2lf      %7.2lf           %7.2lf
    %50.2lf", deb_len, m1, m2, m1m2d, debond_stress_current[dl], SP1);    */
     SP2a=(a*a-b*b)*D*Ef*(m2*exp(m2d)-m1*exp(m1d)+(m1-m2)*exp(m1m2d));
     SP2b=(a*a-b*b)*Em*Poss_f-a*a*Ef*Poss_m;
     SP2c=(2*mu/a)*(exp(m1d)-exp(m2d));
       SP2 = ((SP2a/SP2b)-SP2c)* stress_shrnk;
     SP3a=(a*a-b*b)*Em*Poss_f*(m1*exp(m1d)-m2*exp(m2d))-a*a*Ef*Poss_m*(m1-
    m2)*exp(m1m2d);
     SP3b=(a*a-b*b)*Em*Poss_f-a*a*Ef*Poss_m;
     SP3c=2*mu*Em*Poss_f*(exp(m1d)-exp(m2d))/(a*D*Ef);
       SP3=((SP3a/SP3b)+SP3c);
       stress_pout[dl]= (SP1+SP2)/(SP3);   /* stress_pout[dl] is partial
    debond pullout stress   */

    /* For the calculated fiber pullout stress, check if separation of
    matrix-fiber interface has taken place in the debonded region */
    if(stress_pout[dl] < debond_stress_current[dl])
    {
       /* means, separation of fiber and matrix has taken place in the
    debonded region & hence frictional stress is zero in the debonded region
    */
       stress_pout[dl] = debond_stress_current[dl];
       separation=1;
    }
    else
    {
     separation=0;
    }
    Pullout_stress[ITER]=stress_pout[dl];
    Pullout_Bond_component[dl] = debond_stress_current[dl];
```

```
Pullout_Friction_component[dl] = Pullout_stress[ITER] -
Pullout_Bond_component[dl];
Pullout_Load[ITER] = Pullout_stress[ITER] * Fiber_area;
Pullout_Load_Friction_component[dl] = Pullout_Friction_component[dl] *
Fiber_area;
Pullout_Load_Bond_component[dl] = Pullout_Bond_component[dl] *
Fiber_area;


fprintf(PO_STRESSvsDL, "%7.2lf          %7.2lf              %7.2lf
 \n", deb_len, debond_stress_current[dl], stress_pout[dl]);
 /*    fprintf(STP, "%7.2lf  %7.2lf  %7.2lf  %7.2lf  %7.2lf   %7.2lf
 %7.2lf  %7.2lf  %7.2lf \n", SP1, SP2a, SP2b, SP2c, SP2, SP3a, SP3c, SP3,
 Pullout_stress[ITER]);   */

  A3a=stress_pout[dl];
  A3b= (stress_shrnk/Poss_m)*(1-b*b/(a*a))*D;
A3[dl] = -(A3a+A3b)/denom;
if(dl>0)
B[dl] = (stress_pout[dl]-debond_stress_current[dl]*exp(m2d)-
(A3[dl]/A2)*(1-exp(m2d)))/(exp(m1d)-exp(m2d));
else
B[dl]= 0;
fprintf(PO_STRESSvsDL, "%7.2lf          %7.2lf              %7.2lf
\n", deb_len, debond_stress_current[dl], stress_pout[dl]);

  /* fprintf(TEST, "%50.2lf     %50.2lf     %10.2lf  \n",  SP2, SP3,
stress_pout[dl]);   */
  /* fprintf(TEST, "A3[dl]=%20.2lf  B[dl]=%20.2lf  \n",  A3[dl], B[dl]);
*/


/*  Calculate fiber displacement for each partial debond pullout stress
*/
 if(dl<2*L)
 {
  /* calculate fiber displacement for the bonded part  */
  LDEB1=Alpha*(L-deb_len);
  LDEB2=-Alpha*(L-deb_len);
  m1dexp = exp(m1d);
  m2dexp = exp(m2d);
  ub1 = (a*a*debond_stress_current[dl])/(a*a*Ef+(b*b-a*a)*Em);
  ub2a = (((b*b/(a*a))-1)*(Em/Ef)-1)/Alpha;
  ub2b = exp(LDEB1)+exp(LDEB2)-2;
  ub2c = exp(LDEB1)-exp(LDEB2);
  ub2 = ub2a*ub2b/ub2c;
  ub[dl] = ub1*((L-deb_len)+ ub2);


  /* Caculate fiber displacement for the debonded portion of the embedded
   length   */
  if(separation==0) /* That is interfacial frictional exists on the
   interface */
  {
   US1=A3[dl]*deb_len/(A2*Ef);
    /*   fprintf(TEST," A3[%7.2lf]=%7.2lf   A2=%7.2lf  m2=%7.2lf
  m2dexp=%27.11f   \n", deb_len, A3[dl], A2, m2, m2dexp);   */
```

```
        US2=A3[dl]*(1-m2dexp)/(A2*m2*Ef);
        US3=B[dl]*(((m1dexp-1)/m1) - ((m2dexp-1)/m2))/Ef;
        US4=(m2dexp-1)*debond_stress_current[dl]/(m2*Ef);
        USSS=US4+US3+US2;
        US[dl] = (US1+US2+US3+US4);

        Fiber_disp[ITER] = ub[dl] + US[dl];
        Fiber_disp_2sides[ITER] = 2*Fiber_disp[ITER];

        fprintf(PO_DISP, "%d   %7.2lf    %7.2lf      %9.6lf     %9.6lf
        %7.2lf     %7.2lf     %7.2lf      %7.2lf      %7.2lf      %7.2lf \n",
        ITER, deb_len,  debond_stress_current[dl], Fiber_disp[ITER],
        Fiber_disp_2sides[ITER], Pullout_stress[ITER],
        Pullout_Bond_component[dl], Pullout_Friction_component[dl],
        Pullout_Load[ITER], Pullout_Load_Bond_component[dl],
        Pullout_Load_Friction_component[dl]);

         /* fprintf(TEST, "A3[%d]=%7.2lf    B[%d]=%7.2lf   DSC[%d]=%7.2lf
        US1=%37.11f   US2=%37.11f    US3=%37.11f    US4=%37.11f
        USSS=%37.11f\n", dl, A3[dl], dl, B[dl], dl, debond_stress_current[dl],
        US1, US2, US3, US4, USSS); */
       }
       else  /* That is when interface is not in contact in the debonded
        region, separation==0 */
       {
        US[dl]= debond_stress_current[dl]*deb_len/Ef;  /* that is, fiber
        pullout stress equal to current debond stress */
        Fiber_disp[ITER] = ub[dl] + US[dl];
        Fiber_disp_2sides[ITER] = 2*Fiber_disp[ITER];
         fprintf(PO_DISP, "%d   %7.2lf    %7.2lf      %9.6lf     %9.6lf
        %7.2lf     %7.2lf     %7.2lf      %7.2lf      %7.2lf      %7.2lf \n",
        ITER, deb_len,  debond_stress_current[dl], Fiber_disp[ITER],
        Fiber_disp_2sides[ITER],
               Pullout_stress[ITER], Pullout_Bond_component[dl],
        Pullout_Friction_component[dl], Pullout_Load[ITER],
        Pullout_Load_Bond_component[dl], Pullout_Load_Friction_component[dl]);

       }
      }
      else   /* that is when dl=2*L (ie, debond length equal to fiber length
 */
      {
if(separation==0)  /* that is, when interface is in contact in the debonded
 region */
{
 m1dexp=exp(m1d);
 m2dexp=exp(m2d);
 ub[dl]=0.0;
 US1=A3[dl]*deb_len/(A2*Ef);
 US2=A3[dl]*(1-m2dexp)/(A2*m2*Ef);
 US3=B[dl]*(((m1dexp-1)/m1) - ((m2dexp-1)/m2))/Ef;
 US4=(m2dexp-1)*debond_stress_current[dl]/(m2*Ef);
 USSS=US4+US3+US2+US1;
 US[dl] = (US1+US2+US3+US4);
 Fiber_disp[ITER] = ub[dl] + US[dl];
 Fiber_disp_2sides[ITER] = 2*Fiber_disp[ITER];
```

```
 fprintf(PO_DISP, "%d   %7.2lf    %7.2lf      %9.6lf     %9.6lf     %7.2lf
%7.2lf     %7.2lf      %7.2lf      %7.2lf      %7.2lf \n", ITER, deb_len,
debond_stress_current[dl], Fiber_disp[ITER], Fiber_disp_2sides[ITER],
        Pullout_stress[ITER], Pullout_Bond_component[dl],
Pullout_Friction_component[dl], Pullout_Load[ITER],
Pullout_Load_Bond_component[dl], Pullout_Load_Friction_component[dl]);

/* fprintf(TEST, "%7.6lf   %7.6lf   %7.6lf   %7.6lf \n", US1,US2,US3,US4);
 */
/* fprintf(TEST, "A3[%d]=%7.2lf B[%d]=%7.2lf A2=%7.3lf m2=%8.5lf
m2dexp=%8.5lf,DSC[%d]=%7.2lf US1=%37.1lf US2=%37.1lf US3=%37.1lf US4=%37.1lf
USSS=%37.1lf\n",dl,A3[dl],dl,B[dl],A2,m2,m2dexp,dl,debond_stress_current[dl],
US1,US2, US3, US4, USSS); */


       /*  fprintf(PO_DISP, "%d   %7.2lf    %7.3lf     %7.2lf   %7.1lf
USP[dl]=%7.3lf   UP3=%7.3lf\n", ITER, emb_len,  Fiber_disp[ITER],
Pullout_stress[ITER], debond_stress_current3, USP[dl], UP3[dl]);    */
      }
      else   /* that is when interface is not in contact in the debonded
region */
      {
       ub[dl]=0.0;
       US[dl]= debond_stress_current[dl]*deb_len/Ef;  /* that is, fiber
        pullout stress equal to current debond stress */
       Fiber_disp[ITER] = ub[dl] + US[dl];
       Fiber_disp_2sides[ITER] = 2*Fiber_disp[ITER];
        fprintf(PO_DISP, "%d   %7.2lf    %7.2lf      %9.6lf     %9.6lf
        %7.2lf     %7.2lf     %7.2lf      %7.2lf      %7.2lf      %7.2lf \n",
        ITER, deb_len,  debond_stress_current[dl], Fiber_disp[ITER],
        Fiber_disp_2sides[ITER], Pullout_stress[ITER],
        Pullout_Bond_component[dl], Pullout_Friction_component[dl],
        Pullout_Load[ITER], Pullout_Load_Bond_component[dl],
        Pullout_Load_Friction_component[dl]);

         /*  fprintf(PO_DISP, "%d   %7.2lf    %7.3lf     %7.2lf   %7.1lf
       USP[dl]=%7.3lf   UP3[dl]=%7.3lf\n", ITER, emb_len,  Fiber_disp[ITER],
       Pullout_stress[ITER], debond_stress_current3, USP[dl], UP3[dl]);   */
      }
     }



    /* Calculate stress distribution in fiber and interface when fiber
                partially debonded  */

    /* calculate stress distribution in the bonded region  */
    if(dl<2*L)
    {
      for(zzyy=2*L-dl; zzyy>=0; --zzyy)
      {
       zy=2*L-dl-zzyy;
       deb_pos=0.0;
       z = 0.5*zy;
       LZ = L-deb_len-z;
       pullout_strs = debond_stress_current[dl];
       /* calculate axial stress distribution in fiber */
```

```
  FAS1 = (a*a*Ef*pullout_strs)/(a*a*Ef+(b*b-a*a)*Em);
   FAS2 = ((b*b/(a*a))-1) * (Em/Ef) * (exp(Alpha*z)-exp(-
   Alpha*z))/(exp(Alpha*(L-deb_len))-exp(-Alpha*(L-deb_len)));
   FAS3 = (exp(-Alpha*(L-deb_len-z)) - exp(Alpha*(L-deb_len-
   z)))/(exp(Alpha*(L-deb_len)) - exp(-Alpha*(L-deb_len)));
   Fiber_axial_stress[zy] = FAS1*(1+FAS2+FAS3);
   Fiber_axial_load[zy] = Fiber_axial_stress[zy] * Fiber_area;
   Fiber_axl_load_bond_compo[zy]= Fiber_axial_load[zy];
   Fiber_axl_load_frictional_compo[zy]=0.0;
   Total_bond_load = Fiber_axl_load_bond_compo[zy];


    /* calculate interfacial shear stress distribution    */
    ISSb1 = ((b*b/(a*a))-1) * (Em/Ef) * (exp(Alpha*z) + exp(-
    Alpha*z))/(exp(Alpha*(L-deb_len))-exp(-Alpha*(L-deb_len)));
    ISSb2 =  (exp(-Alpha*(L-deb_len-z)) + exp (Alpha*(L-deb_len-
    z)))/(exp(Alpha*(L-deb_len)) - exp(-Alpha*(L-deb_len)));
    ISb3  =  ((1+Poss_m)*(1+(b*b/(a*a)-1)*(Em/Ef))*(b*b*log_ba-(b*b-
    a*a)/2));
    ISSb3 = (2/a)* pow(ISb3, 0.5);
    Interfacial_shear_stress[zy] = -pullout_strs*((ISSb1+ISSb2)/ISSb3);
    /*   fprintf(TEST, "ISS1=%7.11f  ISS2=%7.21f    ISS3=%7.21f
   ISS[z=%7.21f]=%7.21f\n", ISS1, ISS2, ISS3, z,
    Interfacial_shear_stress[zz][dl]);   */
    fprintf(STRS_DISTR, "%d    %7.21f    %7.21f    %7.21f    %7.21f
    %7.21f    %7.21f     %7.21f     %7.21f     %7.21f \n", Counter,
    stress_pout[dl], deb_len, deb_pos, z, Fiber_axial_stress[zy],
    Interfacial_shear_stress[zy], Fiber_axial_load[zy],
    Fiber_axl_load_bond_compo[zy], Fiber_axl_load_frictional_compo[zy]);
   }
}
else
{
   /*   fprintf(STRS_DISTR, "I am here \n");   */
   deb_pos=0.0;
   zy=0;
   z=0.05*zy;
   zzz=0.01;
   LZ = L-deb_len-z;
   DST_Num = ((1+Poss_m)*(1+(b*b/(a*a)-1)*(Em/Ef))*(b*b*log_ba-(b*b-
   a*a)/2));
   DST_Numerator = (2/a) * pow(DST_Num,0.5);
   DST_Denominator = (((b*b/(a*a)-1)*(Em/Ef))/tanh(Alpha*(0.01)))+
   2/(exp(Alpha*(0.01))-exp(-Alpha*(0.01)));
   debond_stress_current01  = -ISS * DST_Numerator/DST_Denominator;
   pullout_strs01 = debond_stress_current01;
   pullout_strs = debond_stress_current[dl];

    /* calculate axial stress distribution in fiber */
    FAS1 = (a*a*Ef*pullout_strs)/(a*a*Ef+(b*b-a*a)*Em);
        /*  fprintf(STRS_DISTR, "but i moved slightly 1\n");  */
    FAS2 = ((b*b/(a*a))-1) * (Em/Ef) * (exp(Alpha*z)-exp(-
   Alpha*z))/(exp(Alpha*(L-deb_len+0.00000001))-exp(-Alpha*(L-
   deb_len+0.00000001)));
        /*  fprintf(STRS_DISTR, "but i moved slightly 2\n");  */
```

```
        FAS3 = (exp(-Alpha*(L-deb_len-z)) - exp(Alpha*(L-deb_len-
       z)))/(exp(Alpha*(L-deb_len+0.00000001)) - exp(-Alpha*(L-
       deb_len+0.00000001)));
            /*  fprintf(STRS_DISTR, "but i moved slightly \n");   */
        Fiber_axial_stress[zy] = FAS1*(1+FAS2+FAS3);
       Fiber_axial_load[zy] = Fiber_axial_stress[zy] * Fiber_area;
       Fiber_axl_load_bond_compo[zy]= Fiber_axial_load[zy];
       Fiber_axl_load_frictional_compo[zy]=0.0;
       Total_bond_load = Fiber_axl_load_bond_compo[zy];
            /*  fprintf(STRS_DISTR, "but i moved slightly 3\n");  */


        /* calculate interfacial shear stress distribution   */
ISSb1 = ((b*b/(a*a))-1) * (Em/Ef) * (exp(Alpha*z) + exp(-
Alpha*z))/(exp(Alpha*(L-deb_len+0.01))-exp(-Alpha*(L-deb_len+0.01)));
ISSb2 =  (exp(-Alpha*(L-deb_len-z)) + exp (Alpha*(L-deb_len-
z)))/(exp(Alpha*(L-deb_len+0.01)) - exp(-Alpha*(L-deb_len+0.01)));
ISb3  =  ((1+Poss_m)*(1+(b*b/(a*a)-1)*(Em/Ef))*(b*b*log_ba-(b*b-a*a)/2));
ISSb3 = (2/a)* pow(ISb3, 0.5);
Interfacial_shear_stress[zy] = -pullout_strs01*((ISSb1+ISSb2)/ISSb3);
fprintf(STRS_DISTR, "%d    %7.21f    %7.21f    %7.21f    %7.21f    %7.21f
%7.21f     %7.21f     %7.21f     %7.21f \n", Counter, stress_pout[dl],
deb_len, deb_pos, z, Fiber_axial_stress[zy], Interfacial_shear_stress[zy],
Fiber_axial_load[zy], Fiber_axl_load_bond_compo[zy],
Fiber_axl_load_frictional_compo[zy]);
    }

          fprintf(STRS_DISTR, "debonded!!!!!!!!!!!!!!! \n");



    /* Calculate stress distribution in the debonded region  */
    fprintf(TEST, "separation=%7.21f \n", separation);
    for(zx=0; zx<=dl; ++zx)
    {
     if(separation==0)  /* that is when the interface is in contact in the
      debonded region */
     {
      z=0.5*zx;
      deb_pos=L-deb_len+z;
      m1z=m1*z;
      m2z=m2*z;

      /* axial stress distribution in fiber when fiber partially debonded
      */
      Fiber_axial_stress[zx] = (A3[dl]/A2) * (1-exp(m2z)) + B[dl]*(exp(m1z) -
      exp(m2z)) + debond_stress_current[dl]*exp(m2z);
      Fiber_axial_load[zx] = Fiber_axial_stress[zx] * Fiber_area;
      Fiber_axl_load_bond_compo[zx] = Total_bond_load;
      Fiber_axl_load_frictional_compo[zx]= Fiber_axial_load[zx] -
      Total_bond_load;

      /*  deb_component= debond_stress_current[dl]*exp(m2z);  */
      /*  fric_component= (A3[dl]/A2) * (1-exp(m2z)) + B[dl]*(exp(m1z) -
      exp(m2z));  */
```

```
      /*   fprintf(STRS_DISTR, "deb comp = %7.2lf  fric compo =  %7.2lf
      \n", deb_component, fric_component);  */

      /* interfacial shear stress distribution when fiber partially debonded
      */
      Interfacial_shear_stress[zx]= -(a/2)*((-A3[dl]/A2)*m2*exp(m2z) +
      B[dl]*(m1*exp(m1z) - m2*exp(m2z)) +
      debond_stress_current[dl]*m2*exp(m2z));

      /*calculate reduction in radial compressive stress due to poisson's
      contraction of fiber  */
      shrnk_strss_net[zx]=stress_shrnk-(Interfacial_shear_stress[zx]/mu -
      stress_shrnk);

      fprintf(STRS_DISTR, "%d    %7.2lf    %7.2lf    %7.2lf    %7.2lf
      %7.2lf    %7.2lf    %7.2lf    %7.2lf    %7.2lf    %7.2lf \n",
      Counter, stress_pout[dl], deb_len, deb_pos, z,
            Fiber_axial_stress[zx], Interfacial_shear_stress[zx],
      Fiber_axial_load[zx], Fiber_axl_load_bond_compo[zx],
      Fiber_axl_load_frictional_compo[zx], shrnk_strss_reduction[zx]);

     }
     else   /* that is when the interface separated in the debonded region */
     {
      z=0.5*zx;
      deb_pos=L-deb_len+z;
      m1z=m1*z;
      m2z=m2*z;

      Fiber_axial_stress[zx]=debond_stress_current[dl];
      Fiber_axial_load[zx]=Fiber_axial_stress[zx]*Fiber_area;
      Fiber_axl_load_bond_compo[zx] = Total_bond_load;
      Fiber_axl_load_frictional_compo[zx]= 0.0;

      Interfacial_shear_stress[zx]=0;
      shrnk_strss_net[zx]=stress_shrnk- (Interfacial_shear_stress[zx]/mu -
      stress_shrnk);
     }
      fprintf(STRS_DISTR, "%d    %7.2lf    %7.2lf    %7.2lf    %7.2lf
      %7.2lf    %7.2lf    %7.2lf    %7.2lf    %7.2lf    %7.2lf \n",
      Counter, stress_pout[dl], deb_len, deb_pos, z,
            Fiber_axial_stress[zx], Interfacial_shear_stress[zx],
      Fiber_axial_load[zx], Fiber_axl_load_bond_compo[zx],
      Fiber_axl_load_frictional_compo[zx], shrnk_strss_net[zx]);


    /*   fprintf(STRS_DISTR, "%d    %7.2lf    %7.2lf    %7.2lf    %7.2lf
%7.2lf    %7.2lf    %7.2lf    %7.2lf    %7.2lf    %7.2lf \n", Counter,
stress_pout[dl], deb_len, deb_pos, z, Fiber_axial_stress[zx],
Interfacial_shear_stress[zx], Fiber_axial_load[zx],
Fiber_axl_load_bond_compo[zx], Fiber_axl_load_frictional_compo[zx]);     */

    }


   ITER=ITER+1;
   }
```

```
/* ------------------------------------------------------------------ */
/*  FIBER COMPLETELY DEBONDED ALONG ITS LENGTH & IS BEING PULLED OUT  */
/* ------------------------------------------------------------------ */

   /* Calculate pullout stress (pullout case) for various pullout lengths
*/
   ITER=ITER-1;
   for(dl=0; dl<=2*L; ++dl)
   {
     po_len = 0.5*dl;
     emb_len=L-po_len;
     EMBD_LEN=2*emb_len;
     m1m2 = m1+m2;
     m1d = m1*emb_len;
     m2d = m2*emb_len;
     m1m2d = (m1+m2)* emb_len;
       SP1 = 0.0;
     SP2a=(a*a-b*b)*D*Ef*(m2*exp(m2d)-m1*exp(m1d)+(m1-m2)*exp(m1m2d));
     SP2b=(a*a-b*b)*Em*Poss_f-a*a*Ef*Poss_m;
     SP2c=(2*mu/a)*(exp(m1d)-exp(m2d));
       SP2 = ((SP2a/SP2b)-SP2c)* stress_shrnk;
     SP3a=(a*a-b*b)*Em*Poss_f*(m1*exp(m1d)-m2*exp(m2d))-a*a*Ef*Poss_m*(m1-
      m2)*exp(m1m2d);
     SP3b=(a*a-b*b)*Em*Poss_f-a*a*Ef*Poss_m;
     SP3c=2*mu*Em*Poss_f*(exp(m1d)-exp(m2d))/(a*D*Ef);
       SP3=(SP3a/SP3b)+SP3c;
       stress_pout3[dl]= (SP1+SP2)/SP3;   /* stress_pout[dl] is partial
      debond pullout stress   */
       Pullout_stress[ITER]=stress_pout3[dl];
       debond_stress_current3=0.0;
       debond_stress_current[dl]=0.0;
       Pullout_Bond_component[dl] = 0.0;
       Pullout_Friction_component[dl] = Pullout_stress[ITER];
       Pullout_Load[ITER] = Pullout_stress[ITER] * Fiber_area;
       Pullout_Load_Friction_component[dl] = Pullout_Friction_component[dl] *
       Fiber_area; Pullout_Load_Bond_component[dl] = 0.0;


     fprintf(PO_STRESSvsDL, "%7.2lf           %7.2lf             %7.2lf  \n",
      emb_len, debond_stress_current3, stress_pout3[dl]);

      /* calculate A3[dl] and B[dl] for various pullout lengths */
      A3a=stress_pout3[dl];
      A3b= (stress_shrnk/Poss_m)*(1-b*b/(a*a))*D;
        A3[dl] = -(A3a+A3b)/denom;   /* Infact, A3[dl] remains same for all
      pullout lengths */
      if(dl<2*L)
        B[dl] = (stress_pout3[dl]-(A3[dl]/A2)*(1-exp(m2d)))/(exp(m1d)-
exp(m2d));   /*B[dl] is zero for all pullout lengths */
      else
        B[dl]= 0;


  /*  calculate fiber displacement for the pullout case  */
  /* Caculate fiber displacement for the debonded portion of embedded length
      */
      USP1=A3[dl]*emb_len/(A2*Ef);
```

```
      USP2=A3[dl]*(1-exp(m2d))/(A2*m2*Ef);
      USP3=B[dl]*(((exp(m1d)-1)/m1) - ((exp(m2d)-1)/m2))/Ef;
      USP4=(exp(m2d)-1)*debond_stress_current3/(m2*Ef);
      USP[dl] = (USP1+USP2+USP3+USP4);
      mm2dexp=exp(m2d);
         /* fprintf(TEST, "USP1=%7.6lf      USP2=%7.6lf     USP3=%7.6lf
      A2=%7.2lf   m2=%8.5lf   mm2dexp=%8.5lf\n", USP1, USP2, USP3, A2, m2,
      mm2dexp);  */
         /* fprintf(TEST, "A3[2*L]=%7.2lf  B[2*L]=%100.98lf  m1dexp=%20.15lf
      m2dexp=%20.15lf  m1=%20.15lf   m2=%20.15lf  Ef=%7.2lf  USP3=%7.2lf\n",
      A3[2*L], B[2*L], m1dexp, m2dexp, m1, m2, Ef, USP3);   */
      /* calculate fiber displacement for the pulled out portion of the fiber
      */
      UP3[dl]=0.5*dl*(1+stress_pout3[dl]/Ef);

      /* Add */
      Fiber_disp[ITER] = USP[dl]+UP3[dl];
      Fiber_disp_2sides[ITER] = 2*USP[dl] +  0.5*dl*(1+2 *
stress_pout3[dl]/Ef);
       fprintf(PO_DISP, "%d   %7.2lf    %7.2lf      %9.6lf     %9.6lf
      %7.2lf     %7.2lf     %7.2lf      %7.2lf      %7.2lf      %7.2lf \n",
      ITER, po_len,  debond_stress_current[dl], Fiber_disp[ITER],
      Fiber_disp_2sides[ITER],
      Pullout_stress[ITER], Pullout_Bond_component[dl],
      Pullout_Friction_component[dl], Pullout_Load[ITER],
      Pullout_Load_Bond_component[dl], Pullout_Load_Friction_component[dl]);


     /* find area under the pullout curve
      pd_previous=parts;
      pd_last=pd-1/pd_previous;
      area[pdist]=(PO_LD_Fric[pdist]+PO_LD_Fric[pdist-1])/(2*parts);  */
     area1[ITER]=(Pullout_stress[ITER]+Pullout_stress[ITER-1])
     *(Fiber_disp[ITER]-Fiber_disp[ITER-1])/2;
     fprintf(AREA, "%d     %7.2lf      \n", dl, area1[ITER]);


    /* Calculate stress distribution in fiber and interface when fiber being
     pulled out  */
    for(zxpo=0; zxpo<=EMBD_LEN; ++zxpo)
    {
     z=0.5*zxpo;
     m1z=m1*z;
     m2z=m2*z;
     m1m2z=(m1+m2)*z;

     /* axial stress distribution in fiber when fiber partially debonded   */
         /* note: A3[dl] same for all pullout lengths */
         /* note: B[dl] same for all pullout lengths - infact equal to zero
     */
     Fiber_axial_stress[zxpo] = (A3[dl]/A2) * (1-exp(m2z)) + B[dl]*(exp(m1z)
     - exp(m2z));
       Fiber_axial_load[zxpo] = Fiber_axial_stress[zxpo] * Fiber_area;
       Fiber_axl_load_bond_compo[zxpo]= 0.0;
       Fiber_axl_load_frictional_compo[zxpo]= Fiber_axial_load[zxpo];
```

```
      /* interfacial shear stress distribution when fiber partially debonded
*/
      Interfacial_shear_stress[zxpo]= -(a/2)*((-A3[dl]/A2)*m2*exp(m2z) +
      B[dl]*(m1*exp(m1z) - m2*exp(m2z)));

      fprintf(STRS_DISTR, "%d    %7.2lf    %7.2lf    %7.2lf    %7.2lf
      %7.2lf    %7.2lf     %7.2lf     %7.2lf     %7.2lf  \n", Counter,
      stress_pout3[dl], po_len, emb_len, z, Fiber_axial_stress[zxpo],
      Interfacial_shear_stress[zxpo], Fiber_axial_load[zxpo],
      Fiber_axl_load_bond_compo[zxpo], Fiber_axl_load_frictional_compo[zxpo]);


     }

      ITER=ITER+1;
    }


}
```

Appendix C

```
/* Computer Program to Predict Pullout Load versus Displacement Response
                    Using the Progressive Debonding Model    */


#include <stdio.h>
#include <float.h>
#include <math.h>
#include <stdlib.h>
#include <memory.h>
#include <malloc.h>

#define TT 200
#define N  3

main ()
{
 FILE *input_file;
 FILE *STRS_DISTR;
 FILE *STRS_DISTR2;
 FILE *PO_DISP;
 FILE *PO_DISP2;
 FILE *DEBLEN_DEBSTRSS;
 FILE *DEBLEN_DEBSTRSS2;
 FILE *PO_STRESSvsDL;
 FILE *PO_STRESSvsDL2;
 FILE *TEST;
 FILE *TESTIN;
 FILE *AREA;


int L, dl, zz, parts, pdist;

double a, b, Poss_m, Poss_f, Em, Ef, ABS, mu, contact_stress,
Initial_debonding_stress, row, alpha, eps1, eps2, eps3, eps4, epsilon,
theta1, theta2, theta, beta1, beta, cnstnt1, cnstnt2, omega, deb_len,
deb_pos, Fiber_area, z, zzz, debond_length, omega1, LL, PDS, FD1, FD2, FAS1,
FAS2, FAS3, pd, pullout_distance, FDP1, FDP2, FDP3, FASP1, FASP2,
zero_stress, muinitial, mufinal, C, pd_previous, pd_last;

float Pullout_Bond_component[TT] [N], Pullout_Friction_component[TT] [N],
Fiber_disp_2sides[TT] [N], Pullout_Load[TT] [N],
Fiber_axial_stress[TT] [N], Interfacial_shear_stress[TT] [N],
Fiber_axial_load[TT] [N], Fiber_axl_load_bond_compo[TT] [N],
Fiber_axl_load_frictional_compo[TT] [N], ISS[TT], Fiber_displacement[TT],
Fiber_displacement2[TT], Progressive_dbnd_stress[TT],
Progressive_POstress[TT], PO_LD_Bond[TT], PO_LD_Fric[TT],
Progressive_POload[TT], area[TT], area1[TT];


input_file = fopen("inpmu","r");
STRS_DISTR = fopen("stress","w");       /* stress distribution in fiber */
STRS_DISTR2 = fopen("stress2", "w");
PO_DISP = fopen("disp","w");      /* pullout stress and fiber displacement */
PO_DISP2 = fopen("disp2", "w");
DEBLEN_DEBSTRSS = fopen("dbsdbl","w"); /*debond length vs. debond stress */
DEBLEN_DEBSTRSS2 = fopen("dbsdbl2", "w");
PO_STRESSvsDL = fopen("posdl","w");    /* pullout stress vs. debond length */
```

```
DEBLEN_DEBSTRSS2 = fopen("dbsdbl2", "w");
PO_STRESSvsDL = fopen("posdl","w");    /* pullout stress vs debond length  */
PO_STRESSvsDL2 = fopen("posdl2", "w");
TEST = fopen("testout", "w");
TESTIN = fopen("in", "w");
AREA = fopen("area", "w");


  /* read the input file */
  fscanf(input_file, "%lf  %lf  %lf  %lf  %lf  %lf  %d   %lf %lf %lf  %lf
%lf", &a, &b, &Poss_f, &Poss_m, &Em, &Ef, &L, &ABS, &mu, &contact_stress,
&mufinal, &C);

  fprintf(TESTIN, "%lf  %lf  %lf  %lf  %lf  %lf  %d   %lf %lf \n", a, b,
Poss_f,     Poss_m, Em, Ef, L, ABS, mu);

  fprintf(DEBLEN_DEBSTRSS, "Debond Length       Debond Stress \n");

/*   ABS  -  Adhesional Bond Strength    */
  row=a*a/(b*b-a*a);
  alpha=Em/Ef;
  eps1=2/(a*a*(b*log(b/a)-(b-a)));
  eps2=(0.5*b*b*b*log(b/a)-b*(b*b-a*a)/4);
  eps3=0.5*a*(b*b-a*a);
  eps4=(b*b-a*a)/3;
  epsilon=eps1*(eps2+eps3-eps4);
  theta1=a*a*(1+Poss_m);
  theta2=(b/(b-a))*log(b/a)-1;
  theta=1/(theta1*theta2);
  beta1= (theta*(row+alpha-row*epsilon*alpha)/(row*epsilon))+alpha*theta;
  beta=pow(beta1,0.5);
  cnstnt1=row+alpha-row*epsilon*alpha+alpha*epsilon;
  cnstnt2=alpha-row*epsilon*alpha+alpha*epsilon;
  omega1=(Ef/Em)*((a*a+b*b)/(b*b-a*a)+Poss_m)+(1-Poss_f);
  omega=Poss_f/omega1;
  Fiber_area = 3.14*a*a;

  fprintf(PO_DISP, "Deb Len   Dbnd Strs   PO Strs   Fib Disp   Progr PO Ld
Bnd   PO Ld   Fric PO Ld\n");
  fprintf(PO_DISP2, "Deb Len   Dbnd Strs   PO Strs   Fib Disp2   Progr PO Ld
     Bnd PO Ld   Fric PO Ld\n");
  fprintf(STRS_DISTR, "Dbnd Strs  Deb Lt  Deb Pos  Axl Pos  Axl Strs  Shr
Strs        Axl Lod  Bnd Ld  Fric Ld \n");
  fprintf(PO_STRESSvsDL, "PO Strss   Deb Len   Prog Dbnd Strss \n");
  fprintf(AREA, "pdist  pd_previous  pd  area \n");
  fprintf(TESTIN, "alpha=%10.5lf   beta=%10.5lf   row=%10.5lf
epsilon=%10.5lf   omega=%7.5lf \n", alpha, beta, row, epsilon, omega);
```

```
/*  ------------------------------------------------------------------------*/
/*  Fiber completely bonded along the entire embedded fiber length          */
/*  ------------------------------------------------------------------------*/

  deb_len=0.0;
  deb_pos=0.0;
  dl=deb_len;
  zero_stress=0.0;
  Initial_debonding_stress=-2*ABS*(row+alpha-
  row*epsilon*alpha+alpha*epsilon)*sinh(beta*L)/((a*beta)*((alpha-
  row*epsilon*alpha+alpha*epsilon)*cosh(beta*L)+row));
  Progressive_dbnd_stress[dl]=Initial_debonding_stress;
  Progressive_POstress[dl] = zero_stress;
  Progressive_POload[dl]=0.0;
  PO_LD_Bond[dl]=0.0;
  PO_LD_Fric[dl]=0.0;
  Fiber_displacement[dl]=zero_stress/(Ef*(row+alpha-
  row*epsilon*alpha+alpha*epsilon))*((alpha-row*epsilon*alpha+alpha*epsilon-
  row)*(cosh(beta*L)-1)/(beta*sinh(beta*L))+row*L);
  Fiber_displacement2[dl] = 2*Fiber_displacement[dl];
  fprintf(PO_DISP, "%7.21f   %7.21f   %7.21f   %7.51f       %7.21f
  %7.21f      %7.21f\n", deb_len, Progressive_dbnd_stress[dl],
  Progressive_POstress[dl], Fiber_displacement[dl], Progressive_POload[dl],
  PO_LD_Bond[dl], PO_LD_Fric[dl]);
  fprintf(PO_DISP2, "%7.21f   %7.21f   %7.21f   %7.51f       %7.21f
  %7.21f      %7.21f\n", deb_len, Progressive_dbnd_stress[dl],
  Progressive_POstress[dl],   Fiber_displacement2[dl],
  Progressive_POload[dl], PO_LD_Bond[dl],       PO_LD_Fric[dl]);

  deb_len=0.0;
  deb_pos=0.0;
  dl=deb_len;
  Initial_debonding_stress=-2*ABS*(row+alpha-
  row*epsilon*alpha+alpha*epsilon)*sinh(beta*L)/((a*beta)*((alpha-
  row*epsilon*alpha+alpha*epsilon)*cosh(beta*L)+row));
  Progressive_dbnd_stress[dl]=Initial_debonding_stress;
  Progressive_POstress[dl] = Initial_debonding_stress;
  Progressive_POload[dl]=Progressive_POstress[dl]*Fiber_area;
  PO_LD_Bond[dl]=Progressive_dbnd_stress[dl]*Fiber_area;
  PO_LD_Fric[dl]=Progressive_POload[dl]-PO_LD_Bond[dl];
  Fiber_displacement[dl]=Initial_debonding_stress/(Ef*(row+alpha-
  row*epsilon*alpha+alpha*epsilon))*((alpha-row*epsilon*alpha+alpha*epsilon-
  row)*(cosh(beta*L)-1)/(beta*sinh(beta*L))+row*L);
  Fiber_displacement2[dl] = 2*Fiber_displacement[dl];
  fprintf(PO_DISP, "%7.21f   %7.21f   %7.21f   %7.51f       %7.21f
  %7.21f      %7.21f\n", deb_len, Progressive_dbnd_stress[dl],
  Progressive_POstress[dl], Fiber_displacement[dl], Progressive_POload[dl],
  PO_LD_Bond[dl], PO_LD_Fric[dl]);
  fprintf(PO_DISP2, "%7.21f   %7.21f   %7.21f   %7.51f       %7.21f
  %7.21f      %7.21f\n", deb_len, Progressive_dbnd_stress[dl],
  Progressive_POstress[dl], Fiber_displacement2[dl], Progressive_POload[dl],
  PO_LD_Bond[dl], PO_LD_Fric[dl]);
```

```
/*  fprintf(PO_DISP, "%7.2lf   %7.2lf   %7.2lf   %7.5lf \n", deb_len,
      Progressive_dbnd_stress[dl], Progressive_POstress[dl],
      Fiber_displacement[dl]);      */
/*  fprintf(PO_DISP2, "%7.2lf   %7.2lf   %7.2lf   %7.5lf \n", deb_len,
      Progressive_dbnd_stress[dl], Progressive_POstress[dl],
      Fiber_displacement2[dl]);      */
  fprintf(PO_STRESSvsDL, "%7.2lf   %7.2lf   %7.2lf \n",
      Progressive_POstress[dl], Fiber_displacement[dl],
      Progressive_dbnd_stress[dl]);

  parts=2;
  for(zz=0; zz<=parts*L; ++zz)
  {
   deb_len=0.0;
   deb_pos=0.0;
   zzz=zz;
   z=zzz/parts;

   Fiber_axial_stress[zz] [1] =
      (Initial_debonding_stress/cnstnt1)*(cnstnt2*sinh(beta*z)/sinh(beta*L)-
   row*sinh(beta*(L-z))/sinh(beta*L)+row);
   Interfacial_shear_stress[zz] [1] =  -
   (a*beta*Initial_debonding_stress/(2*cnstnt1))*(cnstnt2*cosh(beta*z)/sinh(b
   eta*L)+row*cosh(beta*(L-z))/sinh(beta*L));
   ISS[zz] = -
   (a*beta*Initial_debonding_stress/(2*cnstnt1))*(cnstnt2*cosh(beta*z)/sinh(b
   eta*L)+row*cosh(beta*(L-z))/sinh(beta*L));
   Fiber_axial_load[zz] [1] = Fiber_axial_stress[zz] [1] * Fiber_area;
   Fiber_axl_load_bond_compo[zz] [1] = Fiber_axial_load[zz] [1];
   Fiber_axl_load_frictional_compo[zz] [1] = 0.0;
   fprintf(TESTIN, "%lf  %lf\n", Initial_debonding_stress,
   Fiber_displacement);
   fprintf(STRS_DISTR, "%7.2lf  %7.2lf  %7.2lf  %7.2lf  %7.2lf  %7.2lf
   %7.2lf   %7.2lf  %7.2lf \n", Initial_debonding_stress, deb_len, deb_pos,
   z, Fiber_axial_stress[zz] [1], Interfacial_shear_stress[zz] [1],
   Fiber_axial_load[zz] [1], Fiber_axl_load_bond_compo[zz] [1],
   Fiber_axl_load_frictional_compo[zz] [1]);

  }

/*  ------------------------------------------------------ */
/*  Fiber partially bonded along its embedded length       */
/*  ------------------------------------------------------ */

  for(dl=0; dl<=parts*L; ++dl)
  {
   debond_length=dl;
   deb_len=debond_length/parts;
   deb_pos=L-deb_len;

   LL=parts*L;
   if(dl<LL)
   /* calculate progressive debonding stress */
    Progressive_dbnd_stress[dl]=-2*ABS*(row+alpha-
   row*epsilon*alpha+alpha*epsilon)*sinh(beta*(L-deb_len))/((a*beta)*((alpha-
   row*epsilon*alpha+alpha*epsilon)*cosh(beta*(L-deb_len))+row));
   else
```

```
  Progressive_dbnd_stress[dl]=0.0;


/* calculate progressive pullout stress and fiber displacement */
Progressive_POstress[dl]=-
contact_stress/omega+(Progressive_dbnd_stress[dl]+contact_stress/omega)*exp
(-2*mu*omega*deb_len/a);
 if(Progressive_POstress[dl]<Progressive_dbnd_stress[dl])
   Progressive_POstress[dl]=Progressive_dbnd_stress[dl];
      Progressive_POload[dl]=Progressive_POstress[dl]*Fiber_area;
      PO_LD_Bond[dl]=Progressive_dbnd_stress[dl]*Fiber_area;
      PO_LD_Fric[dl]=Progressive_POload[dl]-PO_LD_Bond[dl];
FD1=Progressive_dbnd_stress[dl]/(Ef*(row+alpha-
    row*epsilon*alpha+alpha*epsilon))*((alpha-
row*epsilon*alpha+alpha*epsilon-row)*(cosh(beta*(L-deb_len))-
1)/(beta*sinh(beta*(L-deb_len+0.000000001)))+row*(L-deb_len));
FD2=-contact_stress*deb_len/(Ef*omega)-
a/(2*Ef*mu*omega)*(Progressive_dbnd_stress[dl]+contact_stress/omega)*(exp(-
2*mu*omega*deb_len/a)-1);
Fiber_displacement[dl]=FD1+FD2;
Fiber_displacement2[dl] = 2*Fiber_displacement[dl];
fprintf(PO_DISP, "%7.21f   %7.21f   %7.21f   %7.51f       %7.21f
%7.21f      %7.21f\n", deb_len, Progressive_dbnd_stress[dl],
Progressive_POstress[dl], Fiber_displacement[dl], Progressive_POload[dl],
PO_LD_Bond[dl], PO_LD_Fric[dl]);
fprintf(PO_DISP2, "%7.21f   %7.21f   %7.21f   %7.51f       %7.21f
%7.21f      %7.21f\n", deb_len, Progressive_dbnd_stress[dl],
Progressive_POstress[dl],   Fiber_displacement2[dl],
Progressive_POload[dl], PO_LD_Bond[dl],       PO_LD_Fric[dl]);
fprintf(PO_STRESSvsDL, "%7.21f   %7.21f   %7.21f \n",
    Progressive_POstress[dl], Fiber_displacement[dl],
    Progressive_dbnd_stress[dl]);

/* calculate fiber axial stress distribution & interfacial shear stress
    distribution  */
/* over the bonded zone of the partially debonded fiber  */
for(zz=0; zz<=parts*L-dl; ++zz)
{
 zzz=zz;
 z=zzz/parts;

 Fiber_axial_stress[zz] [2] =
    (Progressive_dbnd_stress[dl]/cnstnt1)*(cnstnt2*sinh(beta*z)/sinh(beta*(
 L-deb_len))-row*sinh(beta*(L-deb_len-z))/sinh(beta*(L-deb_len))+row);
 Interfacial_shear_stress[zz] [2] =  -
 (a*beta*Progressive_dbnd_stress[dl]/(2*cnstnt1))*(cnstnt2*cosh(beta*z)/sin
 h(beta*(L-deb_len+0.000001))+row*cosh(beta*(L-deb_len-z))/sinh(beta*(L-
 deb_len+0.000001)));
 Fiber_axial_load[zz] [2] = Fiber_axial_stress[zz] [2] * Fiber_area;
 Fiber_axl_load_bond_compo[zz] [2] = Fiber_axial_load[zz] [2];
 Fiber_axl_load_frictional_compo[zz] [2] = 0.0;
 /* fprintf(TESTIN, "%lf  %lf\n", Initial_debonding_stress,
    Fiber_displacement);  */
 fprintf(STRS_DISTR, "%7.21f  %7.21f  %7.21f  %7.21f  %7.21f  %7.21f
 %7.21f  %7.21f  %7.21f \n", Progressive_dbnd_stress[dl], deb_len, deb_pos,
 z, Fiber_axial_stress[zz] [2], Interfacial_shear_stress[zz] [2],
```

```
 Fiber_axial_load[zz] [2], Fiber_axl_load_bond_compo[zz] [2],
 Fiber_axl_load_frictional_compo[zz] [2]);
}

/* calculate fiber axial stress distribution & interfacial shear stress
    distribution  */
/* over the debonded zone of the partially debonded fiber  */
for(zz=parts*L-dl; zz<=parts*L; ++zz)
{
 zzz=zz;
 z=zzz/parts;
 FAS1=contact_stress/omega;
 FAS2=Progressive_dbnd_stress[dl]+contact_stress/omega;
 FAS3=exp(2*omega*mu*(L-deb_len)/a)*exp(-2*omega*mu*z/a);
 Fiber_axial_stress[zz] [2]=-FAS1+FAS2*FAS3;
 Interfacial_shear_stress[zz] [2]=mu*omega*FAS2*FAS3;
 Fiber_axial_load[zz] [2] = Fiber_axial_stress[zz] [2] * Fiber_area;
 Fiber_axl_load_bond_compo[zz] [2] = Progressive_dbnd_stress[dl] *
 Fiber_area;
 Fiber_axl_load_frictional_compo[zz] [2] = Fiber_axial_load[zz] [2] -
    Fiber_axl_load_bond_compo[zz] [2];
 /* fprintf(TESTIN, "%lf  %lf\n", Initial_debonding_stress,
    Fiber_displacement);  */
 fprintf(STRS_DISTR, "%7.2lf  %7.2lf  %7.2lf  %7.2lf  %7.2lf  %7.2lf
 %7.2lf  %7.2lf  %7.2lf \n", Progressive_dbnd_stress[dl], deb_len, deb_pos,
 z, Fiber_axial_stress[zz] [2], Interfacial_shear_stress[zz] [2],
 Fiber_axial_load[zz] [2], Fiber_axl_load_bond_compo[zz] [2],
 Fiber_axl_load_frictional_compo[zz] [2]);

}

}

/*  ------------------------------------------------------ */
/*  Fiber completely debonded along its length             */
/*  ------------------------------------------------------ */

muinitial=mu;
for(pdist=0; pdist<=parts*L; ++pdist)
{
 pullout_distance=pdist;
 pd=pullout_distance/parts;
  /* L_new=L-pout_dist; */
 Progressive_dbnd_stress[pdist]=0.0;

/* calculate mu  */
mu=(muinitial-mufinal)*exp(-C*pd)+mufinal;

/* calculate progressive pullout stress and fiber displacement */
Progressive_POstress[pdist]=-contact_stress/omega*(1-exp(-2*mu*omega*(L-
    pd)/a));
Progressive_POload[pdist]=Progressive_POstress[pdist]*Fiber_area;
PO_LD_Fric[pdist]=Progressive_POload[pdist];
PO_LD_Bond[pdist]=0.0;
FDP1=contact_stress/(Ef*omega);
FDP2=a/(2*mu*omega)*(exp(-2*mu*omega*(L-pd)/a)-1);
FDP3=pd*(1-exp(-2*mu*omega*(L-pd)));
```

```
  Fiber_displacement[pdist]=pd-FDP1*((L-pd)+FDP2+FDP3);
  Fiber_displacement2[pdist] = pd-FDP1*(2*(L-pd)+2*FDP2+FDP3);
  fprintf(PO_DISP, "%7.2lf   %7.2lf   %7.2lf   %7.5lf       %7.2lf
  %7.2lf      %7.2lf\n", pd, Progressive_dbnd_stress[pdist],
      Progressive_POstress[pdist], Fiber_displacement[pdist],
      Progressive_POload[pdist], PO_LD_Bond[pdist], PO_LD_Fric[pdist]);
  fprintf(PO_DISP2, "%7.2lf   %7.2lf   %7.2lf   %7.5lf       %7.2lf
  %7.2lf      %7.2lf\n", pd, Progressive_dbnd_stress[pdist],
      Progressive_POstress[pdist], Fiber_displacement2[pdist],
      Progressive_POload[pdist], PO_LD_Bond[pdist], PO_LD_Fric[pdist]);
  fprintf(PO_STRESSvsDL, "%7.2lf   %7.2lf   %7.2lf \n",
      Progressive_POstress[pdist], Fiber_displacement[pdist],
      Progressive_dbnd_stress[pdist]);

  /* find area under the pullout curve  */
  pd_previous=parts;
  pd_last=pd-1/pd_previous;
  area[pdist]=(PO_LD_Fric[pdist]+PO_LD_Fric[pdist-1])/(2*parts);
  area1[pdist]=(PO_LD_Fric[pdist]+PO_LD_Fric[pdist-
  1])*(Fiber_displacement[pdist]-Fiber_displacement[pdist-1])/2;
  fprintf(AREA, "%d   %7.2lf      %7.2lf       %7.2lf         %7.2lf\n",
  pdist, pd_last, pd, area[pdist], area1[pdist]);


  /* calculate fiber axial stress distribution & interfacial shear stress
      distribution  */
  /* over the debonded zone of the partially debonded fiber  */

  for(zz=0; zz<=parts*(L-pd); ++zz)
  {
   zzz=zz;
   z=zzz/parts;
   FASP1=contact_stress/omega;
   FASP2=exp(-2*omega*mu*z/a);
   Fiber_axial_stress[zz] [3]=-FASP1*(1-FASP2);
   Interfacial_shear_stress[zz] [3]=mu*contact_stress*FASP2;
   Fiber_axial_load[zz] [3] = Fiber_axial_stress[zz] [3] * Fiber_area;
   Fiber_axl_load_bond_compo[zz] [3] = Progressive_dbnd_stress[pdist] *
      Fiber_area;
   Fiber_axl_load_frictional_compo[zz] [3] = Fiber_axial_load[zz] [3] -
      Fiber_axl_load_bond_compo[zz] [2];
   fprintf(STRS_DISTR, "%7.2lf  %7.2lf  %7.2lf  %7.2lf  %7.2lf  %7.2lf
%7.2lf      %7.2lf  %7.2lf \n", Progressive_dbnd_stress[pdist], pd, z, z,
      Fiber_axial_stress[zz] [3], Interfacial_shear_stress[zz] [3],
      Fiber_axial_load[zz] [3],
      Fiber_axl_load_bond_compo[zz] [3], Fiber_axl_load_frictional_compo[zz]
      [3]);

  }


  }
}
```